

CHAPTER 5: THICK LIQUID BLANKET CONCEPT

Contributors

Lead Author: Alice Ying

UCLA: Karani Gulec, Neil Morley, Sergy Smolentsev, Mahmoud Youssef, Tom
Sketchley, Mohamed Abdou

ORNL: Brad Nelson, Paul Fogarty, Steve Zinkle

LLNL: Ralph Moir (with assistance from M. Ohnishi on FRC), Tom Rognlien, Marv
Resnink

ANL: Dai-Kai Sze

UW: Hesham Khater, John Santarius

5. THICK LIQUID BLANKET CONCEPT

5.1 Introduction

The advantages of high power density, high reliability due to simplicity, high availability and reduced activation of materials, resulting from elimination of the first wall by replacing it with a flowing liquid of about seven mean free paths thickness (~0.5 m of Flibe), are both enormous and quite possibly necessary to make fusion practical and economical. Our emphasis here is to show feasibility, that is, how can one make liquid walls work? The first job is to produce the liquid flow configuration. This involves inlet nozzle designs that avoids “drips”, a free surface flow section, and an exit nozzle that accepts the flow and converts it from a free surface flow to a channel (pipe) flow.

Candidate liquids are molten salt (Flibe) and liquid metals such as Li or $\text{Sn}_{75}\text{Li}_{25}$. Molten salt has such low electrical conductivity that it will flow virtually unimpeded across magnetic fields. Electric field induced galvanic corrosion must be considered. Liquid metals have such a high electrical conductivity that they will not flow across the magnetic field unless insulators are employed to block the induced flow of current that generates strong drag. These insulators then become an integral part of the flow configuration and will become a critical R&D item.

The power emanating from the burning plasma striking the liquid will cause its surface temperature to rise as it passes along the walls of the chamber. Evaporation from the liquid impinges on the edge plasma or the corona surrounding the burning core plasma. The ability of the edge plasma to shield the core plasma from contamination by the evaporating liquid is the primary feasibility issue with liquid walls for magnetic fusion and is the subject of Chapter 12 of this report. The contamination in the core plasma from Li or F (and other elements) must be so low that its radiation does not drain away too much of the fusion power as to lose ignition or in other words to put out the fusion fire. About 20% of the fusion power is in the form of helium that can be used to heat new fuel. Radiation by contaminants will cut into this fraction. Also, contaminants tend to dilute the fusion fuel, lower the fusion power density, and thereby hurting economics.

The potential benefits of liquid walls over solid walls can be illustrated through system analysis. Example calculations were performed for field-reversed configurations (FRCs) using WISC (Wisconsin Systems Code). The physics and engineering models used in the present analysis are standard models (for example, see Ref. [1]), and details are described in a related paper that analyzes a D-T FRC power plant with solid walls [2]. The global power balance flow diagram is shown in Figure 5.1-1 [2]. Total powers are calculated by integrating over radial profiles.

Although WISC presently does not include models for liquid-walled power plants, we have run it with solid-wall models using APEX limits on the neutron wall load. In addition, the current-drive input power has been legislated to be 40 MW, because the power required for current drive by compact-toroid injection remains uncertain. The solid-wall case invokes rotating magnetic field (RMF) current drive [3]. The resulting

case is exhibited in Table 5.1-1; it leads to feasible engineering parameters and what would most likely be an economically attractive power plant. For comparison, a more conventional, solid-walled D-T FRC power plant case also appears in Table 5.1-1. Both have been assumed to have thermal efficiency=0.40. Although the calculations are approximate, the resulting mass of the solid-wall FRC is over three times as large as that of the liquid-wall FRC, indicating that liquid walls, if proved viable, would likely give a considerable cost savings.

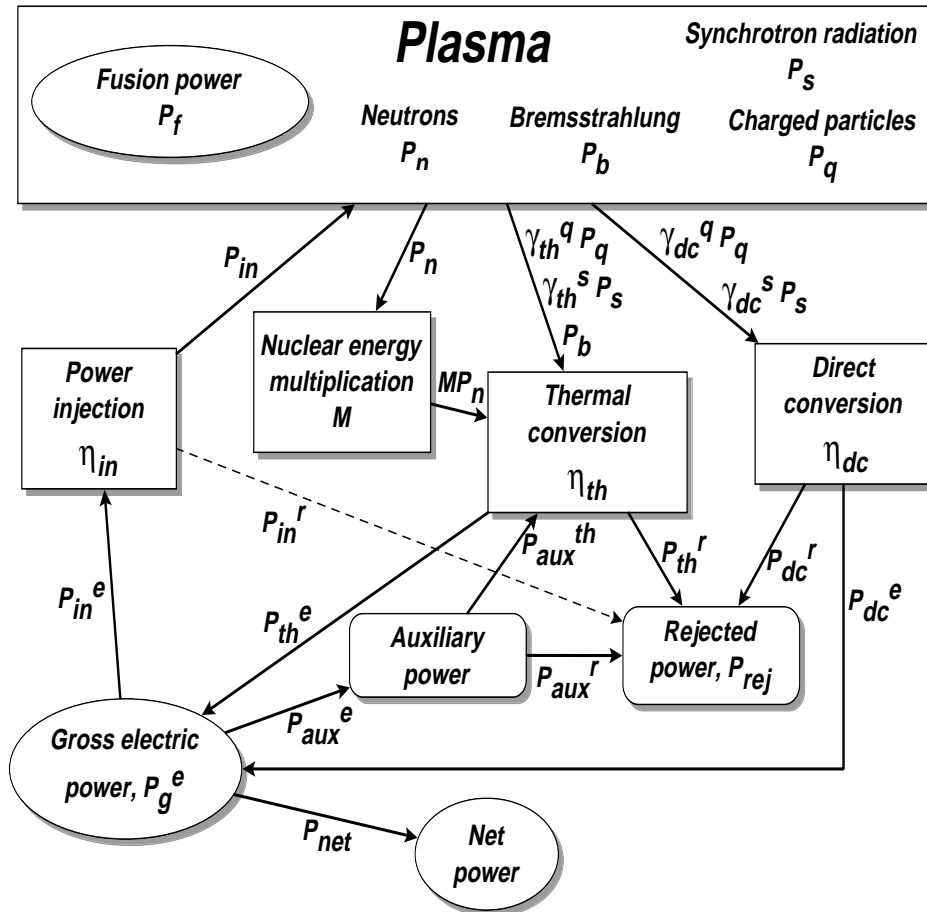


Figure 5.1-1 Global power balance flow used in WISC.

This chapter discusses the present state of understanding of thick liquid blanket concepts. While their feasibility is not assured, success would profoundly improve the prospects for magnetic fusion energy to compete in the future energy marketplace.

Table 5.1-1 Typical D-T FRC Power Plant Parameters.

	Liquid-Wall FRC	Solid-Wall FRC
Wall radius, m	1.5	2.0
Separatrix radius, m	0.39	0.88
Separatrix length, m	8	25
Core plasma volume, m ³	3.1	49
First-wall area, m ²	75	314
Average ion temperature, keV	12	13
Average ion density, 10 ²⁰ m ⁻³	18	4.3
Peak ion density, 10 ²⁰ m ⁻³	38	8.8
Z _{eff}	1.5	1.5
Volume-averaged beta	0.97	0.90
Magnetic field, T	4.6	2.4
Energy confinement time, s	0.08	0.31
Ash particle confinement time, s	0.16	0.62
Neutron wall load, MW/m ²	25	6.2
Surface heat load, MW/m ²	1.1	0.24
Neutron power, MW	1902	1947
Bremsstrahlung radiation power, MW	82	75
Charged-particle transport power, MW	435	454
Input power, MW	40	40
Fusion power, MW	2379	2436
Thermal conversion efficiency	0.40	0.40
Fusion core mass, Mg	572	1988
Net electric power, MWe	1000	1000

5.1 References

- 1 Bathke, C.G. and the ARIES Team, "Systems Analysis in Support of the Selection of the ARIES-RS Design Point," *Fusion Engineering and Design* **38**, 59 (1997).
- 2 Nguyen, C.N., et al., "Systems Analysis of a D-T Field-Reversed Configuration Power Plant," in preparation (1999).
- 3 Hoffman, A.L., "Flux Buildup in Field Reversed Configurations Using Rotating Magnetic Fields," *Physics of Plasmas* **5**, 979 (1998).

5.2 Description and Rationale

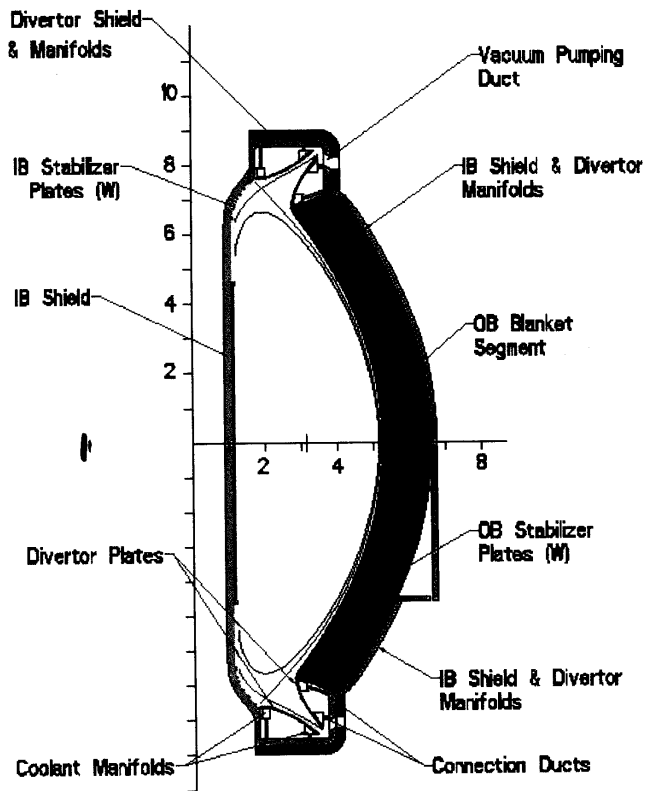
The free surface liquid first-wall/blanket concept is an innovative approach that involves flowing liquid layer around the plasma to serve the function of first wall, blanket, and divertor (heat and particle extraction, tritium breeding, etc.). Ideally, only liquids (with little or no structural materials) are contained inside the vacuum vessel. The liquid wall is considered to have the capability to tremendously enhance the attractiveness of fusion as an energy source. Compared to traditional solid first wall/shield blanket concepts, the liquid wall/liquid blankets offer the following major advantages:

- Liquid first-wall/blanket concept allows for a renewable first wall surface with a very high power density capability.
- Neutronically thick liquid first-wall/blanket concept will dramatically reduce radiation damage and activation in structural materials.
- Lower failure rates, particularly because of elimination of welds in high radiation field regions.
- Easier maintainability of in-vessel components.
- Improved tritium breeding potential.
- Liquid first-wall/blanket concept is applicable to a wide range of confinement schemes.
- Less material constraint problems
- Liquid first-wall/blanket concept reduces R&D requirements concerning both cost and time scale. Required facilities are simpler and cheaper because they reduce the need for testing in the nuclear environment.

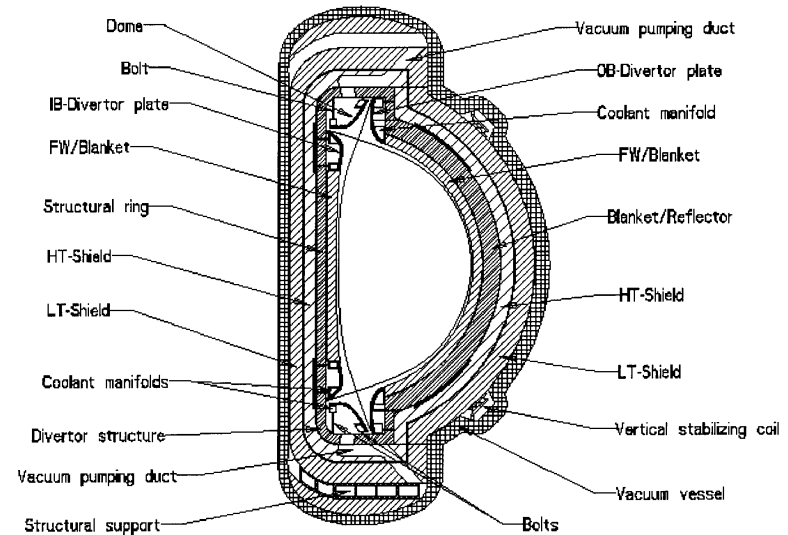
In this section, design ideas for establishing thick liquid walls are addressed for use in the Tokamak (such as ARIES-RS), Spherical Torus (ST), and Field Reverse Configuration (FRC). The fact that structural wall topologies differ among confinement schemes requires different liquid wall design approaches. For example, the swirling liquid layer idea is more applicable to the ST configuration than to the ARIES-RS configuration (see Figure 5.2-1). This is because the ST geometry has a larger radius of curvature in the poloidal direction (~8.0 m. vs. ~ 4.0 m) and a smaller radius of curvature in the toroidal direction relative to the poloidal direction (5.0 m as compared to 8.0 m). Toroidal rotation of the liquid layer may result in a substantial increase in the centrifugal acceleration of the flow towards the back wall (266 % at the inlet and 160 % at mid plane). The ST is higher than the ARIES-RS (~12.0 m. vs. ~ 6.0 m) and the effect of gravity in the hydrodynamic characteristics of the flow is more important and requires additional passive mechanisms to overcome thinning. However, being highly elongated, the fluid takes more time to travel through the chamber if only one coolant stream is used. This implies that the free surface side may be over heated from a long exposure time. As another confinement scheme example, a typical FRC reactor can be viewed as a long cylinder in which a football shape of plasma lies at the center of the chamber (see Figure 5.2-2). The FRC confinement scheme appears more amenable to thick liquid walls due to its geometrical simplicity.

Figure 5.2-1 Hydrodynamics Configurations of Thick Liquid Walls may be Very Different for ARIES-RS and ARIES-ST. Both configurations are converted to single null at the bottom of the plasma compatible with liquid wall configuration.

Elevation View of ARIES-ST Blanket/Divertor



	ARIES-RS	ARIES-ST
Major Radius (m)	5.52	2.8
Minor Radius (m)	1.38	2
Plasma Aspect Ratio	4	1.4
Elongation		3.75
Fusion Power (MW)	5480	5470
(Modified for APEX)		
FW Surface Area (m ²)	438.8	541
Neutron Wall Load (MW/m ²)	10	8.085
Surface Heat Flux (MW/m ²)	2	2



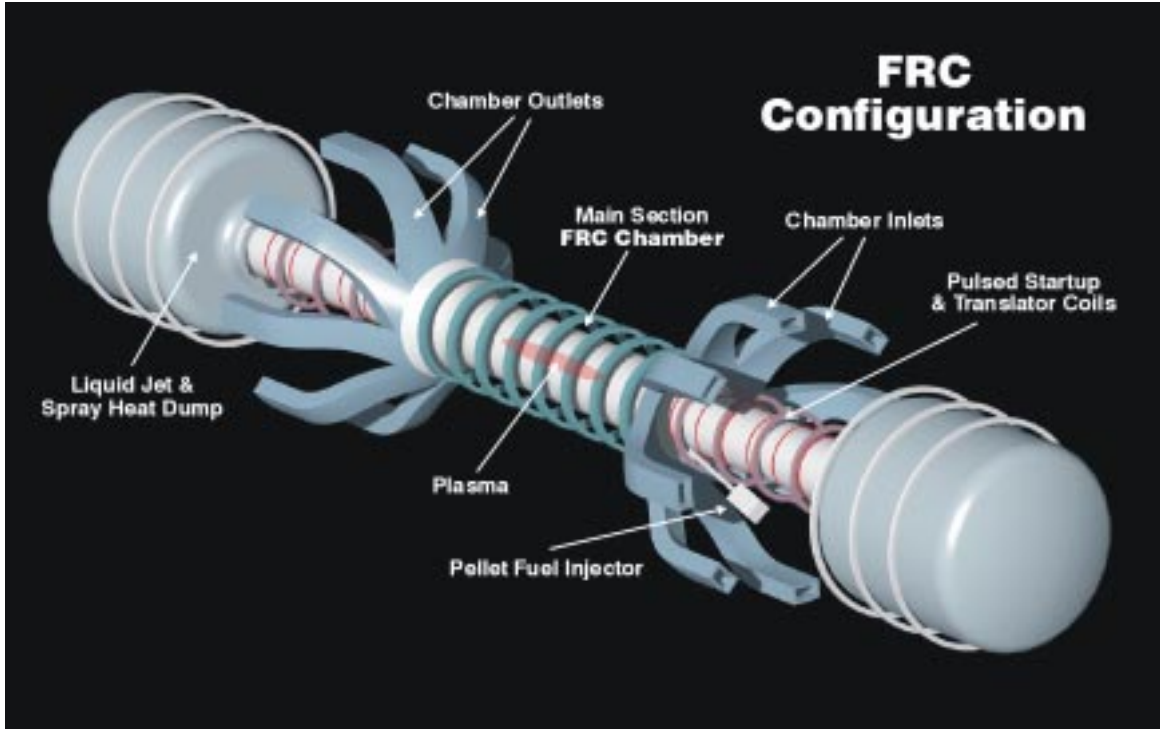


Figure 5.2-2 General layout of a FRC power plant design.

5.2.1 Application of Thick Liquid Walls to Tokamak Configurations

Design exploration of a thick liquid wall in a tokamak configuration has been guided by the following functional requirements: **1)** remove a surface heat flux of 2 MW/m^2 , yet remain compatible with the plasma operation, **2)** provide adequate tritium breeding and radiation shielding, **3)** achieve high thermal conversion efficiency, and **4)** allow for simplified maintenance and fast replacement time. A typical thick liquid FW/blanket wall involves an inlet nozzle array to inject the fluid, a central region of liquid flowing over a curved solid surface while facing the plasma, and an outlet collector to receive the fluid and convert the free surface flow to a channel flow. In order to incorporate the liquid wall into the reactor, the double null ARIES-RS is converted to a single null configuration in order to provide space for piping and liquid-forming manifolds. Conceptually, a thick liquid FW/blanket design concept for an advanced tokamak configuration is shown in Figure 5.2-3. In addition, hydrodynamics parameters of three candidate fluids for thick wall concepts in typical tokamak device are shown in Table 5.2.1.

The simplest way to form a thick Flibe liquid FW/blanket is to propel the liquid using gravitational and momentum forces. Such type of flow has been modeled with FLOW-3D [1]; it is a 3-D, time-dependent Navier-Stokes Solver that uses Reynolds Averaged Navier-Stokes (RANS) Equation for turbulence modeling and the volume of fluid (VOF) free surface tracking algorithm of free surface incompressible fluid flow. FLOW-3D results, as shown in Figure 5.2-4, demonstrate that stable, thick fluid

configuration can be established and maintained throughout a tokamak confinement configuration.

Table 5.2-1 Hydrodynamic Parameters for Thick Liquid FW/Blankets.

Property		Flibe (550C)	Lithium (500C)	Tin-Lithium ^{*1}
Composition	Mole %	66%LiF, 34%BeF2	100% Li	80% Sn, 20% Li
Melting Point, T _m	K	733	459	599
Density, ρ	Kg/m³	2011	485	6800
Dynamic Viscosity, μ	Kg/ms	0.0116	0.32x10 ⁻³	1.2x10 ⁻³
Electrical Cond., σ	1/Ωm	184	2.83x10 ⁶	1.67x10 ⁶
Thermal Cond., k	W/mK	1.06	49.6	33.44
Specific Heat, C _p	J/KgK	2380	4170	317
Surface Tension, γ	N/m	0.2	0.35	0.53

Thick Liquid Hydrodynamic Parameters

Liquid Thickness, D	m	0.45	0.40	0.40
Liquid Velocity, V	m/s	8.1	10	10
Channel ½ Width, W	m	0.68	0.57	0.07
Flow Length, L	m	8	8	8
Toroidal Field, B _T	T	8	8	8
Radial Field, B _R	T	0.2	0.2	0.2
Radius of Curvature, R	m	6.7	6.7	6.7

Dimensionless Numbers

Aspect Ratio, β	D/W	0.66	0.70	5.7
Reynolds No., Re	DVρ/μ	6.32x10 ⁵	6.187x10 ⁶	2.27x10 ⁶
Hartmann No., Ha _T	B_TW(σ/μ)^{1/2}	685.14	4.288x10 ⁵	2.09x10 ⁴
Modified Hartmann, Ha _D	Ha_Tβ²	453.3	3.0x10 ⁵	1.19x10 ⁵
Radial Hartmann, Ha _R	B_RW(σ/μ)^{1/2}	17.12	1.0x10 ⁴	522.5
Interaction No., N ^{*2}	(Ha_D)²/Re	0.325	1.46x10 ⁴	6249
Froude No., Fr _L	V²/(gD)	0.836	1.275	1.275
Froude No., Fr _C	V²/(gR)	1	1.52	1.52
Thermal Diffusivity,	k/(ρC_p)	2.2x10 ⁻⁷	2.4x10 ⁻⁵	1.5x10 ⁻⁵
Prandtl No., Pr	C_pμ/k	25.56	0.0269	0.0114
Modified Reynolds ^{*3}	Re/(Ha_Tβ)	1394	20.62	19.07
Expected MHD impact		Heat transfer	Velocity profile	Pressure drop

*1 Data is taken from Sn (Section 5-8). No data is available for Tin-Lithium yet.

*2 Interaction Number indicates effect of MHD on heat transfer (40% reduction on heat transfer coefficient based on the closed channel data at N=0.325)

*3 Modified Reynolds Number scales amount of turbulence. (>500 indicates turbulence)

Nevertheless the analyses indicate that some amount of thinning results from the gravitational acceleration and flow area expansions as the flow proceeds downstream. As shown, the fluid thickness is reduced by about a factor of 2 at the reactor midplane for an initial injection velocity of 8 m/s. This thinning reduces the liquid's potential for radiation protection of solid walls behind it and creates an unfavorable situation for shielding. The jet thinning effect can be overcome by increasing the initial jet velocity; and a fairly uniform thick liquid film can be obtained throughout the plasma core if the jet is injected at velocities of 15 m/s or above. Another approach to the thinning problem is to start out with more thick fluid than 0.5 m.

The thinning effect due to the gravitational acceleration can be offset by the MHD drag from the Hartmann velocity profile in a liquid metal flow. Numerical analyses are performed to determine whether or not an insulator is needed for free surface Liquid Metal Magnetohydrodynamics (LMMHD) flow, and to define the initial velocity of lithium that enables a uniform thickness to be maintained throughout the plasma chamber in the presence of the toroidal magnetic field. The preliminary analysis shows that the MHD drag effect significantly increases the layer thickness and causes the associated reduction in the velocity. Thus, there is a need of insulators for a free liquid metal flow if a segmented toroidal liquid metal flow configuration is considered. MHD analyses have shown that an almost perfectly uniform, thick (40 cm) lithium wall can be formed throughout the reactor in an insulated open channel at a velocity of about 10 m/s. This is slightly lower than the velocity required for Flibe to form a uniform thick liquid wall. Details of the discussion on the analyses and results are addressed in Section 5.4.1. No accounting for effects from developing flow and field gradients are included in these preliminary analyses.

These hydrodynamic calculations (with or without the effect of magnetic field) indicate that a fairly uniform thick liquid wall can be formed in the aforementioned fusion relevant configurations as long as the injected fluid carries an adequate initial momentum (e.g., corresponding to a velocity of 10 m/s). Moreover, the pumping power requirement becomes less of a concern for higher and higher power density confinement concepts as shown in Figure 5.2-5.

Regarding the accommodation of fluid passing penetrations, FLOW-3D simulations are performed to understand the underlying scientific phenomena and provide design guidance. As illustrated in Figure 12, Flow3D results show a much reduced level rise, no splash occurring at the stagnation point, and no separation in the flow field. These results are encouraging and provide "mechanism" for solving penetration issues in thick liquid wall concepts (in which much more fluid has to be dealt with.) The problem associated with penetration accommodation is considered as one of the high priority issues to be continuously addressed.

However, for a thick liquid wall concept to work, there exists many remaining design issues, particularly in the areas of moving liquid in and out of the reactor and of accommodating of penetrations. Preliminary FLOW-3D simulation results have provided guidance on how to accommodate Flibe flow surrounding the penetration. The challenges

for accommodating penetration include flow stagnation at the front point of the penetration resulting in discharge of the fluid towards the plasma, rising of the fluid level surrounding the penetration due to the obstruction of flow path, and wake formation that persists downstream of the penetration. Different means have been proposed to avoid fluid splashing and to minimize disturbance. Preliminary analyses for CLIFF concepts (2-cm thick convective liquid layer) confirm the effectiveness of the proposed schemes. These involve modification of penetration shapes, introduction of guiding grooves and fins, and alteration of the back wall topology. The most promising modification (alteration of the back wall topology) is described in Figure 5.2-6. The hydrodynamic characteristics of the Flibe liquid layer (based on FLOW-3D calculations) flowing surrounding the penetration over an altered back wall topology is presented in Figure 5.2-8. The 2-D vector plots of velocity components (in Figure 5.2-8) in planes perpendicular to the flow direction at different downstream locations (as seen Figure 5.2-8) indicate that, the fluid level rise is reduced through the increase of the flow area and redirection of the flow by alteration of back wall topology. The 3-D liquid layer distribution surrounding the penetration can also be seen in Figure 5.2-9. More details regarding the penetrations are described in Section 7.3.1.3.

The challenges of the liquid wall designs go beyond achieving a low surface temperature in order to be compatible with the plasma operation, but also to maintain a mean bulk temperature greater than 600°C for high thermal efficiency. This temperature can theoretically be higher than the maximum allowable free surface temperature. Consequently, a thick liquid wall design might require two different coolant streams: one for surface heat removal and the other for neutronics heat deposition in order to simultaneously achieve these two temperature requirements. The fast flowing layer can either adhere to a thin back plate to ensure maximum flow stability by means of centrifugal and inertial forces or be guided by deflector plates without using a continuous structural plate. These thin deflector plates will encounter a moderate temperature gradient from the neutron heating and therefore a manageable magnitude of thermal stress.

A thick yet slower liquid wall approach could involve the use of flow deflector to help restrain the liquid inside a pocket structure. The fast moving jet in front of the pocket provides resistive forces for preventing the liquid from entering the plasma core. The fluid temperature inside the pocket is maintained by continuously circulating a small amount of liquid in and out of the pocket. These specially designed deflectors prevent the liquid entering the plasma core have to be periodically replaced. Analyses based on this approach are described in Section 5.4.1.5. Additional ideas of incorporating thick liquid blankets into a tokamak type configurations are under exploration.

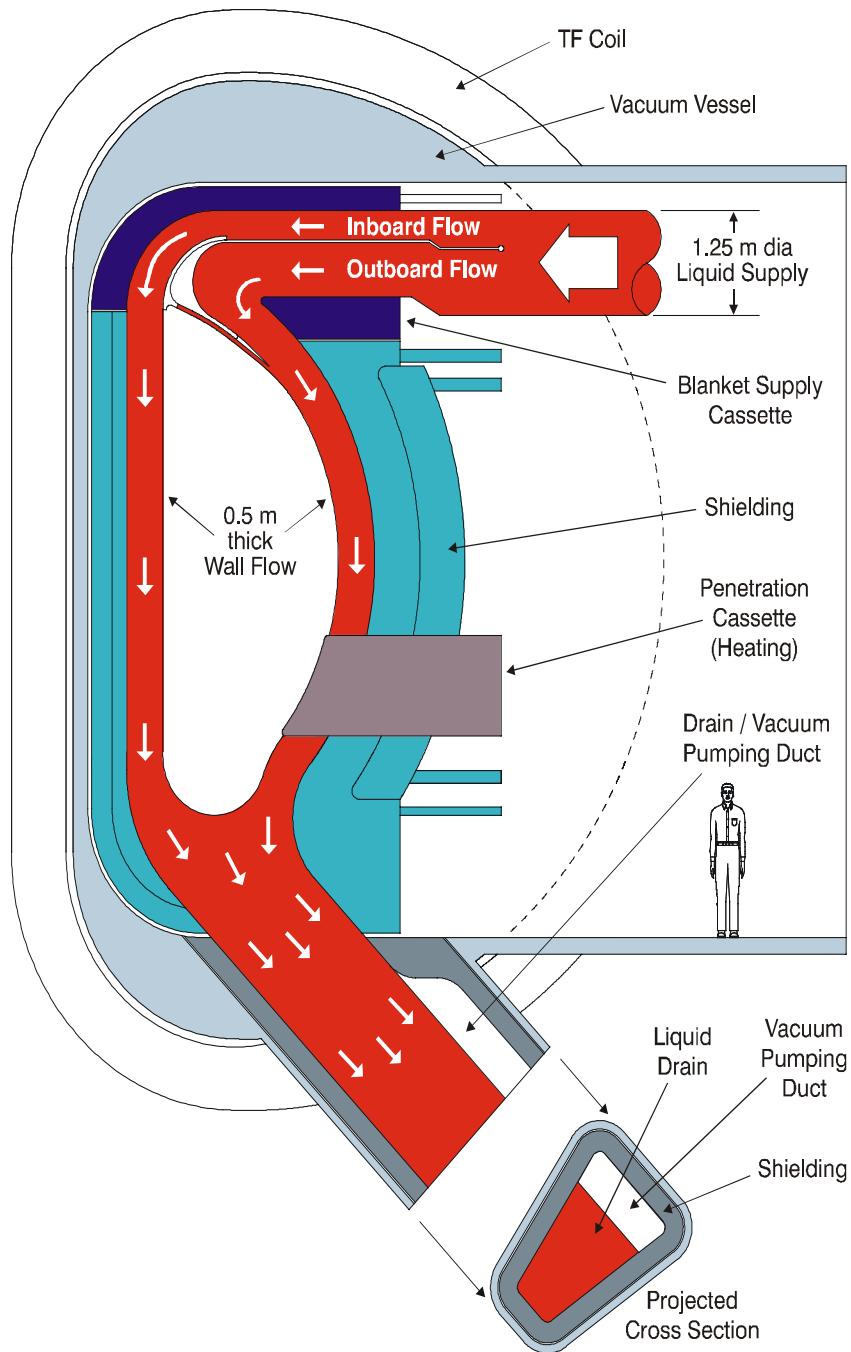


Figure 5.2-3 A thick FW/blanket design incorporated into the ARIES-RS configuration.

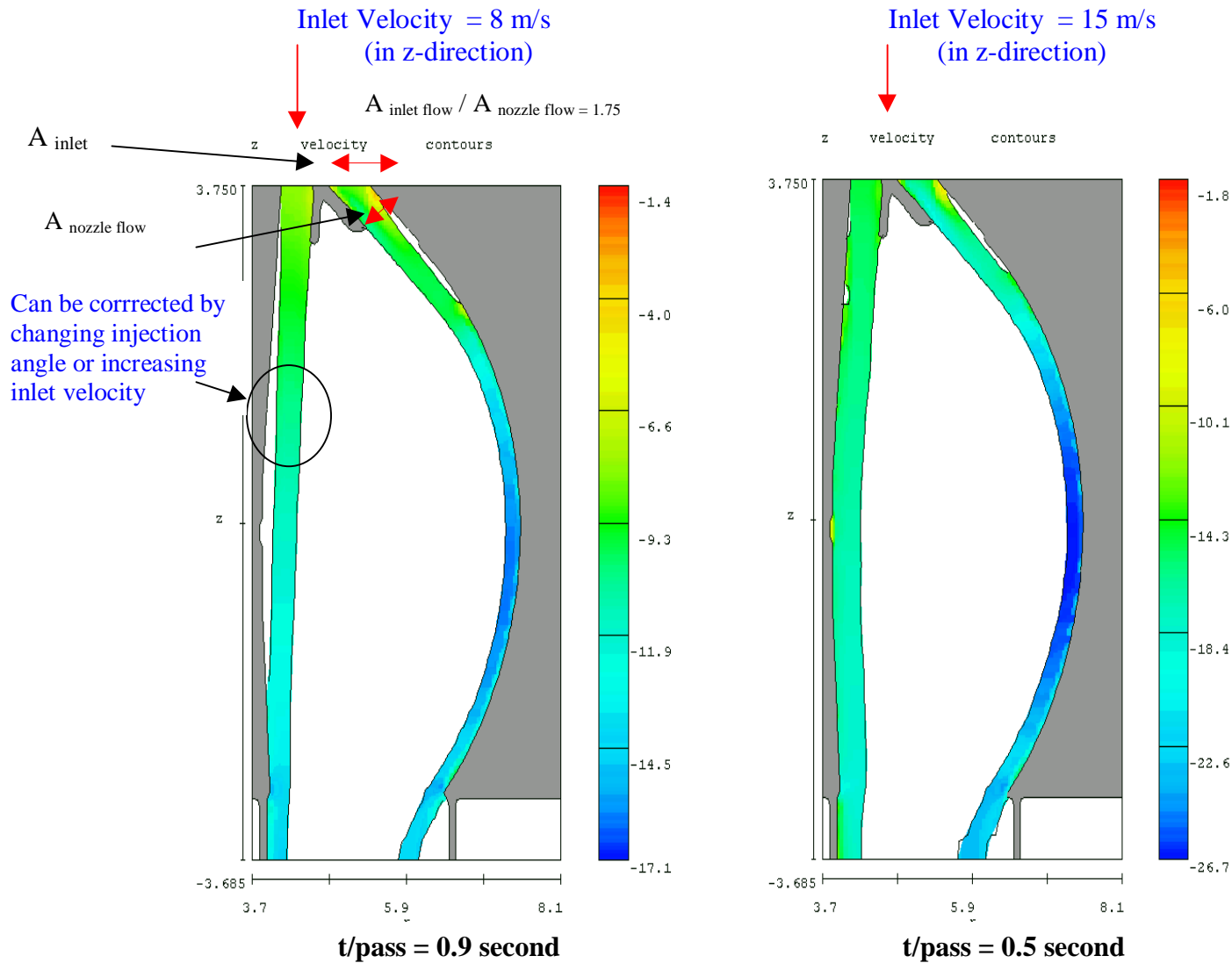


Figure 5.2.4 Some amount of thinning was observed along the poloidal path due to gravitational acceleration and toroidal area expansion (Z-velocity components increase along the structural inner walls from 3-D hydrodynamics calculations).

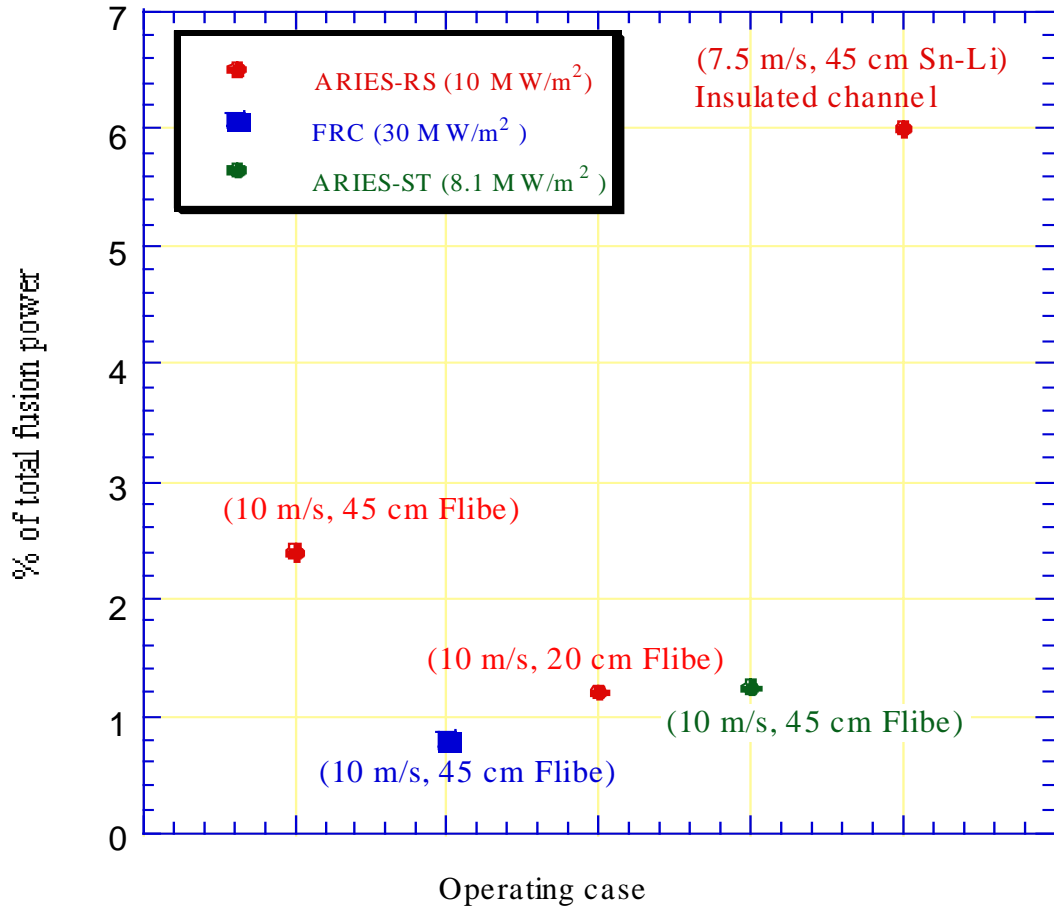


Figure 5.2-5 Ratio of pumping power requirement to the fusion power for various confinement configurations and operating liquids.

REFERENCE CASE PARAMETERS

V_{in} (m/s)	10.0		
a_z (m ² /s)	25.0		
g_y (m ² /s)	9.8		
Wall Roughness (m)	10^{-5}		
Fluid-Wall Contact Angle	0.0		
Penetration Dimensions (m)	a	b	H
	.1	.45	0.02

Flibe at 550 °C is used as a working fluid.
Fluid Wets the Structure .

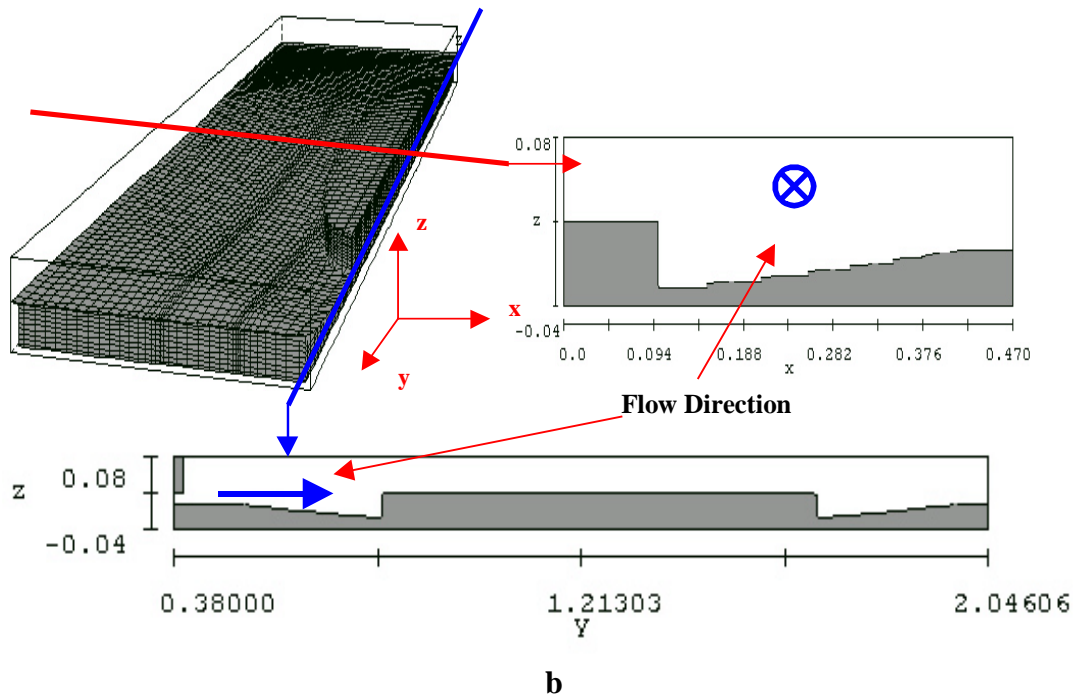
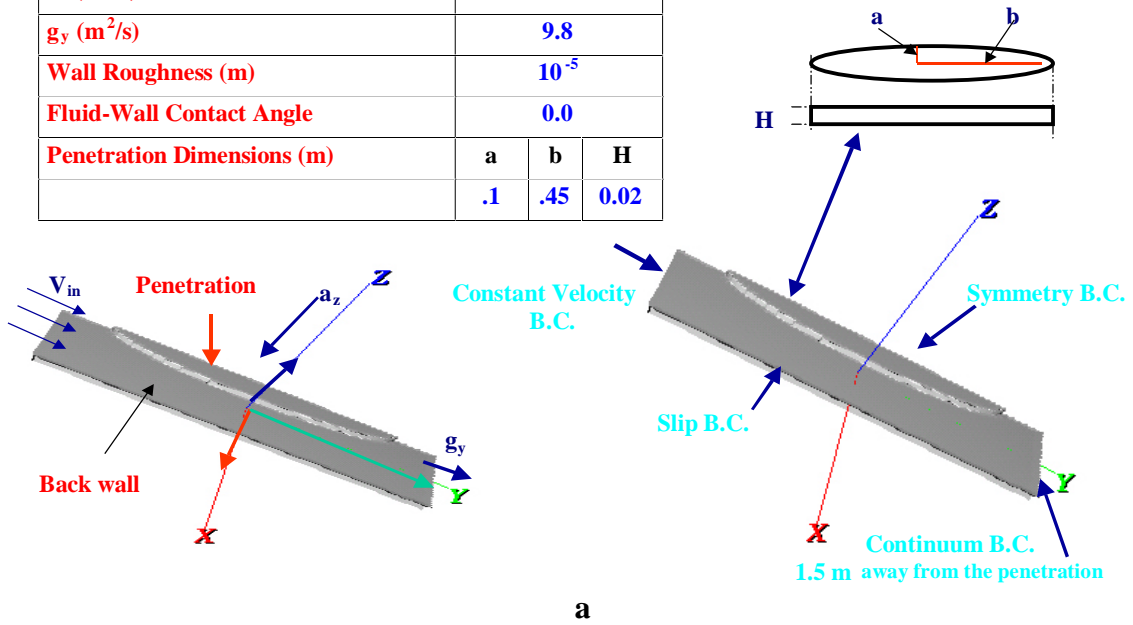


Figure 5.2-6 a. Reference penetration case operating conditions and dimensions.
b. Tailoring of the back-wall contour surrounding the reference penetration and related dimensions.

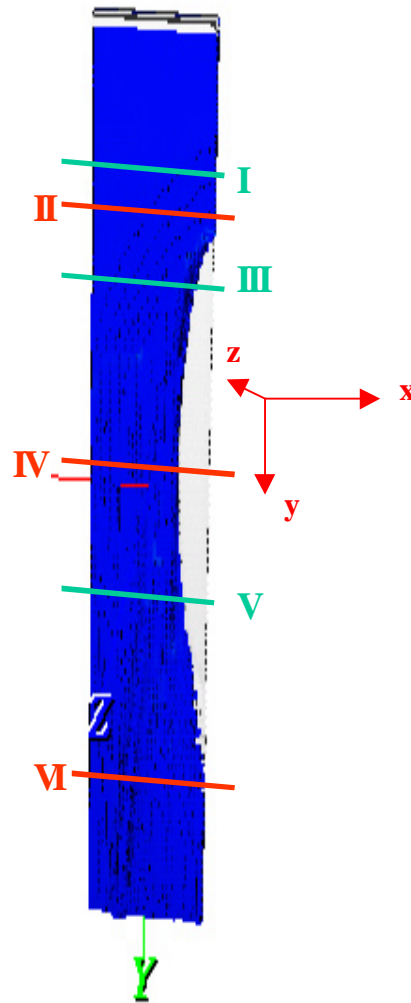
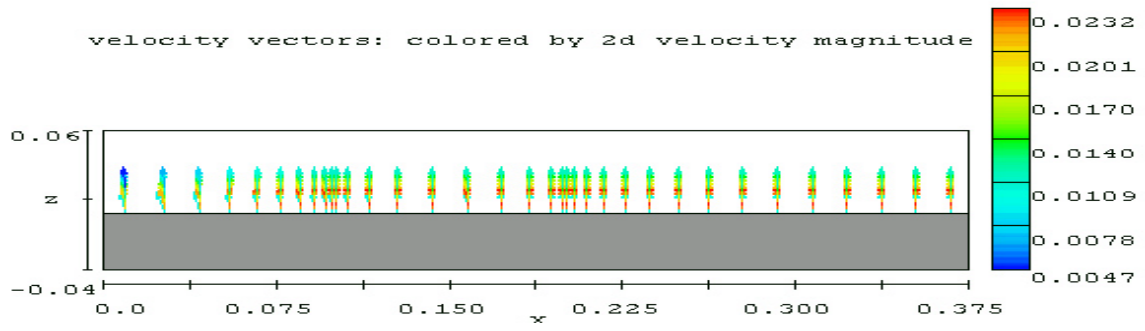
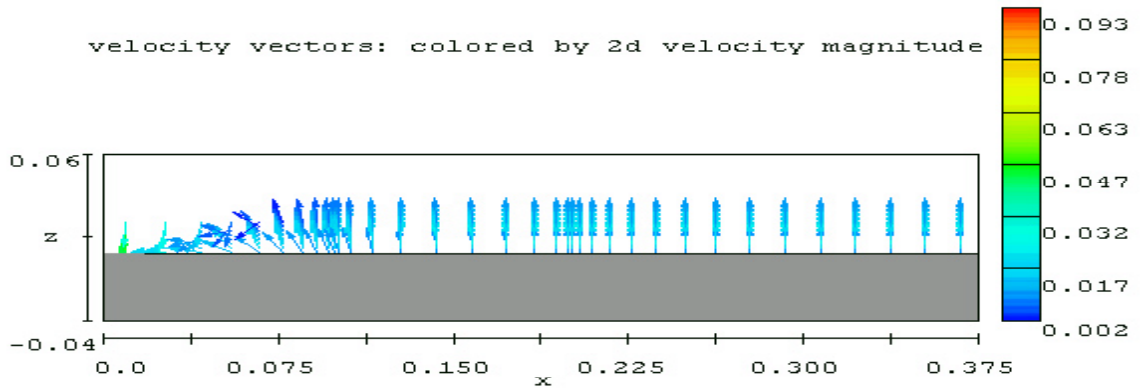


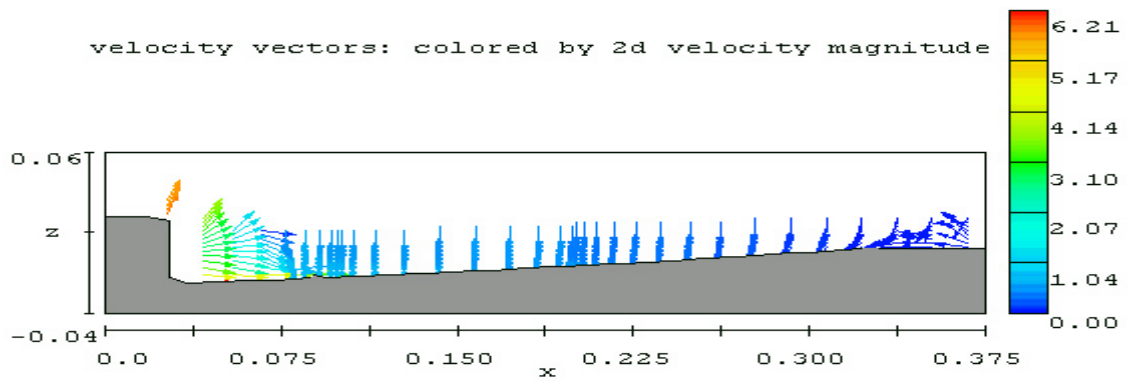
Figure 5.2-7 FLOW-3D results of Flibe flowing around a penetration surrounded by a tailored backwall as shown in Figure 5.2-6.



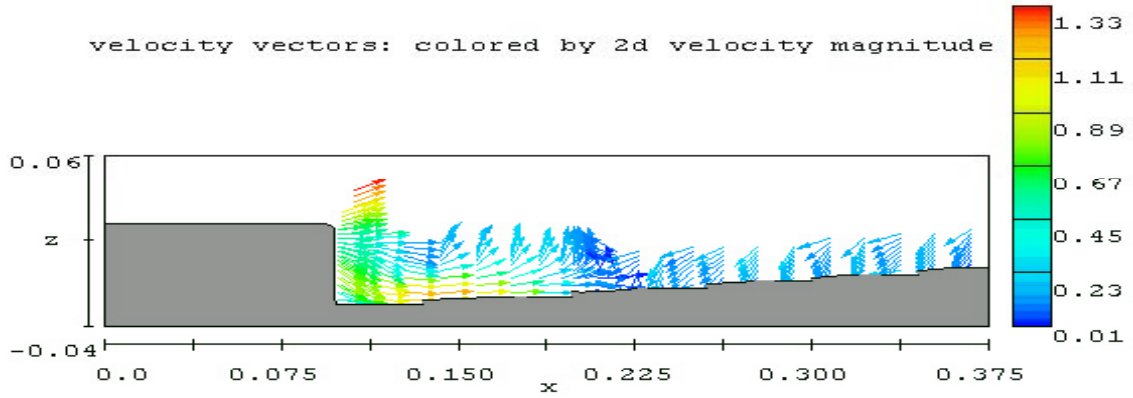
I



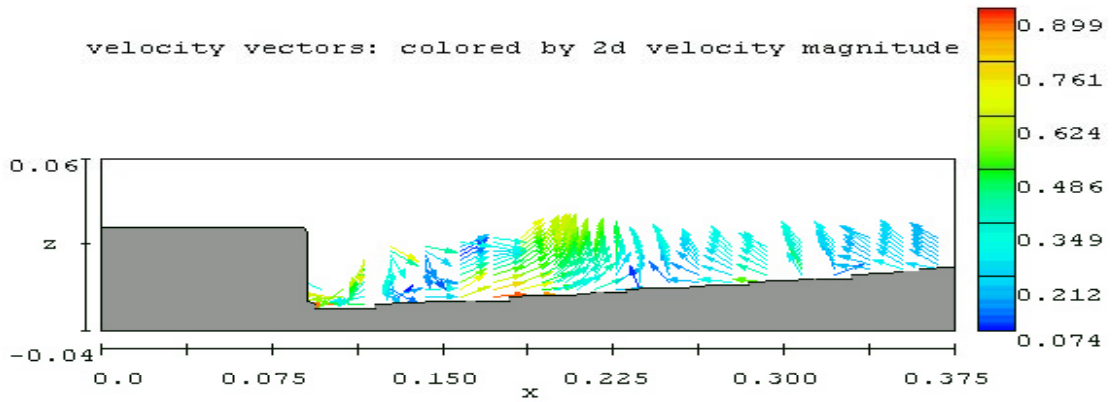
II



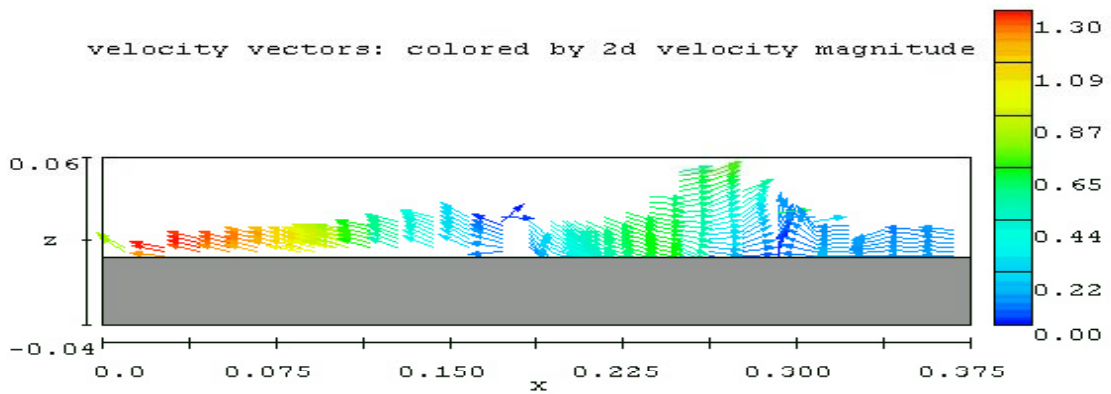
III



IV



V



VI

Figure 5.2-8 2-D velocity vectors at planes perpendicular to the flow direction at various locations as illustrated as in Figure 5.2-7.

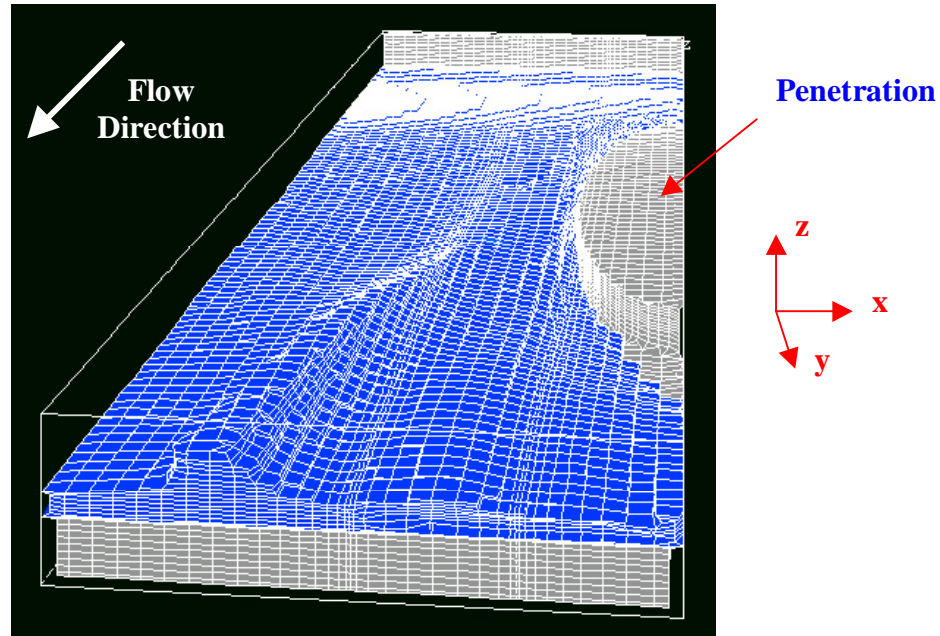


Figure 5.2-9 3-d view of flow distribution surrounding the penetration at a distance from the end section of penetration.

5.2.2 Thick Liquid Wall for Alternative Confinement Configurations

5.2.2.1 Field-Reversed Configuration (FRC)

Field-reversed configuration (FRC) power plants possess cylindrical geometry, which facilitates the design of tritium-breeding blankets, shields, magnets, and input-power systems. The high β ($\beta = \text{plasma pressure} / \text{magnetic field pressure}$) allows a high plasma power density and compact fusion core. The FRC, therefore, appears to match well with liquid walls operating at high power density.

The FRC equilibrium configuration is a compact plasma toroid immersed in an axially aligned solenoidal magnetic field. The external field lines guide the charged-particle transport power toward the end walls, where the magnetic flux tube can be expanded to reduce the surface heat flux to the desired level. Linear geometry also serves effectively to shield the core plasma from impurities. Because of the scaling of the fusion power density, $P/V \propto \beta^2 B^4$, where V is the plasma volume, B is the magnetic field, and β is the ratio of plasma pressure to the magnetic pressure, the FRC can be an extremely high power density system.

Encouraging recent physics progress by the small worldwide FRC research community has enhanced the prospects for successful FRC development [2-5]. Highlights include indications that natural minimum-energy FRC states exist [6], stable operation at moderate s (plasma radius/average gyroradius) [3], startup by merging two

spheromaks to form an FRC [7,8], and theoretically efficient current drive by rotating magnetic fields [3-9].

Why current drive by rotating magnetic fields are predicted to be in feasible in the presence of a liquid wall.

It was first thought to drive current as in [8] by locating the antenna deep (5 mean free paths or more for 14 MeV neutrons) within the low conductivity molten salt. However, calculations show the skin depth at 32 kHz to be ~ 0.33 m ($\sigma = 70$ (ohm \cdot m) $^{-1}$ for 500 °C Li₂BeF₄). This means too much power would field of the antenna leaving little to drive and sustain the FRC current. Uonted on struts or end mounted to avoid penetrations through the flowing salt. Would then be located between the FRC plasma ($r \sim 1$ m) and the flowing liquid wall ($r \sim 1.5$ to 2 m). The problem that appears fatal for this soslution is the vapor density is $\sim 10^{13}$ to 10^{14} /cm³, which is near the minimum in the Pachen breakdown curve. Discharges would occur. We have not yet quantitatively determined the magnitude of the resulting power drain to see that it is clarly excessive and leave this to the future. However, the concern has led us to adopt for now the CT (compact toroid) fueling method to be discussed next.

Compact Toroid Fueling and Current Drive

The idea of using compact toroids (CT's, either FRC's or spheromaks) for tokamak fueling and current drive has been under investigation for nearly twenty years [10-13]. Experimental tests of injecting CT's into tokamaks have been performed [14,15], but definitive conclusions regarding whether such techniques would be useful for tokamak power plant design have not yet been reached.

Recent theoretical and experimental research indicates that the FRC may be very robust and possibly relax to a self-organized state when perturbed [6-8,16]. In particular, experiments show that spheromaks can be merged to create either larger spheromaks or FRC's, depending on the total amount of magnetic helicity contained: $\mathbf{K} \equiv \int \mathbf{A} \cdot \mathbf{B} d^3x$, where \mathbf{A} is the magnetic vector potential and \mathbf{B} is the magnetic field. The essential physics of the merging process appears in Figure 5.2.10 [8]. If \mathbf{K}_{norm} , the total helicity normalized to the so-called Taylor helicity [17], is less than ~ 0.4 , the spheromaks relax to form an FRC; otherwise, they relax to a spheromak, as illustrated in Figure 5.2.11 [8].

Although experiments in which spheromaks are injected into large FRC's have not yet been performed, the merging-spheromak results [7,8] indicate the plausibility of spheromak current drive of FRC's. The viability of current drive in a large FRC by injecting small FRC's hinges on the details of self-organized FRC theory [6], and that subject has not yet been developed sufficiently to judge definitively. The crucial question of whether either technique would work out quantitatively is beyond the resources and scope of the present investigation. Nevertheless, the robustness of the merging process and of FRC's in general implies that CT-fueling of FRC's shows considerable promise.

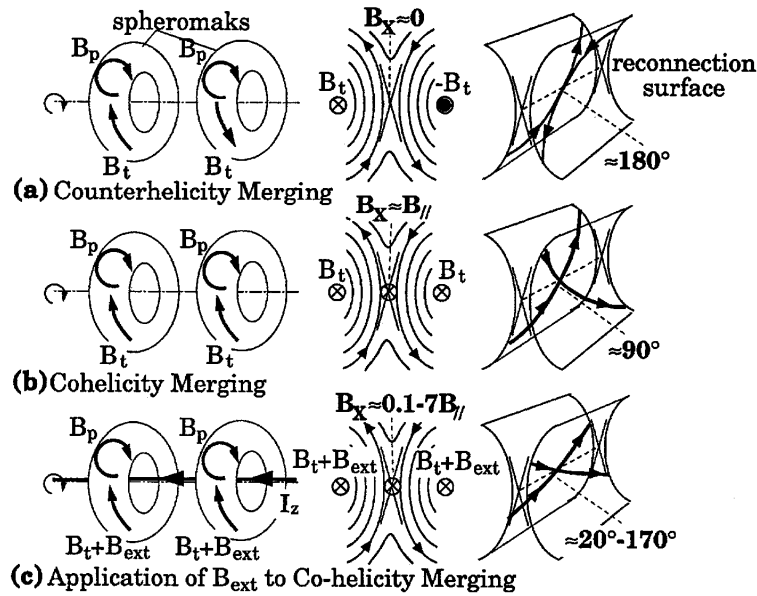


Figure 5.2-10 Three-dimensional structures involved in spheromak reconnection [7]

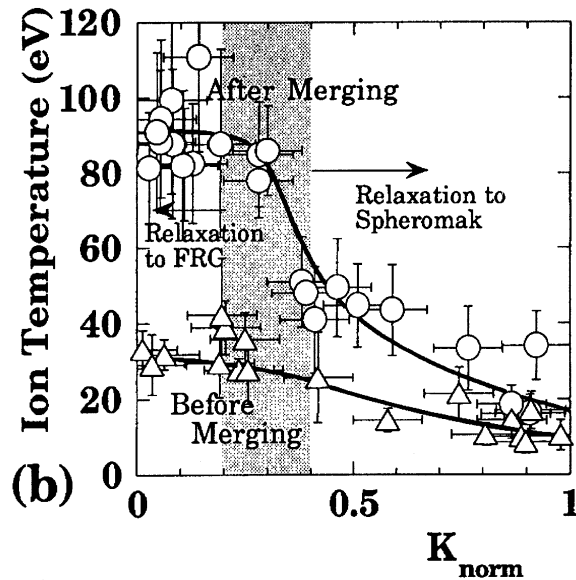


Figure 5.2-11 Relaxation characteristics of merged spheromaks [8].

Together, these considerations raise the question of whether compact toroids could be used to fuel and provide current drive for an FRC power plant. The use of CT's for FRC fueling and current drive is analogous to the tokamak case but would differ in detail. The basic geometry of the concept appears in Figure 5.2-12.

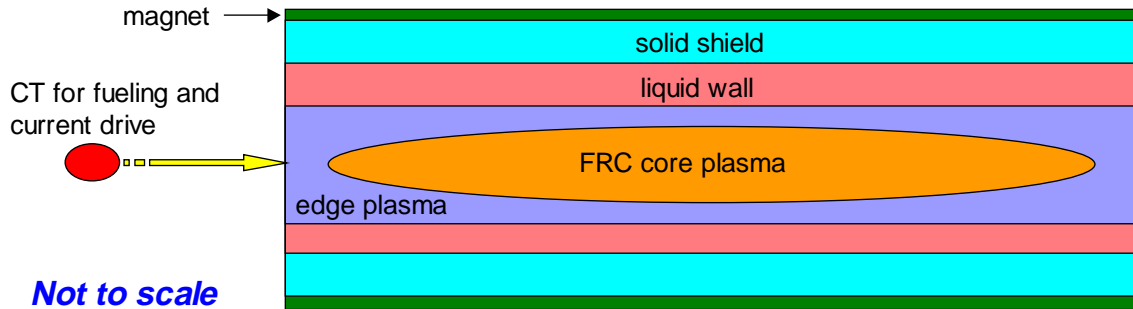


Figure 5.2-12 Basic geometry of CT fueling and current drive of a FRC fusion core.

5.2.2.2 Applications of Thick Liquid Wall to FRC and ST Confinement Configurations

The present thick liquid FW/blanket idea for FRC and ST configurations evolved from the thick liquid wall (TLW) concepts proposed by Moir [18,19] for magnetic fusion energy configurations. The idea is now being investigated, modified and developed in the APEX study [20], which is aimed at exploring innovative concepts of handling high power density that may enhance the potential of competitiveness of fusion as an energy source. In the present study, the swirling liquid layer idea is explained both analytically and computationally in detail for an FRC configuration, and its application to the ST is also presented.

A conceptual FRC configuration has more than a 25-m length and its components include: the main section (where plasma exists) located at the center, the two liquid jets (i.e. spray heat dump), and pulsed start-up sections located on both sides of the main section (Figures 5.2-1 and 5.2-13).

A thick liquid first-wall/blanket (> 0.5 m) can be established and maintained in the main section by injecting the liquid layer from one side of the circular vacuum chamber through a swirl flow generating inlet with axial and azimuthal velocity components (Figure 5.2-13). Then, the liquid layer adheres to the inner walls of the cylindrical chamber by means of centrifugal acceleration ($> \sim 3.2$ g) as a result of its high azimuthal velocity (> 8 m/s) and the small radius of curvature of the cylindrical chamber (< 2 m). As an example, the inner wall of the main section (with radius of 2 m) can be covered by a fast moving liquid layer of ~ 0.5 m thick with inlet velocities of 8 to 12 m/s in the azimuthal direction and > 8 m/s in the axial direction. The liquid layer is diverted towards the outlet by centrifugal force on the diverging conical back wall structure that is located at the other end of the main section. Swirl flow makes ~ 1 rotation during its travel between the inlet and outlet sections.

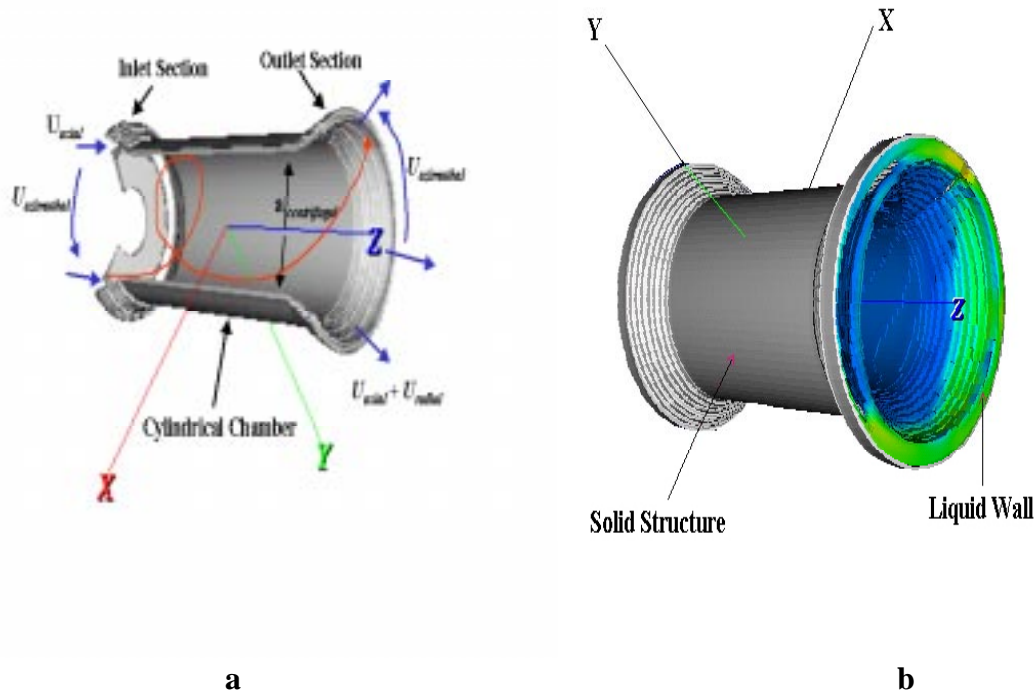


Figure 5.2-13 a. Illustration of the swirl flow mechanism in the main section with converging inlet and diverging outlet sections.
b. The 3-D fluid distribution of FRC swirl flow. (Result of CFD simulation.)

The idea presented here is in the exploratory phase and may be developed into a mature design concept when the several fundamental issues stated here are addressed in the future phase of the current study. In the preliminary analysis the constraints are (1) liquid blanket thickness > 0.45 m, (2) velocity at the liquid wall surface facing to the plasma > 8 m/s, (3) elimination of liquid splash or drip to the plasma. The design variables for preliminary study are (1) axial and azimuthal inlet velocities, (2) chamber radius and (3) lengths and slopes of the inlet/outlet in both the converging and diverging sections. Designs of the inlet nozzle, outlet recovery section, and related hydrodynamic characteristics have not been done.

The swirl flow concept can also be applied to the ST outboard FW/blanket region (Figure 5.2-13). In this case, a thick liquid carrying both vertical and azimuthal velocity components is injected at the top of the chamber. The centrifugal acceleration (> 35 m/s²) pushes the fluid outward and prevents the flow from deflecting into the plasma core. The axial velocity increases as the flow proceeds downstream due to the gravitational acceleration, and this leads to flow thinning. The thinning effect is further manifested in the ST because of the toroidal area expansion along the flow direction (the flow area

increases by a factor of 2 as the flow approaches the mid-plane as can be seen in Figure 5.2.4).

Various numerical simulations were performed to identify “ways” to slow down the velocity and to reduce the thinning effect. Preliminary results, based on Flow-3D calculations, indicate that the thinning effect can be mitigated by tailoring the back wall contour and by incorporating a step along the flow direction. The “step” of about 0.2-m high located at the reactor mid-plane, helps to maintain the liquid layer thickness greater than 0.3 m, as shown in Figure 5.2-14. In contrast to the rotational flow for the outboard blanket, a fast annular liquid layer is used at the inboard FW/blanket zone. Detailed hydrodynamics analyses of swirl flow concept application to FRC and ST configurations are described in Section 5.4.2.

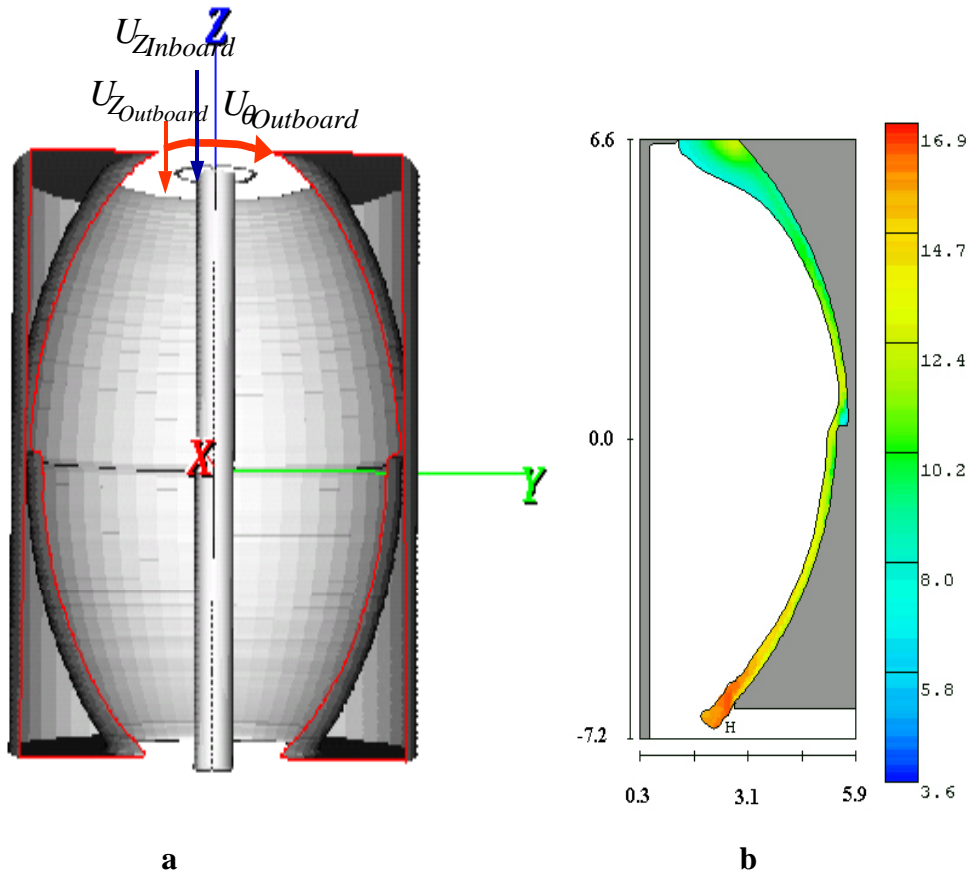


Figure 5.2-14 a. The structural modeling of ST geometry including the modification in the outboard topology.
b. 2-D velocity magnitude contour at r-z plane at the outboard and liquid layer height distribution in the z-direction at an arbitrary azimuthal angle.

5.2 References

- 1 Flow3D, Flow3D Users Manual Version 7.1, 1997.
- 2 Steinhauer, L.C. et al., "FRC 2000: A White Paper on FRC Development in the Next Five Years," *Fusion Technology* **30**, 116 (1996).
- 3 Hoffman, A.L., et al., "The Large-s Field-Reversed Configuration Experiment," *Fusion Technology* **23**, 185 (1993).
- 4 Tuszewski, M., "Field Reversed Configurations," *Nuclear Fusion* **28**, 2033 (1988).
- 5 Momota, H. and J.F. Santarius, "Summary of the U.S.-Japan Workshop on the Physics of D-³He Fusion," *Fusion Technology* **28**, 1763 (1995).
- 6 Steinhauer, L.C. and A. Ishida, "Relaxation of a Two-Species Magnetofluid and Application to Finite- \square Flowing Plasmas," *Physics of Plasmas* **5**, 2609 (1998).
- 7 Yamada, M., et al., "Study of Driven Magnetic Reconnection in a Laboratory Plasma," *Physics of Plasmas* **4**, 1936 (1997).
- 8 Ono, Y., et al., "Experimental Investigation of Three-Component Magnetic Reconnection by Use of Merging Spheromaks and Tokamaks," *Physics of Plasmas* **4**, 1953 (1997).
- 9 Hoffman, A.L., "Flux Buildup in Field Reversed Configurations Using Rotating Magnetic Fields," *Physics of Plasmas* **5**, 979 (1998).
- 10 Hartman, C.W. and J.H. Hammer, "New Type of Collective Accelerator," *Physical Review Letters* **48**, 929 (1982).
- 11 Perkins, L.J., S.K. Ho, and J.H. Hammer, "Deep Penetration Fueling of Reactor-Grade Tokamak Plasmas with Accelerated Compact Toroids," *Nuclear Fusion* **28**, 1365 (1988).
- 12 Parks, P.B., "Refueling Tokamaks by Injection of Compact Toroids," *Physical Review Letters* **61**, 1364 (1988).
- 13 Ho, S.K., L.J. Perkins, and J.H. Hammer, "Potential High-Q, Noninductive Current Drive in Tokamaks via Accelerated Compact Toroids," *Fusion Technology* **17**, 658 (1990).
- 14 Brown, M.R. and P.M. Bellan, "Spheromak Injection into a Tokamak," *Physics of Fluids B* **2**, 1306 (1990).
- 15 Slough, J.T. and A.L. Hoffman, "Penetration of a Transverse Magnetic Field by an Accelerated Field-Reversed Configuration," *Physics of Plasmas* **6**, 253 (1999).
- 16 Steinhauer, L.C. and A. Ishida, "Relaxation of a Two-Species Magnetofluid," *Physical Review Letters* **79**, 3423 (1997).
- 17 Taylor, J.B., "Relaxation and Magnetic Reconnection in Plasmas," *Reviews of Modern Physics* **58**, 699 (1986).
- 18 Moir, R. W., "Rotating Liquid Blanket For Toroidal Fusion Reactor," *Fusion Engineering and Design*, Vol. 5, pp. 269-272 (1987)
- 19 Moir, R. W., "Liquid First Walls for Magnetic Fusion Energy Configurations," *Nuclear Fusion*, Vol. 37, No. 4, pp. 557-566, (1997)
- 20 Abdou, M. A., and the APEX Team, 1998. "Exploring Novel High Power Density Concepts for Attractive Fusion Systems," *Fusion Engineering and Design*, Vol. 145, pp 145-167 (1999).

5.3 Nuclear Analysis

In this section we present the nuclear analysis for the Gravity and Momentum Driven (GMD) thick liquid FW/Blanket concept. Section 5.3.1 is devoted to assessing the penetration depth inside the liquid layer from the X-rays that carry most of the surface heat load. The nuclear heating profiles, power multiplication, tritium production profiles, tritium breeding ratio, and damage parameters (DPA, helium and hydrogen production) are discussed in Section 5.3.2 for two design configurations (shielding outside and inside the vacuum vessel, respectively). Section 5.3.3 is devoted to the activation and afterheat calculations.

5.3.1 X-rays Heat Deposition Due to X-rays Penetration

In a plasma, free electrons are accelerated in the magnetic field needed to confine the plasma. Because of their lighter mass, the electrons undergo larger acceleration than the ions. This leads to radiation losses from the plasma that requires heating to maintain the plasma. The electrons are accelerated by collisions, the resulting radiation is the Bremsstrahlung radiation; and they are subject to the acceleration of their cyclotron motion, leading to losses through synchrotron radiation. In the presence of impurities the Bremsstrahlung radiation is enhanced. There are also further losses due to the atomic processes of line radiation and recombination.

In this section we discuss the energy deposited from the X-rays radiation emitted from the plasma and the extent to which this radiation penetrates the liquid FW/Blanket system. In solid first wall, this surface heating source is assumed to be deposited at the surface and no penetration occurs. Because of the lighter atomic number of the constituents of the liquid layer, energy from X-rays can be deposited volumetrically throughout a measurable penetration length, as described in this section. The objectives of this section are: (a) determination of the spatial range over which X-rays from the plasma deposits its energy across the protective liquid layer under a realistic spectrum, and (b) evaluation of the impact of difference in the neutron moderation among the liquid studied on the volumetric heat deposition rate across the layer. This assessment gives the correct input source for the thermal hydraulic analysis and leads to a large decrease in the liquid surface temperature. Liquid lithium, Flibe, and $\text{Li}_{17}\text{Pb}_{83}$ are candidate protective layers. In the present study, the Flibe Li_2BeF_4 is considered (rather than LiBF_3) since it has 10 times lower viscosity but a high melting point of 460°C.

The spectrum of X-rays depends on the plasma operating conditions (e.g. electron temperature, impurities, etc.) Most of the emitted X-rays are in eV- keV energy range and photoelectric absorption is the main mechanism of attenuation [1]. The steepness of power deposition profiles depends on the X-rays attenuation characteristics in the layer material. Volumetric heating from incident neutrons, however, is deposited evenly through the layer with much lower steepness. Profiles of power deposition rate from 1 MW/m² surface wall loads on layers up to 5-cm thick are given here with comparison to nuclear heating from 7 MW/m² neutron wall load. The impact of the volumetric

deposition of the X-rays energy on the thermal hydraulics of the liquid FW/blanket is addressed elsewhere in this Chapter.

5.3.1.1 Attenuation Length of X-rays in Liquid Materials

Figure 5.3-1 shows the attenuation length versus photon energy (30 eV-30 keV) of X-rays incident perpendicularly on several materials. This length is defined as the penetration depth at which the photon intensity is 1/e of its initial incident value (i.e., equivalent to the mean free path $1/\Sigma$ for absorption.) Photon attenuation properties in materials can be found in Refs. 2-7.

Attenuation Length of X-Rays Versus Photon Energy

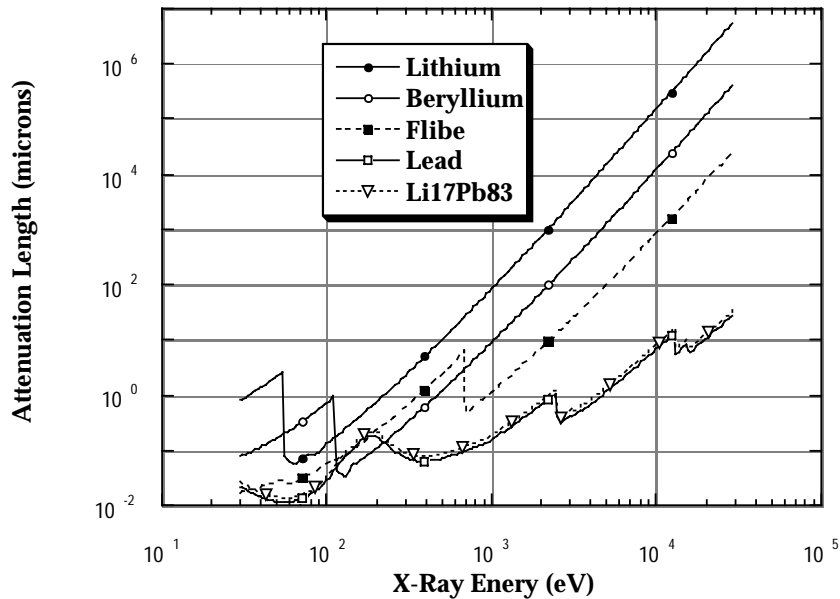


Figure 5.3-1 Attenuation Length of X-rays in Lithium, Beryllium, Flibe, Lead, and Li₁₇Pb₈₃ VS. Photon Energy

The attenuation length for mono-energetic X-rays of 1 keV inside Li, Flibe, and Li₁₇Pb₈₃ are ~100, ~1, and ~0.12 microns, respectively. The corresponding length at 10 keV are $\sim 1.3 \times 10^5$, ~1000, and ~10 microns. The attenuation coefficient of Li is thus ~2 orders of magnitude lower than in Flibe whereas the attenuation coefficient of Flibe is 1-2 orders of magnitude lower than in Li₁₇Pb₈₃. Because of the very short attenuation length of X-rays in Li₁₇Pb₈₃, the present analysis focuses on profiles of heat deposition rate (HDR) in Li and Flibe and X-rays wall load in Li₁₇Pb₈₃ is considered deposited at the surface only. Figure 5.3-2 shows the depth in the layer at which a given fraction of the incident power is deposited. In a 5-cm thick Flibe layer, 100% of the incident power is

deposited within a depth of 10 micron, 0.01 cm, 0.06 cm, 0.2 cm, and 0.4 cm for 2, 4, 6, 8, and 10 keV X-rays. In Li, 100% of the power is deposited within 0.4 cm and 3.7 cm for 2 and 4 keV X-rays, respectively. For 6, 8 and 10 keV X-rays, ~84%, ~50%, and ~28% of the power is deposited in the 5 cm thick layer (~16%, ~50%, and 72% fraction of power transmitted). This shows that Li is more transparent to X-rays than Flibe and volumetric heat deposition can be realized at measurable depth inside the Li layer.

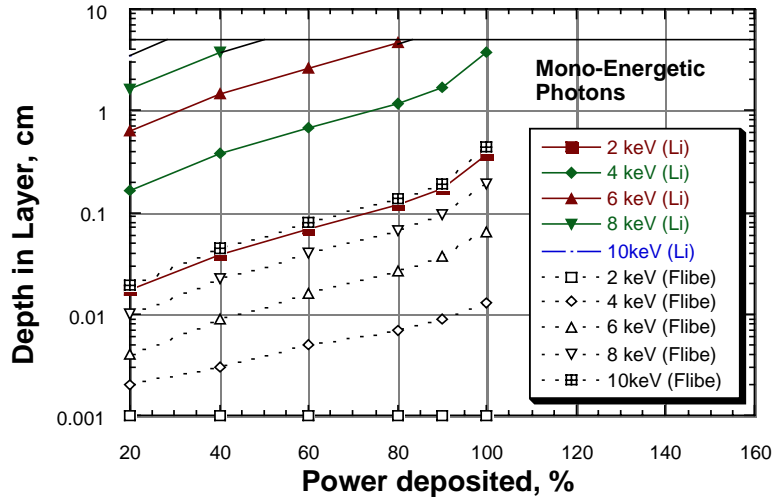


Figure 5.3-2 Depth in Convective Layer at which a given Fraction of Incident Power is Deposited from Mono-energetic X-rays.

5.3.1.2 X-rays from Classical Bremsstrahlung Radiation

For the most part, the X-rays incident spectrum is mainly due to Bremsstrahlung with superimposed line spectra from impurities [8]. For the sake of comparison with mono-energetic X-rays, the surface load is assumed to be Bremsstrahlung radiation whose spectrum is a function of the electron temperature T_e . The classical Bremsstrahlung radiation is used as representative spectrum and is given by:

$$E_x \cdot \frac{dN}{dE_x} = a \cdot n_e \cdot n_i \cdot g_{ff} \cdot \exp(-E_x / T_e) / \sqrt{T_e} \tag{5.3-1}$$

Where,

- T_e = Electron temperature, eV
- a = $9.6 \times 10^{-20} \text{ eV}^{1/2} \text{ m}^3 \text{ s}^{-1}$
- g_{ff} = Gaunt Factor ~ unity

E_x = X-rays energy, eV

$dN/d E_x$ = the number of quanta emitted per eV per second into 4π steradians by plasma of volume 1 m^3 .

The Bremsstrahlung radiation power, P_{br} , is given by:

$$P_{br} = 5.35 \times 10^{-37} Z^2 n_e n_z (T_e)^{1/2}, \text{ W m}^{-3}, T_e \text{ in keV} \tag{5.3-2}$$

- Z = atomic number of ions
- n_e = electron density per m^3
- $n_z = n_i$ = ion density per m^3 .

Integrating Eq. 5.3-1 between $E_x = 0$ and $E_x = \infty$ gives Eq. 5.3-2 for $Z=1$. It can be shown that the fraction of X-rays in the energy range E_1 and E_2 is $\exp(-E_1/T_e) - \exp(-E_2/T_e)$.

Figure 5.3-3 shows the classical Bremsstrahlung spectrum for various T_e . The energy-integrated spectrum is shown in Figure 5.3-4 as a function of the photon energy E_x . For $T_e = 10 \text{ keV}$, the fraction of spectrum below 100 and 300 eV is $\sim 0.7\%$ and $\sim 2.5\%$ respectively. The corresponding fraction for $T_e = 2 \text{ keV}$ is $\sim 3\%$ and 12% , respectively. On the other hand, the fraction of spectrum above 10 keV is $\sim 37\%$ for $T_e = 10 \text{ keV}$ and $\sim 2\%$ for $T_e = 2 \text{ keV}$. This has implication on the HDR profiles in the Li and Flibe layer.

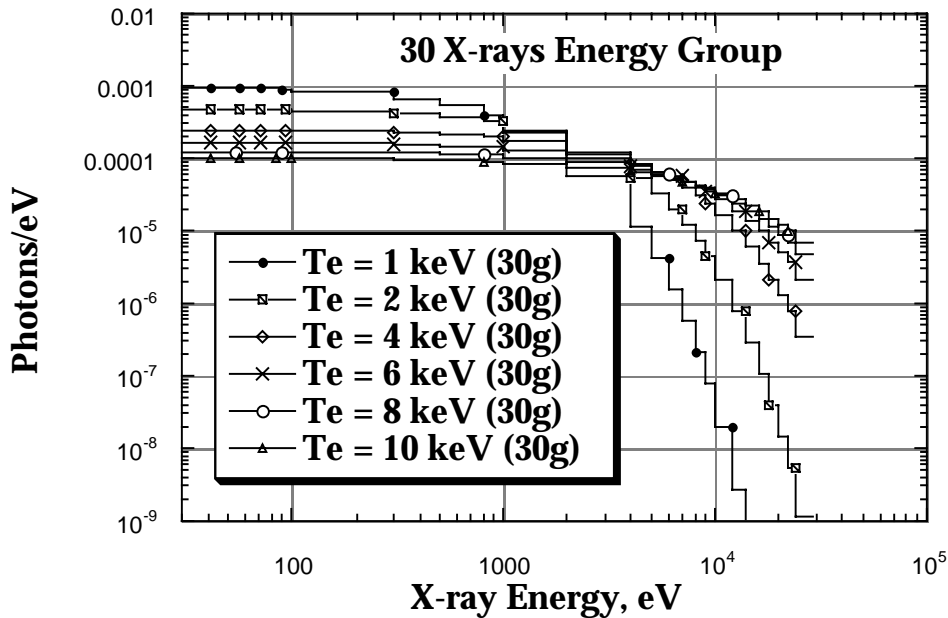


Figure 5.3-3 Classical Bremsstrahlung Spectrum at Various Electron Temperatures (30 photon-energy-group)

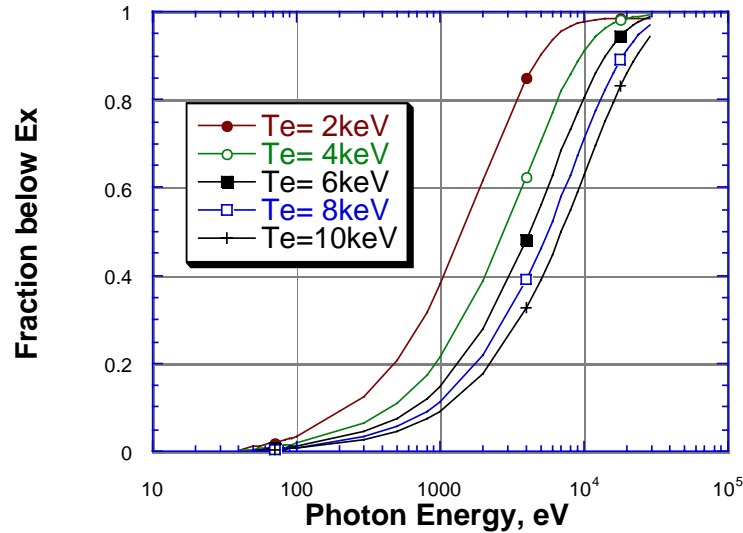


Figure 5.3-4 Integrated Classical Bremsstrahlung Spectrum at Various Electron Temperature T_e as a Function of Photon Energy E_x .

5.3.1.3 Heat Deposition Profiles in Li and Flibe

Figure 5.3-5 shows the HDR from mono-energetic X-rays and Bremsstrahlung spectrum at E_x (or T_e) of 2 and 10 keV incident on Li layer and for surface wall load of 1 MW/m². Values shown can be linearly normalized for other wall load corresponding to the actual surface load. At $E_x = 10$ keV, the mono-energetic X-rays have a more or less HDR of ~ 6 W/cc throughout the Li layer. The HDR for the Bremsstrahlung spectrum peaks at the surface (HDR = $\sim 9 \times 10^4$ W/cc) due to the low-energy component (< 80 eV) and is ~ 8 W/cc in the bulk of the layer. At $E_x = 2$ keV, the profile of the mono-energetic X-rays is steep ($\sim 1.3 \times 10^3$ W/cc at surface and ~ 0.002 W/cc at 1 cm). The Bremsstrahlung spectrum has much larger HDR at the bulk of the layer (~ 6 W/cc at 1 cm) but still the low-energy component of the spectrum contributes appreciably to the HDR at the surface ($\sim 4 \times 10^5$ W/cc). These features are similar in the Flibe layer case but with much shorter depth. The fact that the low-energy component of the Bremsstrahlung spectrum contributes the most to the HDR near the surface is shown in Figure 5.3-6. The HDR profiles from some energy ranges, selected from 30 energy bins that cover the range 30 eV- 30 keV, are shown for Li up to a depth of 1 cm.

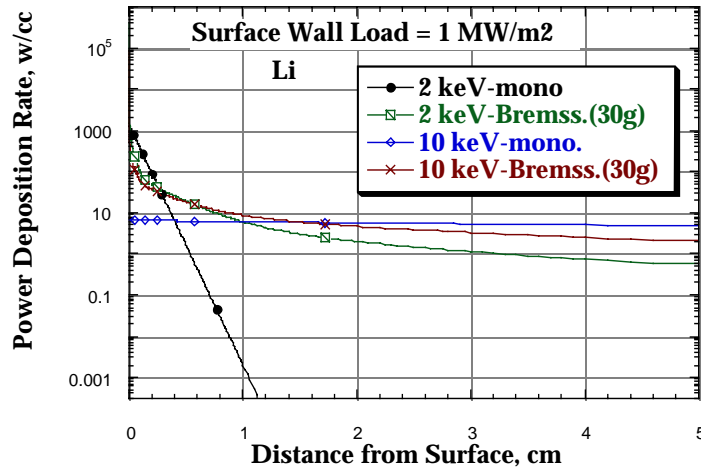


Figure 5.3-5 Comparison of Power Deposition Profile of Mono-energetic X-rays of $T_e = 2$ and 10 keV and Classical Bremsstrahlung Spectrum Incident on Lithium (Depth = 5 cm)

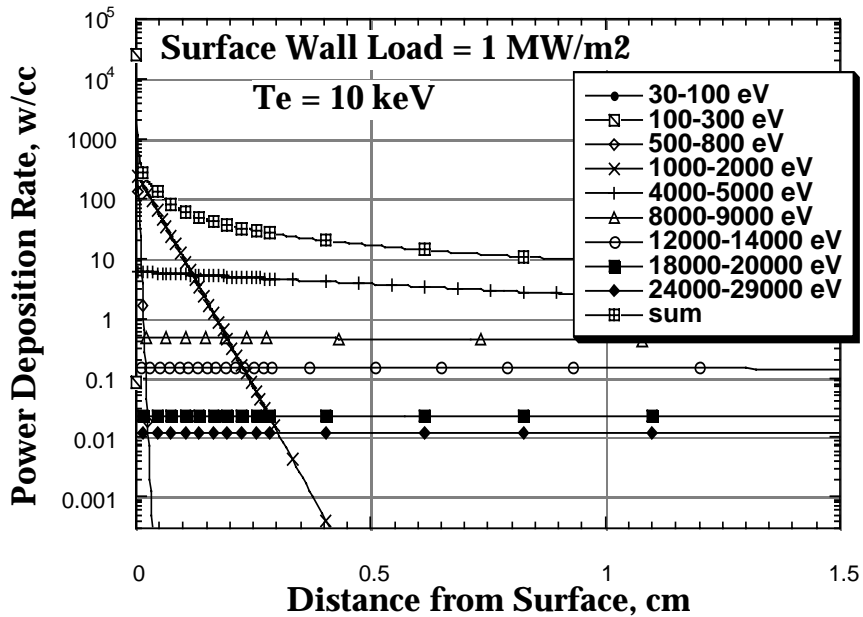


Figure 5.3-6 Power Deposition Profile and Contribution from Each X-rays Energy Range for Classical Bremsstrahlung Radiation Incident on Li (Depth = 1 cm)

The large HDR at the surface of the convective layer can be seen from Figure 5.3-7 which shows a comparison of the attainable HDR for mono-energetic X-rays and Bremsstrahlung spectrum. The surface HDR drops faster with increasing photon energy in the case of mono-energetic X-rays than in the case of Bremsstrahlung spectrum. It drops by ~ 2 orders of magnitudes in the former and by a factor of 4-5 in the latter as E_x or T_e varies from 2 keV to 10 keV. For 10 keV, the surface HDR is $\sim 9 \times 10^4$ W/cc in Li and 4×10^5 W/cc in Flibe. These large values are due to the absorption of low-energy tail of the Bremsstrahlung spectrum below 80 eV in Li and ~ 300 eV in Flibe whose attenuation length is a fraction of a micron as can be seen from Figure 5.3-1. This fraction of the spectrum is $\sim 0.4\%$ and $\sim 2.7\%$, respectively. The HDR profiles are shown in Figure 5.3-8 (depth of 5 cm) and Figure 5.3-9 (depth of 0.03 cm). Clearly the surface temperature becomes larger as the fraction of the Bremsstrahlung spectrum below 80 eV (Li) and 300 eV (Flibe) gets larger as in the case of $T_e = 2$ keV where this fraction is ~ 2 and $\sim 10\%$, respectively (see Figure 5.3-4). This suggests that part of the surface wall load can be treated as truly surface load whereas the rest of the incident load is considered deposited volumetrically throughout the protecting layer. The fraction that can be treated as a purely surface heat load (below 80 eV for Li and 300 eV for Flibe) can be obtained from Figure 5.3-4). This is shown in Figure 5.3-10 which depicts the HDR in Flibe from 1 MW/m² Bremsstrahlung spectrum at $T_e = 10$ keV, considering only the part of the spectrum above a given cut-off energy E_{co} . As shown, the larger E_{co} is, the lower is the surface HDR since larger part of the low energy tail of the spectrum is not accounted for but is treated separately as a pure surface heat load. The fraction of this pure surface load from the 1 MW/m² total load is 2.66%, 3.62%, 4.58%, 6.32%, 6.46%, 7.39%, 8.31%, and 9.2% for E_{co} of 300 eV, 400 eV, 500 eV, 684 eV, 700 eV, 800 eV, 900 eV, and 1 keV, respectively. Generally, the longer attenuation length for X-rays above E_{co} tends to distribute power evenly across the attenuating media which leads to less thermal stresses.

From a practical design point, one would be interested in assessing the depth in the layer at which the HDR from surface wall load is comparable to the volumetric heating resulting from neutrons interaction. Figure 5.3-11 gives this depth in Li and Flibe for a 1 MW/m² Bremsstrahlung radiation of $T_e = 2$ and 10 keV. As shown, a 10 W/cc is attainable at depth of ~ 0.9 cm (Li) and ~ 0.7 cm (Flibe) for $T_e = 10$ keV. Shorter depth is attainable for $T_e = 2$ keV (~ 0.8 cm and 0.1 cm, respectively). For a HDR of ~ 50 -60 W/cc (which is comparable to neutrons/gamma heating at 7 MW/m² neutron wall load, see next section), the depth for $T_e = 10$ keV is ~ 0.08 -0.1 cm (Li) and 0.14-0.16 cm (Flibe). The corresponding depth for $T_e = 2$ keV is ~ 0.15 -0.20 cm (Li) and ~ 0.04 (Flibe). Note that the HDR at and very near to the surface are higher in the Flibe layer than in the Li layer for $T_e = 10$ keV.

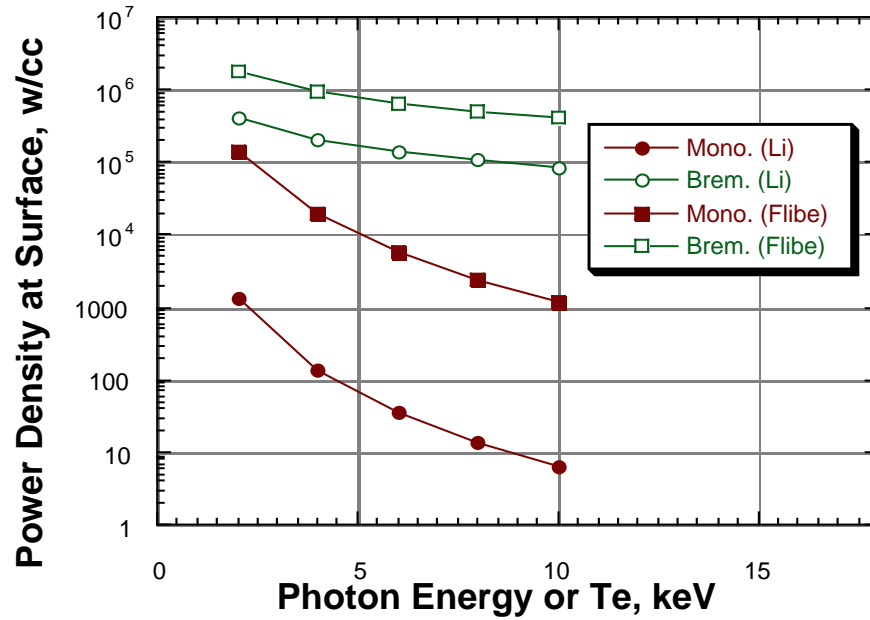


Figure 5.3-7 Surface Power Density from Mono-Energetic X-rays and Bremsstrahlung Spectrum as a Function of Photon Energy/Electron Temperature T_e

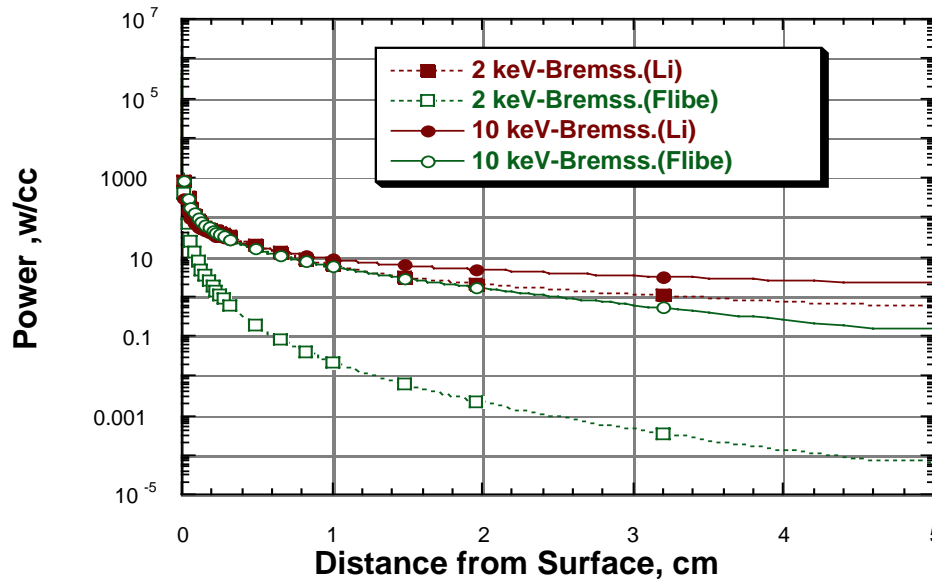


Figure 5.3-8 Power Deposition Rate from 1 MW/m^2 Surface wall Load in Li and Flibe Convective Layer (Classical Bremsstrahlung Spectrum)-depth 5 cm

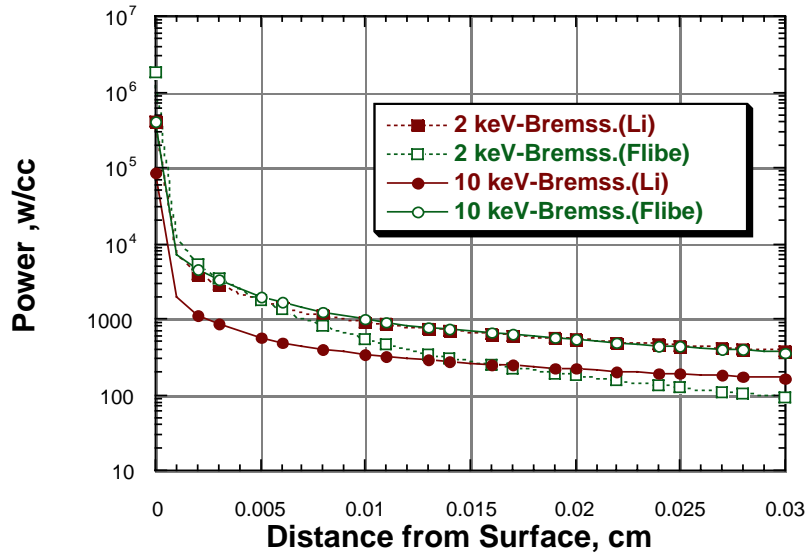


Figure 5.3-9 Power Deposition Rate from 1 MW/m² Surface wall Load in Li and Flibe Convective Layer (Classical Bremsstrahlung Spectrum)-depth 0.03 cm.

Power Deposition Rate in FLIBE above a given cut-off energy in the Bremsstrahlung Spectrum

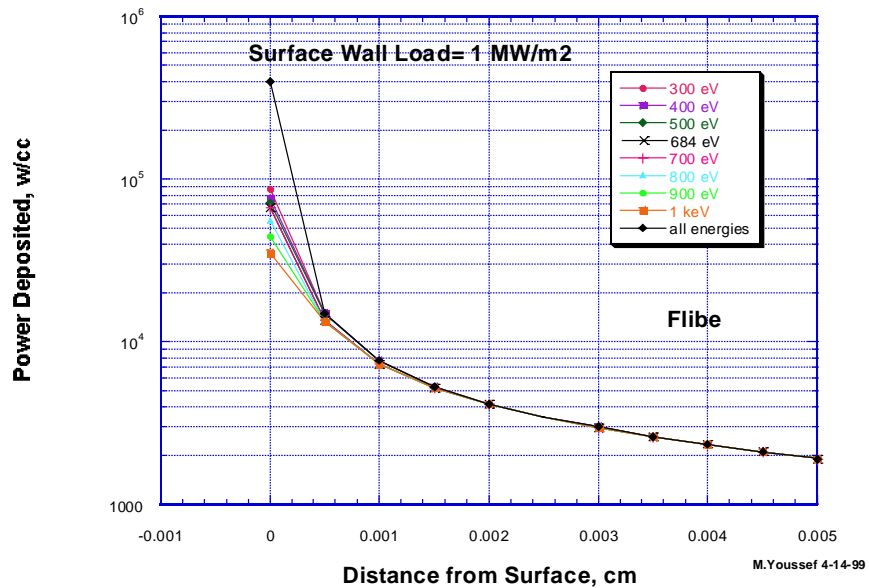


Figure 5.3-10 Power Deposition Rate in Flibe from the fraction of the Incident Bremsstrahlung Spectrum above a give Cut-Off Energy E_{co} . (Total Surface load is 1 MW/m²- depth 0.005 cm - 5 micron spatial step)

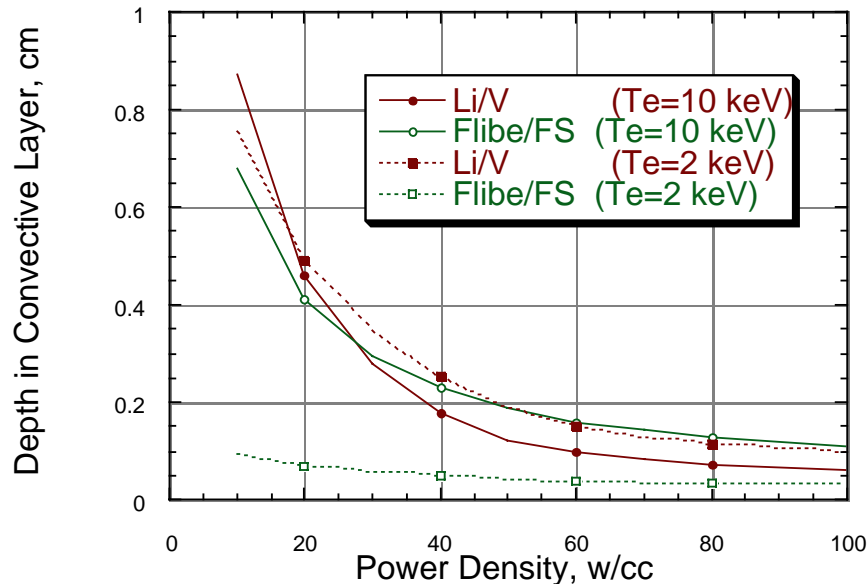


Figure 5.3-11 Depth in the Convective Layer as a Function of the Attainable Power Deposition Rate (Classical Bremsstrahlung Spectrum)

5.3.1.4 Nuclear Heat Deposition Profiles

To assess the nuclear heating profiles of neutrons and scattered gamma rays relative to the profiles of X-rays, a 1-D calculation model was used for neutron/gamma rays transport in the Li and Flibe system as shown in Figure 5.3-12. A representative 50-cm thick blanket and 15-cm thick reflector zone follow the 5-cm thick layer on the Outboard side. In the Li system, the blanket is made of Li:V4Cr4Ti (80:20) and made of Flibe:Ferritic Steel (80:20) in the Flibe system. The reflector considered in both systems is made of Ferritic Steel: water (90:10). It is included to neutronically account for neutron/gamma reflection, regardless of the compatibility concern. No breeding zone is considered on the Inboard side which includes a Be tile. The details of the TFC are considered in the model and the dimensions are those found at the middle plane in ITER configuration [9]. The analysis was performed for 7 MW/m^2 neutron wall load. The ANISN code, along with 175n-42g library based on FENDL/1.0 data [10] in P_5S_8 approximation was used.

The mean free path of neutrons ($\text{MFP}=1/\Sigma$) in Li, Flibe, and $\text{Li}_{17}\text{Pb}_{83}$ is shown in Figure 5.3-13 as a function of neutron energy. At 14 MeV, the MFP is ~16-cm in Li and 7-cm in Flibe. At all energies above ~3 eV, the MFP in lithium is larger than in Flibe by as much as an order of magnitude. At thermal energies (below 1 eV) the MFP in lithium is a factor of ~6-8 lower than in Flibe. Thus, the lithium layer is much more "transparent" to high-energy neutrons and much less "transparent" to low-energy neutrons as compared

to the Flibe. These features have direct impact on the nuclear heating rate throughout the system and on the neutron flux, the dpa, He-4, and hydrogen production rates in structure.

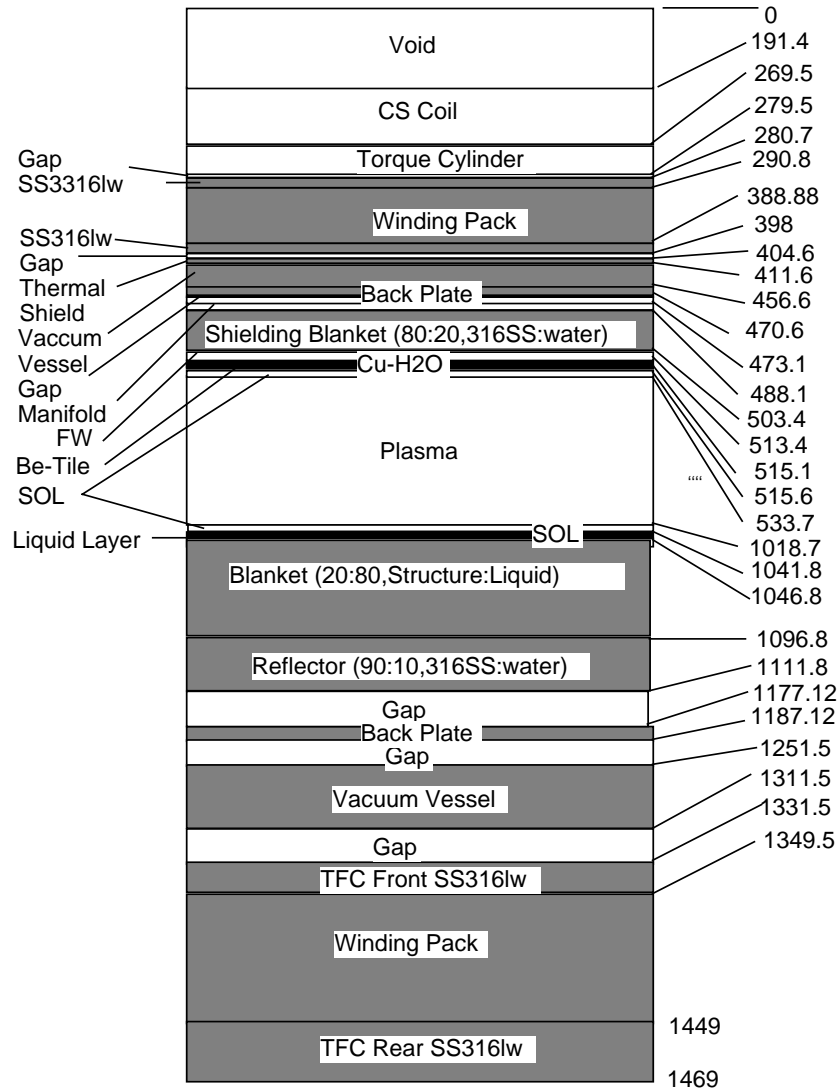


Figure 5.3-12 1-D Calculational Model used in the Analysis (SOL = Scrap Off Layer)

The maximum volumetric nuclear heat deposition rate (VNHDR) in the convective layer is larger in the Flibe than in the Li layer. The maximum attainable VNHDR at the surface are shown in Table 5.3-1. It is larger in Flibe than in Lithium by as much as 30% (natural Li-6) to 18% (90% Li-6). The VNHDR increases in the layer as Li-6 enrichment increases due to the enhancement in Li-6(n,α) reaction which is exothermic (Q ~4 MeV). In the convective layer of Lithium, VNHDR is due mainly to neutrons heating. Non-

negligible contribution from gamma heating exists in the case of Flibe. The profiles across the system are shown in Figs. 5.3-13 and 5.3-14 for the Lithium/(Li-V4Cr4Ti) and the Flibe/(Flibe-FS) case, respectively. The steepness of the profiles in Lithium/(Li-V4Cr4Ti) blanket is much less than in the Flibe/(Flibe-FS) blanket. This is due to the fact that more high-energy neutrons reach the blanket zone in the case of Li layer (the moderation power of Li is much less than Flibe at high energies). Also, as the Li-6 increases, this high-energy component decreases at the back zones resulting in a less VNHDR. In addition, it is clear from Figs. 5.3-14 and 5.3-15 that the VNHDRs across the blanket in the Flibe layer case are a factor of 2-9 lower than the VNHDRs in the Li layer case, which could lead to a substantial reduction in the thermal stresses.

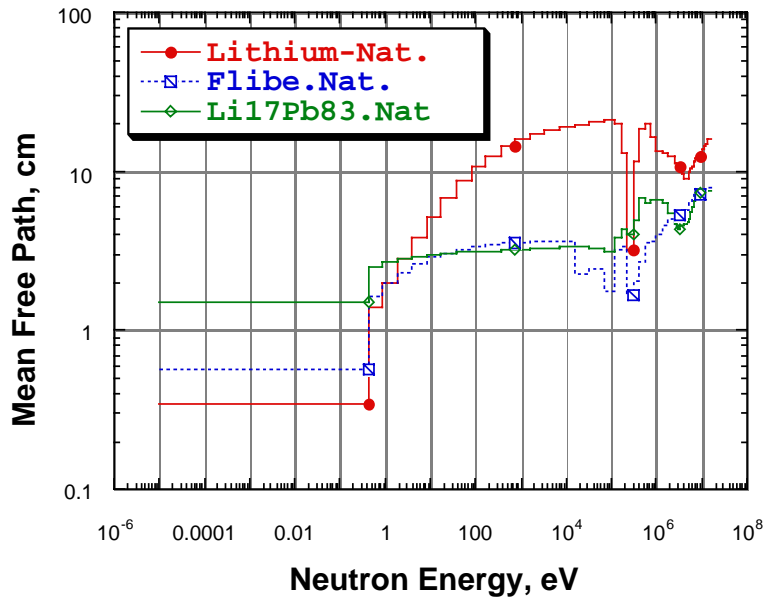


Figure 5.3.1-13 Neutron Mean Free path in Lithium, Flibe, and Li₁₇Pb₈₃.

Table 5.3-1 Maximum Volumetric Heat Deposition Rate in the Convective layer (Neutron wall Load 7 MW/m²)

	Flibe	Lithium
Natural Li-6	50 W/cc	38 W/cc
25% Li-6	55 W/cc	44 W/cc
50% Li-6	60 W/cc	49 W/cc
90% Li-6	64 W/cc	54 W/cc

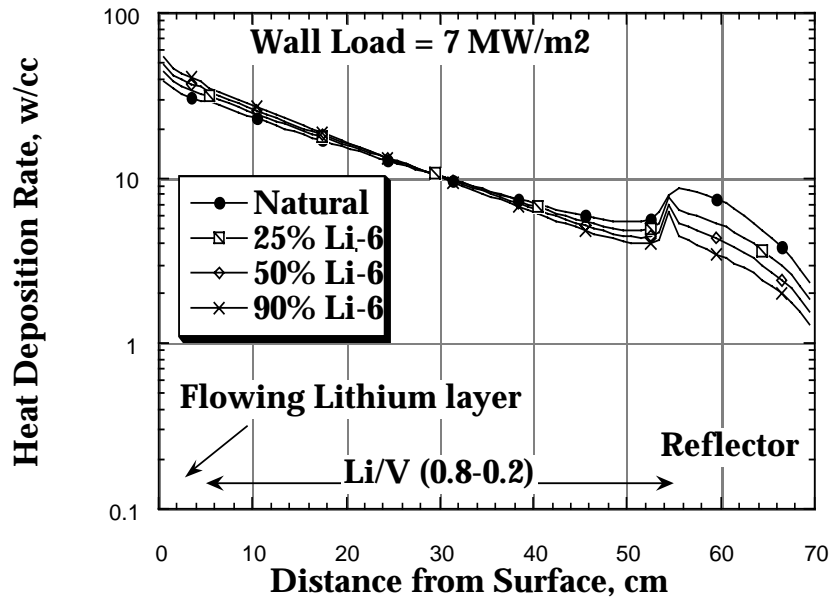


Figure 5.3-14 Volumetric Nuclear Heat Deposition Rate in the Li/(Li-V4Cr4Ti)/Reflector System

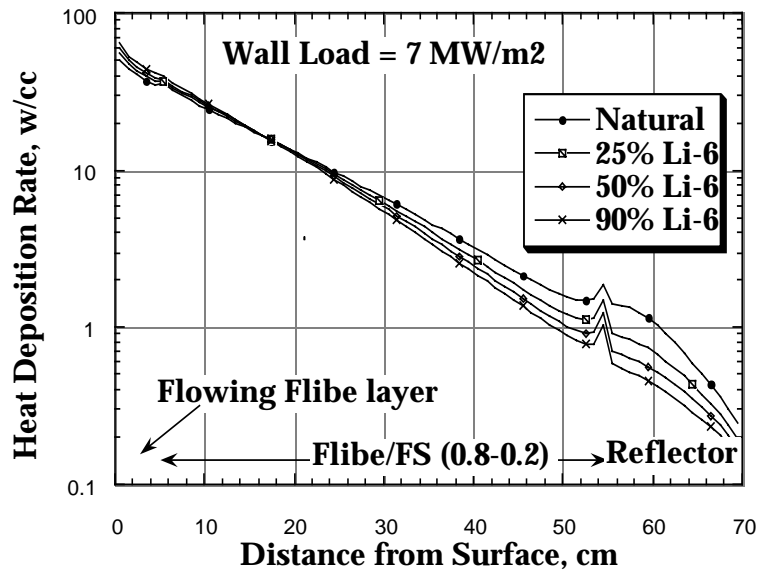


Figure 5.3-15 Volumetric Nuclear Heat Deposition Rate in the Flibe/(Flibe-FS)/Reflector System

5.3.2 Tritium Production, Heat Deposition, and Radiation Damage Characteristics in the Thick Liquid FW/Blanket Concept

In the Gravity and Momentum Driven (GMD) thick liquid FW/blanket concept the fast flowing FW (~2-3 cm) is followed by thick flowing liquid blanket (B) of ~40-50 cm thickness with minimal amount of structure (pocket concept). The liquid FW/B are contained inside the vacuum vessel (VV) with a shielding zone (S) located either behind the VV and outside the vacuum boundary (Case A) or placed after the FW/B and inside the VV (Case B). In this section, we investigate the nuclear characteristics of this concept in terms of: (1) profiles of tritium production rate and tritium breeding ratio (TBR) for several liquid candidates, and (2) profiles of heat deposition rate and power multiplication, and (3) attenuation capability of the liquid FW/B/S and protection of the VV and magnet against radiation (expressed in terms of DPA, He-4 and H production rate). The candidate liquid breeders considered are Li, Flibe, and Li-Sn. Parameters varied are: (1) FW/B thickness, L, (2) Li-6 enrichment, and (3) thickness of the shield. The structure used in the Li case is V-4Cr-4Ti while Ferritic Steel is used with Flibe and Li-Sn. In this section we will show that: (1) Flibe is more powerful material in attenuating high-energy neutrons. Lithium is a good moderator for both high- and low-energy neutrons. For a bare wall in Case A, the ratio of He-4/DPA in the VV is ~ 11 for the Flibe system and 3.2 for the Li system. At L=50 cm, this ratio drops to the value of 6.2 and 1.5, respectively. This damage index can be lowered by providing a shield of ~50 cm which will make the VV a life-time component, (2) TBR in the Li and Flibe cases is the highest at natural Li-6 and is the largest in the Li case; an inherit property for these breeders in liquid FW concepts, and (3) Li-Sn gives larger TBR than Flibe at 90%Li-6 but marginal for both breeders which may require a neutron multiplier, and (4) Power multiplication is the largest in the Li-Sn case which could improve the thermal cycle with this new breeder that exhibits low vapor pressure, an additional advantage for deployment in liquid FW/B concepts.

5.3.2.1 Case A: No Shielding Inside the Vacuum Vessel

The 1-D model describing this configuration is shown in Figure 5.3-16. The convective liquid layer shown in the figure constitutes the FW/B and its thickness, L, was assumed to be 50 cm-thick. In the present analysis, no structural material was considered inside the convective layer. The VV walls are 4 cm-thick and made of either V-4Cr-4Ti alloy in the case of Li breeder or ferritic steel (FS) in the case of Flibe and Li-Sn breeders. The inner zone of the VV is assumed to be cooled with the same type of breeders used in the convective layer with structure to coolant ratio of 20:80. In the model shown, we assess the impact of Li-6 enrichment on: tritium production rate profiles, tritium breeding ratio TBR, heat deposition rate, and power multiplication. We also establish a relationship between TBR and M. The neutron wall load considered is 10 MW/m².

5.3.2.1.1 Tritium Breeding

The profiles of tritium production rate (TPR) from Li-6 (T6) and from Li-7 (T7) are shown in Fig. 5.3-17 as a function of Li-6 enrichment in the Li/V-alloy system. The corresponding profiles in the Flibe/Ferritic Steel system are shown in Fig. 5.3-18. The contribution from Li-7 is comparable to the contribution from Li-6 at the front location in the convective layer in the case of Li/V-alloy system. However, this contribution drops rapidly at deep locations where T6 dominates. The contribution from Li-6 (T6) is always larger than T7 in the Flibe/FS system. The T7 profiles decrease with Li-6 enrichment, as expected in both system. As for T6 profiles, they also decrease with Li-6 enrichment except at front locations in the liquid layer. The total TPR profiles in both systems are shown in Fig. 5.3-19 where it is clear that the TPR at deep location in the Flibe/FS system are 1-2 orders of magnitude less in the interior zone of the VV compared to the values in the Li/V-alloy system. This is due to the superior moderating power of the Flibe as compared to the Li-breeder.

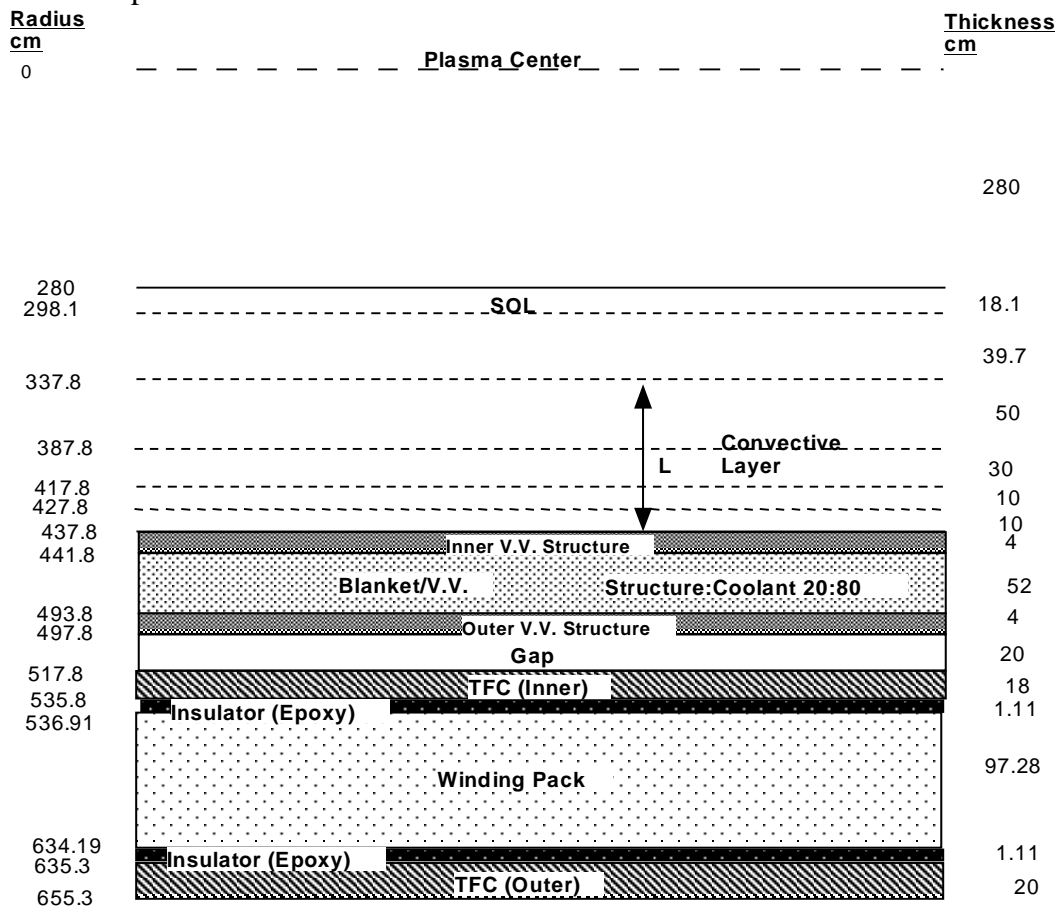


Figure 5.3-16 The 1-D Model of the Liquid FW/Blanket System With no Shielding Inside the Vacuum Vessel

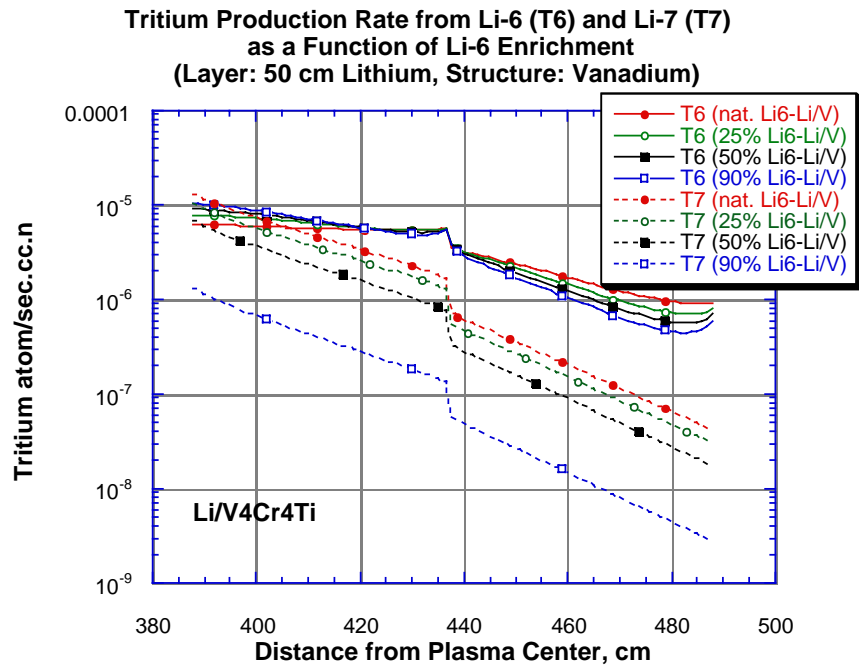


Figure 5.3-17 Profiles of the Tritium Production Rate from Li-6 (T6) and from Li-7 (T7) as a Function of Li-6 Enrichment (Li/V-alloy System)

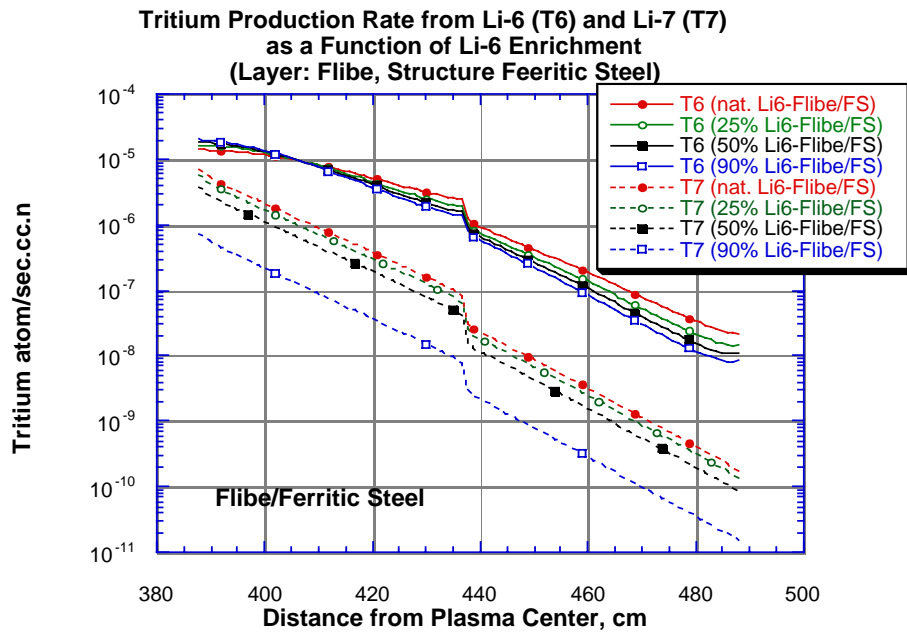


Figure 5.3-18 Profiles of the Tritium Production Rate from Li-6 (T6) and from Li-7 (T7) as a Function of Li-6 Enrichment (Flibe/Ferritic Steel System)

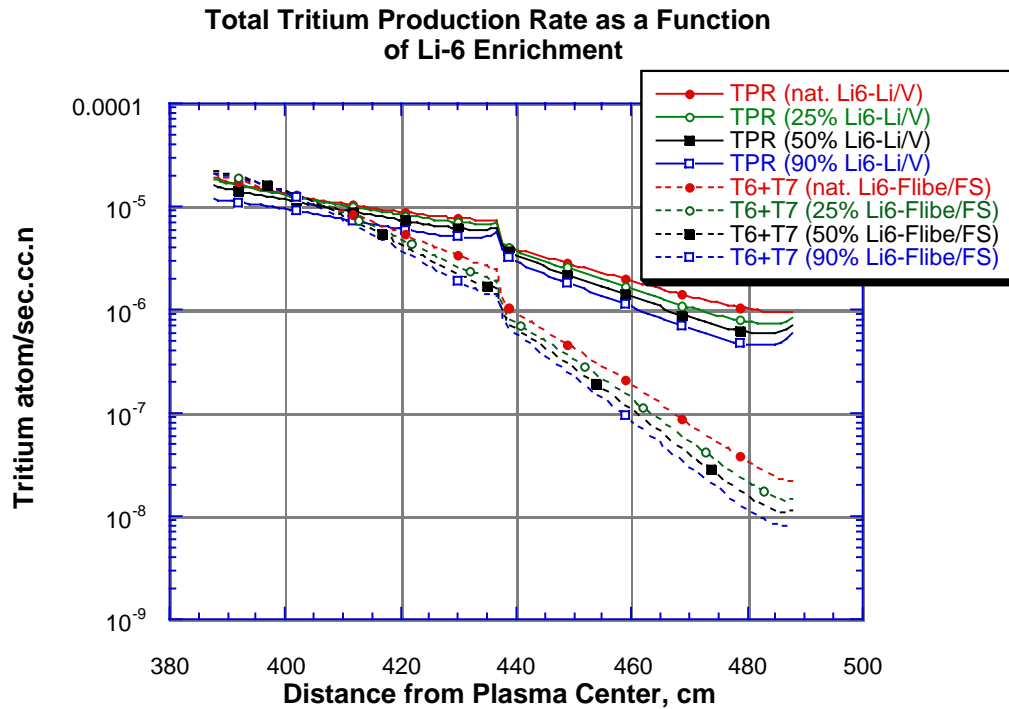


Figure 5.3-19 Profiles of the Total Tritium Production Rate a Function of Li-6 Enrichment

The integrated TPR as one moves across the system is shown in Figure 5.3-20 for various Li-6 enrichment. The total TBR is the value obtained at radius $R=493.8$ cm (see Fig. 5.3-16) that is at a depth of 106 cm from the front edge of the liquid layer. The local TBR is thus ~ 1.74 and ~ 1.24 in the Li/V-alloy and Flibe/FS system, respectively. In both systems, the TBR decreases by increasing Li-6 enrichment. Natural enrichment gives the largest TBR. This feature is true in our case where we have thick (50 cm) liquid layer on both the Inboard (IB) and outboard (OB). Since there is no structure or neutron multiplier (e.g. Be) in this layer, the increase in Li-6 enrichment leads to a decrease in $\text{Li-7}(n,n'\alpha)t$ reaction. This reaction leads to reappearance of neutrons and its decrease worsens the neutron economy in the system. In addition, lithium and Flibe are not good reflectors. The reflected low-energy component from the IB is small which leads to lower contribution from breeding in Li-6 and consequent adverse effect on TBR as Li-6 enrichment increases. The decrease in TBR with Li-6 enrichment is more pronounced in lithium than in Flibe breeder. Going from natural Li to 90 %Li-6 leads to $\sim 32\%$ and $\sim 10\%$ decrease in the local TBR in the Li/V and Flibe/FS system, respectively. Note also that the TBR in Flibe is much less than in lithium system. At natural Li-6, the TBR in Flibe/FS system (1.24) is $\sim 30\%$ less than in the Li/V-alloy system (1.74). The local TBR in the Flibe/FS system appears marginal to account for losses due penetrations, prediction and design uncertainties, radioactive decay, etc. The TBR in lithium layer case keeps rising with increasing layer/blanket thickness whereas it saturates much fast in case of Flibe but to a much lower value. This makes satisfying T self-sufficiency even harder in the Flibe case.

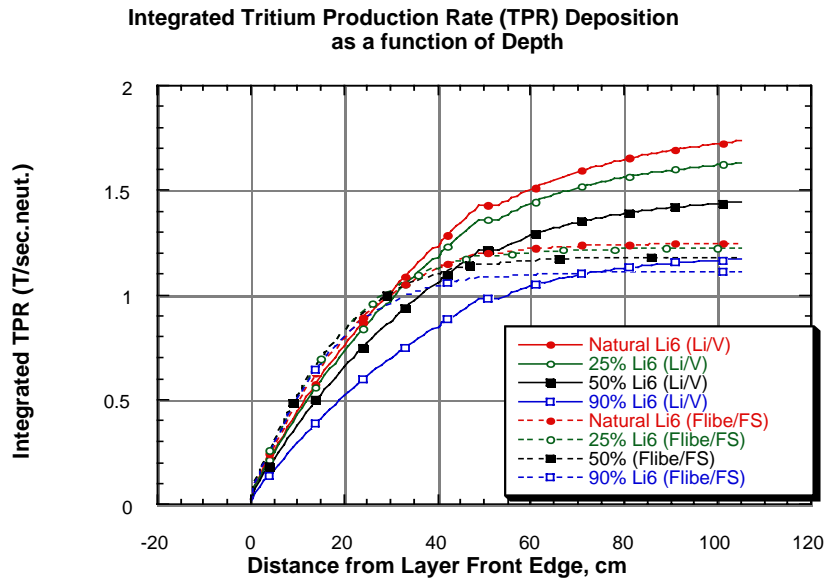


Figure 5.3-20 The Integrated Tritium Production Rate as a Function of Depth in the Convective Liquid Layer and for Various Li-6 Enrichment.

The faster saturation of TBR with increasing the liquid layer thickness can be seen from Figure 5.3-21 with depicts the fraction of the integrated TBR as a function of depth in the liquid layer. For natural Li-6 enrichment, ~44% and ~64% of the total TBR is accumulated at a depth of 20 cm in the Li and Flibe layer, respectively. About 90% of the total TBR is reached at a depth of ~67 cm and ~40 cm in Li and Flibe, respectively.

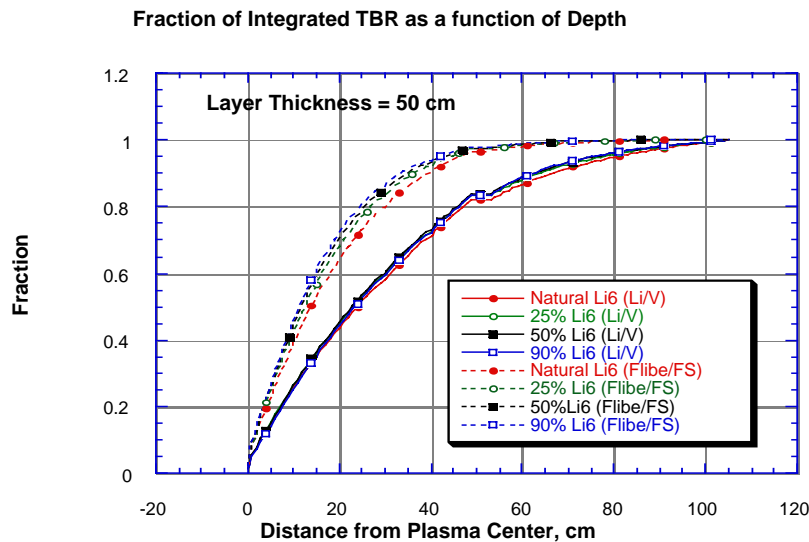


Figure 5.3-21 Fraction of the Integrated Tritium Breeding Ratio as a Function of Depth in the Convective Liquid Layer and for Various Li-6 Enrichment.

5.3.2.1.2 Heat Deposition

The profiles for the heat deposition rate are shown in Figure 5.3-22 across the Li/V-alloy and Flibe/FS systems as a function of the Li-6 enrichment (neutron wall load =10 MW/m²). Because of the higher moderation power of the Flibe, less neutrons and gamma rays reach the back locations and hence lower heating rates occur at these locations with steeper profiles. At front locations in the convective layer, increasing Li-6 enrichment leads to an increase in the heating rates due to the increase in the exthothermic Li-6(n,α) reactions. However, because the overall decrease in the neutron producing Li-7(n,n'α)t reactions, less neutrons reach the back locations which in turn leads to lower heating rates. At natural Li-6 enrichment, the maximum power density in the liquid layer is ~60 w/cc (Flibe) and ~40 w/cc (Li). In this case, the maximum heating rate in the front walls of the VV is ~12 w/cc (Li) and ~5 w/cc (Flibe).

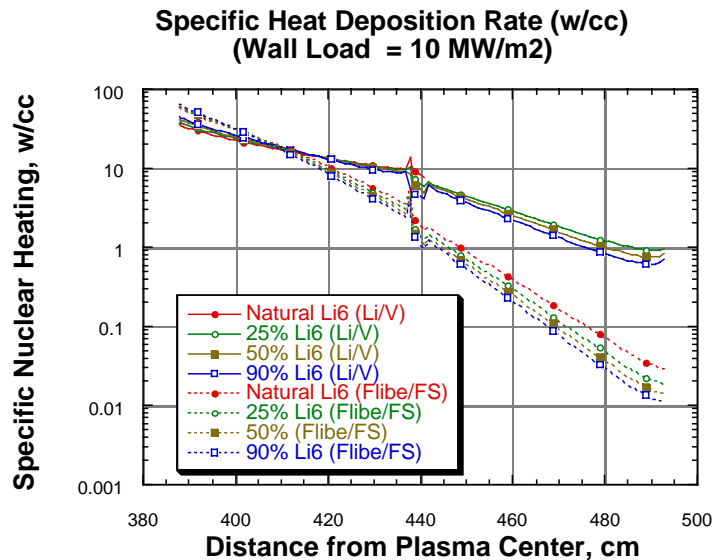


Figure 5.3-22 Profiles of the Heat Deposition Rate as a Function of Li-6 Enrichment.

The integrated power deposition is shown in Figure 5.3-23 as a function of depth throughout the system and for various Li-6 enrichment cases. The integrated power in the system is only considered in the convective layer and the vacuum vessel (small contribution from power deposited in the TF magnet). The values shown in Figure 5.3-23 are per unit height (cm) in the poloidal direction.

The power multiplication factor (M) is defined as the ratio of the total power deposited in the system to the incident neutron power. This factor is shown in Fig. 5.3-24 along with the total power deposited in the system. At natural Li-6 enrichment, M is ~1.18 (Li/V) and ~ 1.13 (Flibe/FS). The corresponding integrated power deposited in the system is ~2.27 x 10⁶ w/cm and 2.17 x 10⁶ w/cm, respectively. The power multiplication

increases slightly with Li-6 enrichment in the Li/V-alloy system and decreases in the Flibe/FS system.

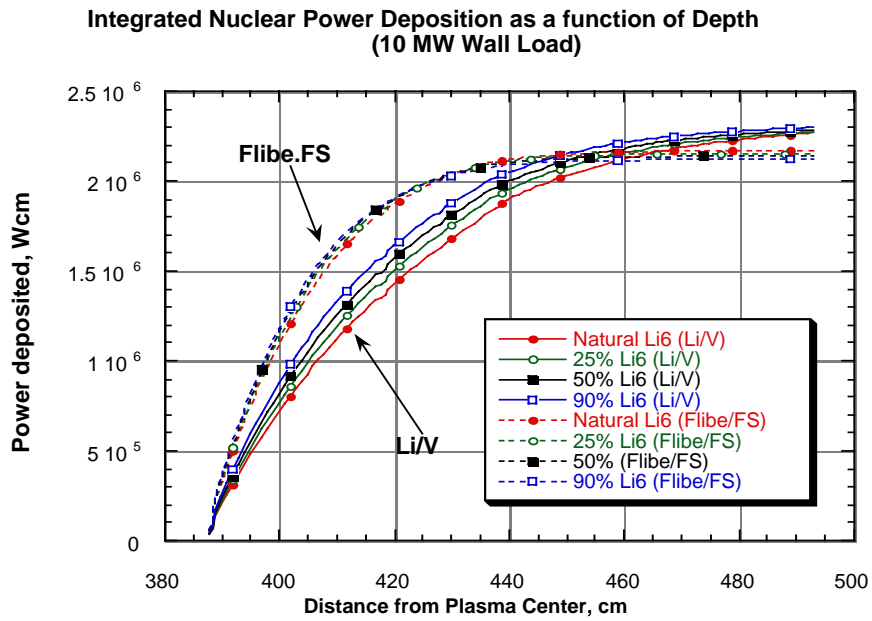


Figure 5.3-23 The Integrated Tritium Production Rate as a Function of Depth in the Convective Liquid Layer and for Various Li-6 Enrichment.

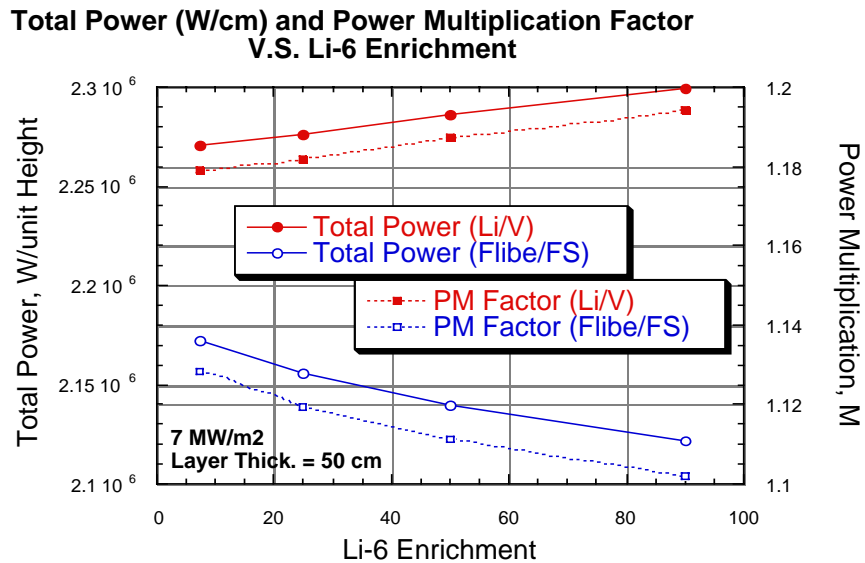


Figure 5.3-24 The total Power Deposited in the System and the Power Multiplication factor, M, as a Function of Li-6 Enrichment

The fraction of the total power deposited in the system as a function of depth throughout the system is shown in Figure 5.3-25. For a given depth, the fraction of power deposited within this depth increases with li-6 enrichment. At natural Li-6, ~47% and ~70% of the total power is deposited in the first 20 cm of the convective layer. About 90% of the total power is deposited in within the depth of 35 cm (Flibe/FS) and ~60 cm (Li/V).

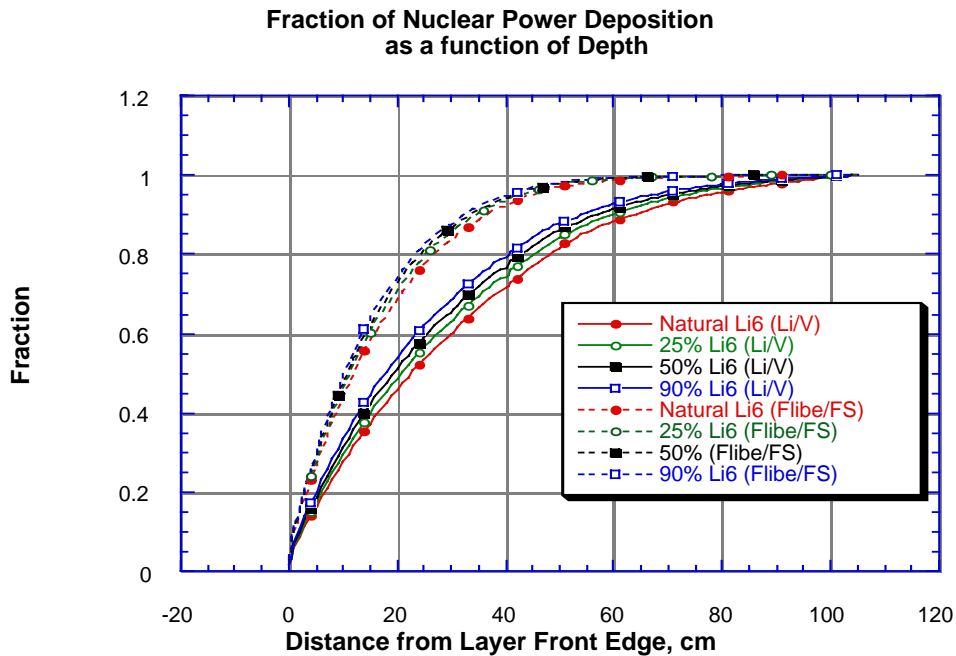


Figure 5.3-25 Fraction of the Integrated Power Deposition as a Function of Depth in the Convective Liquid Layer and for Various Li-6 Enrichment

5.3.2.2. Case B: Shielding Behind the Liquid FW/Blanket

In this configuration, a shielding zone is introduced behind the liquid FW/Blanket (FW/B) inside the vacuum vessel, which is the vacuum boundary in this case. The dimensions adopted in the configuration (see Figure 5.3-26 for the 1-D radial build of the I/B and O/B) are those of the ARIES-RS design [11]. The liquid FW is 2 cm-thick and represents a fast-flowing layer whereas the slow-flowing layer constitutes the blanket and is 40 cm-thick. A backing solid wall of 4 cm-thickness follows the liquid FW/B zone. A shielding zone of 50 cm thickness (O/B) and 49 cm thickness (I/B) is located behind the backing solid wall and is assumed to have the structure to breeder (coolant) ratio of 60:40. In all cases considered, the V.V walls are 2 cm-thick and made of 316SSLN and the interior is 16 cm-thick (I/B) and 26 cm-thick (O/B) with 316SSLN cooled with water with structure:water ratio of 80:20. As in section 5.3.2.1, the calculations were performed with ANISN code along with 46:21 neutron-gamma multi group cross section data library based on FENDL-1 data base [10]. The average neutron wall load is 10 MW/m².

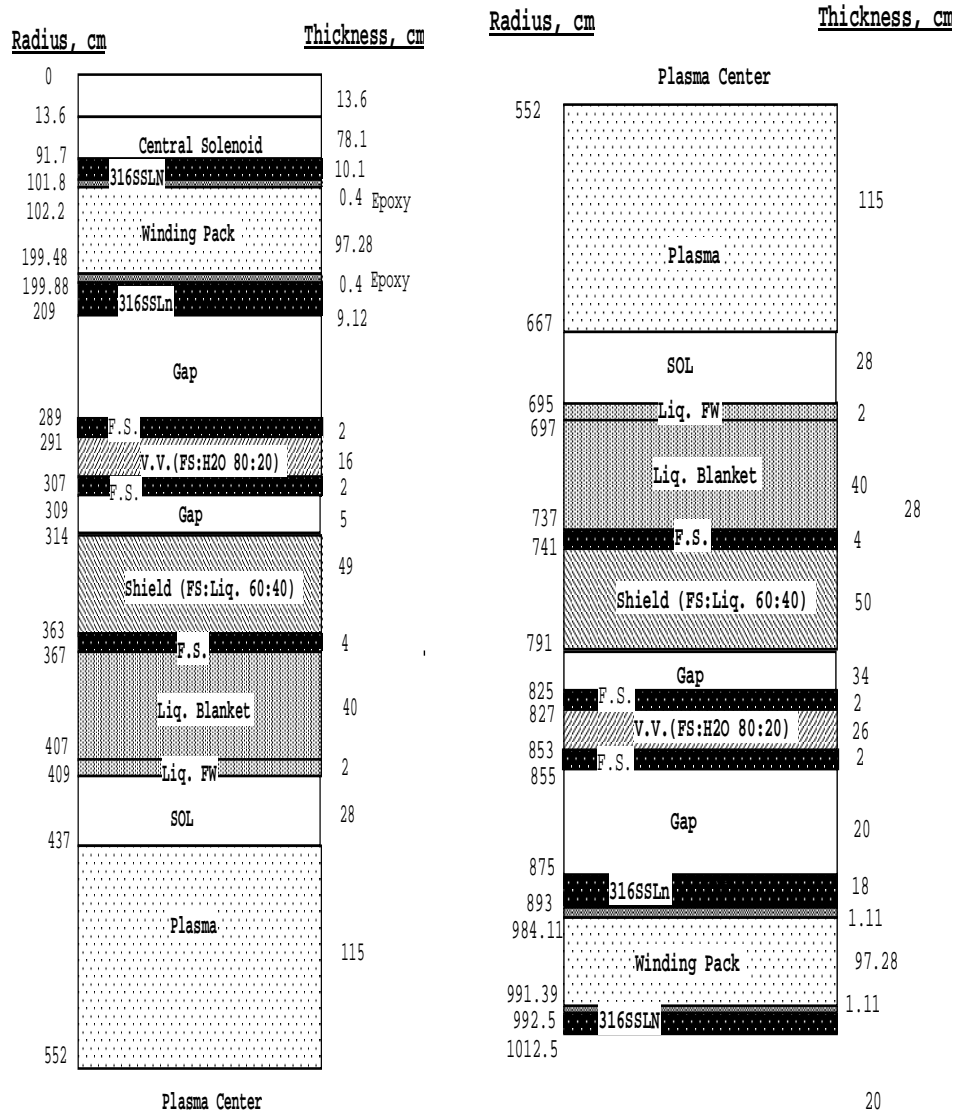


Figure 5.3-26

The Radial Build of the GMD Liquid FW/Blanket Concept with Shielding: (a) Inboard, (b) Outboard

In the following we present the tritium breeding ratio (TBR) and power multiplication (M) for two combinations of breeder/structure in the system, namely Flibe/FS and Li-Sn-/FS. We discuss also the attenuation characteristics of several breeder (Li, Flibe, Li-Sn, and Li17Pb83) and the impact on the damage parameters in the backing solid wall located behind the liquid FW/B. We assess the damage parameters in the V.V. walls and the casing of the TF coil as a function of the shielding thickness for the combination of breeder/structure considered.

5.3.2.2.1 Tritium Breeding ratio and Power Multiplication

Figure 5.3-27 shows the tritium breeding ratio, TBR, and power multiplication, PM, as a function of the Li-6 enrichment. Figure 5.3-28 shows the total power deposited in the system per unit height for 10 MW/m² wall load. The TBR is low (0.43) for Li-Sn with natural Li-6. It increases rapidly with increasing Li-6 enrichment and reaches a value of ~ 1.32 at 90% Li-6 enrichment. In the Flibe case, however, TBR is the largest at natural Li-6 enrichment (~1.22) and it decreases with Li-6 enrichment (~10% decrease at 90% Li-6 enrichment.) Note that TBR was ~1.24 in the model considered in section 5.3.2.1. As explained earlier, this decrease in TBR upon increasing Li-6 enrichment is a characteristic feature for Flibe (and Li) when the flowing liquid FW/B directly faces the plasma without a preceding solid material. In this case, increasing Li-6 enrichment, means a decrease in Li-7 enrichment and hence a decrease in neutron population via Li-7(n,n' α)t reactions. If a structural material were to be present, it would have moderated neutrons via inelastic scattering processes where they can be absorbed in Li-6, leading to an increase in TBR. This can also be seen from Figure 5.3-29 (a) and Figure 5.3-29 (b) which show the neutron spectrum behind the liquid layer (at the backing solid wall when Li-6 enrichment is natural and 90%, respectively.) At natural Li, the neutron spectrum in the Flibe case is generally larger in the low-energy range (where Li-6(n, α) cross section is large) than in the Li-Sn case. This leads to larger TBR. At 90% Li-6 enrichment, the neutron flux in the low-energy range falls below the corresponding flux in the Li-Sn case and hence leads to lower TBR with the Flibe breeder.

The sharp increase in TBR (by ~200%) by increasing Li-6 enrichment from natural Li-6 to 90% leads to noticeable decrease in PM (from 1.52 to 1.32, ~13% decrease). The decrease in PM is only ~ 2% in the case of Flibe (see Table 5.3-2.) The PM is noticeably larger in the case of Li-Sn. This is advantageous from the viewpoint of improving the thermal efficiency of the system. The large PM in this case is due to the large absorption in Sn via Sn(n, γ) reactions, particularly at low neutron energies. This leads to larger gamma-ray flux in the breeding zone, and upon transport, these gamma-rays get absorbed in the structural material (Ferritic steel, FS). The contribution of gamma-ray heating to the total heating is therefore appreciable, particularly at low Li-6 enrichment as can be seen from Figure 5.3-28. This can also be seen from Figure 5.3-30 that depicts the total power deposited in FS structure only per unit height (w/cm) of the FW/blanket/shield system in the poloidal direction. At natural Li-6, the total power deposited in the structure is a factor of ~5 larger in the Li-Sn case. As Li-6 increases, the contribution of gamma-ray heating in the structure (and the system, see Figure 5.3-28) decreases due to the decrease in the Sn(n, γ) reaction which is a competing reaction with Li-6(n, α) reaction.

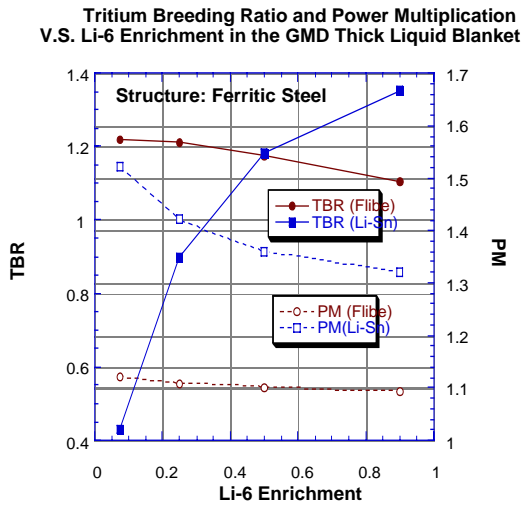


Figure 5.3-27 Tritium Breeding Ratio and Power Multiplication as a Function of Li-6 Enrichment

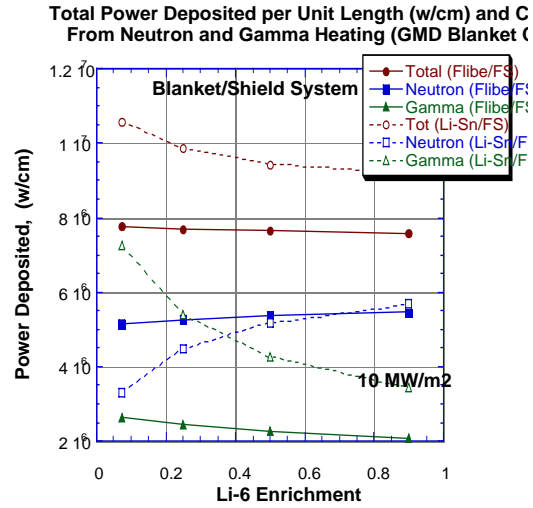
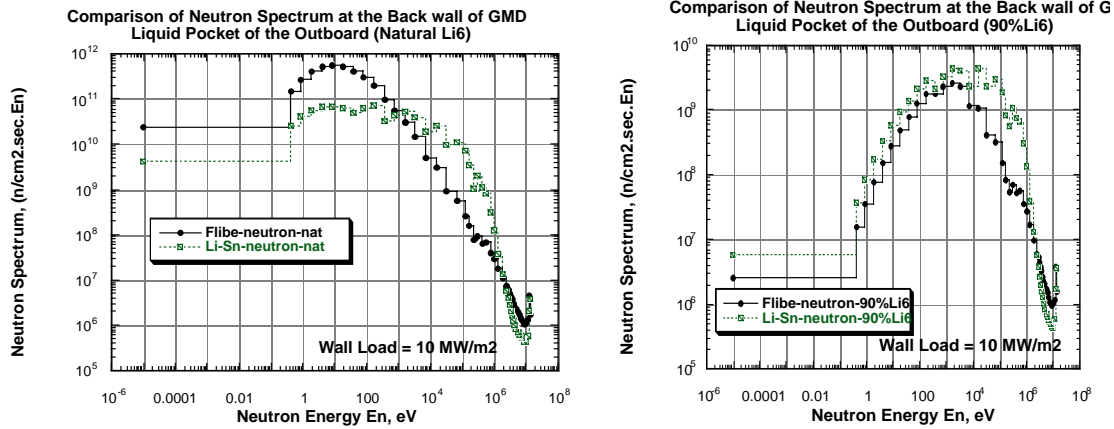


Figure 5.3-28 Total Power Deposited in the System and Contribution from Neutron and Gamma-ray Heating

Table 5.3-2 TBR and Power Multiplication (PM) in the GMD Liquid FW/Blanket Concept

	Natural Li-6		25% Li-6		90% Li-6	
	Flibe	Li-Sn	Flibe	Li-Sn	Flibe	Li-Sn
TBR	1.22	0.43	1.21	0.90	1.11	1.35
PM	1.12	1.52	1.11	1.42	1.09	1.32

The profiles for the heat deposition rate in the case of Flibe/FS system is shown in Figure 5.3-31 (I/B and O/B) and in Figure 5.3-32 (O/B) for 10 MW/m² average neutron wall load and with natural Li-6 enrichment. The maximum heating rate at several locations are summarized in Table 5.3-3. The maximum heating in the Flibe liquid is ~70 w/cc (O/B) where as the heating rate in the backing solid wall is ~8 w/cc (O/B). This value is nearly an order of magnitude lower than the maximum heating rate in the liquid region. Note that heating rates on the O/B side are larger than those on the I/B side, except for heating rates in the magnet casing where the values in the I/B side are almost an order of magnitude larger than those on the O/B side.



(b)

Figure 5.3-29 Neutron Spectrum Behind the Liquid layer at the Backing Solid Wall: (a) Natural Li, (b) 90% Li-6 Enrichment

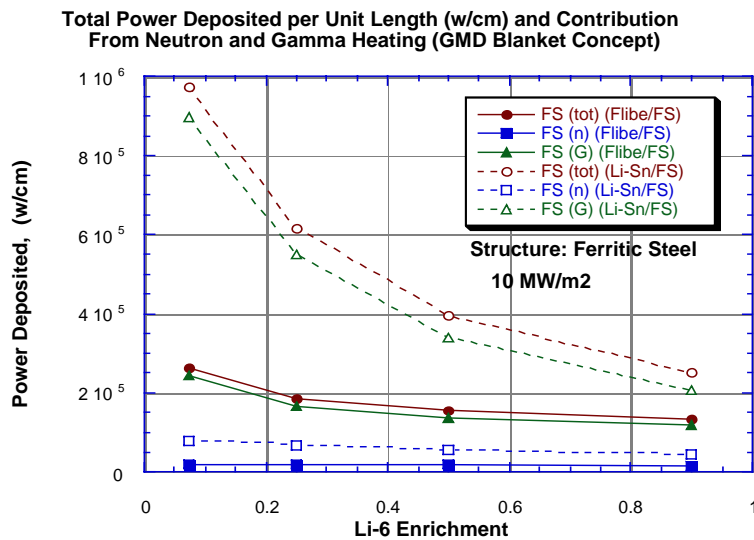


Figure 5.3-30 Total Power Deposited in the Structure (Ferritic Steel) per Unit Length (W/cm) and the Contribution from Neutron and Gamma Heating (the GMD Thick Liquid FW/Blanket Concept)

Table 5.3-3 Maximum Nuclear Heat Deposition Rate, w/cc

	Liquid FW	Backing Solid FW	Shield	V.V. Walls	TF Coil Casing	Winding Pack
I/B	60	6	2.8	0.04	0.003	0.0002
O/B	70	8	6	0.04	0.0004	0.00003

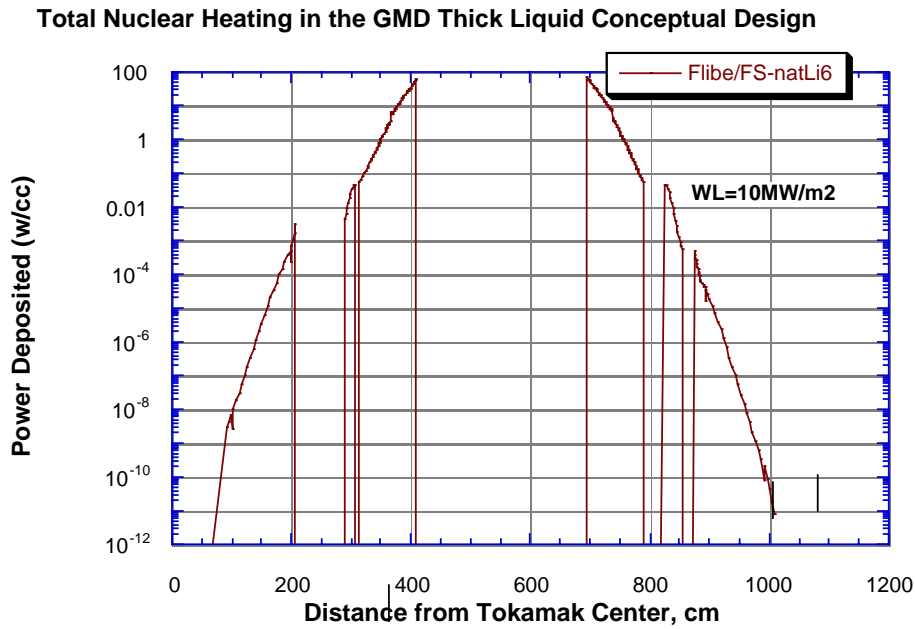


Figure 5.3-31 The profiles of Heat Deposition Rate in the Inboard and Outboard of the GMD Liquid FW/Blanket concept.

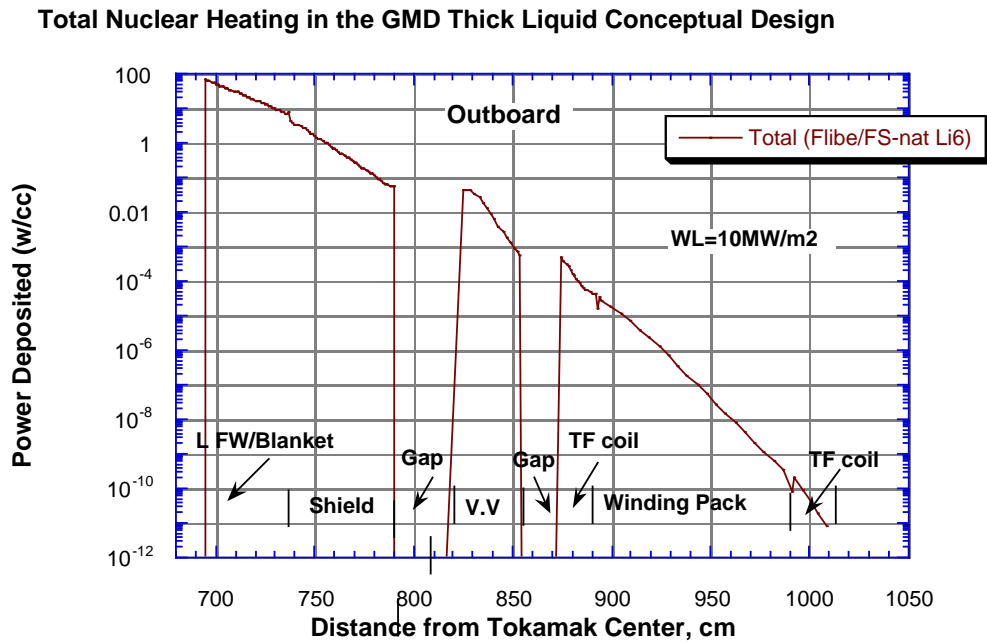


Figure 5.3-32 The profiles of Heat Deposition Rate in the Outboard of the GMD Liquid FW/Blanket concept

5.3.2.2.2 Attenuation Characteristics of Several Liquid Breeders

The impact of the convective layer thickness on the damage parameters in the backing solid wall has been studied for several breeders. For comparison purposes, the ferritic steel is assumed to be the structural material of the backing wall and in the shield zone. The thickness of the convective layer, L, was varied as L=0 cm (bare wall), 10 cm, 20, cm, 30 cm, and 42 cm (reference case). Figure 5.3-33 to Figure 5.3-36 show the DPA rate (DPA/FPY), the helium production rate (appm/FPY), the ratio He-4/DPA, and the hydrogen production rate (appm/FPY), respectively. The breeders considered for the liquid layer and the coolant in the shielding zone are Li, Flibe, Li-Sn, and Li-Pb.

Without the liquid layer (bare wall case), the helium and hydrogen production rates in the backing solid wall are comparable in the four breeders. However, because Li-Pb exhibits larger reflection, the low-energy neutron flux is larger at the solid wall which resulted in larger DPA rate (occurs at all energies). This also gives smaller He-4/DPA ratio in the case of Li-Pb breeder (~8.7) as compared to the value with the other breeders (10-11).

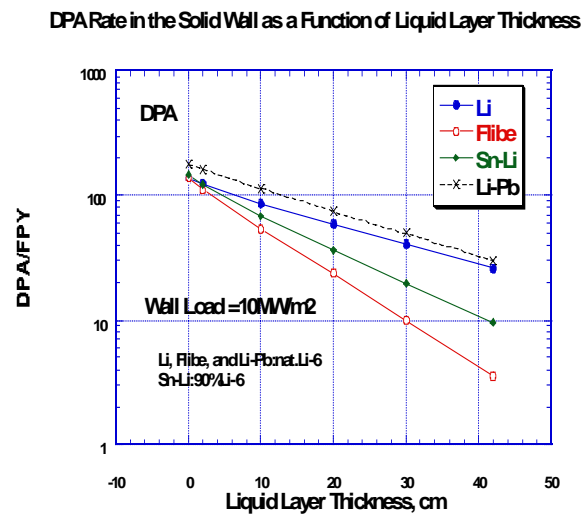


Figure 5.3-33 The DPA Rate in the Backing Solid Wall.

As the thickness of the convective layer increases, the reduction in these damage parameters varies among the four breeders. The lithium is weakest material in moderating neutrons as compared to the other breeders. The reduction in DPA rate is less than an order of magnitude for L=42 cm while the reduction in helium and hydrogen production is about an order of magnitude. The attenuation characteristic of the Li-Pb breeder for the DPA rate is similar to lithium. However, the Li-Pb is superior to the other breeders in attenuating the helium and hydrogen production rate in the solid wall. This is due to its larger attenuation power to high-energy neutrons [though (n,2n) and (n,inelastic) reactions] which basically the main contributor to the high-threshold helium

and hydrogen reactions in the solid wall. Because of the smallest He-4 production and the largest DPA rate with the Li-Pb breeder, the ratio He-4/DPA is the smallest (~0.3) at L=42 cm as compared to the values with the other breeders (Li; ~7, Flibe: ~6, Li-Sn: 2). The attenuation characteristics of the Flibe and Li-Sn are similar for the helium and hydrogen production. However, the Flibe gives the best attenuation to the DPA rate since it is capable of attenuating both the high- and low-energy component of the neutrons reaching the backing solid wall.

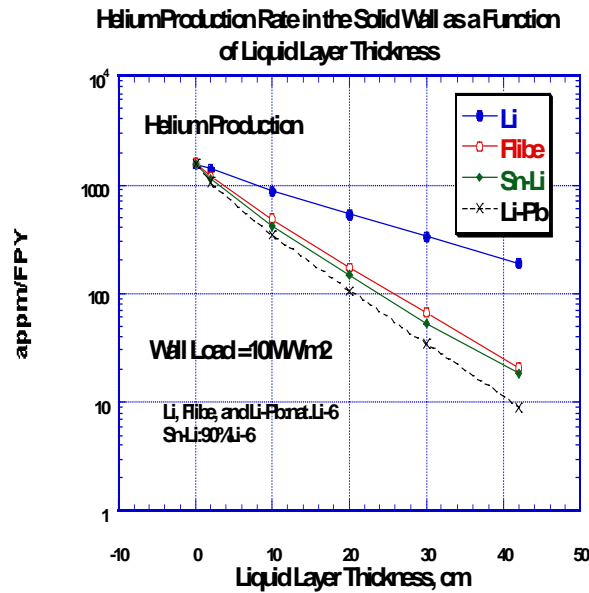


Figure 5.3-34 The Helium Production Rate in the Backing Solid Wall

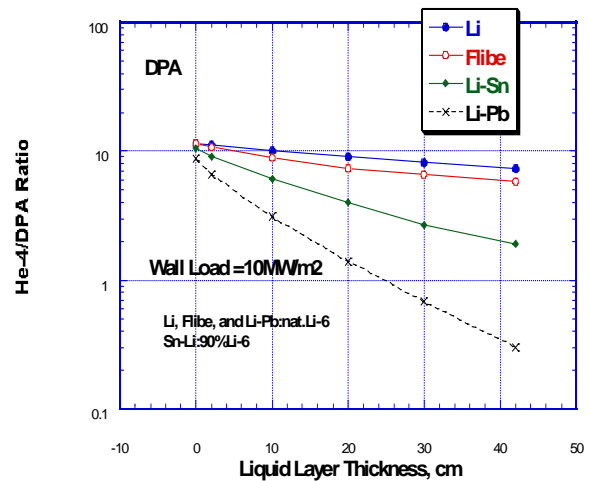


Figure 5.3-35 The He-4/DPA Ratio as a Function of the Liquid Layer Thickness

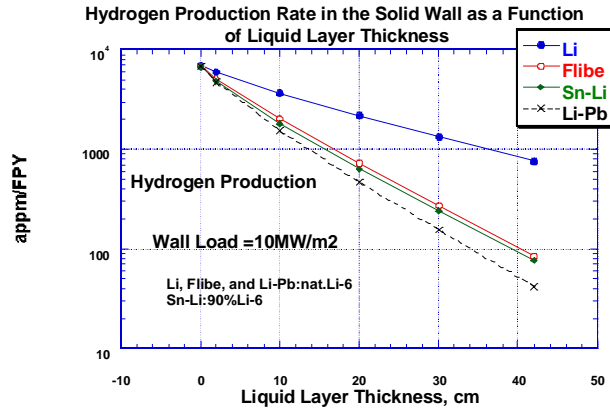


Figure 5.3-36 The Hydrogen Production Rate in the Backing Solid Wall.

Table 5.3-4 gives the damage indices in the backing solid wall with the four breeders for the two cases of liquid layer thickness of $L=0$ cm (bare wall) and $L=42$ cm (reference case). Using the values shown in this table, one can estimate the 10-fold thickness, L_{10} , for each breeder defined as the required thickness of the layer to reduce a particular response, R (damage parameter) by an order of magnitude and is given by:

$$L_{10} = \frac{\ln 0.1}{\ln \frac{R_L}{R_0}}, \tag{5.3-3}$$

where R_L is the response value at $L=42$ cm and R_0 is bare wall value (at $L=0$ cm). This thickness is given in Table 5.3-5 for the various damage parameters and breeders. For helium and hydrogen production rate, ~22 cm is required to achieve an order of magnitude reduction with Flibe and Li-Sn and smaller thickness (~18 cm) is required in the Li-Pb liquid layer. Twice as much thickness is required in the Li case because of its poor attenuation characteristics for helium and hydrogen production. As for the DPA rate, larger thickness is required. It is ~26 cm and ~36 cm for the Flibe and Li-Sn, respectively, but much larger thickness (~58 cm) is required in the Li and Li-Pb to reduce the DPA rate by an order of magnitude.

The DPA rate in backing solid wall is ~26 DPA/FPY, 3.6 DPA/FPY, 9.5 DPA/FPY, and 30 DPA/FPY, with the Li, Flibe, Li-Sn, and Li-Pb liquid layer, respectively. If the 200 DPA is considered as the limit at which the wall and shield zone require replacement, the lifetime of these components would be 7.7 year, 56 year, 21 year, and 7 year, respectively. Clearly the presence of the liquid layer made these components last the lifetime of the plant (30 year) when Flibe is used as the breeder. In the case of Li-Sn, one replacement may be required after ~20 years. But 3-4 replacements may be needed in the case of Li and Li-Pb breeders.

Table 5.3-4 **Damage Parameters in the Backing Solid Wall With and Without the Liquid Layer (Wall Load=10 MW/m²-Liquid Layer = 42 cm)**

	Lithium		Flibe		Li-Sn		Li-Pb	
	Bare Wall	With Layer						
DPA/FPY	137	26	137	3.6	147	9.5	178	30
Helium	1558	191	1567	21	1546	18	1553	9
He-4/DPA	11.4	7.3	11.4	5.8	10.5	1.9	8.7	0.3
Hydrogen	6846	763	6885	85	6801	77	6850	42

Table 5.3-5 **The 10-Fold Thickness of the Liquid Layer***

Parameter	Li/FS	Flibe/FS	Li-Sn/FS	Li-Pb/FS
DPA (dpa/FPY)	~58	~26	~36	~56
Helium Production (appm/FPY)	~46	~22	~21	~18
Hydrogen Production (appm/FPY)	~44	~22	~22	~19

* The thickness required to reduce a response by an order of magnitude

5.3.2.2.3 Shielding Effectiveness

The damage parameters at the wall of the vacuum vessel, at the casing of the TF coil, and at the Cu-stabilizer were investigated for two types of breeders, namely Flibe and Li-Sn, as a function of the shielding zone thickness, X. The thickness X was varied as X=0 cm (no shield), X=20 cm, X=40 cm, and X=50 cm. The breeders selected are also the cooling media in the shielding zone (see Figure 5.3-26). Neutron average wall load is 10 MW/m².

With the Flibe liquid FW/B (42 cm-thick- natural Li-6), the maximum DPA rate in the V.V walls. The casing of the TF coil and the Cu-stabilizer are shown in Figure 5.3-37 as calculated in the I/B and O/B sides. The DPA rate in the V.V. walls of the I/B and O/B are similar. However, the DPA rates in the TF coil casing and the Cu-stabilizer are ~5 and ~10 times larger, respectively, in the I/B side as compared to the values found in the O/B side. The 10-fold attenuation length of the shield (40%Flibe, 60%FS) is ~20 cm, i.e. an order of magnitude reduction in the V.V. DPA rate for every 20 cm of the shield. As shown, in Figure 5.3-37, the DPA rate in V.V at 50 cm-thick shield is ~ 0.01 DPA/FPY. Over 30 years plant lifetime, the accumulated DPA are below the 200 dpa limit which makes the V.V. a lifetime component. This was also found for the backing solid wall as was discussed in the previous section. The helium and hydrogen production rates at these locations are shown in Figure 5.3-38 and Figure 5.3-39, respectively. Again, these rates

are similar at the V.V. walls in the I/B and O/B sides but are larger in the casing of the TF coil of the I/B by a factor of 5-6 as compared to the values in the O/B side. The helium production rate in the walls of the V.V. is ~0.02 appm/FPY. The accumulated value after 30 years is ~0.6, which is below the 1 appm limit for the V.V. to be reweldable.

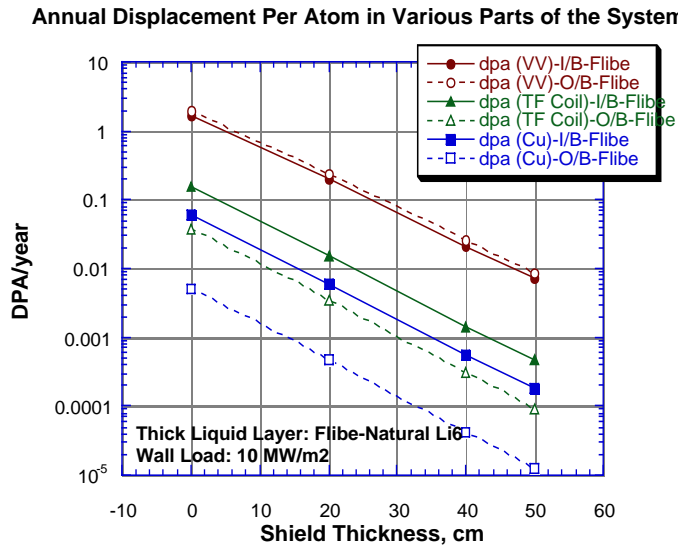


Figure 5.3-37 The DPA Rate in the Vacuum, Casing of the TF Coil and Cu-Stabilizer as a Function of Shield Thickness

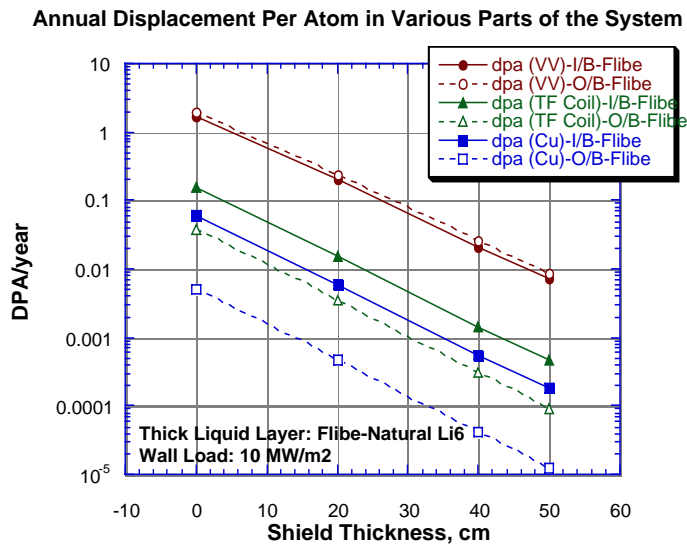


Figure 5.3-38 The Helium Production Rate in the Vacuum and the Casing of the TF as a Function of Shield Thickness.

Hydrogen Production Rate (appm/yr) in Various Parts of the System

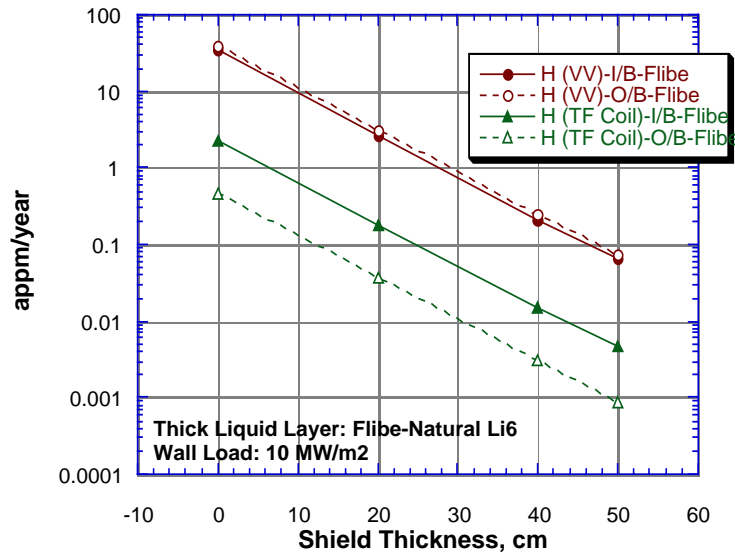


Figure 5.3-39 The Helium Production Rate in the Vacuum and the Casing of the TF as a Function of Shield Thickness

A comparison between Flibe and Li-Sn breeders for the damage parameters in the V.V. and the TF coil in the I/B side are shown in Figure 5.3-40 to Figure 5.3-41, for the DPA, helium and hydrogen production rates, respectively. For the DPA rates, they are larger with the Li-Sn breeder than the values found with the Flibe. If no shielding is present, they are larger by a factor of 2-3. At 50 cm-thick shield, they are larger by ~ an order of magnitude. This is due to the fact that Flibe is more effective in attenuating the nuclear field than Li-Sn, as discussed previously (see Figure 5.3-33). The attenuation length of the Li-Sn shield is ~30 cm. This is smaller than the attenuation length for pure Li-Sn liquid layer (~36 cm, see Table 5.3-5) due to the presence of ferritic steel in the shielding zone.

Because the similarity between the attenuation characteristics of liquid Flibe and Li-Sn for helium and hydrogen production (see Figure 5.3-35 and Figure 5.3-37), the rates of these damage indices are almost identical in the V.V. and the TF coil casing, as shown in Figure 5.3-41 and Figure 5.3-42.

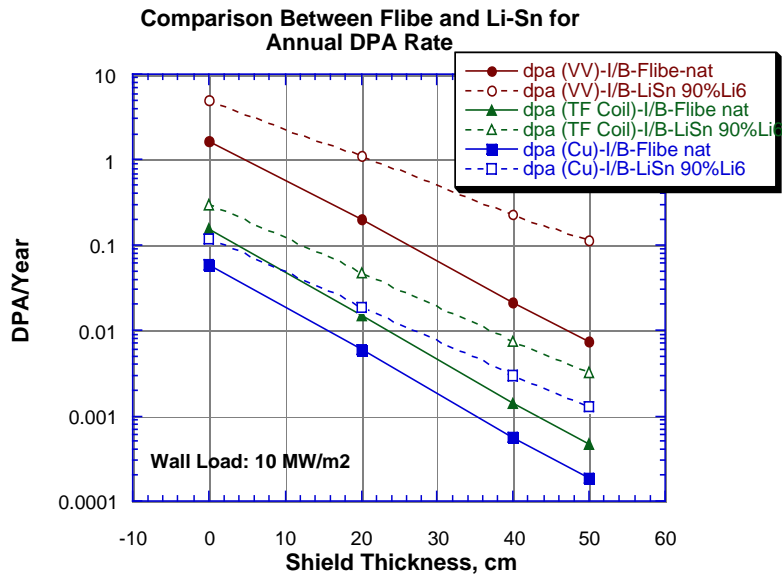


Figure 5.3-40 A comparison between Flibe and Li-Sn for the DPA Rates as a function of the Shield Thickness

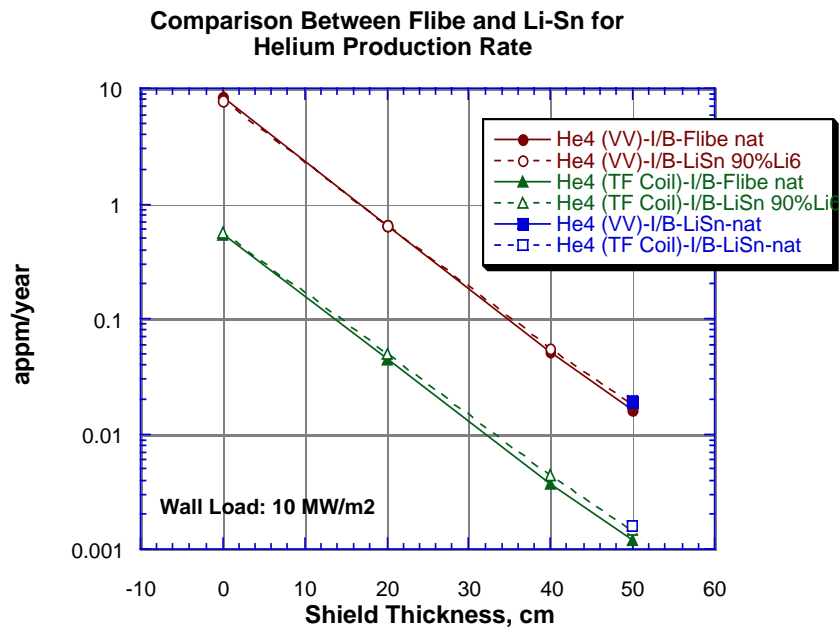


Figure 5.3-41 A comparison between Flibe and Li-Sn for the Helium Production Rates as a function of the Shield Thickness

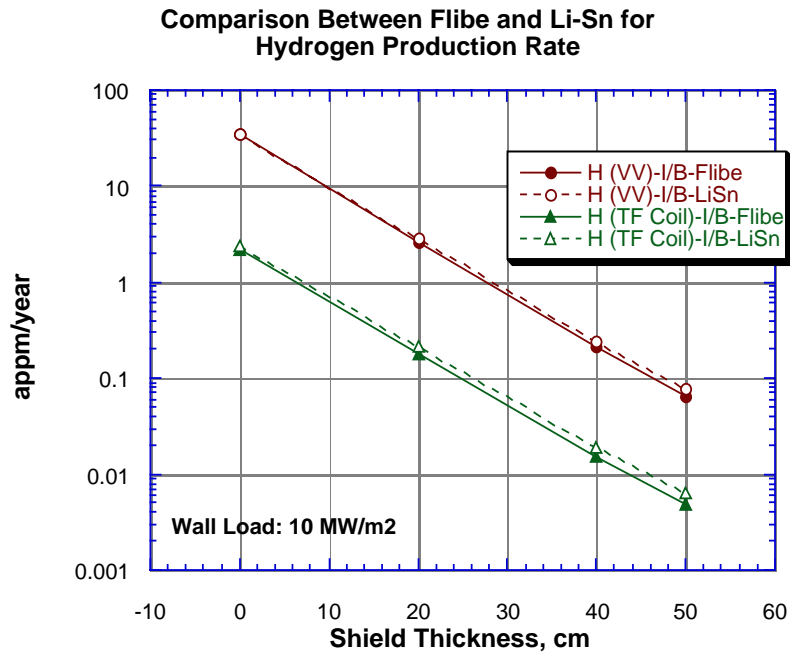


Figure 5.3-42

A comparison between Flibe and Li-Sn for the Hydrogen Production Rates as a function of the Shield Thickness

5.3.3 Activation Analysis

5.3.3.1 Introduction

Activation analysis was performed for the thick liquid metal blanket concept. Calculations are performed assuming neutron wall loadings of 7 and 10 MW/m² at the front layer of the inboard and outboard liquid blankets, respectively. The analysis used the ORNL low activation ferritic steel (LAFS) 9Cr-2WVTa as a structure material and Flibe as breeding material. The elemental composition of the ferritic steel 9Cr-2WVTa alloy is shown in Table 5.3-6. The radial build used in the analysis is based on the uses a 42-cm thick liquid first wall/blanket. Based on dpa limits for steel, all components are life-time components and were assumed to stay in place for 30 FPY. The radial build of the 1-D model used in the calculation is shown in Figures 5.3-43 and 5.3-44 for the inboard and outboard sides, respectively. Neutron transport calculations were performed using the discrete ordinates neutron transport code DANTSYS [12]. The neutron flux obtained from the neutron transport calculations was used in the activation calculations. The activation analysis was performed using the activation code DKR-PULSAR2.0 [13]. The code combined the neutron flux with the FENDL/A-2.0 [14] data library to calculate the activity and decay heat as a function of time following shutdown. Calculated specific activities were used to calculate the waste disposal ratings (WDR) of the different components at the end of their life-time. Results of the decay heat analysis were used to evaluate the temperature variation exhibited by the structure during a loss of coolant accident (LOCA).

A scoping study was performed to examine the advantages this concept might have over a conventional blanket concept. Using the same radial build, the liquid blanket was replaced by a conventional first wall and blanket. The conventional first wall is 2-cm thick and made of the ORNL LAFS 9Cr-2WVTa alloy. The conventional blanket is 40-cm thick and made of 10% ORNL LAFS 9Cr-2WVTa and 90% Flibe. Based on dpa limits for steel, the conventional blanket will need to be replaced every ~ 3 FPY. On the other hand, the shield and vacuum vessel will continue to stay in place for 30 FPY. An analysis comparing the waste disposal ratings and volume of wastes generated in power plants using the two blanket concepts was conducted. In addition, a comparison of the potential hazard of the two concepts was also presented in the form of a comparison of the total off-site dose inventory associated with each concept.

5.3.3.2. Activity and Decay Heat

Figures 5.3-45 and 5.3-46 show the specific activity and decay heat values induced in the different components of the design as a function of time following shutdown, respectively. As shown in the two figures, the ORNL LAFS produces acceptable level of radioactivity after shutdown. The inboard and outboard shields dominate the overall activity and decay heat induced in the structure. Table 5.3-7 shows a list of nuclides that dominate the induced radioactivity at different times following shutdown. As shown in the table, ⁵⁵Fe(T_{1/2} = 2.7 yr), ¹⁸⁵W(T_{1/2} = 75.1 day), and ¹⁸⁷W(T_{1/2} = 23.9 hr) are the main contributors to the induced radioactivity during the first few weeks following shutdown.

⁵⁵Fe($T_{1/2} = 2.7$ yr) and ⁵⁴Mn dominate the induced activity in the intermediate-term following shutdown. The long-term radioactivity (between one and ten years) is mostly generated by the ⁶³Ni($T_{1/2} = 100$ yr) and ⁶⁰Co($T_{1/2} = 5.27$ yr) isotopes. Nuclides with much longer half-lives have no impact on the decay heat generated from the LOCA point of view. However, as shown in the next section, these nuclides dominate the waste disposal ratings.

Table 5.3-6 Elemental Composition of the ORNL LAFS Alloy.

<u>Nuclide</u>	<u>wt% or wppm</u>	<u>Nuclide</u>	<u>wt% or wppm</u>
C	0.1%	Pd	0.18 wppm
Si	0.25%	Ag	0.16 wppm
V	0.025%	Cd	0.05 wppm
Cr	9%	Eu	0.05 wppm
Mn	0.5%	Dy	0.05 wppm
Fe	88.055%	Ho	0.05 wppm
Co	34 wppm	Er	0.05 wppm
Ni	402 wppm	Ta	0.07%
Nb	0.5 wppm	W	2%
Mo	70 wppm	Os	0.02 wppm
		Ir	0.05 wppm
		Bi	0.05 wpp

Table 5.3-7 List of Dominant Nuclides.

	<u>Activity</u>	<u>Decay Heat</u>
Short-term < 1 day	⁵⁵ Fe, ¹⁸⁵ W, ¹⁸⁷ W	⁵⁶ Mn, ¹⁸⁷ W
Intermediate-term < 1 month	⁵⁵ Fe, ⁵⁴ Mn, ⁵¹ Cr	⁵⁴ Mn, ¹⁸² Ta
Long-term > 1 year	⁵⁵ Fe, ⁶³ Ni	⁶⁰ Co, ⁵⁴ Mn

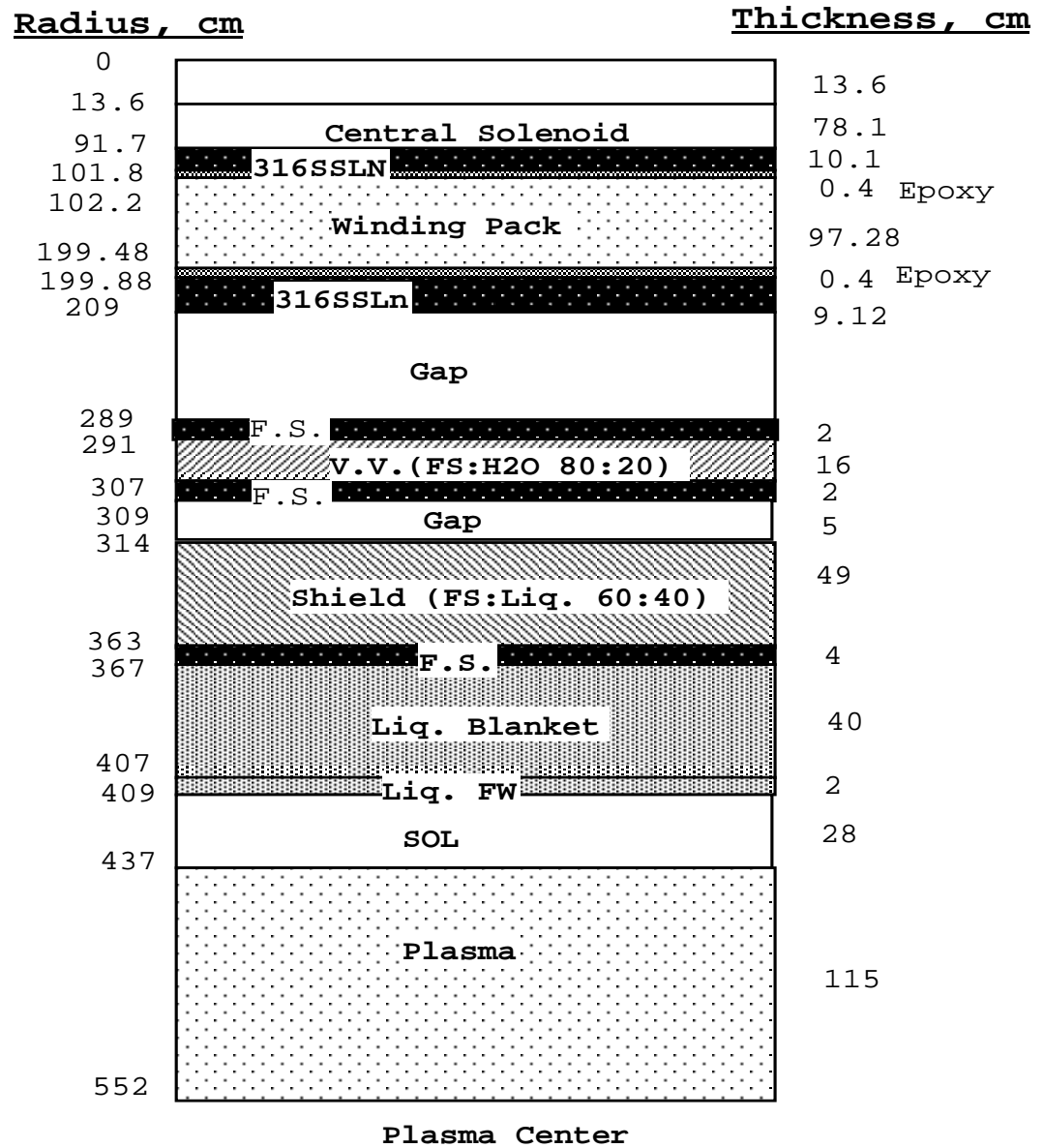


Figure 5.3-43 Radial Build of the I/B Thick Liquid (Pocket) Concept (Inboard).

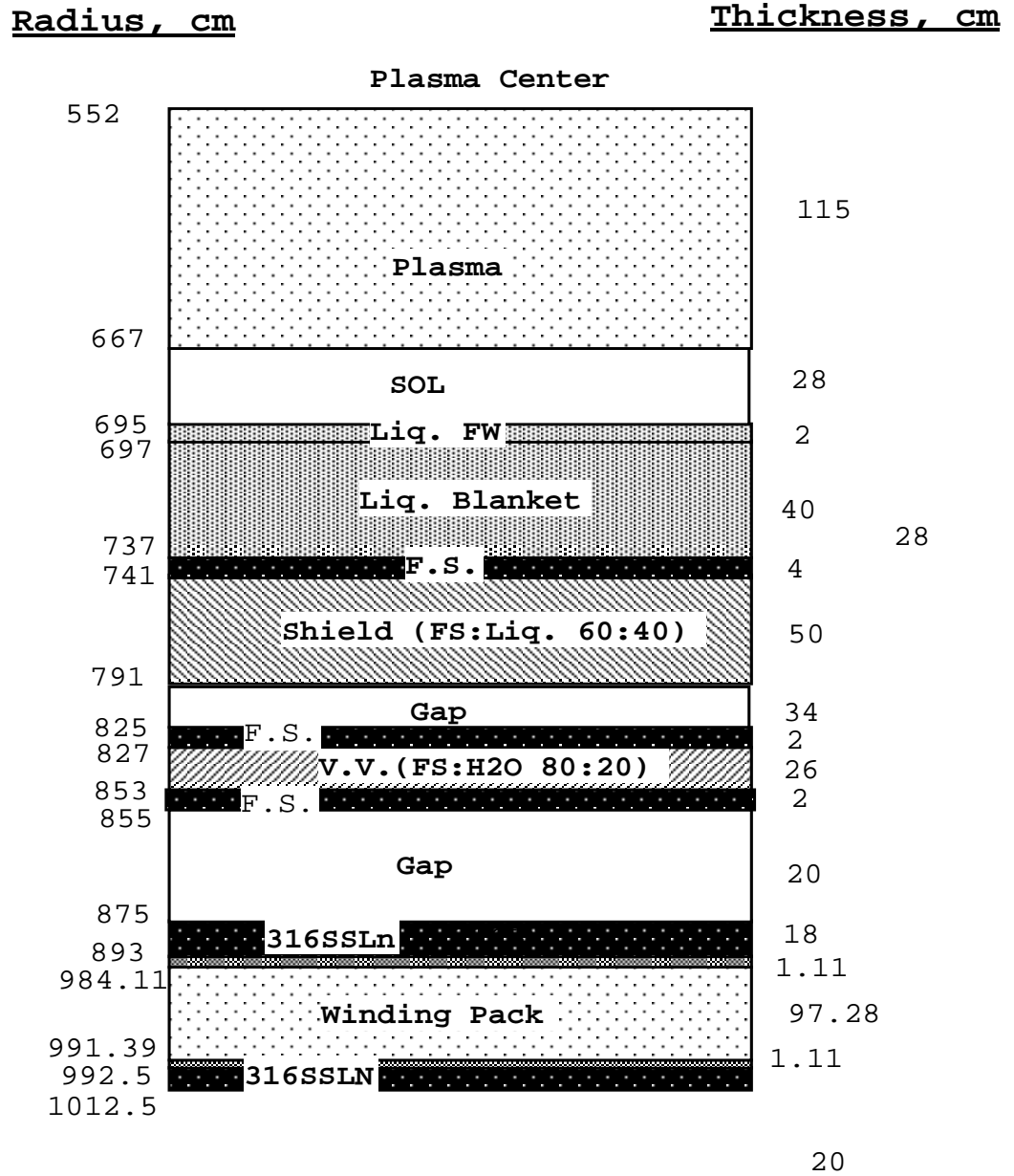


Figure 5.3-44 Radial Build of the I/B Thick Liquid (pocket) Concept (Outboard)

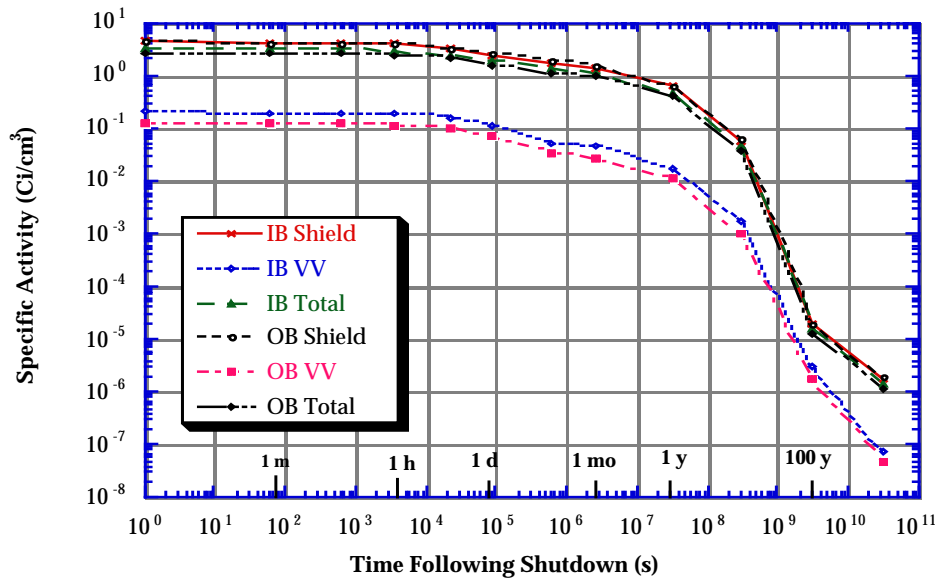


Figure 5.3-45 Activity Induced in the Different Components of Thick Liquid Metal Blanket Concept as a Function of Time Following Shutdown.

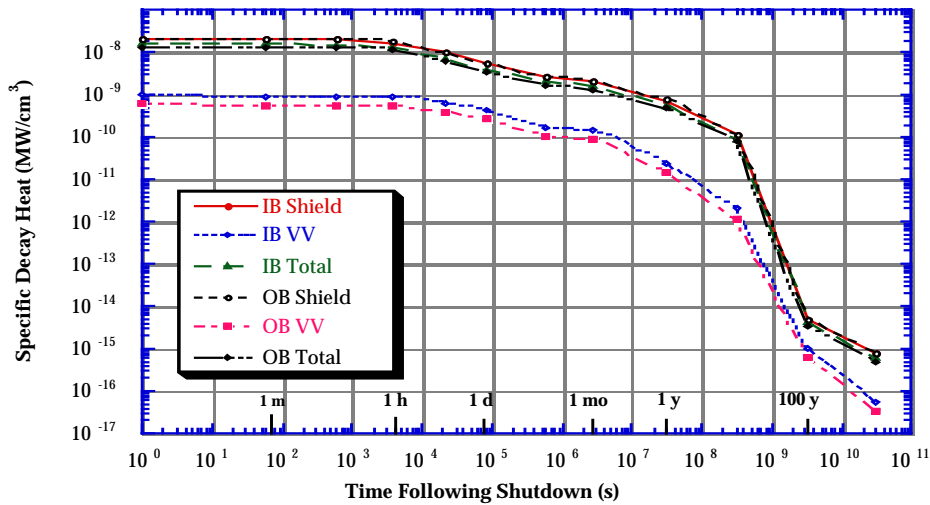


Figure 5.3-46 Decay Heat Induced in the Different Components of Thick Liquid Metal Blanket Concept as a Function of Time Following Shutdown.

5.3.3.3. Waste Disposal Ratings

The radwaste of the different components of the design were evaluated according to both the NRC 10CFR61 [15] and Fetter [16] waste disposal concentration limits (WDL). The 10CFR61 regulations assume that the waste disposal site will be under administrative control for 100 years. The dose at the site to an inadvertent intruder after the 100 years is limited to less than 500 mrem/year. The waste disposal rating (WDR) is defined as the sum of the ratio of the concentration of a particular isotope to the maximum allowed concentration of that isotope taken over all isotopes and for a particular class. If the calculated $WDR \leq 1$ when Class A limits are used, the radwaste should qualify for Class A segregated waste. The major hazard of this class of waste is to individuals who are responsible for handling it. Such waste is not considered to be a hazard following the loss of institutional control of the disposal site. If the WDR is > 1 when Class A WDL are used but ≤ 1 when Class C limits are used, the waste is termed Class C intruder waste. It must be packaged and buried such that it will not pose a hazard to an inadvertent intruder after the 100 years institutional period is over. Class C waste is assumed to be stable for 500 years. Using Class C limits, a $WDR > 1$ implies that the radwaste does not qualify for shallow land burial.

Fetter developed a modified version of the NRC's intruder model to calculate waste disposal limits for a wider range of long-lived radionuclides which are of interest for fusion researchers than the few that currently exist in the current 10CFR61 regulations. Fetter's model included more accurate transfer coefficients and dose conversion factors. However, while the NRC model limits the whole body dose to 500 mrem or the dose to any single organ (one of seven body organs) to 1.5 rem, Fetter limits are based on the maximum dose to the whole body only.

Specific activities calculated by the DKR-PULSAR2.0 code were used to calculate the waste disposal ratings (WDR). The waste disposal ratings for the Fetter and 10CFR61 limits are shown in Tables 5.3-8 and 5.3-9, respectively. Results in the tables are given for compacted wastes. Compacted waste corresponds to crushing the solid waste before disposal (to eliminate voids in the structure) and thus disallowing artificial dilution of activity. The Class C WDR were calculated after a one-year cooling period. The dominant nuclides are given between brackets. As shown in Table 5.3-8, according to Fetter limits, all components would qualify for disposal as Class C waste. The two isotopes, ^{192m}Ir ($T_{1/2} = 240$ yr), and ^{94}Nb ($T_{1/2} = 20,000$ yr) are the dominant source of WDR for all components. ^{192m}Ir and ^{94}Nb are produced by nuclear interactions with the iridium, niobium and molybdenum impurities present in the ORNL LAFS alloy. Finally, as shown in Table 5.3-9, according to the 10CFR61 limits, all components also would qualify for disposal as Class C waste. The waste disposal ratings of all components are dominated by contribution from the ^{94}Nb isotope.

Table 5.3-8 Class C Waste Disposal Ratings Using Fetter Limits.

Zone	FPY	WDR	Dominant Nuclides
<i>Inboard Shield</i>	30	0.81	^{192m} Ir, ⁹⁴ Nb
<i>Inboard VV</i>	30	0.141	^{192m} Ir
<i>Outboard Shield</i>	30	0.795	^{192m} Ir, ⁹⁴ Nb
<i>Outboard VV</i>	30	0.087	^{192m} Ir

Table 5.3-9 Class C Waste Disposal Ratings Using 10CFR61 Limits.

Zone	FPY	WDR	Dominant Nuclides
<i>Inboard Shield</i>	30	0.25	⁹⁴ Nb
<i>Inboard VV</i>	30	4.22×10^{-3}	⁹⁴ Nb
<i>Outboard Shield</i>	30	0.25	⁹⁴ Nb
<i>Outboard VV</i>	30	2.54×10^{-3}	⁹⁴ Nb

5.3.3.4 Comparison between liquid and conventional blankets

Using liquid blankets could possibly have many potential advantages over conventional blankets. In this section a parametric analysis was performed to examine such potential advantages from activation and safety point of view. Using the same radial build, the liquid blanket was replaced by a conventional first wall and blanket. The conventional first wall is 2-cm thick and made of the ORNL LAFS 9Cr-2WVTa alloy. The conventional blanket is 40-cm thick and made of 10% ORNL LAFS 9Cr-2WVTa and 90% Flibe. While the conventional blanket will need to be replaced every 3 FPY, the shield and vacuum vessel will continue to stay in place for 30 FPY. Figure 5.3-47 shows a comparison of the peak specific activities induced in the structure of a power plant while using liquid or conventional blankets. The peak activities are induced in the front

layer of the shield of the thick liquid metal blanket concept and in the first wall of the conventional blanket concept.

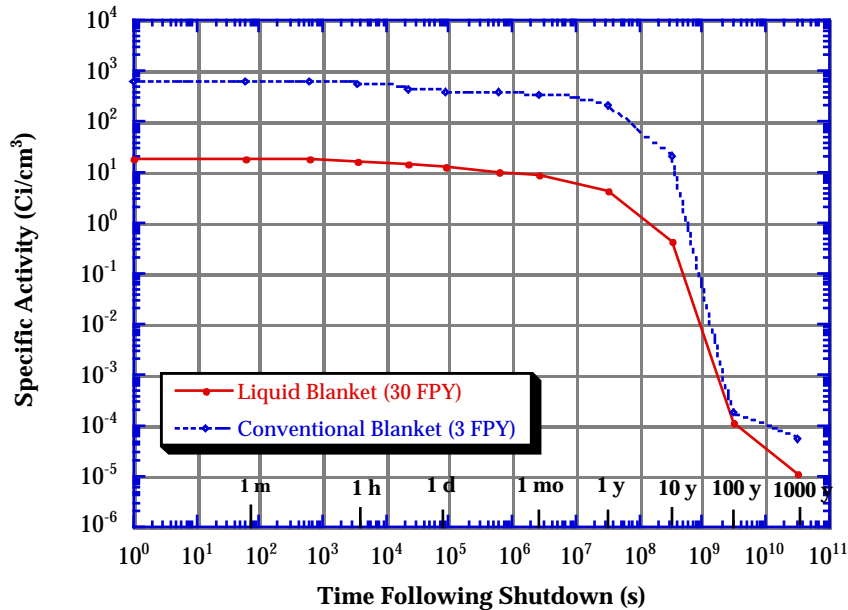


Figure 5.3-47 Comparison of Peak Induced Activities in Thick Liquid Metal Blanket and Conventional Blanket Concepts.

As shown in the figure, at shutdown, the thick liquid metal blanket concept induced about two orders of magnitude less peak activities than a conventional blanket concept. The two order of magnitude difference in induced activities continue during the first year and starts to narrow down after the first year following shutdown. The next step is to find out how this may translate into advantages from both waste generation (dominated by long-lived nuclides) and safety hazard (dominated by short-lived and intermediate-lived nuclides) point of views. An analysis comparing the waste disposal ratings and volume of wastes generated in power plant based on the two concepts was conducted. The waste disposal ratings for the Fetter and 10CFR61 limits are shown in Tables 5.3-10 and 5.3-11, respectively. Results in the tables are given for compacted wastes after one year following shutdown. As shown in Table 5.3-10, according to Fetter limits, all components of the liquid blanket concept would qualify for disposal as Class C waste after 30 FPY. All components of the conventional blanket concept, except for the first wall and blanket, also would qualify for disposal as Class C waste after 30 FPY. The first wall and blanket would not qualify for disposal as Class C LLW unless they were replaced every 2 FPY instead of every 3 FPY. On the other hand, the 10% steel structure in the conventional blanket provided the shield and vacuum vessel behind it with better shielding resulting in lower waste disposal ratings in comparison to the waste disposal ratings of the shield and vacuum vessel behind the liquid blanket. Results in Table 5.3-9 show that according to the 10CFR61 limits, all components of both blanket concepts would qualify for disposal as Class C waste. The absence of contribution from ^{192m}Ir to the waste disposal ratings according to the 10CFR61 limits (10CFR61 has no limits for

^{192m}Ir) resulted in allowing for the disposal of the first wall and blanket of the conventional blanket concept as LLW after 3 FPY.

Table 5.3-10 Comparison of Class C Waste Disposal Ratings Using Fetter Limits.

Zone	FPY	Liquid Blanket Concept	Conventional Blanket Concept
<i>Inboard FW & Blanket</i>	3	---	1.37
<i>Inboard Shield</i>	30	0.81	0.73
<i>Inboard VV</i>	30	0.141	0.1
<i>Outboard FW & Blanket</i>	3	---	1.34
<i>Outboard Shield</i>	30	0.795	0.71
<i>Outboard VV</i>	30	0.087	0.06

Table 5.3-11 Comparison of Class C Waste Disposal Ratings Using 10CFR61 Limits.

Zone	FPY	Liquid Blanket Concept	Conventional Blanket Concept
<i>Inboard FW & Blanket</i>	3	---	0.495
<i>Inboard Shield</i>	30	0.25	0.21
<i>Inboard VV</i>	30	4.22×10^{-3}	2.82×10^{-3}
<i>Outboard FW & Blanket</i>	3	---	0.473
<i>Outboard Shield</i>	30	0.25	0.21
<i>Outboard VV</i>	30	2.54×10^{-3}	1.69×10^{-3}

A power plant based on the conventional blanket concept will produce the equivalent of about ten blankets of additional waste during its life-time. However, power plant based on either the liquid or conventional blanket concepts will generate the same amount of waste from the shield, vacuum vessel, and magnets. As shown in Figure 5.3-48, the volume of the waste generated during the life-time of a power plant (30 FPY) based on the liquid blanket concept could be a factor of six lower than the volume of waste generated during the same life-time if the plant was based on the conventional blanket concept. The factor of six is based on the assumption that the waste is non compacted and the waste does not include the magnets. If the waste is compacted to 100% of its theoretical density, the reduction factor drops from six to two. If the waste is compacted and the magnet waste is included, a power plant based on the conventional blanket

concept will generate about 35% more waste during its life-time (30FPY) than a similar power plant based on the liquid blanket concept.

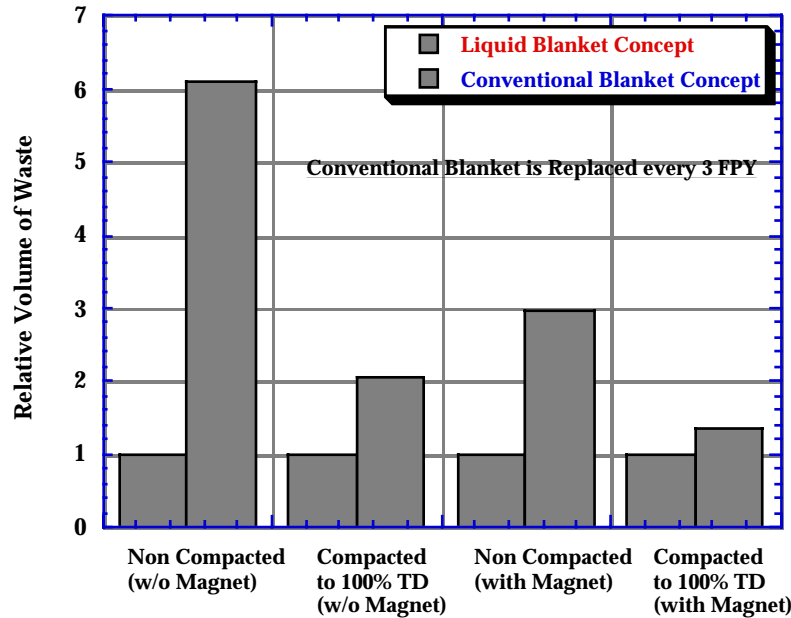


Figure 5.3-48 Comparison of Total Volume of Waste Generated in Power Plants Based on Thick Liquid Metal Blanket and Conventional Blanket Concepts.

Finally, a power plant based on a liquid blanket concept is expected to have an advantage over a similar plant utilizing a conventional blanket from the point of view of safety hazard. To quantify such an advantage, the specific activities induced in all components of power plants based on the two blanket concepts were used to calculate the early dose inventories of the two plants. The early dose inventory represents the hypothetical early dose produced at the site boundary due a total release (100% release) of the radioactive inventory. The off-site dose inventories were calculated under worst release conditions. These conditions are ground release, atmospheric stability class F, 1 km site boundary and 1 m/s wind speed. Even though it is impossible to release 100% of the radioactive inventory present in any power plant during an accident, using such a comparison is appropriate for such a scoping study where the final design is not fine tuned and, at this stage of the analysis, no detailed safety analysis was conducted. As shown in Table 5.3-12, a power plant based on the conventional blanket concept would produce a total early dose inventory which is about factor of eight higher than the early dose inventory produced by a similar plant utilizing the liquid blanket concept.

Table 5.3-12 Comparison of Early Dose Inventory (Sv/cm height at midplane).

Zone	Liquid Blanket Concept	Conventional Blanket Concept
<i>Inboard FW & Blanket</i>	---	<i>16.24</i>
<i>Inboard Shield</i>	<i>2.245</i>	<i>4.57</i>
<i>Inboard VV</i>	<i>0.063</i>	<i>0.043</i>
<i>Outboard FW & Blanket</i>	---	<i>32.2</i>
<i>Outboard Shield</i>	<i>5.22</i>	<i>10.18</i>
<i>Outboard VV</i>	<i>0.16</i>	<i>0.11</i>
Total	7.69	63.35

5.3 References

1. I. Kaplan, "Nuclear Physics," Addison-Wesley Pub. Comp. Inc., Reading Massachusetts, Palo Alto, London, (1964).
2. D. E. Cullen, et al., "Tables and Graphs of Photon Interaction Cross Sections from 10 eV to 100 GeV Derived from LLNL Evaluated Photon data Library (EPDL), Part A: Z = 1 to 50 and Part B: Z = 51 to 100," UCRL-5000400, Lawrence Livermore National Laboratory, CA., 1989.
3. J. A. Bearden and A. F. Burr, "Reevaluation of X-Rays Atomic Energy Levels," Rev. Mod. Phys. **39**, 125 (1967).
4. M. Cardona and L. Ley, Eds., "Introduction (to Photo emission in Solids I) - General Principles," (Springer-Verlag, Berlin, 1978).
5. J. C. Fuggle and N. Martensson, "Core-Level Binding Energies in Metals," J. Electron Spectrosc. Relat. Phenom. , **21**, 275 (1980).
6. S. Kraft, J. Stumpel, P. Becker, and U. Kuetgens, "High Resolution X-rays Absorption Spectroscopy with Absolute Energy Calibration for Determination of Absorption Edge Energies," Rev. Sci. Instrum. **67**, 681 (1996).
7. J. R. De Laeter, K. G. Heumann, "Atomic Weights of the Elements 1989 (Reprinted from the Pure and Applied Chem., Vol. **63**, (1991) 975)," J. Phys. Chem. Ref. Data **20**, 1313 (1991).
8. J. Wesson, "Tokamaks," Clarendon Press Oxford, (1987).
9. "Technical Basis for ITER Detail Design Report, Cost Review, and Safety Analysis." ITER Document, International Thermonuclear Experimental Reactor, (November, 1996).
10. A.B. Pashchenko, "Completion of FENDL-1 and Start of FENDL-2," INDC(NDS)-352, IAEA Nuclear Data Section, International Atomic Energy Agency, (March, 1996).
11. F. Najmabadi, et al., "Overview of the ARIES-RS Reversed-Shear Tokamak Power Plant Study", Fusion Engr. & Design, 38 (1997) 3-35.
12. R. O'Dell et al., "User's Manual for ONEDAT: A code Package for One-Dimensional, Diffusion-Accelerated, Neutral particle Transport," Los Alamos National Laboratory report, LA-9184-M (1982)
13. J. Sisolak, Q. Wang, H. Khater and D. Henderson, "DKR-PULSAR2.0: A Radioactivity Calculation Code that Includes Pulsed/Intermittent Operation," to be published.
14. A. Pashchenko et al., "FENDL/2.0: Neutron Activation Cross-Section DATA Library for Fusion Applications," Report INDC (NDS)-173, IAEA Nuclear Data Section, March 1997.
15. Nuclear Regulatory Commission, 10CFR part 61, "Licensing Requirements for Land Disposal of Radioactive Waste," Federal Register, FR 47, 57446 (1982).
16. S. Fetter, E. Cheng and F. Mann, "Long Term Radioactive Waste from Fusion Reactors," Fusion Engineering and Design, 13, 239-246 (1990).

5.4 Hydrodynamics Analysis

In this section, hydrodynamics configurations are addressed and analyzed for advanced tokamak, ST and FRC confinement schemes. It is believed that an understanding of the basic hydrodynamics performance of the free surface liquid flows is imperative for the ultimate development of a practical design. The adaptation of liquid flows to the topological constraints of toroidal plasma devices, including penetrations, represents a hydrodynamics challenge.

The hydrodynamics analyses are performed and addressed for three lithium-containing liquids: Flibe – a good neutron absorber and poor electrical conductor, lithium – a low Z material with high thermal and electrical conductivity, and tin-lithium – an extremely low vapor pressure liquid. Both lithium and tin-lithium are good electric conductors. Utilization of these two materials will have to deal with MHD effects, not just in the surface flows, but in supply lines and feed systems, and requires electrical insulating coatings.

5.4.1 Hydrodynamics of APEX Liquid Wall

5.4.1.1 Influence of magnetic field on hydrodynamics and heat transfer for free surface flows

The influence of the magnetic field on liquid wall flow characteristics, pressure drop and heat transfer is crucial for thick liquid wall concepts. As two sorts of liquids are the candidates for the working fluid, the molten salt (Flibe) and the liquid metals (Li, Sn-Li), two separate treatments are needed. These two approaches should take into account differences in physical properties, mostly in the electrical and thermal conductivity and, as a consequence, different mechanisms of MHD interaction. Four independent parameters or their combinations specify the problem of MHD interaction for conducting fluids. They are the Reynolds number Re , Hartmann number Ha , the flow aspect ratio β number, and the orientation of the applied magnetic field relative to the flow field. Typically, the order of magnitude of the Hartmann number built through the flow half-width, w , (in the toroidal field direction) in the liquid wall concepts is 10^5 for liquid metals, while it is 10^2 for Flibe. This large difference between these two cases does not mean that the MHD effects are negligible for Flibe, but they differ strongly both qualitatively and quantitatively.

As for liquid metals, complete suppression of three-dimensional turbulence is expected. In accordance with numerous experimental observations for MHD duct flows [1]: if the ratio Ha/Re exceeds a certain critical value, the measured law for the friction coefficient is in good agreement with the laminar theoretical predictions. This fact is the reason why many authors speak of laminarization of the flow by the magnetic field. Nevertheless, as more detailed measurement results show, a two-dimensional large-scale turbulence often persists even when the parameter Ha/Re is greater than its critical value [1].

The phenomena of turbulence transformation in the presence of the magnetic field give grounds to define high Hartmann, high Reynolds number flows in terms of laminar flows. Along with the effect of turbulence suppression, there are different MHD effects due to interaction of the applied magnetic field with the induced electrical currents, which manifest themselves in different ways both in laminar and turbulent MHD flows. Most typical MHD effects of this type can be clearly observed in high Hartmann number laminar MHD flows. They are the Hartmann effect, the M-type velocity profile formation, the significant increase in the MHD drag force, *etc.* In what follows, we will refer to these effects as those caused by the interaction between the magnetic field and the mean flow. These effects are described in details in a special literature on MHD flows [1].

As for Flibe flows, significant manifestation of such effects can be expected for the thick wall flows, especially if the side-walls or the backplate are conducting, since the Hartmann number and the parameter β are relatively large, and hence MHD interaction is stronger. At the same time, the effects of MHD on turbulent flow characteristics and heat transfer for slightly conducting liquids, such as Flibe, can be significant as demonstrated by experimental observations for aqueous electrolytes [2].

5.4.1.2 Mathematical model for Liquid Metal MHD Flow

Mathematically free surface liquid flows over a concave surface can be described by a set of Navier-Stokes equations for incompressible fluids and Maxwell equations for electromagnetic phenomena. Although a lot of attempts have been made recently to work out numerical codes that allow MHD flow calculations for the nuclear fusion applications [3]-[14], only few of them were relatively successful. These were mostly for the laminar MHD flows in pipes and closed ducts of rectangular cross-section [9]-[14]. Unfortunately, the most important cases, including turbulent free surface flows of conducting fluids, cannot be properly computed on the basis of a complete three-dimensional set of the Navier-Stokes-Maxwell equations. These computations are now limited by the computer technology capabilities and by the existing numerical analysis methods. It is unlikely that, in the near future, these computations could be performed over the parameter range of practical interest. At the same time, the numerical solutions based on the two-dimensional magnetohydrodynamic equations can be performed in practice for any values of governing parameters for ducts of various geometries. It is from this context that the development of two-dimensional models, which are sufficiently adequate for describing MHD free surface flows of incompressible, electrically conducting media, is of primary importance.

The dimensionless parameters governing the problem are the Reynolds number ($Re=U_0h_0/\nu$), the Froude number ($Fr=U_0^2/gh_0$), the Hartmann number ($Ha=B_0w\sqrt{\sigma/\nu\rho}$), the magnetic Reynolds number ($Re_m=U_0h_0\mu_0\sigma$), the Weber number ($We=\rho h_0U_0^2/\sigma_s$), and two geometrical parameters ($\beta=h_0/w$ and $\chi=h_0/R$). Here, U_0 and h_0 are the initial velocity and the initial layer thickness respectively; R is the radius of curvature of the concave

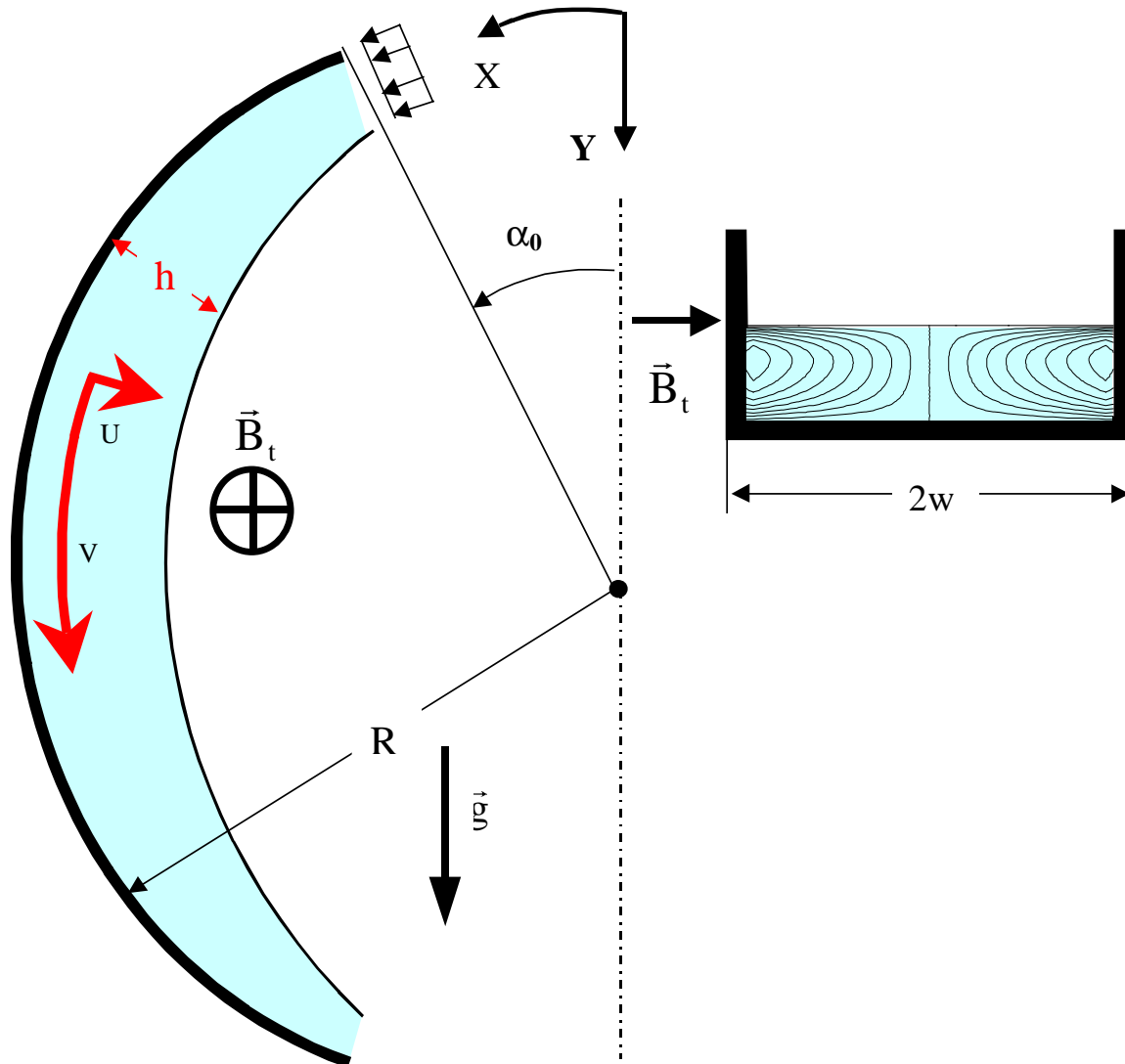


Figure 5.4-1 Illustration of the problem: flow sketch in the XY-plane (left) while a typical distribution of induced currents over the cross-sectional area shown on (right)

(cylindrical) wall, while w is half of the distance between the two side walls segmenting the flow domain in the toroidal direction. Typically R is 4 m and w is 0.5-1 m. Based on the characteristic values of the dimensionless parameters, the flows under consideration

can be qualified as high Reynolds number ($Re \sim 10^4 - 10^5$), low magnetic Reynolds number flows, with $\beta < 1$ and $\chi \ll 1$. Hence some simplifications can be adopted.

First, the boundary layer or shallow water approximation is used. Usually this approximation is valid for high Reynolds number flows if two geometrical scales, the longitudinal (L , the length of the flow domain), and the cross (δ , the thickness of the boundary layer), differ from one another significantly, $L \gg \delta$. It allows describing the flow using parabolic flow equations (Prandtl equations), which from the mathematical or computational viewpoint are much simpler than the original Navier-Stokes ones. Physically, the possibility of using Prandtl equations instead of Navier-Stokes ones comes from the fact that there is no any reverse flow over the whole flow domain.

Second, the thin layer approximation is assumed, which is based on the assumption that $R \gg h_0$. For both thin and thick liquid walls, this condition is met and some terms, which reflect the influence of the curvature on the flow in the momentum equation, can be neglected. The only exception is the V^2/R term, which stands for the centrifugal force and it cannot be omitted since the layer adhesion depends completely on the balance between the centrifugal and gravitational forces.

Third, the inductionless approximation was also used, $Re_m < 1$. For MHD flows with a low magnetic Reynolds number, the induced magnetic field is negligible in comparison with the applied magnetic field. From the mathematical point of view, it means that the term B (induced magnetic field) in the governing equations can be omitted in cases where it appears together with the applied magnetic field, B_0 .

We also assume that the applied magnetic field is transverse and the physical properties of liquid, such as ρ (density), ν (viscosity), σ (electrical conductivity), σ_s (surface tension) are all constant over the integration time and the flow domain. Using the approximations listed and applying the averaging approach [15] to the originally three-dimensional set of the Navier-Stokes-Maxwell equations written in the boundary fitted coordinates (see Fig.5.4-1), one can derive the following set of quasi two-dimensional equations governing the problem:

Continuity equation:

$$\frac{\partial U}{\partial x} + \frac{\partial V}{\partial y} = 0; \quad (5.4-1)$$

Momentum equation:

$$\begin{aligned}
 \frac{\partial U}{\partial t} + U \frac{\partial U}{\partial x} + V \frac{\partial U}{\partial y} = \frac{1}{Fr} [\cos(\alpha + \alpha_0) \frac{\partial h}{\partial x} + \sin(\alpha + \alpha_0)] - \chi \frac{\partial}{\partial x} \left(\int_y U^2 dy \right) + \\
 + \frac{1}{Re} \frac{\partial}{\partial y} [(1 + v_t) \frac{\partial U}{\partial y}] + \frac{1}{We} \frac{\partial^3 h}{\partial x^3} + 0.5\beta^2 \int_y (j_z|_{z=1} - j_z|_{z=-1}) dy + \\
 + \frac{0.5\beta^2}{Re} \left(\frac{\partial f}{\partial z} \Big|_{z=1} - \frac{\partial f}{\partial z} \Big|_{z=-1} \right). \tag{5.4-2}
 \end{aligned}$$

Here, U and V are the components of the velocity vector; t is the time; x and y are the boundary fitted coordinates; h is the layer thickness; α is the angle (see Fig.5.4-1); v_t is the turbulent (eddy) viscosity; j_z is the Z-component of the electrical current density vector; f is the function taking into account velocity distribution in the Z-direction. In equations (5.4-1) and (5.4-2), all quantities are written in the dimensionless form using the following scales: $[U]=[V]=U_0$; $[t]=h_0/U_0$; $[x]=[y]=[h]=h_0$; $[v_t]=\nu$; $[j_z]=\rho U_0^2/(B_0 w)$. The averaging approach used to get a two-dimensional form of the governing equations is presented in detail in Ref. [15]. Its application to the shallow water equations for film flows is also described in Ref. [16]. This approach implies that the originally three-dimensional set of the Navier-Stokes-Maxwell equations is integrated analytically in the direction of the applied magnetic field. The integration results in the appearance of two new terms on the right hand side of the momentum equation (two last terms in equation (5.4-2)) standing for the drag Lorentz force and the viscous friction in the Hartman layers at the side-walls, respectively. To close the system of equations (5.4-1), (5.4-2) some additional assumptions on j_z and f are necessary. These assumptions are discussed below. The system is also not complete until an expression or a procedure for calculating v_t is described. This procedure is known as the closure problem and it is also discussed below.

In order to calculate the layer thickness and velocity profiles over the flow domain, the equations (5.4-1) and (5.4-2), together with additional expressions or equations for f, j_z and v_t , should be solved analytically or numerically along with boundary and initial conditions. As for boundary conditions, the no-slip condition at the solid wall and the zero tangential stress condition at the free surface are used on U. A special type boundary condition at the free surface is also used to calculate the layer thickness. It is so-called kinematic free surface condition, which is as follows

$$\frac{\partial h}{\partial t} + U_s \frac{\partial h}{\partial x} = V_s. \tag{5.4-3}$$

Here U_s and V_s are the components of the velocity vector at the free surface.

Numerical Code

A numerical code for solving equations (5.4-1)-(5.4-3) has been carried out on the base of a marching type finite-difference algorithm. The details of the code are presented in Ref. [9]. The specific approaches developed are listed below.

- To reduce a curvilinear flow domain to a rectangular one, a special change of variables was made as follows $(t,x,y) \rightarrow (\tau=t, \xi=x, \eta=y/h)$. Although the equations become more complicated, this approach enables us to avoid approximation errors at the free surface.
- The velocity components U and V at every time step were calculated from the momentum equation (5.4-2) and the continuity equation (5.4-1) respectively. The kinematic free surface condition (5.4-3) was used to calculate free surface changes both in space and time.
- The momentum equation and the continuity equation were approximated implicitly. The kinematic free surface condition was approximated implicitly in calculations of steady-state developing flows, while explicit upwind type approximation was used in calculations of surface instability.
- While calculating the surface instability case, a special procedure of grid reconstruction was applied at every time step to minimize the negative effect of artificial viscosity on the instability growth to a minimum.
- A tri-diagonal solver was used to find a solution of finite-difference equations.

5.4.1.3 Application of the Numerical Code to the Thick Liquid Wall Concept (Lithium)

The mathematical model and the computer code developed is used to estimate liquid thickness evolution for different initial injection conditions, the pressure distribution over the structural wall and the velocity profiles. Ideally, a condition that provides a uniform liquid thickness throughout the reactor is desired. A significant increase in the layer thickness is not accessible, since it is accompanied with the velocity decrease and hence as increase in surface temperature. On the other hand, the pressure at the structural wall, P_w , must not be negative. Negative values of P_w mean that there is flow separation, which is also unacceptable. In addition, there is a risk of the excessive pressure from the liquid to the structural wall in the case of the thick wall. This is not present in the case of thin liquid walls. Therefore, it is desired to keep the wall pressure within reasonable limits. Numerical computations were carried out to check the possibility of establishing a thick liquid wall flow configuration based on the following design parameters as listed in Table 5.4-1.

The results of the computations for the layer thickness scaled by the initial layer thickness and for the wall pressure scaled by ρU_0^2 versus the dimensionless coordinate x (the scale is the initial thickness of the layer) in the flow direction are shown in Figs. 5.4-2, 5.4-3.

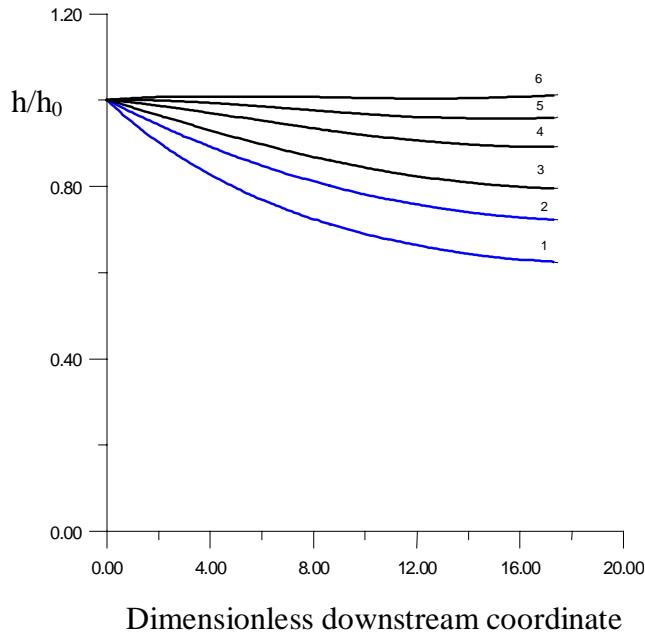


Figure 5.4-2 Dimensionless film thickens versus dimensionless coordinate x for thick lithium FW/blanket concept. Curves 1-6 correspond to $U_0=5-10$ m/s, respectively

Table 5.4-1 Dimensional and dimensionless flow parameters (Lithium, thick wall)

U_0	h_0	w	R	α_0	$\Delta\alpha$	Re	Fr	Ha	β	χ
m/s	m	m	m	degree	degree					
5	0.4	0.57	6.7	30	60	$2.35 \cdot 10^6$	6.25	$3.76 \cdot 10^5$	0.7	0.06
10						$4.71 \cdot 10^6$	25			

The results show that an almost uniform thick layer flow can be established within the flow domain for the initial velocities in the range of 8 to 10 m/s. At the same time, the conditions for the flow adhesion to the structural wall are provided if the initial velocity is more than 6 m/s. Maximum wall pressure at the end of the flow domain was also found from the plot, and it is no more than 4800 N/m^2 .

Another application of the code to the thick liquid wall concept is related to the idea of a "submerged wall". In accordance with this idea, walls submerged into the flowing liquid are used in order to produce additional drag MHD force in the flow regions adjacent to the structural wall. As a result of this extra drag effect, the flow velocity at the structural wall decreases. And, at the same time due to the mass

conservation, it increases at the free surface where the MHD drag force is absent and the gravitational, inertial and viscous forces drive the flow. In doing so, the two-layer flow is realized. The fast external layer removes the heat flux, while the slow internal layer serving as a blanket, is used for the tritium production.

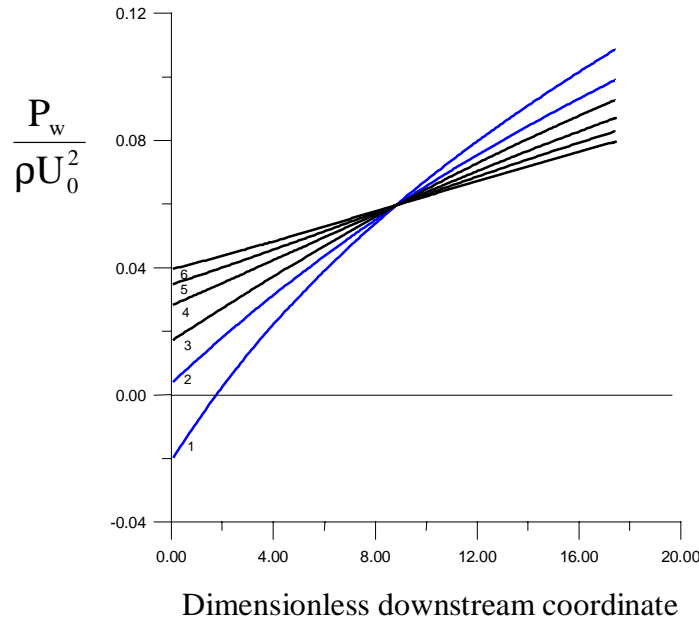


Figure 5.4-3 Dimensionless pressure exerted on the back wall versus dimensionless coordinate x for thick lithium FW/blanket concept. Curves 1-6 correspond to $U_0=5-10$ m/s.

This idea is illustrated in Figs. 5.4-4 and 5.4-5. The submerged wall is electrically isolated ($c_w=0$) and has the thickness of half of the initial layer depth ($h_w=0.5$). The layer is about uniform over the whole flow length (Fig. 5.4-4), while the velocity profiles (plotted in different cross-sections) are extremely non-uniform (Fig. 5.4-5). In the lower part, the flow resembles usual MHD free surface flow along the concave structural wall in the presence of two electrically isolated side-walls. The gradient boundary layer at the structural wall and the slug-type core can be seen. In the upper part, the flow looks like developing ordinary free surface flow with an almost parabolic boundary layer at the edge of the submerged wall. In both lower and upper parts, the flow develops over the whole flow length as demonstrated by changes in the velocity profiles. Both layers, external and internal, have approximately the same thickness, but velocity in the upper layer is almost two times more. This flow pattern proves a principal possibility of establishing the two-layer flow by means of MHD effects caused by the submerged wall. In spite of the attractiveness of this idea, its effectiveness is open to question because further calculations, including heat transfer computations, are still needed. From the design viewpoint, the ideal two-layer flow should consist of an external layer that is much faster and much thinner than the internal layer. The difficulty in realizing this design is that the flow is not restricted by a solid boundary from the top, so the liquid can move up

if the drag force increases. Thus, the external layer is thickened, and the velocity in it decreases.

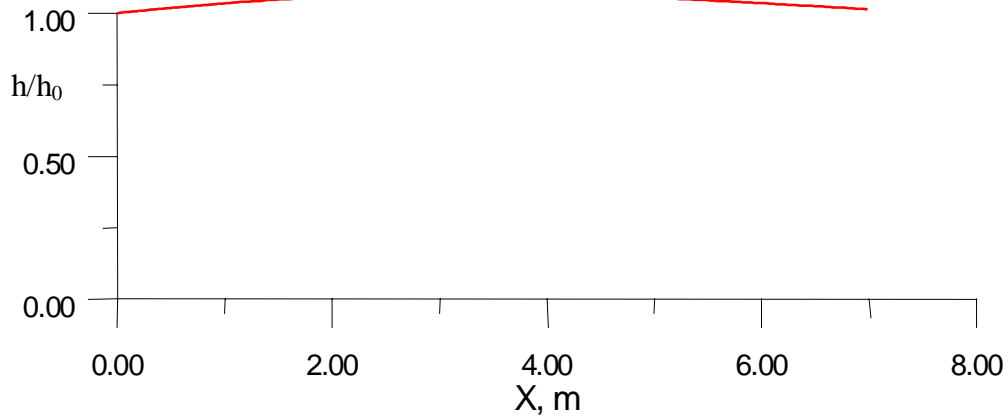


Figure 5.4-4 Changes in the layer thickness in the submerged channel two-layer flow. $U_0=10$ m/s, $h_w=0.5$, $c_w=0$. For other parameters see Table 5.4-1

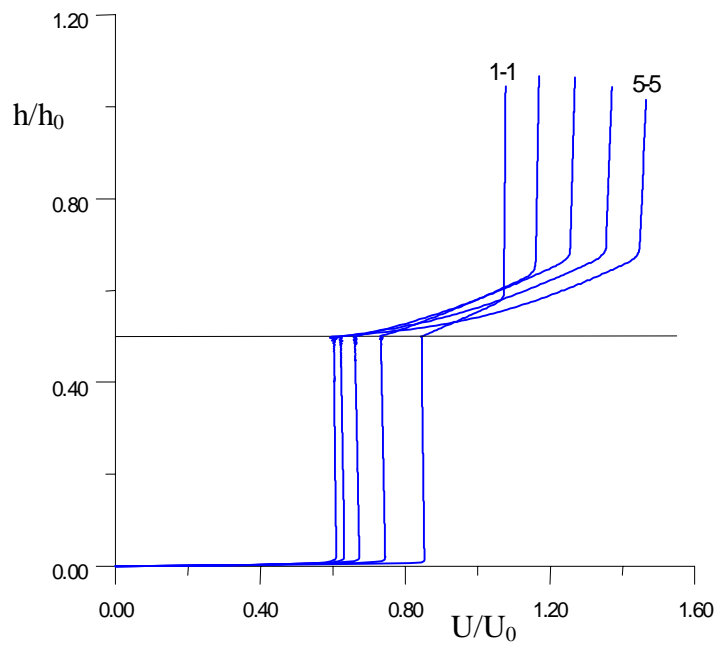


Figure 5.4-5 Velocity profiles in the submerged channel two-layer flow: $h_w=0.5$, $c_w=0$. $X_{1-1}=1.7$ m; $X_{2-2}=3.4$ m; $X_{3-3}=5.1$ m; $X_{4-4}=6.8$ m; $X_{5-5}=8.3$ m

In addition to the analysis made, another variant of the submerged wall was considered. In this variant, the height of the submerged wall is equal to the initial layer thickness, and the wall itself is electrically conducting ($c_w=2.0 \cdot 10^{-6}$). The results are shown in figs. 5.4-6 and 5.4-7.

Due to the greater electrical conductivity of the submerged wall, the MHD drag force is larger and the layer thickness increases by about 30%. The velocity profile in the internal layer is the same, while in the external layer only the parabolic boundary layer is seen. And, in the core the uniform velocity distribution is absent. This variant looks more attractive in comparison with the previous one as the external layer is thinner, about 40% of the internal layer thickness, and its velocity is 1.5-2 times larger than the internal layer velocity

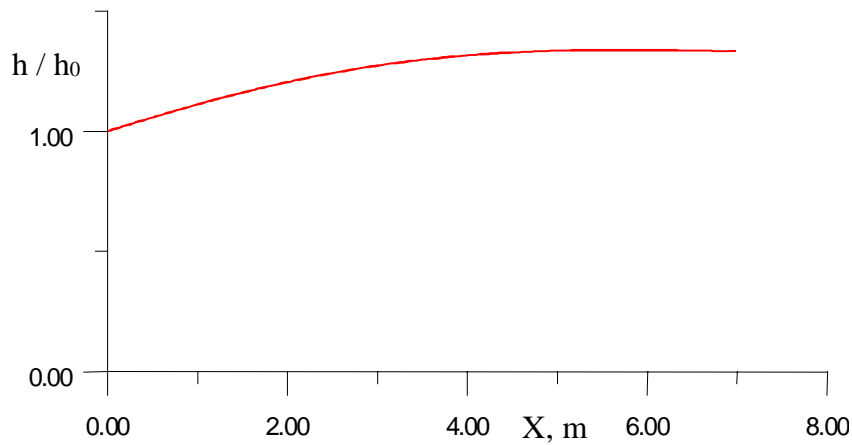


Figure 5.4-6 Changes in the layer thickness in the two-layer flow. $U_0=10$ m/s, $h_w=1.0$, $c_w=2.0 \times 10^{-6}$. For other parameters see Table 5.4-1.

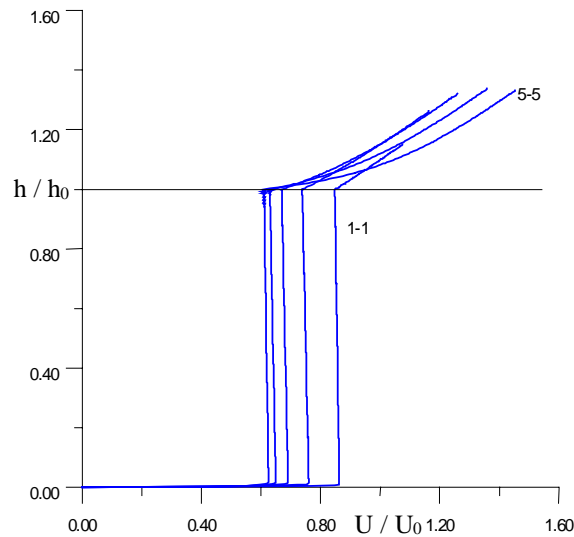


Figure 5.4-7 Velocity profiles in the two-layer flow in different cross-sections: $h_w=1.0$, $c_w=2.0 \cdot 10^{-6}$ $X_{1-1}=1.7$ m; $X_{2-2}=3.4$ m; $X_{3-3}=5.1$ m; $X_{4-4}=6.8$ m; $X_{5-5}=8.3$ m

5.4.1.3.1 Effect of the conducting walls on the liquid metal free surface flows

It is well known that the presence of electrically conducting walls can lead to larger electrical currents in the flow domain and, as a result, to a significant increase in the MHD drag effect. In the case of free surface MHD flows this effect manifests itself in the increase of the layer thickness with the accompanying reduction in the velocity. Detailed analysis of the influence of electrically conducting walls on the layer thickness increase are analyzed for CLiFF LM wall (see Chapter 7) using two-dimensional MHD model equations.

The influence of the conducting backplate on LM flow characteristics is negligible unless a radial field component exists. Estimations for the effect of the conducting backplate caused by the MHD interaction between the induced electrical current and the radial field component were carried out using a different Hartmann-type MHD model taking into account only one small, but not negligible, radial component of the magnetic field. Since the radial magnetic field does not interact with the electrical currents at the side-walls, a simplified flow geometry with no side-walls was assumed (Fig. 5.4-8).

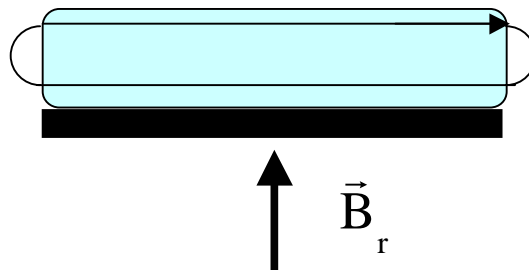


Figure 5.4-8 Cross-sectional area in the model with the radial field component.

In the flow sketch shown in Fig. 5.4-8, the induced electrical current flows parallel to the backplate as it takes place in the classical Hartmann problem. The MHD interaction manifests itself in the Lorentz force, which accelerates the flow within the thin Hartmann boundary layer at the backplate and brakes it in the core. The MHD equations and the boundary conditions based on this model are written in the shallow water approximation in terms of the velocity components U , V and the x -component of the induced magnetic field, B_x , as follows

$$\begin{aligned} \frac{\partial U}{\partial t} + U \frac{\partial U}{\partial x} + V \frac{\partial U}{\partial y} = \frac{1}{Fr} [\cos(\alpha + \alpha_0) \frac{\partial h}{\partial x} + \sin(\alpha + \alpha_0)] - \chi \frac{\partial}{\partial x} \left(\int U^2 dy \right) + \\ + \frac{1}{Re} \frac{\partial}{\partial y} [(1 + \nu_t) \frac{\partial U}{\partial y}] + \frac{1}{We} \frac{\partial^3 h}{\partial x^3} + \frac{Ha}{Re} \frac{\partial B_x}{\partial y}; \end{aligned} \tag{5.4-4}$$

$$\frac{\partial^2 B_x}{\partial y^2} + \text{Ha} \frac{\partial U}{\partial y} = 0; \quad (5.4-5)$$

$$\frac{\partial U}{\partial x} + \frac{\partial V}{\partial y} = 0; \quad \frac{\partial h}{\partial t} + U_s \frac{\partial h}{\partial x} = V_s \cdot \quad (5.4-6)$$

with the boundary conditions:

$$y=0: U=V=0, C_w \partial B_x / \partial y - B_x = 0; \quad (5.4.7)$$

$$y=h: \partial U / \partial y + \partial V / \partial x = 0, B_x = 0. \quad (5.4-8)$$

Equation (5.4-4)-(5.4-8) were solved numerically using a finite-difference algorithm similar to that described in the Chapter 7 for the flow parameters relevant to CliFF. The analyses conclude that the metal backplate is acceptable if the radial magnetic field is no more than 0.1-0.15 T. On the other hand, if the radial magnetic field is larger than 0.5 T, neither metal nor non-metallic electrically conducting compounds are acceptable, the isolation is necessary (see Chapter 7 for more conclusions).

5.4.1.4 Hydrodynamics Characteristics of Tokamak Flibe Thick Liquid Walls

One of the most fundamental issues for thick liquid blanket is how to form, establish, and maintain a thick liquid layer flow in a Tokamak reactor such as the ARIES-RS as shown in Figure 5.2-1. The simplest approach that can be conceived for a thick liquid blanket is free falling liquid layer under the effect of gravitational force. This hydrodynamic approach is analyzed using a fluid hydrodynamic computational code named FLOW-3D: a 3-D, time dependent, free-surface flow simulation code for incompressible flows that uses Volume of Fluid (VOF) free surface tracking algorithm. Conceptually, the thick liquid layer is injected at the top of reactor chamber with an angle tangential to the backing structural wall. Meanwhile the fluid adheres to the structural wall by means of centrifugal and inertial forces and is collected and drained at the bottom of the reactor. As shown in Figure 5.2-4, the 3-D hydrodynamic calculation indicates that a stable thick Flibe liquid layer can be established in an advanced Tokamak configuration. However, the law of mass conservation results in thinning of the liquid layer proceeds downstream due to the increase of fluid velocity as a result of gravitational acceleration. Thinning of the liquid layer is a serious issue because it may result in void gaps through which radiation may stream through and reach the structure behind the blanket region. Increasing the initial velocity to a point where the gravitational acceleration effect becomes small as compared to the initial momentum can reduce this thinning effect. Furthermore, the flow cross sectional area expands as the flow proceeds to the mid-plane of the reactor and contracts as it approaches to the bottom of the reactor. The increase in the circumferential parameter in the toroidal direction as one moves from top section to the mid-plane may also cause liquid layer flow thinning. For example, as shown in Figure 5.2-4, this combined effect of gravitational acceleration and area expansion results in ~ 30% reduction in the liquid thickness at the mid-plane of the

reactor for an initial velocity of 15 m/s. This high velocity raises concerns about the pumping power consumption, particularly if a neutronically thick liquid blanket is desired. Further hydrodynamics analyses are required in the areas of liquid layer inlet and exit systems. In particular, innovative solutions for converting the fluid from a free surface flow to a closed channel flow while recovering most of the dynamic head of the fluid have to be explored.

The other key question to be addressed in a thick liquid wall design is how to manage the fluid temperatures for thermal conversion and for plasma performance. The demand of a thick liquid blanket/first wall in a Tokamak configuration results in a large amount of resident liquid inventory due to high velocity requirement against the gravity thinning. The subsequent drawbacks include a negligible temperature increase and a consequent difficulty to de-couple the liquid surface temperature from the bulk temperature. A possible solution of operating the fluid at lower velocities while achieving a relatively uniform thick fluid throughout the reactor is discussed below, although further concept explorations along this line are needed.

5.4.1.5 GMD with Pocket Designs for Tokamak Devices

This concept as a modification to the gravity and momentum driven liquid layer attempts to use some structural materials to aid in establishing and maintaining the liquid layer thickness. The concept involves two main sections. The front section, facing the plasma, has a high velocity, thin liquid jet flowing in the poloidal direction. The second section has a series of fluid compartments along the poloidal and toroidal directions as shown in Figure 5.4-9. In addition, the fluid used in the primary jet is designed to be recirculated in the compartments until a desired outlet temperature is achieved (for higher thermal efficiency).

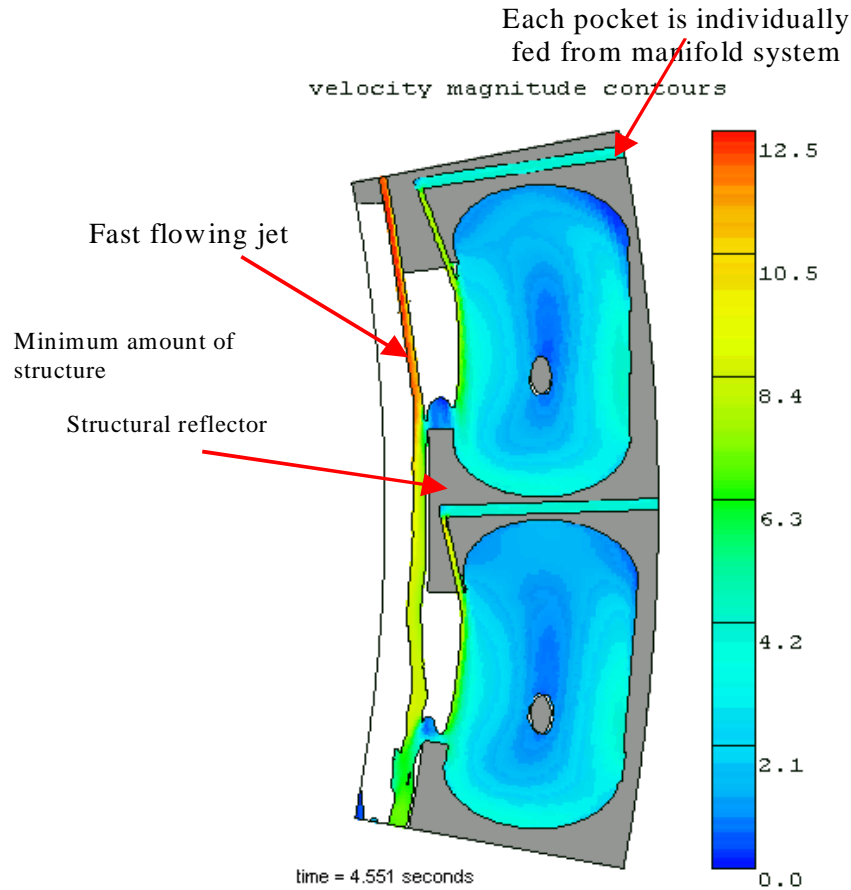


Figure 5.4-9 GMD with Pocket: A concept as a modification to the free fall, gravity and momentum driven liquid blanket that attempts to ensure that the first wall surface temperature can be maintained within the maximum allowable values while achieving a high exit temperature for a high power conversion efficiency.

The liquid used for the front section is injected into the vacuum chamber at a rate high enough (15 m/s) to actively convect away high surface heat flux (2 MW/m²). The pressure due to centrifugal force of high velocity of a 1 cm thick liquid layer flow over a 4 m radius concave surface (R_s : 3.99 m (radius of curvature of liquid-layer free surface) and R_b : 4. m (radius of curvature of back wall)) is estimated using potential flow velocity profile across the liquid layer depth.

$$P_c = \frac{1}{2} \rho V_s^2 \left(1 - \left(\frac{R_s}{R_b} \right)^2 \right) \quad (5.4-9)$$

is only equal to the static pressure of 5.5-cm fluid height. Therefore, in the secondary section, the compartment shape, and its inlet and operating conditions are designed in a way that a fluid circulation can be achieved to maintain the fluid thickness and height in

the compartment with minimum disruption to the primary jet. As seen in Figure 5.4-10, the liquid is injected into the compartment through a slot nozzle located at the front top section of the compartment with a 20° angle toward the back of it. The vertical component (V_z) of the injected liquid velocity into the compartment is designed to be adequate to promote circulation in the compartment by shear, while the horizontal component of the velocity (V_x) is designed to have an adequate dynamic pressure to sustain the fluid in the pocket towards the back wall.

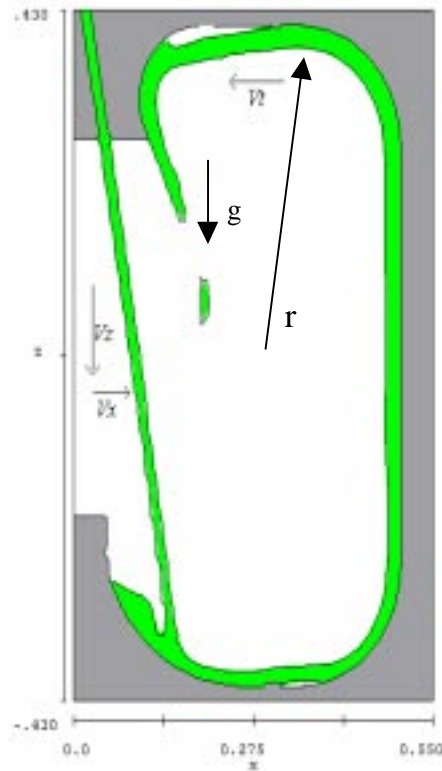


Figure 5.4-10 2-D Cross-section of a single compartment during filling. (Primary section-fast moving jet-is not shown).

For design considerations, an efficient circulation of the coolant (the longer the path the fluid travels inside the compartment, the higher its residence time) is desired to provide a maximum coolant temperature at the outlet of the compartment. Therefore, the geometric shape of the compartment and the circulation affecting the temperature profile are closely related to the thermal-efficiency of the reactor system. The contour of the compartment inner walls is thus shaped to prevent fluid separation, meanwhile minimizing the losses in the kinetic energy of the fluid as it changes its direction and rotates inside the compartment.

The minimum required inlet velocity for the compartment is determined by the condition that during the start-up, flow should have a tangential velocity component at the top section of the compartment (see Figure 5.4-10) so that it will not fall due to gravity. In determining the minimum required operating velocity, friction losses are neglected and the flow is assumed to have a constant velocity distribution throughout its thickness. The required condition for the flow not to fall from the top section of the compartment is

$$\bar{a}_c = \frac{V_t^2}{r} > \bar{g} \quad V_t^2 > \bar{g} \cdot r, \quad (5.4-10)$$

where a_c is the acceleration due to centrifugal force, \bar{g} is the gravitational acceleration and V_t is the tangential velocity of the liquid layer at the top section of the compartment. Balancing the kinetic and static energy of the flow at the bottom and top section of the compartment results in a relationship for the minimum required compartment inlet velocity.

$$\frac{1}{2}m \cdot V_{inlet}^2 = m \cdot g \cdot h + \frac{1}{2}m \cdot V_t^2 \rightarrow \frac{1}{2}m \cdot V_{inlet}^2 \geq m \cdot g \cdot h + \frac{1}{2}m \cdot g \cdot r \quad (5.4-11)$$

where V_{inlet} is the minimum required compartment inlet velocity, h is the compartment height and r is the average radius of curvature of the circular motion of liquid layer flow inside the compartment (Figure 5.4-10.) The minimum required compartment inlet velocity was determined to be ~ 4.5 m/s, when the radius of the rotating fluid in the compartment is taken as 0.41 m. (The radius of curvature is taken as half of the compartment height, when the gravitational effect on the vertical location of the vortex core is neglected.)

To demonstrate the idea of circulation and to locate the exit section for the blanket fluid in the compartment, 2-D thermal-hydraulics analyses were performed for different outlet locations and shapes including circular, semi-elliptical ducts at the vortex core location by using FLOW-3D. The analysis begins to fill the compartment with a continuous supply of the fluid flowing at 7.5 m/s from the inlet (0.015 m thick) and then initiates the discharge as the compartment is full. The discharge of the fluid leaving the calculation domain is simulated by a uniformly distributed mass sink boundary condition distributed over the obstacle located slightly below the mid-plane where the vortex core is located. A FLOW-3D hydrodynamics simulation of the fluid field inside the compartment is illustrated in Figure 5.4-11 for an elliptic outlet mass sink structure.

As shown in Figure 5.4-12, there exists a gap at the vortex center. This is due to absorption of the fluid on the structure and the tangential component of the circulating flow that pushes it away from the outlet section. This result suggests that removing fluid from the vortex center in the vacuum operating condition is not directly related to the suction mechanism, but rather is more related to the hydrodynamic characteristics of the circulating flow which is a function of the inlet velocity, wall contours, and shapes.

The circulation is caused by the change of the flow direction and velocity gradients. The z velocity component decreases to zero as the fluid moves toward the core of the vortex, and then gradually increases, but in the opposite direction as the distance moves away from the exit and becomes zero at the wall. However, it is noticed that the fluid in front of the outlet is forced to move away from the compartment induced by the static pressure and kinetic energy of the fluid behind. Further modification of the compartment configuration is needed to eliminate this problem.

The question is how to remove the fluid out of the pocket. A simple idea is to induce a pressure gradient by modifying the shape of the compartment along the toroidal direction (length). A decrease in the area of the compartment along the toroidal plane decreases the pressure and results in a pressure difference across the pocket. This pressure gradient creates a motion of the vortex core in the pocket towards the outlet hole that is placed at the same level of the vortex core on the smaller area of side wall (see Figure 5.4-13). An additional benefit of this passive liquid removal scheme is the elimination of extra pumping power requirement.

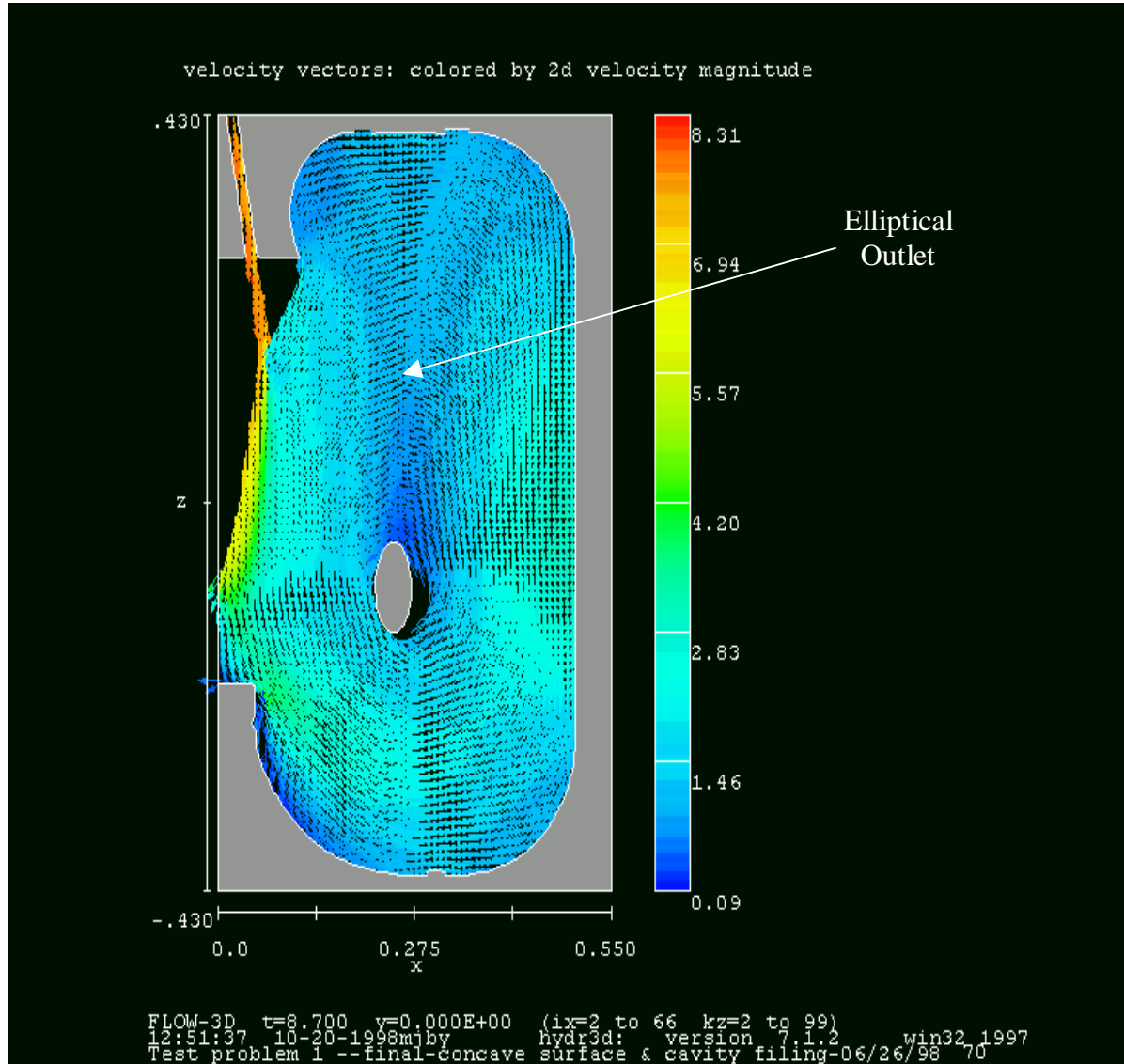


Figure 5.4-11 Velocity vectors plot showing flow circulation inside the compartment. Elliptical outlet located below the mid-plane of the compartment.

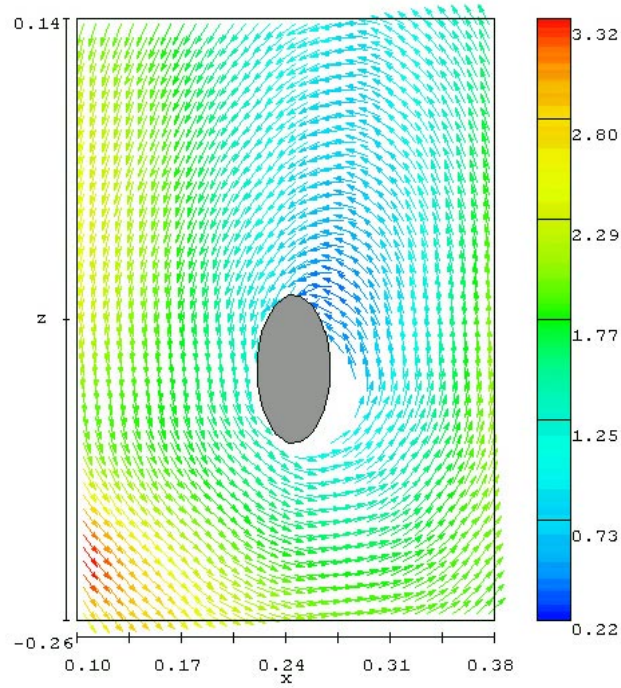


Figure 5.4-12 2-D velocity vector distribution in the single compartment at close distance from exit.

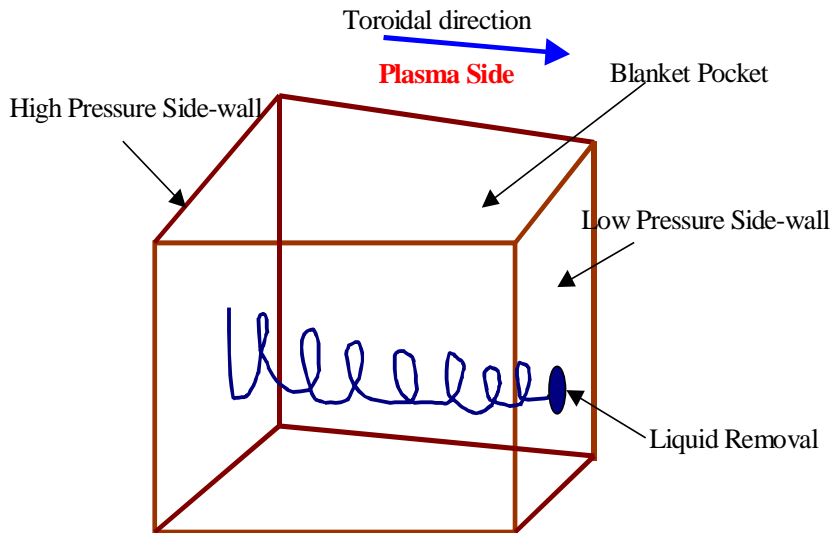


Figure 5.4-13 Schematic view of inherent outlet generating mechanism (Pressure gradient is induced through a varying compartment flow area along toroidal direction.)

The above idea has been verified by FLOW-3D calculations. As shown in Figure 5.4-14, a pressure gradient of about 2000 Pa was generated along the toroidal plane, that forced the fluid to leave the pocket through an outlet opening located at the low pressure plane.

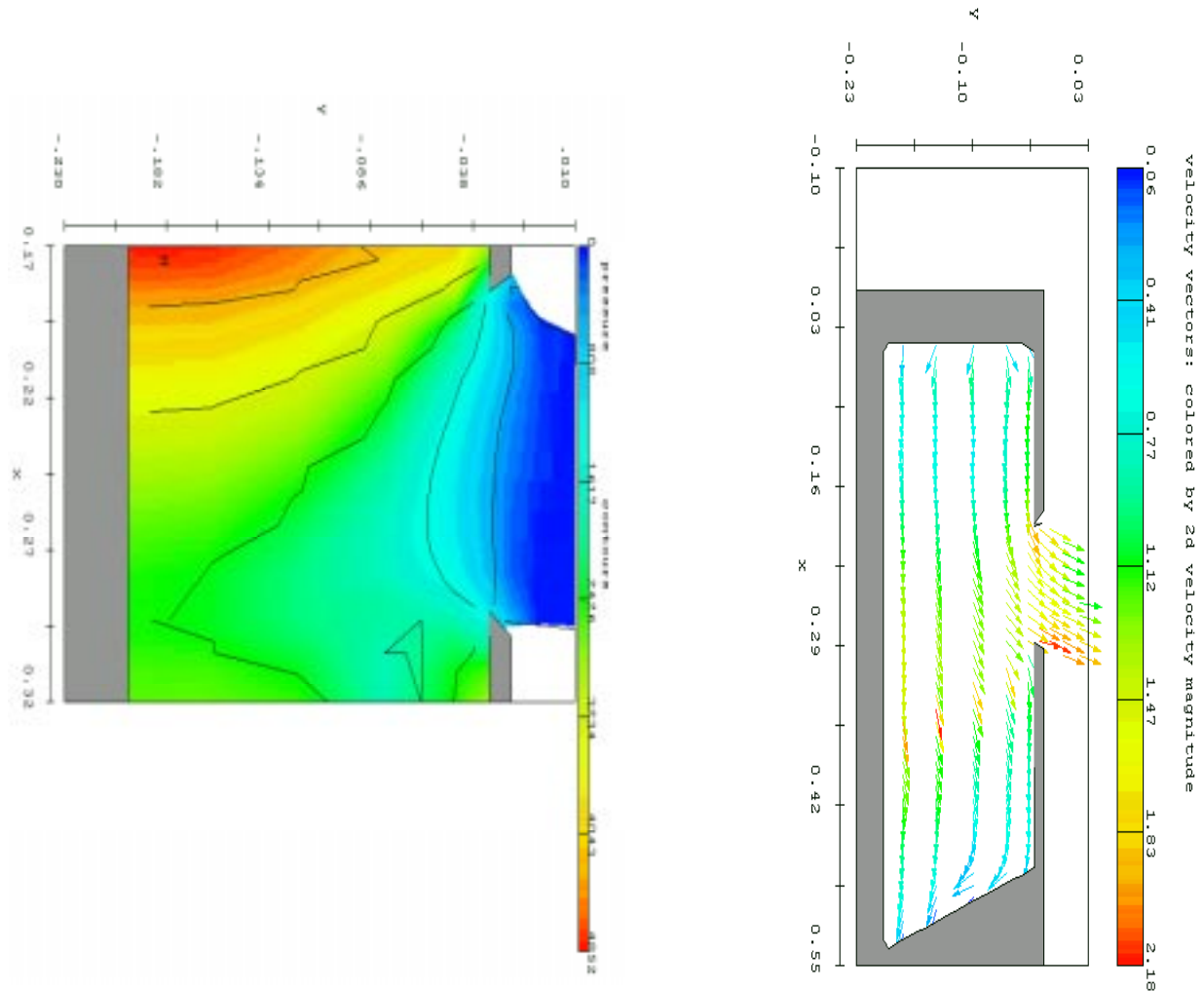


Figure 5.4-14 Pressure gradient is the driving force for liquid discharge from the pocket.

As seen in Figure 5.4-15, there exists a fluid motion at the vortex center in the negative pressure direction as caused by the pressure gradient. There also exists a cavity on the opposite side of the outlet as a result of vortex core discharge. Further parametric analyses are planned to modify the compartment sidewall contour in the toroidal direction and inlet velocity distribution and outlet dimensions to optimize the vortex core motion along the compartment axis.

The analysis demonstrates how a minimal-structure thick-liquid-wall design can be formed in a fusion Tokamak reactor. The concept involves two main sections. A high

velocity, thin Flibe liquid jet is injected into the front first wall section for surface heat removal. The fluid then enters into a series of 84-cm long and 45-cm deep fluid pockets at lower velocity for further heating. The analysis based on heat-mass transfer analogy indicates that the Flibe heat transfer due to surface turbulence can be high enough to ensure a low free surface temperature for plasma operation under a specified surface heat flux of 2 MW/m².

The thermal-hydrodynamics analyses based on FLOW-3D calculations demonstrate that the fluid is indeed circulating inside the pocket meanwhile achieving a uniform temperature profile. The exit of the blanket fluid is located at the core of the vortex where the fluid temperature is the hottest. An optimum thermal-hydraulics for such a design involving a 1 cm jet flowing at 15 m/s enters the front section at 540 °C and leaves the blanket at 650 °C (discussed in Section 5.5). Further design analysis will be conducted if this design is considered as a reference option.

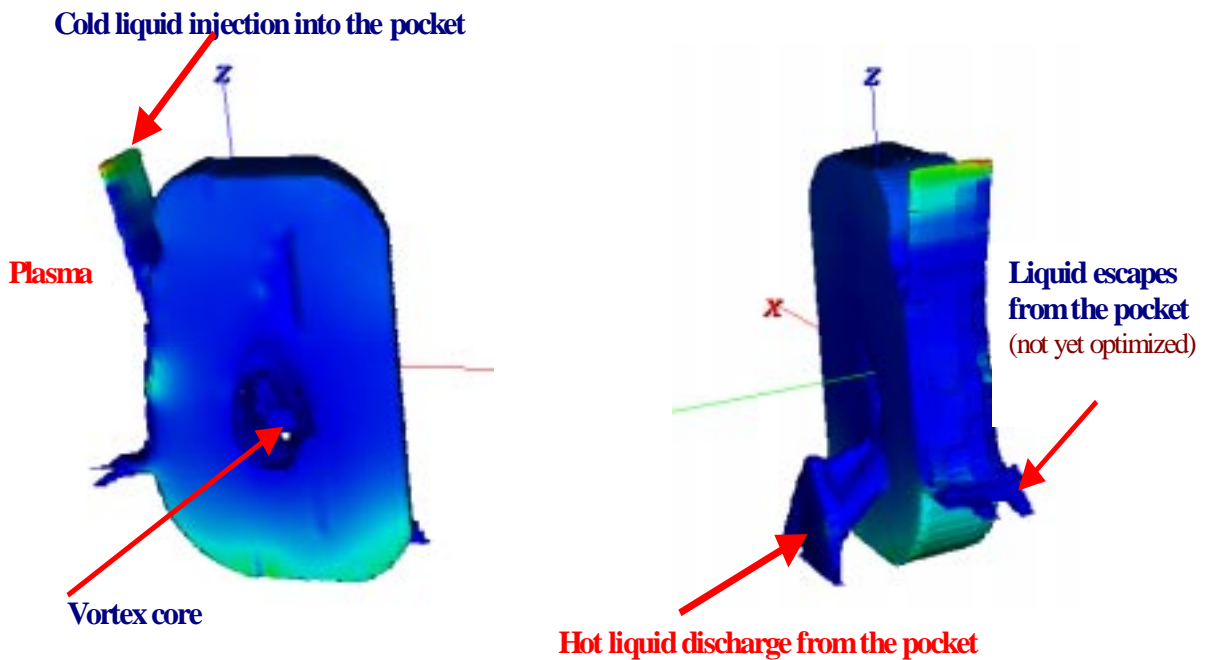


Figure 5.4-15

Preliminary 3-D hydrodynamic characteristics of the liquid wall concept flow in the compartment.

5.4.2 Hydrodynamic design of swirl flow for FRC configuration

The primary condition for free vortex flow in the cylindrical chamber is that the centrifugal force pushing the fluid towards the wall should be greater than the weight of the fluid at the top section of the cylindrical FRC chamber (at location of 90° as seen in Figure 5.4-16.)

$$\int_{R_s}^{R_b} \rho \frac{U_{\theta}^2(r)}{r} r dr d\theta > \int_{R_s}^{R_b} \rho \cdot \vec{g} \cdot r dr d\theta \tag{5.4-12}$$

where R_b is the radius of cylindrical chamber, R_s is radius of flow surface, g is the gravitational acceleration, ρ is the operating fluid density, θ is the unit angle in the neighborhood of 90° (where gravitational acceleration direction is in the opposite direction of centrifugal acceleration) and V_{θ} is the velocity of the liquid layer in the azimuthal direction. The minimum required azimuthal surface velocity for the liquid layer to swirl inside the chamber is:

$$C^2 > g \frac{[R_b + R_s] R_b}{2 R_s} \tag{5.4-13}$$

where C is the azimuthal velocity at the flow surface, when the velocity profile of potential flow in the azimuthal direction is assumed as [16,17],

$$U_{\theta} = C \frac{R_s}{r} \tag{5.4-14}$$

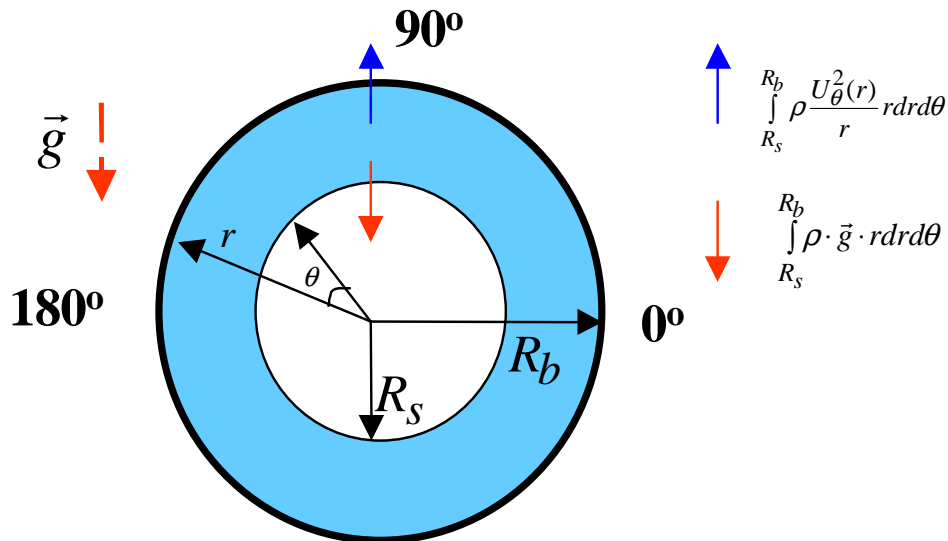


Figure 5.4-16 2-D (r-θ) illustration of liquid layer for FRC configuration.

The minimum required azimuthal surface velocity is 4.8 m/s for a chamber radius of 2 m and liquid wall thickness of 0.5 m. However, computational results show that there is a 35 % difference in the liquid layer thickness between the flow at the bottom (270°) and the top (90°) sections. This non-uniformity in the liquid layer thickness on planes perpendicular to the flow direction is due to gravitational acceleration and can be minimized using the relationship of

$$\frac{U_{\theta}^2}{2gR_s} 0.5 > 10 \quad (5.4-15)$$

This relationship is determined to satisfy the condition of $\Delta\vec{a}/\vec{a} < 0.1$ where \vec{a} is the total acceleration including the gravitational acceleration affecting the flow in the radial direction and $\Delta\vec{a}$ is the difference in the radial acceleration between the top and bottom sections. Analytical derivations suggest that the effect of gravitational acceleration on the hydrodynamic characteristics of the liquid jet can be minimized for $U_{\theta} > 13.6$ m/s, for a liquid layer thickness of 0.5 m and chamber radius of 2 m.

Numerical hydrodynamic analyses are performed using Flow3d cod. Flibe is used as the operating fluid. Preliminary design exploration study is performed using constant axial inlet azimuthal and axial velocities to a converging (radius converges from 2.75-m radius to 2 m within 1.5-m axial flow length) chamber that opens into a constant radius cylindrical chamber.

As seen in Figures 5.4-17 and 5.4-18, base operating variables and dimensions for FRC configuration of 10 m/s axial and 10 m/s in azimuthal inlet velocities can maintain a certain liquid layer thickness along the flow axis. Results also indicate that there exists a continuous decrease in the liquid layer thickness from 0.85 m to .6 m in the axial direction. This may be due to the free outlet boundary condition at the exit of the main section. The decrease in the flow thickness in the axial direction may be minimized by increasing the axial inlet velocity or using a slight contraction in the cylindrical chamber radius towards the outlet that moves the cyclostatic pressure balance towards the axis of the chamber. The velocity distribution in the axial direction confirms that both a convergent inlet and a divergent outlet section may work properly. However, better design is needed for the convergent section. As the chamber radius decreases, the centrifugal acceleration effect on the flow increases. This condition results a thicker liquid layer. Although this hydrodynamic shape close to the inlet may be desired for elimination of neutron streaming, thickening of the liquid layer results in lower axial surface velocity. This condition may not be desirable since the duration of the flow surface exposed to the plasma radiative heating becomes higher (which may cause an increase in the liquid evaporation rate).

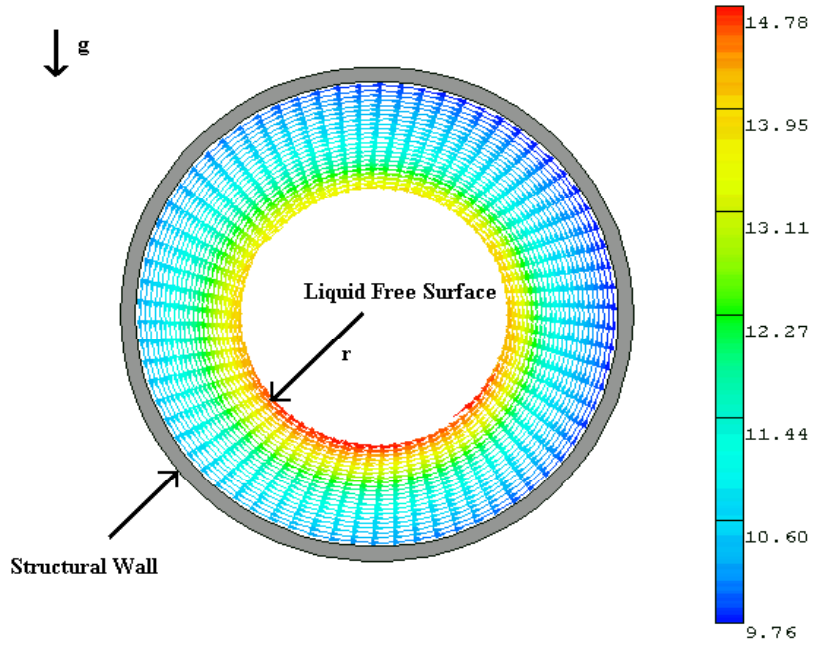


Figure 5.4-17 2-D (r - θ) Velocity distribution and liquid layer height distribution in the azimuthal direction at 5-m away from inlet.

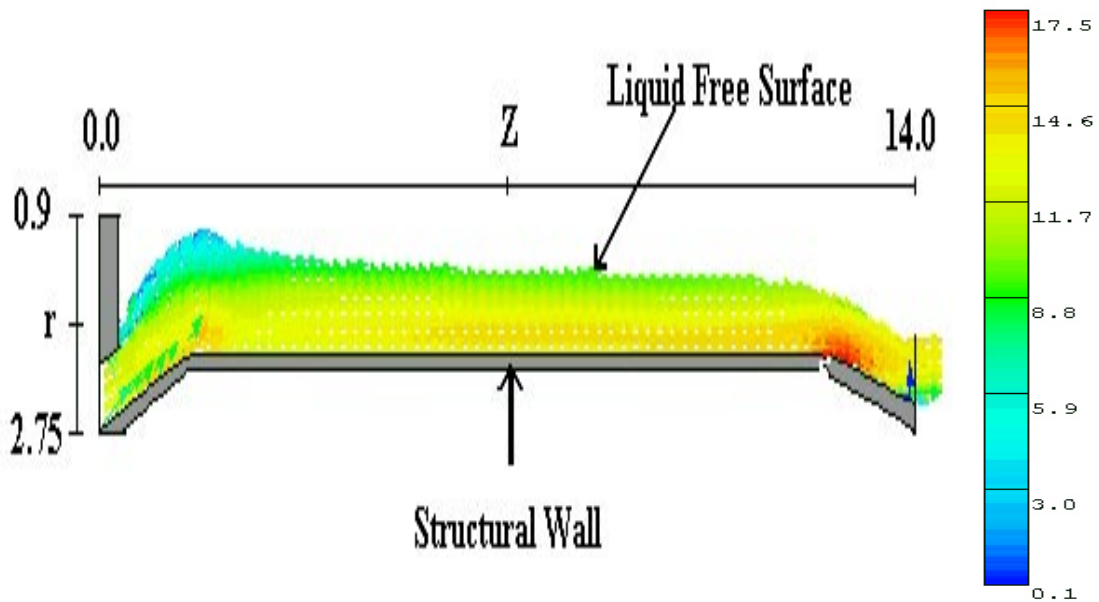


Figure 5.4-18 2-D (r - z) Velocity distribution and liquid layer height distribution in the axial direction at 0° (see Figure 5.4-16).

Preliminary parametric computational analysis for swirling/non-swirling with horizontally/vertically located FRC chamber configurations suggest that a horizontally located chamber with a swirl flow may be an attractive configuration. As seen in Tables 5.4-2, 5.4-3 and 5.4-4, the horizontally located chamber configuration with swirl flow has advantages over the vertically located chamber configuration because it: (1) minimizes the required pumping power for high thermal efficiency, (2) can maintain a uniform blanket thickness in the chamber with no minimum/maximum velocity requirement in the horizontal direction (3) may enable the use of a smaller chamber and extraction of higher power density when the heat transfer/heat transfer-enhancement at the flow free surface is addressed.

Table 5.4-2 Structural positioning of FRC chamber and varied operational parameters for parametric study.

Relative Positioning	Structural Modification	Inlet Radius	Outlet Radius	Varied Parameters
Horizontal	yes	2.0 m	1.75 m	U_{axial} , $U_{azimuthal}$
Horizontal	no	2.0 m	2.0 m	U_{axial} , $U_{azimuthal}$
Vertical	yes	2.0 m	1.75 m	U_{axial}
Vertical	no	2.0 m	2.0 m	U_{axial}

Table 5.4-3 Required operation conditions and observed blanket symmetry for horizontally and vertically located FRC chamber cases.

Modification of FRC Wall	Blanket Symmetry	Rotational Flow	Azimuthal Velocity	Axial Velocity	Velocity Magnitude
Horizontally oriented FRC	yes	Required	> 11 m/s	>10 m/s	>14.8 m/s
Horizontally oriented FRC	no	Required	> 7.5 m/s < 11 m/s	< 10 m/s	< 12.5 m/s
Vertically oriented FRC	yes	no	----	> 20 m/s	> 20 m/s

In addition, the advantages of swirl flow may be that: (1) an inherent stratification in the flow may be formed due to the high centrifugal acceleration that may result in a possibility of easy separation of the hot fluid at the surface from the colder one at the

outlet section to achieve higher thermal efficiency, and (2) there is no structural requirement in the chamber for flow regulation.

Table 5.4-4 Required operation conditions and observed blanket symmetry conditions for horizontally and vertically located FRC chamber cases when the chamber structural wall topology is modified.

Modification of FRC Wall	Blanket Symmetry	Rotational Flow	Azimuthal Velocity	Axial Velocity	Velocity Magnitude
Horizontally oriented FRC	yes	Required	> 8 m/s	> 8 m/s	> 11.4 m/s
Vertically oriented FRC	yes	no	----	> 15 m/s	> 15 m/s

The structure of the FRC chamber can be modified to minimize surface temperature rise due to radiation heating. One way is to lessen the exposure time of the flow to the radiation by a factor of two by taking advantage of the hydrodynamic conditions due to swirl flow. As seen in Figure 5.4-19, a cusp-like liquid surface may be obtained by driving a swirling liquid layer into the interior of a cylindrical structural shell from both sides with an azimuthally symmetric outlet in the magnetic cusp region, so that the liquid streams are ejected by their own centrifugal momentum. The outer radius and the thickness of the liquid flow is chosen so radiation damage in structural materials may be reduced to an acceptable level.

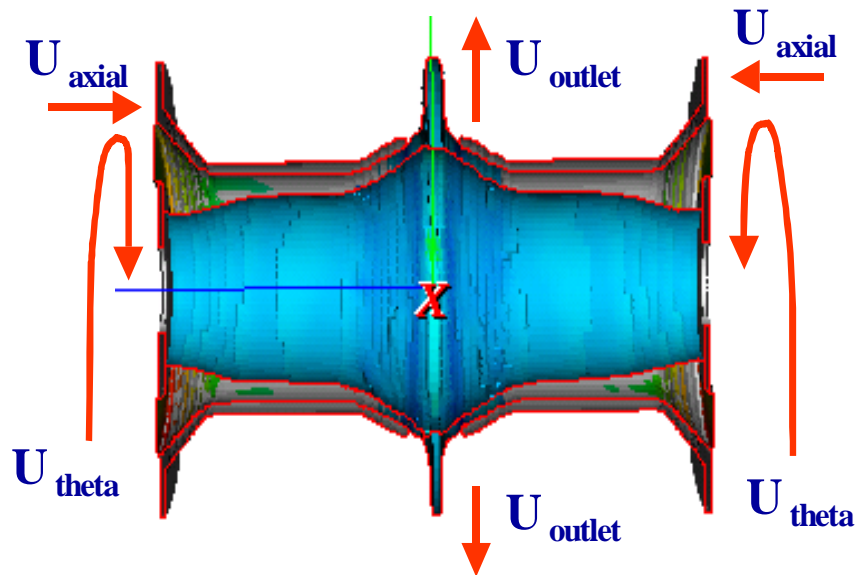
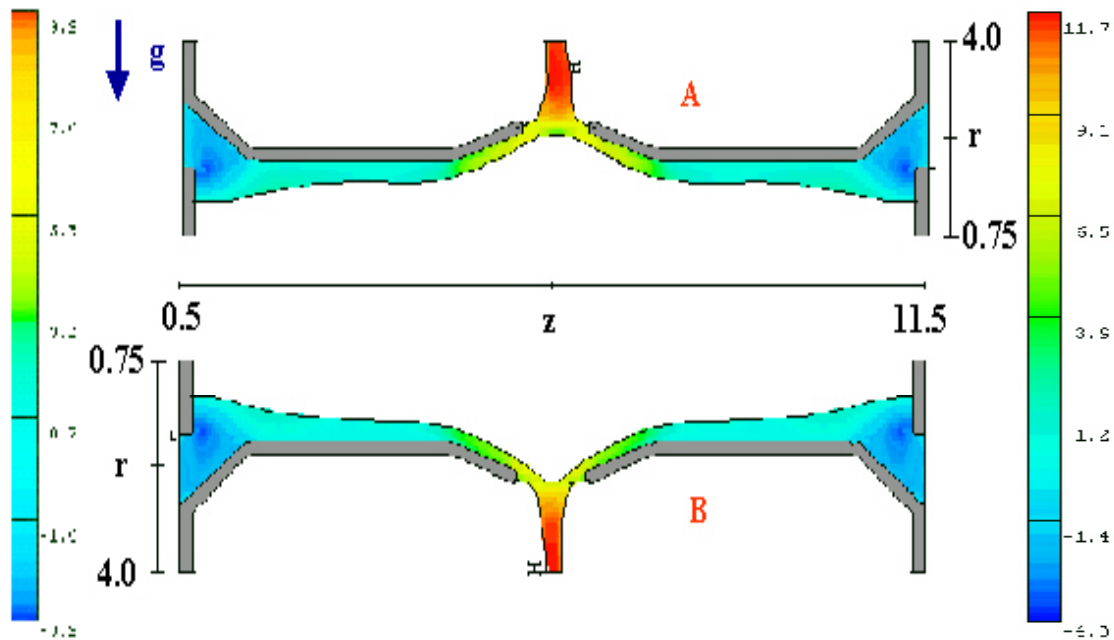


Figure 5.4-19 A cross-section of 3-D fluid distribution in modified FRC chamber.

A preliminary modified FRC configuration for hydrodynamic simulation analysis consists of two identical structures located 1 m away from each other, each having 1.5 m long converging sections (2.75 m radius to 2 m radius) on the far ends, 3 m long

cylindrical sections with 2 m radius and 1.5 m long diverging sections (2 m radius to 2.75 m radius) towards the middle. Initial results are obtained for inlet velocities of $V_{\text{azimuthal}} = 12 \text{ m/s}$, $V_{\text{axial}} = 2 \text{ m/s}$. Preliminary analysis suggests that a swirling liquid wall in the cylindrical and cusp shaped liquid wall at the outlet sections can be maintained and the formation of the cusp is strongly dependent on azimuthal velocity component. The distance between two cylindrical section becomes lower and the fluid drip into the target section may be eliminated when the initial axial inlet velocity is minimized.

As seen in Figure 5.4-20, there is an asymmetry in the cusp due to the effect of gravitational acceleration on the hydrodynamic behavior of the swirling liquid flow. The slope of the cusp is constant due to the structural constraint, however the thickness of the liquid wall on the diverging section varies due to the gravitational acceleration. Increasing the azimuthal flow velocity may minimize this condition. The outlet velocity varies as the direction of gravitational acceleration with respect to the axial flow direction changes.



A **B**
Figure 5.4-20 Radial velocity distribution in r-z plane and liquid layer height distribution in the axial direction at an azimuthal angle where **A**) the gravitational acceleration is in the opposite direction with the centrifugal acceleration, **B**) the gravitational acceleration is in the same direction with the centrifugal acceleration.

An optimization analysis for diverging cusp section (angle, length) and liquid wall operating conditions will be performed to eliminate droplet formation, maximize heat transfer, and maintain the wall thickness along the axial and azimuthal flow directions.

5.4.3 Hydrodynamic design of swirl flow for ST

The swirl concept may be applied to several configurations such as the ST. Application of swirling liquid layer to this configuration is explained in this section. As

seen in Figure 5.4-21, in the ST configuration, a thick liquid layer flows from the reactor top in the outboard with vertical and azimuthal velocity profiles. The liquid layer becomes attached to the outer board due to centrifugal acceleration from the toroidal liquid layer velocity. Formation of a 0.25 m high step in the reactor mid-plane along the poloidal direction (where the effect of gravitational acceleration on the liquid layer thickness is the highest) on outboard vacuum vessel topology helps to maintain liquid layer thickness constant (> 0.3 m). At this location, centrifugal acceleration ($> 35 \text{ m/s}^2$) pushes the fluid towards the outboard and prevents the deflection of the flow into the plasma region.

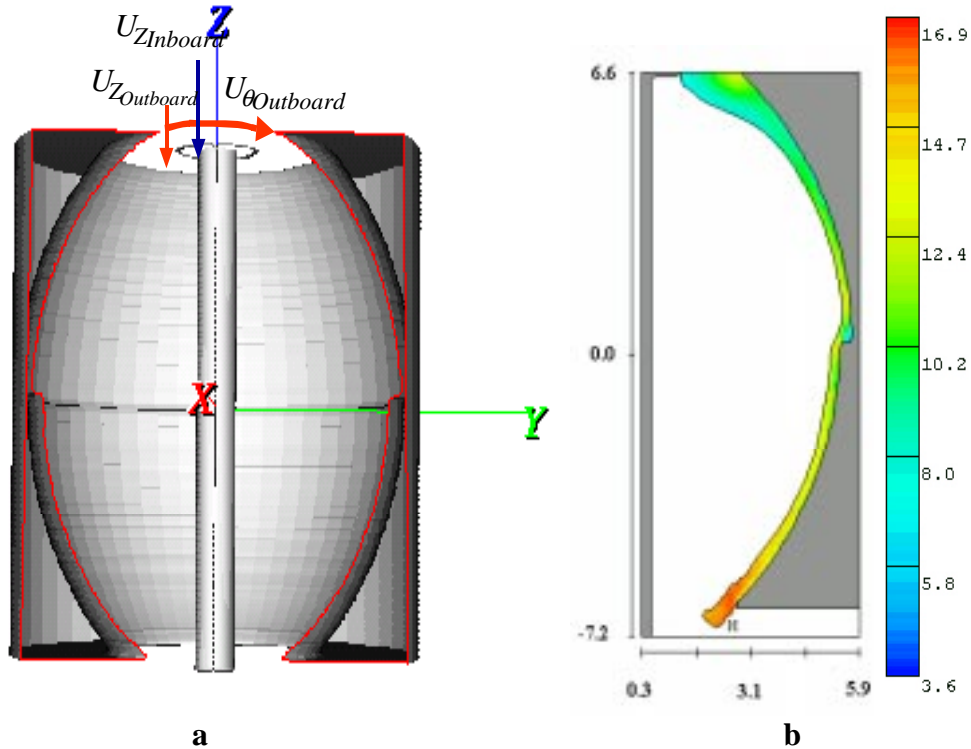


Figure 5.4-21 a. The structural modeling of ST geometry including the modification in the outboard topology. b. 2-D velocity magnitude contour at r-z plane at the outboard and liquid layer height distribution in the z-direction at an arbitrary azimuthal angle.

Preliminary results were obtained for inlet operating condition of $V_{poloidal} = 4.5$ m/s, $V_{toroidal,ave} = 12$ m/s from an annular inlet with an inner radius of 1.8 m and outer radius of 3.3 m. This inlet condition was parametrically obtained by: (1) taking into account the substantial increment in total flow area ($\sim 266\%$) in the vertical direction from top of the reactor to the mid-plane to obtain a 0.3 m minimum liquid layer thickness at the mid plane, (2) minimizing the poloidal velocity at the ST mid plane so that deflection of the flow towards the plasma is prevented. Using a thicker inlet fluid layer may compensate for the increase in the poloidal velocity due to gravitational acceleration (thinning of the liquid layer). Also, a thicker fluid layer with lower velocity requires less pumping power, as the pumping power is proportional to the velocity squared.

In the inner board, a fast annular liquid layer of 0.75 m thick (over an inner radius of 1 m) with 15 m/s vertical velocity is used. High vertical velocity ($V_z > 15$ m/s) prevents excessive thinning in the liquid layer ($< 30\%$). The swirling liquid layer idea is more applicable to the ST configuration than the ARIES-RS configuration. This is because the ST geometry has a larger radius of curvature in the poloidal direction (~ 8.0 m. vs. ~ 4.0 m) and a smaller radius of curvature in the toroidal direction relative to the poloidal direction (5.0 m as compared to 8.0 m). Toroidal rotation of the liquid layer may result in a substantial increase in the centrifugal acceleration of the flow towards the back wall (266 % at the inlet and 160 % at mid plane). The ST is taller than ARIES-RS (~ 12.0 m. vs. ~ 6.0 m) and the effect of gravity in the hydrodynamic characteristics of the flow is more important and requires additional passive mechanisms to overcome thinning.

Preliminary computational hydraulic analysis predicts that swirling flow inside a cylindrical chamber for FRC configurations and inside a quasi-spherical chamber for the ST configuration may form thick liquid walls replacing the customary first wall/blanket system. Parametric computational study indicated that the liquid layer thickness in axial and azimuthal directions is strongly dependent on inlet axial and azimuthal velocity values and gravitational acceleration, and a uniform liquid layer thickness in azimuthal and axial directions can be maintained for axial and azimuthal inlet velocities of 11 m/s and 13 m/s in a cylindrical chamber with 2 m radius and 12 m length. The swirling liquid wall idea can be applied successfully to the ST (by modifying outboard back-wall topology). For the application of the swirl idea to the ST configuration, the topology of the outboard will be modified to minimize the inlet velocity requirement in order to keep the fluid adhered to the wall.

5.4.4 Mechanisms Effecting the Stability of Swirl Flow and Perturbation Sources

There are many studies performed in the literature for high velocity fluid (liquid or gas) layer flow over concave surface and in swirl chambers (which is totally filled with fluid for combustion studies) separately [19,20,21,22]. The experimental results obtained from these studies suggest that the radial distribution of the tangential flow velocity (see Section 5.4-2 and Figure 5.4-16 where U_α notation in the present section corresponds to U_θ) is divided into two regions: a region of forced rotational flow in the center of the chamber and surrounded by a region of quasi-free rotational flow. The proposed FRC swirling liquid layer configuration does not have forced vortex region close to the axis of the chamber. The liquid layer flow in the azimuthal and axial directions have high Reynolds numbers ($Re > 10^6$) where the boundary layer thickness becomes comparably less than the liquid layer thickness along the chamber. As an example, ratio of turbulent boundary layer thickness ($\delta = 0.16 x^{6/7} (\rho U / \mu)^{-1/7}$) to 0.9-m liquid layer thickness for Flibe at 550 C with 12 m/s velocity at a location of 10 m away from the inlet is 0.17. Therefore, potential flow theory can be used for the characterization of azimuthal flow for linear stability analysis. 2-d (r-theta) linear stability analysis is performed using irrotational velocity profile with surface tension, gravitational acceleration and the centrifugal acceleration models. Assumptions are: (1) boundary layer thickness is small compared to the free stream thickness, (2) only azimuthal velocity components are taken

into account, (3) initial infinitely small perturbations are introduced for surface displacement and velocity potential. The system equations: Laplacian of velocity potential and Bernoulli Equation with surface tension, centrifugal acceleration and gravitational acceleration models for a finitely small disturbance in the surface perturbation (ζ) and velocity potential are expressed respectively as,

$$\nabla^2 \phi = 0 \quad (5.4-16)$$

$$\frac{\partial \phi'}{\partial t} + (\nabla \phi_0 \nabla \phi')_{\alpha} = \frac{1}{\rho} \left(\rho \zeta g \sin \alpha + \frac{\sigma}{R_s^2} \frac{\partial^2 \zeta}{\partial \alpha^2} - \rho \frac{U_s^2 \zeta}{R_s} \right) \quad (5.4-17)$$

where $\phi = U_s R_s \alpha$ is the velocity potential, R_s corresponds the radius of curvature at the boundary layer surface, U_s corresponds to the velocity component in alpha direction at the free-surface and r is the radial variable. The definition of variables used in the analytic derivations, geometry of interest and detailed analytic derivations are presented in Section 7.3.1.3. Boundary conditions at the boundary layer surface close to the back wall and free surface [23] are respectively,

$$r_0 \frac{\partial}{\partial r} (U_s R_s \alpha) + r_0 \frac{\partial}{\partial r} \phi' = 0 \quad \rightarrow \quad r_0 \frac{\partial}{\partial r} \phi' = 0 \quad r = R_w \quad (5.4-18)$$

$$\frac{\partial \phi'}{\partial r} = \frac{\partial \zeta}{\partial r} + \left(\frac{U_s R_s}{r} + \frac{1}{r} \frac{\partial \phi'}{\partial \alpha} \right) \frac{1}{r} \frac{\partial \zeta}{\partial \alpha} \quad r = R_s \quad (5.4-19)$$

Since the set of partial differential equations has constant coefficients independent of time and space, method of normal modes are used in the linearization where small arbitrary perturbations of the form $\zeta, \phi' = (\hat{\zeta}, \hat{\phi}') e^{ik\alpha + st}$. The coefficient of small disturbances in the exponent form is derived as,

$$s_{1,2} \cong \frac{U_s}{R_s} ik \pm i \sqrt{\frac{k}{R_2} \frac{1 - \left(\frac{R_w}{R_s}\right)^{2k}}{1 + \left(\frac{R_w}{R_s}\right)^k} \sqrt{g \sin \alpha - \frac{U_s^2}{R_s} - \frac{\sigma k^2}{R_s}}} \quad (5.4-20)$$

Using above equation, liquid layer may be stable when gravitational acceleration, centrifugal acceleration and surface tension are taken into account for the condition of

$$g \sin \alpha < \frac{U_s^2}{R_s} + \frac{\sigma k^2}{R_s} \quad (5.4-21)$$

Above result suggests that the free-vortex swirl flow is always stable when the azimuthal velocity component is taken into account since centrifugal acceleration should be more than gravitational acceleration for liquid layer to adhere to the wall. Gravitational acceleration has stabilizing and destabilizing effect on the flow depending on the direction of the flow with respect to direction of the gravitational acceleration. Surface tension has stabilizing effect for high wave number (short wave wavelength) as expected.

Hydrodynamic stability of the boundary layer on the concave back wall surface may not be an important issue since the boundary layer thickness is expected to be less than ~ 17 % of the total thickness at its maximum point for FRC chamber. However, there may be randomly existing Gortler vortices in the turbulent boundary layer [24,25,26]. Although large-scale inflows and outflows have strong influence on the flow structure in the near wall region, near wall profiles of Reynolds-averaged quantities may show relatively minor differences between the flat and concave back wall cases.

There are also additional physical mechanisms that may effect the performance of the liquid layer for free surface heat transfer and swirl decay. These mechanisms are out of the scope of the present study and may be subject to future experimental work. As an example, evaluation of radial distribution of turbulence intensity in free-vortex along the axial direction and its effect on swirl decay. In addition to that, evaluation of wave formations due to the relaxation of the boundary layer on the liquid layer surface leaving the nozzle section is directly related to upstream conditions such as relaminarization of the flow inside the nozzle or swirl generating generator (contraction ratio, upper wall surface curvature, etc) [27,28].

5.4 References

- 1 Branover G.G. Magnetohydrodynamic Flow in Ducts. New York: J.Willey; Jerusalem: Israel University Press (1978).
- 2 Blums E., Mikhailov Yu.A., Ozols R. Heat and Mass Transfer in MHD Flows. Series in Theoretical and applied Mechanics, Vol.3 (1987).
- 3 Kunugi T., Tillack M.S., Abdou M.A. Analysis of Liquid Metal MHD Fluid Flow and Heat Transfer Using the KAT Code, UCLA-FNT-44 (1990).
- 4 Sterl A. Numerical Simulation of Liquid Metal MHD Flow in Rectangular Ducts, J.Fluid Mech., 216, 161 (1990).
- 5 Kim C.N., Abdou M.A. Numerical Method for Fluid Flow and Heat Transfer in Magnetohydrodynamic Flow, Fusion Technology, 15, 2, 2B, 1163 (1989).
- 6 Singh B., Lal J. Effect of Magnetic Field Orientation and Wall Conductivity on MHD Channel Flows Using Finite Element Method, Comp. Meth in Appl. Mech. and Eng., 40, 159 (1983).
- 7 Winowich N.S., Hughes W.F. A Finite Element Analysis of Two-Dimensional MHD Flow, Liquid Metal Flows and Magnetohydrodynamics, ed. by H.Branover, P.S.Lukoudis , A.Yakhot, 313 (1983).
- 8 Evtushenko I.A., Smolentsev S.Yu., Tananaev A.V. Hydrodynamics and Exchange of Heat in Thin Liquid Metal Layers within a Magnetic Field, Magnetohydrodynamics, 3, 287 (1991).
- 9 Smolentsev S.Yu., Tananaev A.V. Development of a Computer Code for Analysis of Heat Transfer in Liquid Metal MHD Flows in Ducts, Magnetohydrodynamics, 4, 414 (1995).
- 10 Morley N.B. and Abdou M.A. Study of Fully-Developed, Liquid Metal, Open-Channel Flow in a Nearly Coplanar Magnetic Field, Fusion Technology, 31, 135 (1997).
- 11 Tillack M.S. Application of the Core Flow Approach to MHD Fluid Flow in Geometric Elements of a Fusion Reactor Blanket, Liquid Metal Magnetohydrodynamics, ed. by J.Lielpeteris, R.Moreau, 47 (1989).
- 12 Hua T.Q., Walker J.S. Numerical Solutions of Three-Dimensional MHD Flows in Strong Non-Uniform Transverse Magnetic Fields, Liquid Metal Magnetohydrodynamics, ed. by J.Lielpeteris, R.Moreau, 13 (1989).
- 13 Buhler L. Liquid Metal Flow in Arbitrary Thin-Walled Channels under a Strong Transverse Variable Magnetic Field, Fusion Eng. and Design, 17, 215 (1991).
- 14 Smolentsev S.Yu. Averaged Model in MHD Duct Flow Calculations, Magnetohydrodynamics, 1, 42 (1997).
- 15 Aitov T.N., Ivanov A.B., Tananaev A.V. Flow of Liquid Metal in a Chute in a Coplanar Magnetic Field, Magnetohydrodynamics, 1, 78 (1987).
- 16 Moir, R. W., 1987, Rotating Liquid Blanket For Toroidal Fusion Reactor, Fusion Engineering and Design, Vol. 5, pp. 269-272.
- 17 Moir, R. W., 1997, Liquid First Walls for Magnetic Fusion Energy Configurations, Nuclear Fusion, Vol. 37, No. 4, pp. 557-566.
- 18 Abdou, M. A., and the APEX Team, 1998. Exploring Novel High Power Density Concepts for Attractive Fusion Systems, Fusion Technology.
- 19 Kelsall, D. F., A Study of the Motion of Solid particles In a Hydraulic Cyclone,

- Trans. Instn. Chem. Engrs., Vol. 30, 1952.
- 20 Bradley, D. , The Hydrocyclone, Pergamon Press, First Edition, 1965.
- 21 Wang S., Rusak Z., 1996, On the Stability of an Axisymmetric Rotating Flow in a Pipe, Physics of Fluids, Vol. 8 (4), pp. 1007-1016.
- 22 Ligrani P.M. et al., 1998, Flow Phenomena in Swirl Chambers, Experiments in Fluids, Vol. 24., pp. 254-264.
- 23 Lamb H., 1960, Hydrodynamic Stability, Cambridge University Press, p 8-9.
- 24 Tani I, 1962, Production of Longitudinal Vortices in the Boundary layer Along a Concave Wall, Journal of Geophysical Research, Vol. 67, No. 8, pp. 3075-3080.
- 25 Ramaprian, B. R., Shivaprasad, B. G., 1978, The structure of Turbulent boundary layers Along Mildly Curved Surfaces, J. Fluid Mech. , Vol. 85, Part 2, pp. 273-303.
- 26 Bradshaw P., Muck K.C., Hoffman P.H., 1985, The Effect of Concave Surface Curvature On Turbulent Boundary Layers, J. Fluid Mech. , Vol. 161, pp. 371-403.
- 27 Brennen C, 1970, Cavity Surface wave Patterns and General Appearance, J. Fluid Mech., Vol. 44, part 1, pp. 33-49.
- 28 Hassberger J.A, 1983, Comparison Between Measured and Predicted Performance of a High Speed Free Surface Liquid Jet Flowing along a Curved Wall, Nucl. Technol. Fusion, Vol. 4, pp. 433-438.

5.5 Heat Transfer and Thermal-Hydraulics

The temperature of the free liquid surface facing the plasma is the critical parameter governing the amount of liquid that evaporates into the plasma chamber. Such a liquid surface temperature can only be determined if the heat transfer at the free surface/vacuum boundary is well understood. Unlike solid metallic walls that only depend on conduction, for liquid walls the heat transfer is intimately connected to the motion of the liquid through the convection terms. The heat transfer at liquid/vacuum interface is governed by several physical mechanisms: conduction into bulk fluid, convection into bulk fluid such as turbulent fluctuations and secondary flows, convection along flow, and x-ray penetration- a phenomena that high-energy photons from core radiation can penetrate into low z liquids. The relative magnitude of different mechanisms depends on the choice of working liquid.

It is believed that an understanding of the basic thermal-hydraulics performance of the liquid FW/blanket is imperative for the ultimate development of a practical design. Specifically, this includes liquid inlet/outlet temperatures, pressure drop and pumping power requirement. To be noticed that achieving an integrated optimum performance might result in conflicting requirements. For example, in order to keep the free surface temperature as low as possible, a fast flowing liquid is desired for the surface heat removal while the resultant high-mass flow rate leads to an enormous pumping power consumption.

In this section, the free surface temperatures are first calculated for Flibe, lithium and tin-lithium. Liquid metal flows will be laminarized by the magnetic field. Thus, the heat transfer at the liquid metal free surface strongly depends on the heat conduction. However, the molten salt Flibe, which conducts heat very poorly, is not fully laminarized by the presence of the magnetic field. The heat transfer at the Flibe free surface wall is dominated by the rapid surface renewal from turbulent eddy generated either near the free surface due to temperature gradient driven viscosity variations, or near the back wall or nozzle surfaces by frictional shear stresses. The effectiveness of these turbulent structures in cycling energy from the free surface into the bulk flow is also affected by the degree of damping by the magnetic field. The effects of turbulence and of MHD suppression on Flibe free surface temperature are addressed by κ - ϵ model and discussed in section 5.5.2. Issues concerning power conversion and pumping power requirements and blanket core temperature distributions are addressed in Sections 5.5.3 and 5.5.4.

5.5.1 Liquid Wall Surface Temperature Estimation and Heat Transfer

Since the fluid surface is directly exposed to the plasma, the plasma-liquid interactions are very important. Concerns about impurity transport to the plasma will set a limit on the amount of material allowed to evaporate from the liquid surfaces. This evaporation limit will in turn gives a surface temperature limit of the flowing liquid. Such limits have to be derived from the sophisticated plasma-edge modeling analysis and are discussed in Chapter 12. On the other hand, the temperature profile of the liquid surface can be readily calculated as a function of heat loads and flow parameters if the surface

heat transfer phenomena are well understood. The objectives of the heat transfer and thermal-hydraulic analysis are to determine at what operating conditions the liquid surface temperature can be lower than the maximum allowable, what typical surface temperatures are under APEX operating conditions, and to evaluate how engineering designs be influenced by the requirements.

The temperature profile of the liquid metal FW is calculated using a three-dimensional finite difference heat transfer code for a combined surface heat load of 2 MW/m² and neutron wall load of 10 MW/m². The code takes the velocity profile as an input parameter and solves the energy equation:

$$\rho C_p \left[V_x \frac{\partial T}{\partial x} + V_y \frac{\partial T}{\partial y} + V_z \frac{\partial T}{\partial z} \right] = k \nabla^2 T + q''' \quad (5.5-1)$$

The volumetric heating due to both neutron and x-ray interactions are accounted in the source term, q''' . Details of the neutronics analysis are included in Section 5.3. In cases where x-ray penetration is insignificant such as the case for tin-lithium, the surface heat flux is accounted for as a boundary condition. To adequately simulate the sharp heat deposition gradient, finer meshes are required in the first 1 cm of the liquid wall close to the plasma side.

Although the code is adapted readily to calculate 3-D temperature profiles for any complicated velocity fields, the analyses were performed for slug velocity profiles. Such velocity profiles are applicable for the liquid metal flow where flow laminarization is expected in the presence of strong magnetic fields. The velocity profile for the non-electrically conducting Flibe is somewhat complicated because it is operated in the turbulent regime where velocity profiles are more complicated to describe mathematically.

The temperature profiles of the liquid FW have been calculated using a three-dimensional finite difference heat transfer code for a slug velocity profiles under a combined surface heat load of 2 MW/m² and neutron wall load of 10 MW/m². The surface and bulk temperature distributions as fluids proceed downstream are shown in Figures 5.5-1 and 5.5-2 for lithium and tin-lithium slug velocity profiles, respectively; while temperature profiles into the liquid layers at about 2.0 m downstream are shown in Figures 5.5-3 and 5.5-4. As shown, accounting for x-ray penetration reduces the lithium surface temperature by about 40 °C. But this is not the case for Sn-Li because of its high Z. The surface heating due to a 2 MW/m² surface heat load results in an about 300 °C temperature increase on the surface at 5 m downstream flowing at 10 m/s while it only increases by about 20 °C at the bulk. Liquid metals such as lithium and Sn-Li have high thermal conductivity, the conduction can be much effective while the temperature gradient across the film is less steeper as compared to that of the Flibe (see Figure 5.5-3).

The surface and bulk temperature distributions as fluids proceed downstream for Flibe using a slug velocity profile (a laminar flow) are shown in Figures 5.5-5. Noticed that accounting for x-ray penetration significantly reduces the Flibe jet surface temperature. However, the Flibe surface temperature appears high and would not be

acceptable for plasma operation. Furthermore, most of the Bremsstrahlung radiation is deposited within the first few mm meanwhile resulting in a steep temperature gradient across the region as shown in Figure 5.5-6. Such a temperature gradient could cause the jet to become a two-layer shear flow due to a large variation of liquid viscosity as a function of temperature (as insert in Figure 5.5-6). Subsequently, the jet involves a low viscous layer flowing on top of a high viscous layer, in which the interface acts as a turbulence promoter. In addition, because the jet is highly turbulent, it is expected that the Flibe layer free surface temperature can be reduced with the help of turbulent eddies/patches. Preliminary estimations of free surface temperatures of turbulent Flibe layer flow are based on Reynolds analogy for heat and mass transfer. Further analyses of Flibe surface temperatures are performed using κ - ϵ model.

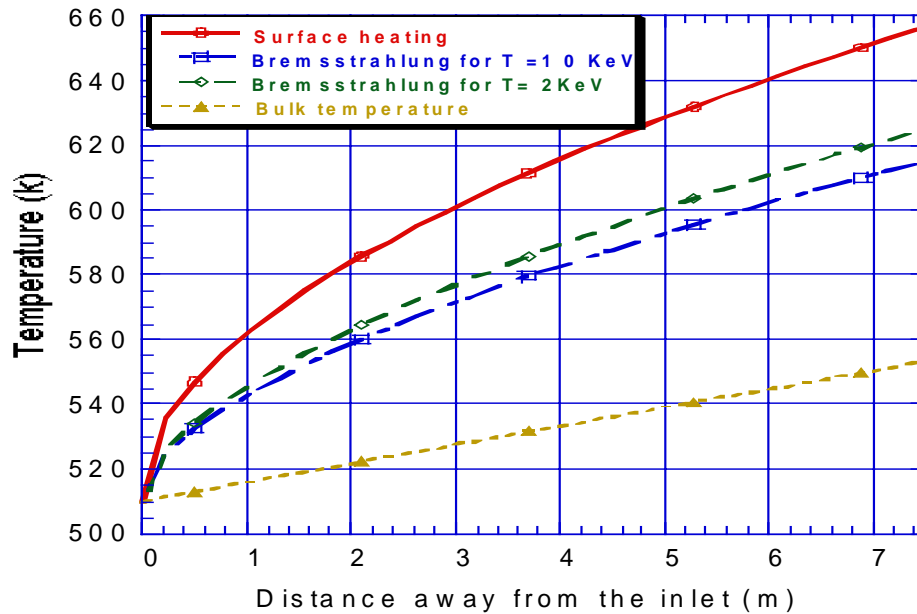


Figure 5.5-1 Lithium free surface and bulk temperature profiles as flow proceeds downstream. Notice that the surface temperature is reduced when x-ray penetration is taken into account.

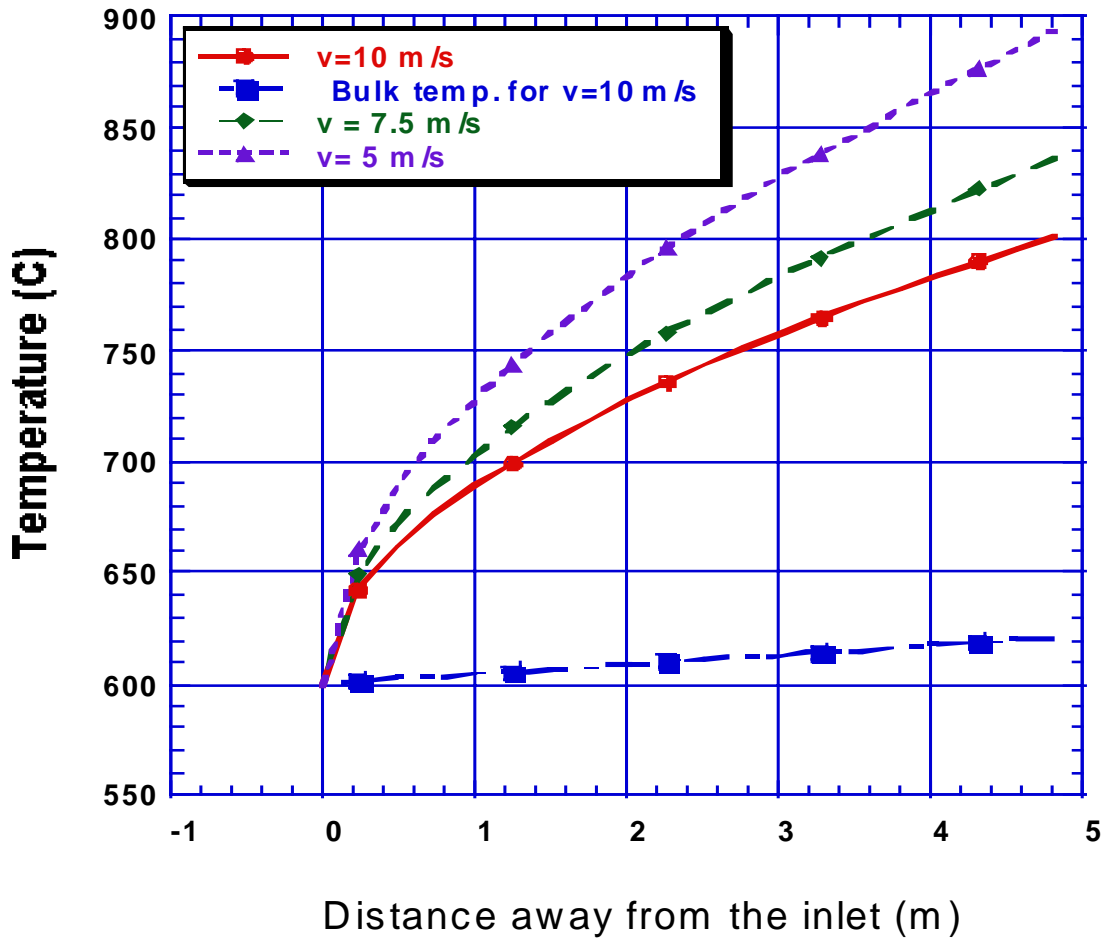


Figure 5.5-2

Sn-Li surface and bulk temperature profiles as flow proceeds downstream.

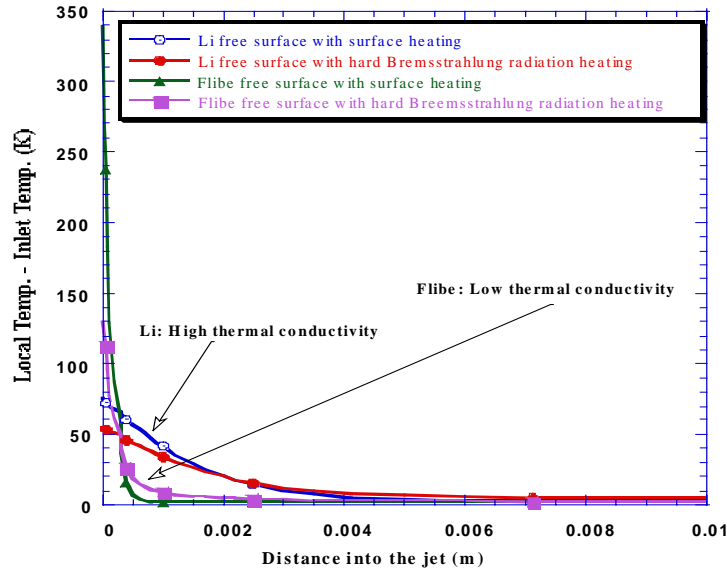


Figure 5.5-3

Temperature profiles into lithium and Flibe films at reactor mid-plane. The temperature gradient across the film is much steeper for Flibe than that for lithium.

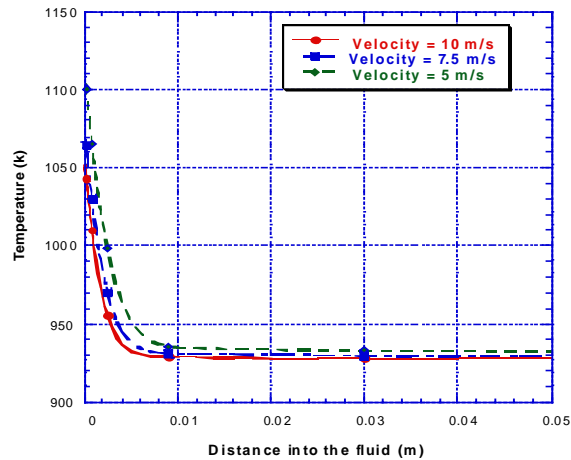


Figure 5.5-4

Temperature profile into the Sn-Li film (at about 2.5 m downstream) indicating all the surface heat is deposited within 1 cm of the film. In addition, the high thermal conductivity of Sn-Li helps conducting the heat into the bulk.

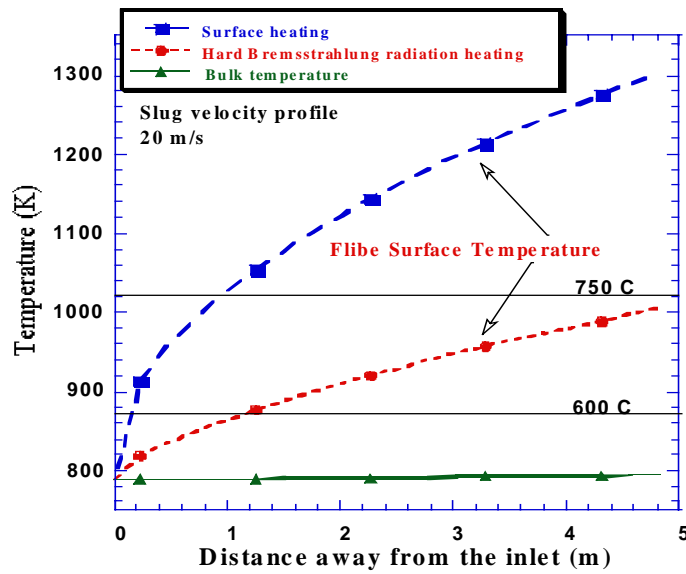


Figure 5.5-5

Flibe free surface and bulk temperature profiles as flow proceeds downstream for slug velocity profiles. Notice that the surface temperature is reduced significantly when Bremsstrahlung penetration is taken into account.

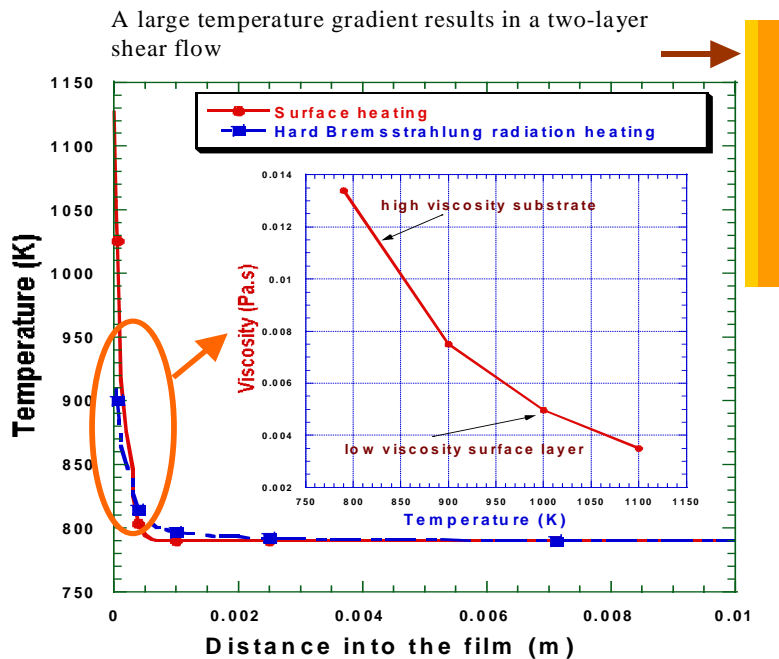


Figure 5.5-6

A large temperature difference between the surface and the bulk leads to a two-layer shear flow due to a significant drop of viscosity as the temperature of Flibe increases.

5.5.1-1 Flibe Surface Temperature Estimation Based on Reynolds Analogy for Mass and Heat Transfer

As described in 5.4.1.2, an idea of “GMD with pocket” thick liquid wall was introduced to ensure that the first wall surface temperature can be maintained within the maximum allowable value while achieving a high exit temperature for a high power conversion efficiency without using a continuous first wall structure. It is desired to know how much heat transfer and what temperature magnitude can be achieved on the Flibe surface, and at what operating velocity and flow thickness are needed for such a fast moving film. However, without understanding the detailed hydrodynamics structure of free surface flow and yet no experimental data available, the problem was addressed based on the Reynolds analogy for mass and heat transfer and numerical analyses. (To the authors’ knowledge, no experimental data are available that could be used for predicting liquid surface temperature taking into account the turbulence structure.) The analysis then provides a cross-benchmark for calculations based on κ - ϵ models discussed in the next section.

The analogy is based on the similarity in the form of the rate equations for heat and mass transfer through the corresponding dimensionless numbers: Nusselt number (Nu) for heat transfer and Sherwood number (Sh) for mass transfer. In analogy, the measured mass transfer coefficient is used to derive a corresponding heat transfer coefficient since all the other quantities are based on physical properties of the materials involved. The derived heat transfer coefficient provides the first initial data for design conceptualization purpose.

Much work has been done on the mass transfer into turbulent jet/films, in which the experimental mass transfer coefficient was correlated in terms of fluid properties and flow variables. The most sophisticated model incorporates hydrodynamics structures and the transport mechanisms and identifies that the transfer rate is conducted through the patches ejected from the wall [1]. As ejections reach the interface, they form renewed surface patches and then roll back towards the walls. Komori [2] also confirmed that the surface is renewed by large energy containing eddies which are responsible for heat and mass transfer across the free surface. Their simultaneous velocity and temperature measurements showed that the large eddies which re-new the free surface come back into the bulk. These findings provide the basis of the surface renewal type concepts and lead to a mass transfer coefficient expressed as:

$$k_L = (D/T)^{1/2} \quad (5.5-2)$$

where D is the mass transfer coefficient and T may be thought of as the mean time between surface renewals. The surface renewal time is further correlated, by studying the detailed turbulence characteristics near the interface, as a function of burst frequency, surface velocity, and patch residence time. A general equation for the average mass transfer coefficient at the shear-free non-wavy interfaces is expressed as [1]:

$$k_L = 0.0077(v_m v_w)^{1/2} Sc^{-1/2} \quad (5.5-3)$$

A case more directly applicable to the jet flow turbulent heat transfer configuration in which the wall shear does not exist, would be related to the eddy diffusivity modes proposed primarily by Levich [3] and later Davies [4]. They employed the basic Levich postulate that the dynamic thrust of an eddy at the free interface is balanced by the excess surface pressure associated with the deformation of the surface by the eddy. Accordingly, the mass transfer coefficient given by the rate of diffusion through the mathematically equivalent diffusion layer is expressed by:

$$k_l = D / \delta = 0.32D^{1/2}v_o^{1/2}\rho^{1/2}\sigma^{-1/2} \quad (5.5-4)$$

where δ is the free surface liquid layer deformation, v_o is the estimated characteristic eddy velocity, ρ is the liquid density and σ is the surface tension of the liquid. By assuming that the turbulence in the exit jet, follows exactly the turbulence within the pipe, one can apply the Blasius equation for the estimation of the characteristic eddy velocity, v_o . The resultant mass-transfer property for the liquid-phase, in terms of dimensionless groups is interpreted as:

$$Sh = 0.028(Sc)^{1/2}We(Re)^{5/16} \quad (5.5-5)$$

where Sc is the Schmidt dimensionless number and We is the Weber dimensionless number.

The calculated heat transfer coefficients based on mass-heat transfer analogy and the corresponding first wall and blanket thermal-hydraulics parameters are listed in Table 5.5-1. The analysis was meant to provide the information needed for the idea conceptualization, but not to quantify the degree of the accuracy of the approach. No doubt that the experimental data is needed to examine the accuracy of the approach. In the calculation, the outlet coolant temperature is purposely set at 650 °C to obtain a high thermal conversion efficiency. This then determines the inlet and free surface temperatures for the specified first wall thermal-hydraulics operating conditions. The desire of reducing the overall in-reactor mass inventory to achieve a high exit coolant temperature and a low surface temperature while maintaining a fairly uniform thickness can be realized in Case 2 as shown in Table 5.5-1, if indeed the heat transfer coefficient can be as high as predicated. The corresponding first wall jet thickness and velocity are 1 cm and 15 m/s, respectively.

Table 5.5-1 Flibe GMD with Pocket Design Case Studies (10 MW/m² neutron wall load, 2 MW/m² surface heat load) ARIES-RS reactor parameters/total fusion power = 5479.75 MW.

Parameters	Case 1	Case 2	Case 3	Case 4	Case 5
Layer thickness, cm	1	1	1	2	2
Inlet velocity, m/s	10	15	20	10	15
Outlet velocity, m/s	15.45	19.12	23.18	15.45	19.12
% thinning at outlet	30	18	10	30	18
Mass flow rate, kg/s	13104.2	19656.3	26208.4	26233.2	39349.8
Desired outlet T, °C	650	650	650	650	650
Layer T increase, °C	28.11	18.74	14.05	14.02	9.36
BK T increases, °C	140.56	93.7	70.28	70.21	46.81
Layer T inlet, °C	481.33	537.56	565.67	565.75	593.84
Reynolds No. (\bar{T})	13148	25042	36453	36453	68815
h^1 , W/m ² K	18926	28798.9	37550.6	18776	24468.8
h^2 , W/m ² K	32012.5	45960	74776	26435	43060
h^3 , W/m ² K	15589.2	23386.7	31164.0	15589.2	23386.7
$T_{surface}^2$ at outlet, °C	571	599.8	606.5	655.4	649.64
$T_{surface}^3$ at outlet, °C	637.4	641.82	643.89	707.8	688.74
Ha @ 12 T	12.22	13.776	14.4	28.788	32.29
Re/Ha	1075	1817	2532	1266	2130

(1) Dittus-Boelter heat transfer coefficient for channel turbulent fluid flow [5]

(2) And (3) Reynolds analogy heat transfer coefficient is calculated based on the mass transfer coefficients: (2) J. Davies for turbulent restrained jets. (3) M. Rashidi surface renewal theory.

5.5.2 Numerical and analytical calculations of turbulence and turbulent heat transfer

In this section two different approaches to the problem of turbulent heat transfer for MHD flows of low conductivity liquids are considered. The first one is a so-called two-layer model. In this model, two different layers, the bulk and the near-surface layer, are introduced. In the bulk, the turbulent transport is predominant, while in the near-surface layer the heat transfer mechanism is laminar due to suppression of turbulence by surface effects. This approach is relatively simple and allows a solution in the analytical form. In spite of its attractiveness, it is incomplete, since there are some parameters, which cannot be obtained within the model itself. Some rough approximations are used to close this model. The second one is the "k-epsilon" model of turbulence. This model is more sophisticated and gives information on the distribution of turbulent characteristics over the flow domain. Although this model is complete, it must be properly adjusted by using available experimental data. In what follows, these two heat transfer models are presented in details, and a preliminary heat transfer analysis is done based on simple estimations for closure parameters.

5.5.2.1 Two-layer model for free surface MHD turbulent flows and its application to heat transfer calculations

In this section, a simplified physical model for fully developed turbulent heat transfer in thin layer flows is suggested. On the basis of this model an analytical solution for the surface temperature is derived. Finally, some estimations for the temperature rise (the surface temperature minus the bulk temperature) are made with consideration for the effects of the magnetic field on the turbulent thermal conductivity.

We assume the following physical mechanism to be responsible for the turbulent transport in the layer and the heat transfer enhancement by turbulence. The turbulent eddies are generated within the shear layer at the backplate, and then they move away from the wall to the free surface, off of which, they are reflected. This upward and downward eddy motion leads to the intensive mixing, which causes a significant heat transfer enhancement. This mechanism can be described in terms of the increase of the effective coefficient of thermal conductivity, $\lambda_{\text{eff}} = \lambda + \lambda_t$. Here, λ_{eff} , λ , and λ_t are the effective, molecular, and turbulent thermal conductivity, respectively. The experimental data indicate that the presence of a free surface has a great impact on the distribution of fluctuating energy among the various components. The normal component is damped by the free surface, while the two others are enhanced due to continuity. This effect of turbulence redistribution by the free surface also implies that the length scale of the turbulence is reduced due to geometrical restrictions. Consequently, the dissipation rate at the free surface is increased. Therefore, there is a thin, near-surface layer where the normal component of the turbulent motion is absent. Since this component is responsible for the surface turbulent thermal transport, the laminar thermal conductivity is the only heat transfer mechanism at the free surface. This phenomenon resembles the thermal transport near a solid wall within a laminar sublayer, however its details are different.

Based on this consideration, the following scheme for turbulent heat transfer is suggested. There are two layers over the flow height. In the near-surface layer with the thickness δ , the turbulent convection in the normal direction is absent. The thermal transport is characterized by the effective thermal conductivity, λ_s , which coincides with the ordinary laminar coefficient of thermal conductivity. In the bulk layer, which is much thicker than that at the near-surface, turbulent processes mostly determine the thermal transport. Within this layer, the effective coefficient of thermal conductivity, λ_b can be defined as a sum of two components, $\lambda_b = \lambda + \lambda_t$, where λ and λ_t are the laminar and turbulent thermal conductivities, respectively. An important parameter in this scheme is the thickness of the near-surface layer. To our knowledge, there is no direct or indirect data on this parameter. It can be expected that the near-surface dissipation processes determine the thickness of this layer, and hence it can be expressed as a function of the surface mixing length, l_s , or using the characteristic scale of surface eddies. In accordance with the recommendations proposed by Naot et al. [8], [13], $l_s = 0.07h$ (here in this paragraph h is the layer thickness), but any data on the sizes of surface eddies are not available. More accurate information on the parameter δ could be provided from experiments on turbulent heat transfer and turbulent spectra near the free surface, or from DNS (Direct Numerical Simulation) computations.

Let us consider a fully developed, turbulent free surface flow with the thickness h , which is constant over the whole flow domain. For the sake of simplicity, the slug velocity profile is assumed, $U = U_0$. A uniform heat flux is applied to the free surface, while there is no heat flux applied to the backplate. The energy equation and the boundary conditions, which describe the problem, are the following:

$$\rho C_p U \frac{\partial T}{\partial x} = \frac{\partial}{\partial y} (\lambda_{\text{eff}}(y) \frac{\partial T}{\partial y}); \quad (5.5-6)$$

$$y=0 \text{ (wall): } \lambda \frac{\partial T}{\partial y} = 0; \quad y=h \text{ (free surface): } \lambda_{\text{eff}} \frac{\partial T}{\partial y} = q_s.$$

Here λ_{eff} is the effective coefficient of thermal conductivity, and it is equal to λ_s or λ_b depending on y . Directly from the equations (5.5-6) one can obtain that the bulk temperature, $T_b(x) = \frac{1}{h} \int_0^h T(x, y) dy$, is a linear function of the longitudinal coordinate:

$$T_b = T_0 + Kx, \quad \text{where } K = q_s / (U_0 \rho C_p h). \quad (5.5-7)$$

The solution of the problem (5.5-6) can be sought in the following form

$$T(x, y) = Kx + f(y). \quad (5.5-8)$$

After substitution of expression (5.5-8) into equations (5.5-6), the ordinary differential equation for the function f is obtained as follows

$$\rho C_p U_0 K = \frac{d}{dy} (\lambda_{\text{eff}} \frac{df}{dy}). \quad (5.5-9)$$

Finally, by solving equation (5.5-9) analytically and using equation (5.5-7) and the boundary conditions to the original problem, (5.5-6), the equation for the surface temperature, is derived as follows

$$\Delta T = T_s - T_b = \frac{q_s h}{\lambda} \int_0^1 d\eta \int_{\eta}^1 \frac{\eta d\eta}{\lambda_{\text{eff}} / \lambda}. \quad (5.5-10)$$

The internal integral on the right hand side of equation (5.5-10) can be written as a sum of two integrals

$$\int_{\eta}^1 \frac{\eta d\eta}{\lambda_{\text{eff}} / \lambda} = \int_{\eta}^{1-\delta/h} \frac{\eta d\eta}{1 + \lambda_t / \lambda} + \int_{1-\delta/h}^1 \eta d\eta. \quad (5.5-11)$$

After taking the internal integral, (5.5-11), along with the external integral in equation (5.5-10) and by neglecting terms with $(\delta/h)^2$ and keeping those with the (δ/h) , the solution for the temperature rise is found as follows

$$\Delta T = T_s - T_b = \frac{q_s h}{\lambda} \left[\frac{1}{3(1 + \lambda_t / \lambda)} + \frac{\delta}{h} \frac{\lambda_t / \lambda}{1 + \lambda_t / \lambda} \right]. \quad (5.5-12)$$

It can be seen from equation (5.5-12) that, for highly intensive turbulent flows with $\lambda_t \gg \lambda$, the temperature rise becomes proportional to the parameter δ :

$$(\Delta T)_{\delta} = \frac{q_s h}{\lambda} \frac{\delta}{h} = \frac{q_s \delta}{\lambda}. \quad (5.5-13)$$

On the other hand, if it is assumed that the near-surface layer is very thin, then only the turbulent processes in the core of the flow determine the surface temperature. In this case, the second term on the right hand side of the equation (5.5-12) is much less than the first one, and

$$(\Delta T)_c = \frac{q_s h}{\lambda} \frac{1}{3(1 + \lambda_t / \lambda)}. \quad (5.5-14)$$

Taking into account formulas (5.5-13) and (5.5-14), the formula (5.5-12) for the temperature rise in the layer can be written as

$$\Delta T = (\Delta T)_{\delta} + (\Delta T)_c. \quad (5.5-15)$$

The physical interpretation of the equation (5.5-15) is that the thermal resistance of the whole layer is a sum of the thermal resistance of both the near-wall layer and that of the core.

In order to calculate the temperature rise for both thick and thin wall flows using the formulas (5.5-13), (5.5-14), or (5.5-15), δ and λ_t , must be known. As there are no recommendations for choosing δ , in our analysis we use $\delta/h=1.0 \times 10^{-4}$. This magnitude is smaller than the surface mixing length and larger than the Kolmogorov's scale. This choice is not strengthened by any other physical arguments. As for the turbulent thermal conductivity, we calculate it using the Dittus-Boelter empirical formula for turbulent heat transfer in closed ducts:

$$Nu = 0.023 Re^{0.8} Pr^{0.4} . \tag{5.5-16}$$

The Nusselt number and the Reynolds number in the equation (5.5-16) are calculated by using the hydraulic diameter. In the case under consideration, the hydraulic diameter is $2h$, since the channel width is much greater than the layer thickness. The heat transfer coefficient, α , is found from the equation (5.5-16), and then the turbulent thermal conductivity coefficient is calculated using the following formula:

$$\lambda_t = \alpha h / 3. \tag{5.5-17}$$

This formula comes from the Newton law, $q_s = \alpha \Delta T$, and the equation (5.5-14) assuming $\lambda_t \gg \lambda$.

Two variants, thin and thick liquid wall flows, were analyzed for Flibe. The velocity is 10 m/s for the thin layer flow, and it is 15 m/s in the other variant. The flow thicknesses are 2 cm and 45 cm, respectively. The surface heat flux is 2 MW/m^2 , and the thermal conductivity is $1.06 \text{ W/(m}\times\text{K)}$. The results of calculations, for the case when the magnetic field is absent, are presented in Table 5.5-2.

Table 5.5-2 Temperature rise estimations for thick and thin liquid wall concepts (no magnetic field)

Concept	$\alpha, \text{W/(m}^2 \times \text{K)}$	$\lambda_t, \text{W/(m}\times\text{K)}$	$\Delta T, \text{K}$	$(\Delta T)_\delta, \text{K}$	$(\Delta T)_c, \text{K}$
thin wall	14100	94	144	4	140
thick wall	10485	1573	281	90	191

Simple calculations to estimate the temperature rise in the presence of the magnetic field were also done. The reduction of heat transfer due to turbulent suppression by the magnetic field has been illustrated experimentally by different authors only for closed channel flows [18]. Here, we use an empirical formula obtained by Blums, which generalizes his experimental data on heat transfer for rectangular duct MHD flows of a water solution of KOH (potassium hydroxide). In accordance with this formula, the heat transfer coefficient must be reduced by $(1-1.2Ha^2/Re)$ times. The dimensionless parameters, Ha and Re , are built through the hydraulic diameter. The results of our

calculations analogous to those in table 5.5-2 are presented in table 5.5-3. In these calculations, the magnetic field was 10 T. The Hartmann numbers were 40.6 and 913.5 for the thin wall and the thick wall, respectively.

Table 5.5-3 Temperature rise estimations for thick and thin liquid wall concepts (with magnetic field)

Concept	$\alpha, W/(m^2 \times K)$	$\lambda_t, W/(m \times K)$	$\Delta T, K$	$(\Delta T)_\delta, K$	$(\Delta T)_c, K$
thin wall	13570	90.5	149.5	4	145.5
thick wall	4586	688	526.7	90	436.7

From the comparison of data in these two tables, it can be seen that the heat transfer degradation due to the magnetic field is small in the thin liquid wall flow, while it is significant, about two times, in the thick wall. It should be mentioned that these calculations were made using very rough approximations for closure parameters and they should be considered as preliminary estimations.

In closing this section, some more points need to be made. In accordance with our considerations, there are two very important parameters, which stand for the turbulent heat transfer in the layer. They are the effective thermal conductivity in the bulk and the thickness of the near-surface layer. Unfortunately, these parameters are not defined clearly up until now for free surface flows, and hence there is a large uncertainty in the model. In the analysis, very rough values of these parameters were used. In order to get more accurate data, an additional analysis is needed. This analysis is beyond the scope of the heat transfer model we have suggested here, and it is much more complicated. Some results for the bulk thermal conductivity are presented in Section 5.5.2.2 coming from the "k-epsilon" model of turbulence computations.

The parameter δ stands for the physics of near-surface turbulence redistribution. Its incorporation into the model is explained by the fact that the normal velocity fluctuations near the surface are damped. However, it is not inconceivable that intensive surface turbulent mixing does occur. For example, large surface eddies can deform the surface. In doing so, some wave-type motion can mix the liquid on the surface. Some surface instabilities can also be an additional cause of surface mixing. Although the analogy is not complete, we would like to refer to the sea waves propagation, which is accompanied by intensive mixing directly in the near-surface layer. So, the experimental studies are needed to clarify if and to what extent turbulent mixing takes place on the surface. In our calculations we used the Dittus-Boelter equation to find the thermal conductivity of the bulk layer. It is apparent that the applicability of this formula to the free surface flow yields very rough results. In reality, thermal conductivity in free surface flows must be much larger. We also assumed that the thermal conductivity is constant over the bulk. This assumption is not quite true, since it is distributed non-uniformly. As computations

based on the "k-epsilon" model show (see Section 5.5.2.2), this distribution is of a parabolic type with the maximum near the centerline.

5.5.2.2 Numerical calculations of turbulence and turbulent heat transfer based on the "k-epsilon" model of turbulence

The low-Reynolds number "k-epsilon" model of turbulence [6] was applied to the thin layer flow of low conducting liquids in order to study the effect of turbulence on the surface temperature. In comparison to the ordinary "k-epsilon" model, the present one was extended to the MHD case by means of additional terms in closure equations [7]. These terms stand for the Joule dissipation by the induced currents. Two variants of boundary conditions on the free surface were used, the Naot's boundary condition [8], and the zero surface turbulence boundary condition. The first one expresses the turbulence redistribution by the free surface. The second one simulates the effect of the near-surface layer, where the normal component of the turbulent motion is absent. It has been shown that the surface temperature can be significantly reduced due to suppression of turbulence by a magnetic field.

The k- ϵ model belongs to the class of Reynolds-averaged flow equations. At present, this model is the most widely used two-equation model [9]. It has been applied to many flows with varying degrees of success. It has been shown that being properly adjusted, this model provides good agreement with the experimental data and hence, it can be used for predictions of different turbulent flows. While the model can be fine tuned for a given application, it is not clear that it is suitable in different situations. For example, it is inaccurate for some important flow classes, such as adverse pressure gradient flows. The model is also difficult to integrate through the viscous sublayer. Unfortunately, no consensus has been achieved on the optimum form of the viscous corrections to simply reproduce the law of the wall for an incompressible flat-plate boundary layer. The MHD interaction is an additional complication, and there is a shortage of information on the extension of this model to the MHD case. Also, there is no any reliable evidence of the applicability of this model to the free surface flows along the concave surfaces. In this connection, the application of the k- ϵ model to the thin/thick liquid wall flows is still questionable, and further studies, mostly validating the model by comparison the results obtained on its basis over those found experimentally or with DNS (Direct Numerical simulation) or LES (Large Eddy simulation) simulations are necessary.

In this study we used low-Reynolds number "k-epsilon" model of turbulence, since it gives some advantages over the standard k- ϵ model, which uses wall functions in the wall boundary conditions in order to incorporate wall law into the model. Namely, the low-Reynolds number model allows ordinary boundary conditions for the velocity components and zero conditions for the turbulent kinetic energy and the dissipation rate directly on the wall. Both modifications of the "k-epsilon" model are based on the classical log law of the wall. It is apparent that the log law breaks down for a case of a strong MHD interaction, and hence the "k-epsilon" model in the vicinity of the solid wall should be modified if the magnetic field is strong enough. Nevertheless, we assumed that the liquid fluid is low conducting, and, we used the classical log variant for the law of the

wall without any modifications. In order to include into the model the mechanism of turbulence suppression by the magnetic field, we applied the MHD extension to the "k-epsilon" model developed in [7] by K.Kitamura and M.Hirata. A similar approach was applied by M.Takahashi et al. to the closed channel MHD flows [10] and by A. Inoue et al. to the air-mercury two-phase stratified flow under a vertical magnetic field [11].

In the present study, to describe mathematically MHD turbulent flows, the flow equations were used together with the low-Reynolds number "k-epsilon" closure equations [6] for the turbulent kinetic energy, k, and the dissipation rate of the turbulent kinetic energy, ε, in the following form

$$\frac{\partial k}{\partial t} + U \frac{\partial k}{\partial x} + V \frac{\partial k}{\partial y} = \frac{1}{Re} \frac{\partial}{\partial y} \left[\left(1 + \frac{v_t}{\sigma_k}\right) \frac{\partial k}{\partial y} \right] + \frac{1}{Re} v_t \left(\frac{\partial U}{\partial y}\right)^2 - \frac{\epsilon}{Re} - \frac{2}{Re} \left(\frac{\partial \sqrt{k}}{\partial y}\right)^2 - \tag{5.5-17}$$

$$- C_3 \beta^2 N k;$$

$$\frac{\partial \epsilon}{\partial t} + U \frac{\partial \epsilon}{\partial x} + V \frac{\partial \epsilon}{\partial y} = \frac{1}{Re} \frac{\partial}{\partial y} \left[\left(1 + \frac{v_t}{\sigma_\epsilon}\right) \frac{\partial \epsilon}{\partial y} \right] + \frac{f_1}{Re} C_1 v_t \frac{\epsilon}{k} \left(\frac{\partial U}{\partial y}\right)^2 - \frac{f_2}{Re} C_2 \frac{\epsilon^2}{k} + \tag{5.5-18}$$

$$+ \frac{2}{Re} v_t \left(\frac{\partial^2 U}{\partial y^2}\right)^2 - C_4 \beta^2 N \epsilon;$$

$$v_t = C_D f_D Re^2 \frac{k^2}{\epsilon} . \tag{5.5-19}$$

There are additional terms on the right hand side of equations (5.5-17) and (5.5-18), containing the interaction parameter $N=Ha^2/Re$, which express the dissipation effect due to the transverse magnetic field [7]. The model constants used are standard [6]. They are shown in Table 5.5-4. The functions "f" were chosen in accordance with [6] as follows

at the wall: $f_1=1$; $f_2=1.0-0.3\exp(-R_t^2)$; $f_D=\exp[-2.5/(1+0.02R_t)]$; $R_t=Re^2 k^2/\epsilon$;

and at the free surface: $f_1=1.0$; $f_2=1.0$; $f_D=1.0$.

These functions are different at the solid wall and at the free surface, since there is no viscous sublayer at the free surface.

Table 5.5-4 Constants in the "k-ε" model

C_1	C_2	C_3	C_4	C_D	σ_k	σ_ϵ	σ_t
1.55	2.00	2/3	1.00	0.09	1.00	1.30	1.00

The constants C_3 and C_4 were chosen in accordance with [10]. The equations (5.5-17) and (5.5-19) are written in the dimensionless form using the following scales for k , ε and ν_t : $[k]=U_0^2$, $[\varepsilon]=\nu(U_0/h_0)^2$, and $[\nu_t]=\nu$ respectively. The turbulent viscosity, ν_t , in the low-Reynolds number "k-epsilon" model is defined by means of the Kolmogorov-Prandtl equation (5.5-19).

The no-slip condition for the velocity together with zero condition for k and ε were used on the solid wall. As for the boundary conditions at the free surface, two variants were considered. In the first variant, Naot's boundary conditions [5.5-8] were used as follows:

$$\frac{\partial k}{\partial y} = 0, \quad \varepsilon = \frac{C_D^{3/2} \text{Re} k^{3/2}}{\kappa 0.07h} \quad (5.5-20)$$

The first of the conditions (5.5-20) is the symmetry condition, while the second one stands for the experimentally established fact that the dissipation length scale at the free surface is equal to the distance from a virtual origin located at a distance of $0.07h$ above the real open surface [8]. In the second variant, the turbulent kinetic energy is zero, but the symmetry boundary condition is used for the dissipation rate

$$k = 0, \quad \frac{\partial \varepsilon}{\partial y} = 0 \quad (5.5-21)$$

As calculations show, these two variants of the boundary conditions give approximately the same results for the hydrodynamic quantities, the layer thickness and the velocity profiles. This is because the processes in the shear, not in the surface-layer, determine the changes in the flow thickness and in the velocity field. Nevertheless, the boundary conditions (5.5-20) and (5.5-21) lead to different results in the surface temperature. The boundary condition (5.5-21) corresponds to the two-layer model for heat transfer described in the previous section as it implies zero turbulent thermal conductivity directly on the free surface and smaller values in the near-surface layer. The boundary conditions (5.5-20) allow surface turbulent kinetic energy, and consequently larger thermal conductivity in the near-surface region. So, the surface temperature calculated with formulas (5.5-21) must be higher than that using the boundary conditions (5.5-20). Although the conditions (5.5-21) are not quite correct from the viewpoint of the flow dynamics, we find them better in the sense of heat transfer, as they are a good simulation of the two-layer model for the turbulent heat transfer described in the previous section.

The flow equations together with (5.5-17)-(5.5-19) and boundary conditions (5.5-20) or (5.5-21) comprise the mathematical model for the turbulent flows of thin or thick liquid layers. To calculate temperature field, an energy equation is used as follows

$$\frac{\partial T}{\partial t} + U \frac{\partial T}{\partial x} + V \frac{\partial T}{\partial y} = \frac{1}{\text{Pe}} \frac{\partial}{\partial y} \left[\left(1 + \frac{\nu_t}{\sigma_T} \text{Pr} \right) \frac{\partial T}{\partial y} \right] + q'' \quad (5.5-22)$$

where $Pe=RePr$ is the Peclet number, q''' is the volumetric heating.

The boundary conditions to the equation (5.5-22) specify the constant heat flux at the free surface and the isolated backplate. The symbol σ_T stands for the turbulent Prandtl number. In our calculations, $\sigma_T=1$.

A numerical code based on the finite-difference procedure was developed. This code includes a simultaneous solution of flow equations along with (5.5-17)-(5.5-19) with calculating the layer thickness from the free surface kinematic condition. The steady-state solution was sought by iterating the equations in time. The distributions for k and ϵ in the initial cross-section (initial conditions) were chosen as a result of preliminary, rough computations with arbitrary initial conditions. Although the code is absolutely stable, the new code covering the whole turbulent problem becomes conditionally stable. The cause of instability is explained in [5.5-9] by the fact that the condition of a diagonally dominant system is not satisfied when the production of turbulence exceeds the dissipation. This is especially important within the initial computational stage when the turbulent boundary layer develops at the backplate. Due to the limitations on the time increment, the calculations are very time consuming. Typically, one variant of computations takes no less than 6-8 hours. Putting some additional terms in the finite-difference approximations can significantly decrease the computation time. These new terms add artificial turbulence dissipation in the finite-difference scheme when iterating the problem. As soon as the steady-state is achieved, they become negligible. At present, this procedure is being realized. Another numerical complication is the steep gradient of calculated quantities near the backplate. It requires very fine meshes near the backplate. To remedy this situation, we used a non-uniform mesh with the concentration of nodes near the wall and the free surface. An adjustable mesh generator was used to provide proper resolution in the gradient sub-regions [5.5-12].

Some preliminary benchmarks were made to validate the code. First of all, it was tested against the analytical solution for the fully developed flow between parallel plates. Both the velocity profile and the Nusselt number are in good agreement with the analytical results. To validate the code in the turbulent regime for the free surface flows, the mixing length calculated by it was compared with that from numerical calculations carried out by Naot et al on the basis of similar "k-epsilon" model [5.5-13]. The results of our calculations are shown in Figure 5.5-7, and the Naot's results are plotted in Figure 5.5-8 (dotted line in the lower plot). It can be seen that these two curves are almost identical. This proves the code correctness. Nevertheless, this comparison is not enough to draw a conclusion about the "k-epsilon" model applicability to the free surface flows along concave walls especially in the presence of a magnetic field. Unfortunately, we have not found any reliable data to validate the model. At present, some benchmarks are being planned to test our results against numerical data from DNS computations.

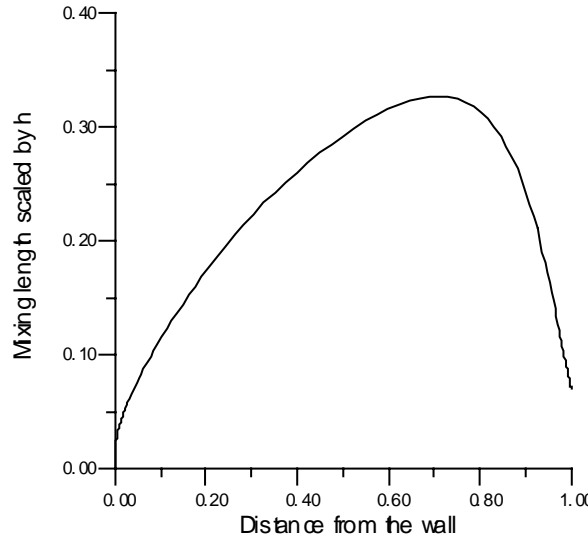


Figure 5.5-7 Mixing length calculated with the present code.

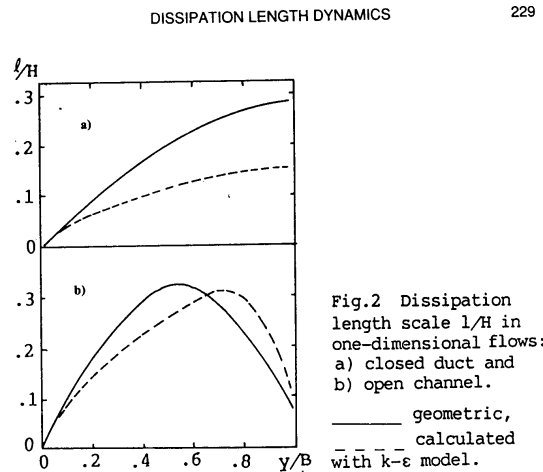


Figure 5.5-8 Mixing length calculated by [13]

The computations were carried out with thin layers ~2 cm of Flibe. The results are shown in Figures 5.5-9,10,11 for the case of zero magnetic field. Due to turbulent viscous friction, the layer thickness increases rapidly over the initial flow section (Figure 5.5-9). The turbulent characteristics in different cross sections calculated with Naot's boundary conditions are shown in Figure 5.5-10. The eddy viscosity is distributed non-uniformly over the layer thickness (Figure 5.5-10) with a maximum close to the centerline. In contrast to the closed channel turbulent flows, all turbulent quantities, the turbulent viscosity, the kinetic energy, and the dissipation rate at the upper boundary are not zero

(Figure 5.5-10). As expected, the turbulent kinetic energy and the dissipation have a maximum at the solid wall. A local maximum in the dissipation rate can be seen on the free surface.

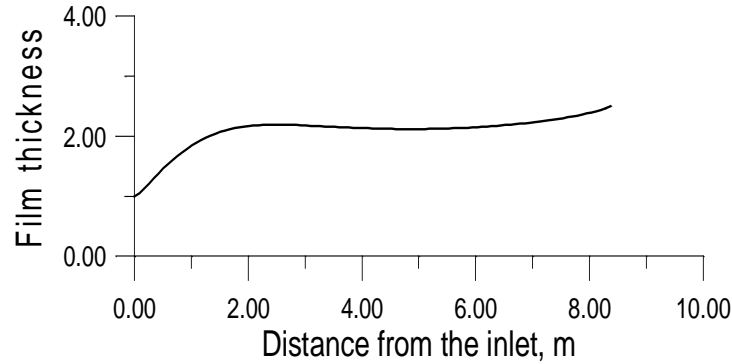


Figure 5.5-9 Turbulent layer thickness calculated from the "k-epsilon" model.

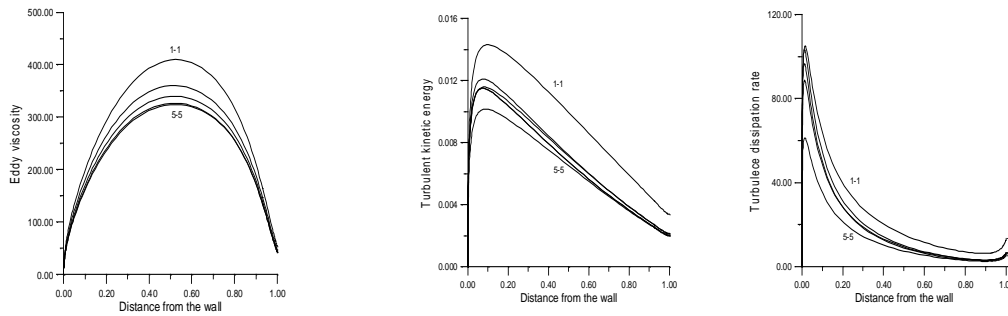


Figure 5.5-10 Distributions of turbulent characteristics in different cross-sections
 $X_{1-1}=1.67$ m; $X_{2-2}=3.35$ m; $X_{3-3}=5.03$ m; $X_{4-4}=6.70$ m; $X_{5-5}=8.37$ m

The surface temperature rise (the surface temperature minus the initial temperature) is shown in Figure 5.5-11. The curve 4 in this figure was calculated using zero surface turbulence boundary conditions. As it was mentioned, this variant of boundary conditions is an attempt to simulate a two-layer heat transfer scheme. In accordance with this curve, the temperature maximum is about 160 K. It corresponds to the value calculated with the two-layer model in the previous section. The curve 2 was calculated using Naot's boundary condition. It goes much lower than the curve 4, since in the variant with the Naot's boundary conditions the near-surface layer is not taken into account. The maximum in this curve also corresponds to that from the calculations using the two-layer model.

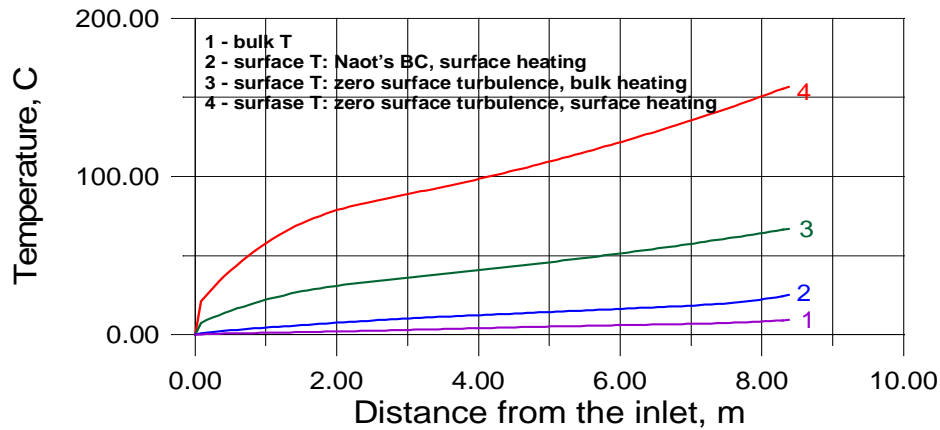


Figure 5.5-11 Temperature rise vs. distance from the inlet cross-section in the turbulent regime

The curve 3 was calculated for zero surface turbulence boundary conditions, but volumetric (Bremsstrahlung) heating [21] was included into the model. This curve goes between the other two. In order to illustrate the effect of turbulence on the surface temperature reduction, the results of calculations for a laminar flow are also presented (Figure 5.5-12). It can be seen that the reduction is significant.

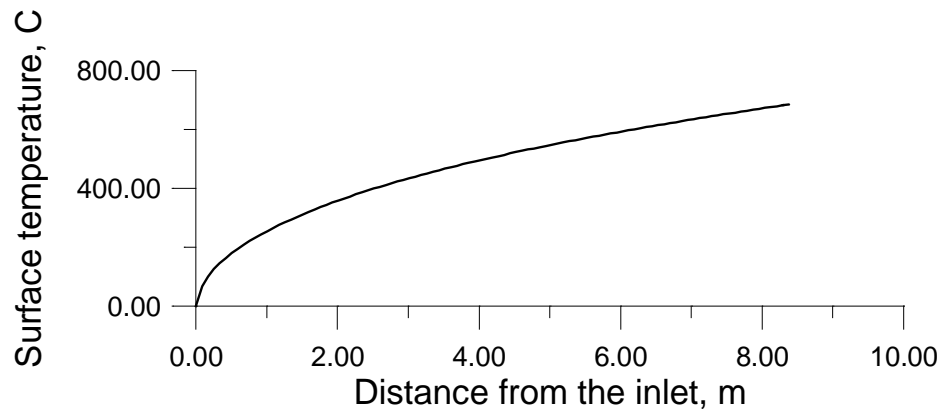


Figure 5.5-12 Temperature rise vs. distance from the inlet cross-section in a laminar regime

The effect of the magnetic field on the flow and the turbulent heat transfer (also for a thin liquid layer ~2 cm thick) is illustrated in Figures 5.5-13,14. The Hartmann number was varied from zero to 3000. As it was discussed earlier, the parameter that stands for the turbulence suppression and heat transfer reduction for low conducting liquids is the interaction number multiplied by β^2 ($N_\beta = \beta^2 Ha^2 / Re$). For example, the heat transfer degradation is 12% if $N_\beta = 0.1$. In our case, N_β is 0.02. That confirms our conclusion about small MHD effect for Flibe. For comparison, $N_\beta = 0.06$ for $Ha = 1000$, and $N_\beta = 0.24$ for $Ha = 2000$. A pronounced MHD effect is also seen from the results of calculations for the turbulent kinetic energy and the turbulent viscosity (Figure 5.5-13). Nevertheless, even though the Hartmann number is 3000, the turbulent viscosity is still large enough, and complete suppression of the turbulent effects does not occur.

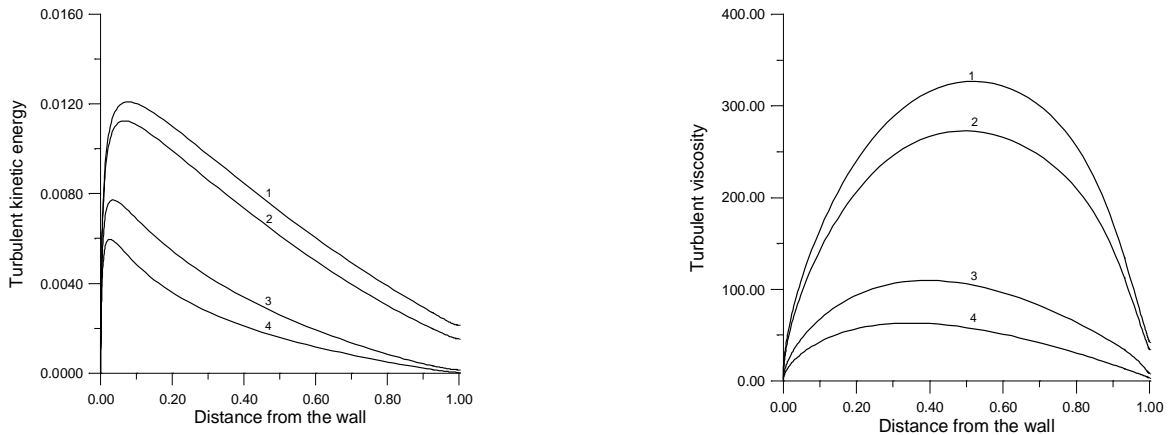


Figure 5.5-13 **Suppression of turbulence by magnetic field: 1 - $Ha=0$; 2 - $Ha=560$; 3 - $Ha=2000$; 4 - $Ha=3000$**

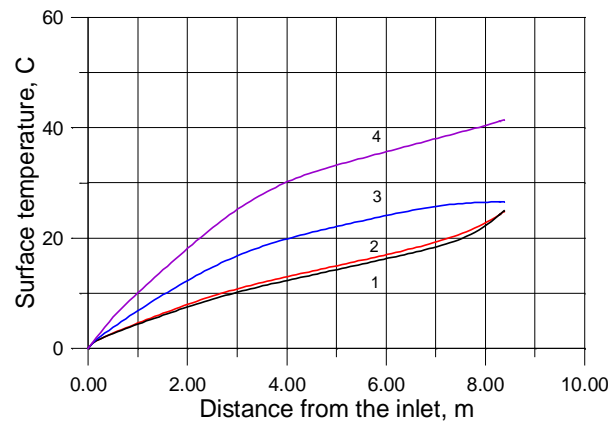


Figure 5.5-14 **The effect of heat transfer degradation due to magnetic field. 1 - $Ha=0$; 2 - $Ha=560$; 3 - $Ha=2000$; 4 - $Ha=3000$**

All curves in Fig.5.5-14 were computed with Naot's boundary conditions for surface heating that correspond to the lower level in our estimations of the temperature rise. The curves 1 ($Ha=0$) and 2 ($Ha=560$) are very close. It confirms again that the influence of the magnetic field on heat transfer for the Flibe thin liquid wall flows is negligible. At the same time, the curves 3 and 4 show much higher temperature rise that is a consequence of the turbulence reduction.

As a final result, we would like to give a range of the maximum temperature rise, which comes from our calculations. In accordance with the "k-epsilon" computations, this range is 30-160 K (depending on which boundary conditions are used). Taking into account the effect of penetration (Bremsstrahlung heating), it is 30-70 K.

We have not put here any results of "k-epsilon" calculations for thick liquid wall flows, since the modification of the code is being done now to reduce the computation time needed and to add some new features to the code.

5.5.2.3 Final conclusions on turbulent heat transfer for low conducting liquids in the presence of the magnetic field

The estimations of the surface temperature rise can be done using two different approaches that we have developed. The first one is based on the two-layer model, which implies an existence of the near-surface layer where the normal component of the eddy motion is suppressed, and the bulk, which has intensive turbulent mixing. There are two uncertain parameters in this model that complicate its applicability: the turbulent thermal conductivity in the bulk and the thickness of the near-surface layer. In our calculations we used rough values of these parameters. The bulk thermal conductivity was estimated using the Dittus-Boelter equation for closed duct flows. The thickness of the near-surface layer was chosen within the range from the Kolmogorov's scale to the mixing length at the surface. The second one is the "k-epsilon" model of turbulence. This model is a more sophisticated tool. It allows calculations of the turbulent viscosity distributions over the flow domain, but still does not give detailed information on the near surface phenomena. In both cases, we need more accurate information on turbulent characteristics near the surface to improve the quality of the models. This information can be obtained either experimentally or by means of DNS or LES computations.

By using these two approaches, we have analyzed the influence of the magnetic field on the Flibe flow hydrodynamics and heat transfer. We found that this influence differs depending on flow parameters. For the thin liquid wall flows, the impact of the magnetic field on both the flow hydrodynamics and heat transfer is negligibly small. On the other hand, it is significant for the thick liquid wall flows where the heat transfer degradation, which is due to the turbulence suppression by the magnetic field, can reach up to 60%.

The thick liquid wall concept casts more doubt on the surface temperature reduction due to turbulence. That is because of two possible reasons. First, there is pronounced heat transfer degradation due to MHD effects. Second, the turbulent eddies, generated in the

shear layer at the backplate, can disappear when moving from the backplate to the free surface due to viscous and Joule dissipation processes. As a result, there could not be the turbulent transport at the free surface or this transport could be sufficiently reduced.

If the turbulence turns out to bring cooler interior liquid to the surface too slowly, or the turbulent eddies do not reach the surface due to viscous and MHD dissipation, then it would be possible to bring a separate stream of cooler liquid straight from the heat exchanger to the front surface and expect this liquid not to mix very much. Then the surface temperature would rise more since it is not mixing the surface heat into the interior, but it would start out at a lower temperature (500 °C for example). Hopefully, this latter case is not the one that occurs, and we base our prediction on mixing, but we strongly encourage experimentation to resolve this issue.

The "k-epsilon" model is a very effective engineering tool for calculating turbulent effects in different applications. Unfortunately, there is still a lot of uncertainty. We can not be confident that this model is applicable to MHD turbulent free surface flows until reliable experimental or DNS based data are obtained. To our knowledge, there is not any information on the flows that we are analyzing now. Here we would like to mention some issues, which are very important in free surface turbulent modeling. First, the accurate measurements of near-surface distributions for temperature and velocity fluctuations along with turbulent spectra are necessary to have accurate boundary conditions on the free surface. Second, all "k-epsilon" models imply the log law of the wall in the vicinity of solid boundaries. This law is not correct if the magnetic field is strong enough. Hence, accurate data on the mean velocity distributions near the wall depending on the Hartmann and Reynolds numbers are also necessary. Third, the turbulent closures with MHD effects are based on limited experimental information. Further experimental studies are necessary to quantify the MHD effects on turbulence, depending on the orientation of the magnetic field, the distance between the walls, and other parameters. Finally, we would like to emphasize the role of initial conditions, since it is another source of turbulence. The turbulent distribution of the flow parameters in the initial cross-section is also a subject for further experimental studies.

5.5.3 Evaporation Estimation for FRC, Spheromak and ST and Core Plasma Contamination Discussion

Introduction

We hope treating the three configurations (FRC, Spheromak and ST) will be instructive for other configurations and this may limit the number of cases we can treat. The FRC is a limiting case of no toroidal field and the edge plasma is guided a long way away (tens of meters) from the core plasma before striking a wall (the divertor). The ST has a large toroidal field (conventional tokamaks have even larger toroidal fields, reversed field pinches, and flow pinches have weaker toroidal fields). The edge plasma is not guided far away from the core plasma but rather is usually "dumped" into the wall (divertor) near the core plasma. This will give the greatest challenge to liquid walls because the power density on the divertor is usually an order of magnitude higher than

that on the wall due to radiation. The Spheromak has a weak toroidal field and represents a case in between the prior two. As will be discussed later, the high power flux on the divertor results in extra vigorous evaporation, necessitating one of two strategies: 1) use a solid more conventional divertor or 2) use a high speed jet or droplet divertor as discussed in the literature [18-20].

5.5.3.1 The geometrical configuration

FRC-The configuration would likely be oriented horizontally but is shown in Fig. 5.5-16, vertically. We break the wall into zones with zone numbers given in the Figures 5.5-16 to 5.5-19. Assume for simplicity the power is uniform over the cylindrical liquid wall from 4 m to -4 m at a radius of 1.5 m and for a plasma radius of ~1-m.

$$\begin{aligned} A_{\text{wall}} &\cong 2\pi \times 1.5 \times 8 = 75.4 \text{ m}^2 \\ V_{\text{plasma}} &\cong 4\pi \times a^2 \times b / 3 = 4\pi \times 1^2 \times 4 / 3 \cong 16.8 \text{ m}^3 \\ S &= \text{liquid flow path receiving power} \cong 8 \text{ m} \\ L &= \text{edge plasma length} \end{aligned}$$

The transit time of the liquid is $S/V_{\text{axial}} = 8/10 = 0.8 \text{ s}$

Liquid flow cross sectional area = $\pi(2^2 - 1.5^2) = 5.5 \text{ m}^2$

For a nominal 10 m/s axial flow of liquid

$$\begin{aligned} \dot{V} &= 5.5 \times 10 = 55 \text{ m}^3/\text{s} \\ \dot{m} &= 2000 \times 55 = 1.1 \times 10^5 \text{ kg/s} \end{aligned}$$

If we take a nominal 10 m/s azimuthal flow then the power in the flowing liquid which is a reasonable measure of the pumping power is as follows:

$$\text{Power} = 0.5 \dot{m} v^2 = 0.5 \times 1.1 \times 10^5 \times (10^2 + 10^2) = 1.1 \times 10^7 \text{ W} = 11 \text{ MW}$$

Again we want to emphasize this configuration is simplified for the sake of analysis but is hopefully representative of the phenomena involved. An alternative flow path is shown in Figure 5.5-16b with the advantages of two shorter liquid flow paths and possibly a better solution to the exit nozzle.

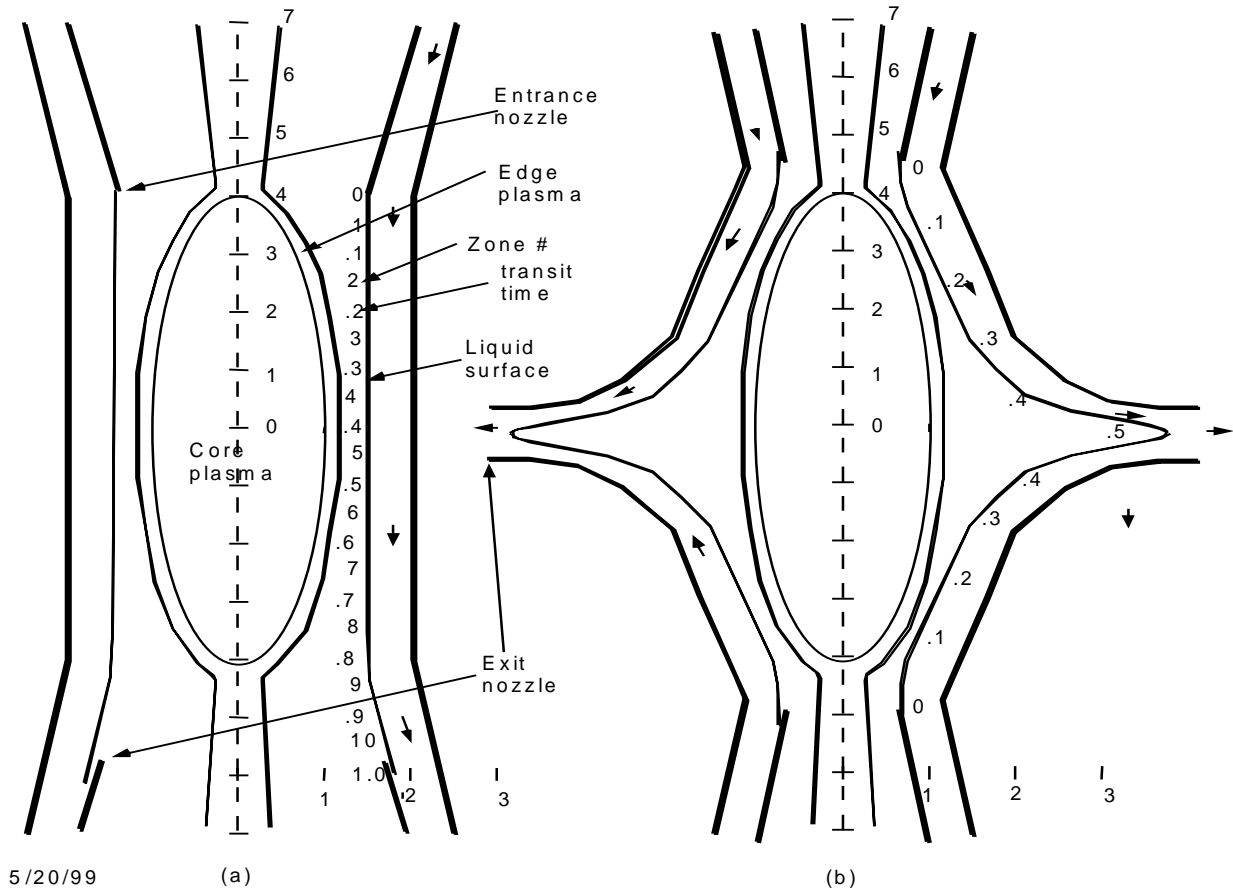


Figure 5.5-16 The FRC liquid flow model is shown. In (a) the flow path is in on one end and out on the other about 8 m in length. In (b) the flow is inward from each end and out in the middle. The flow paths are almost half the length. The temperature rise will be less for each path separately. Also the exit nozzle design may be more practical.

Spheromak- The configuration is shown in Figure 5.5-17. We break the wall into zones with zone numbers given.

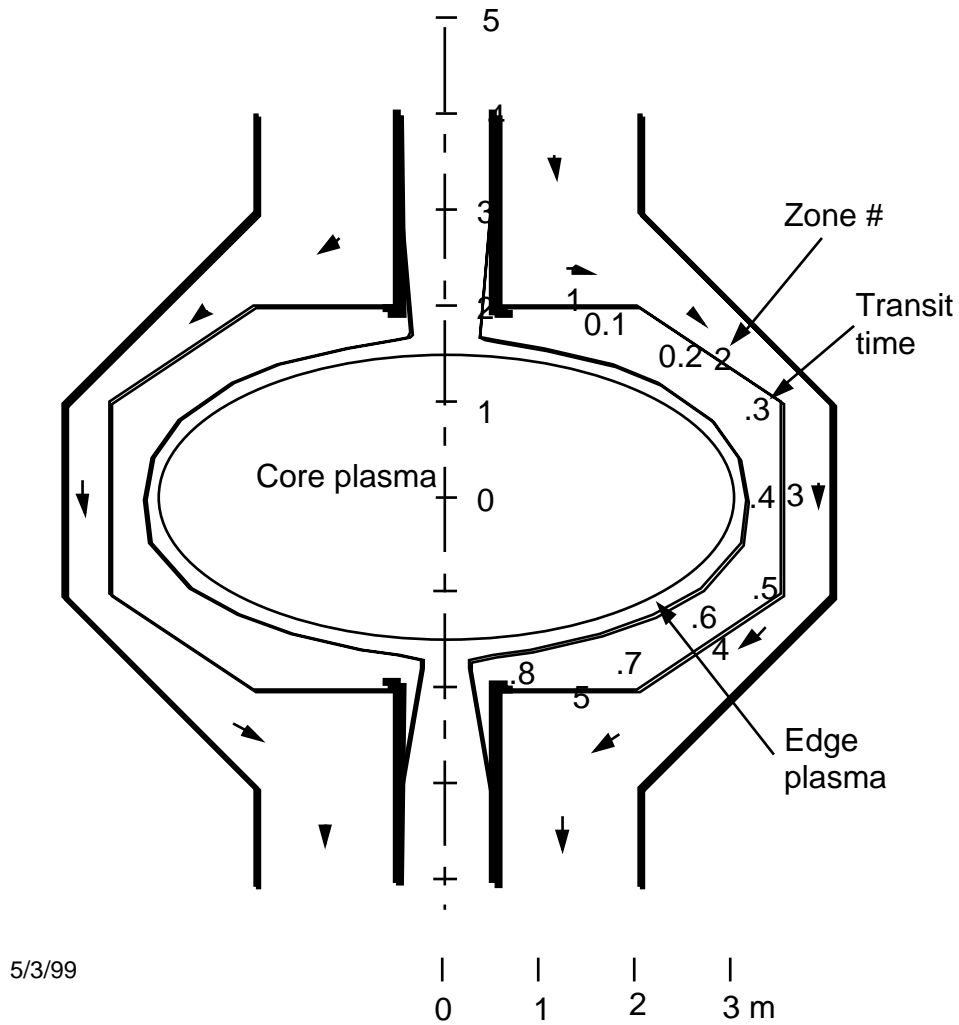


Figure 5.5-17 The Spheromak model is shown.

Zone	1	2	3	4	5
A_{wall}	$\pi (2^2 - 0.6^2)$	$2\pi \times 2.7 \times 1.8$	$2\pi \times 3.7 \times 2$	$2\pi \times 2.7 \times 1.8$	$\pi (2^2 - 0.6^2)$
A_{wall}	11.43 m ²	30.536 m ²	46.496 m ²	30.536 m ²	11.43 m ²
A_{wall}	130.44 m ²				
A_{plasma}	$4\pi \times 2 \times 3 = 75.4$ m ²				

$$V_{plasma} = 4\pi \times 3^2 \times 2/3 = 75.39 \text{ m}^3$$

S = liquid flow path receiving power = 8.3 m

L = edge plasma length = S = 8 m

The transit time of the liquid for a nominal 10 m/s axial flow speed is $S/V_{axial} = 8.3/10 = 0.83$ s.

The liquid flow cross sectional area = $2\pi \times 3.8 \times 0.5 = 11.94$ m²

For a nominal 10 m/s axial flow of liquid

$$\dot{V} = 11.94 \times 10 = 119.4 \text{ m}^3/\text{s}$$

$$\dot{m} = 2000 \times 119.4 = 2.388 \times 10^5 \text{ kg/s}$$

If we take a nominal 10 m/s azimuthal (toroidal direction) flow in addition to the axial flow (poloidal) then the power in the flowing liquid which is a reasonable measure of the pumping power is as follows:

$$\text{Power } 0.5 \dot{m} v^2 = 0.5 \times 2.388 \times 10^5 \times (10^2 + 10^2) = 2.388 \times 10^7 \text{ W} = 23.88 \text{ MW}$$

As in the case of the FRC, we can have an alternative configuration with liquid feed from both ends as shown in Fig. 5.5-18.

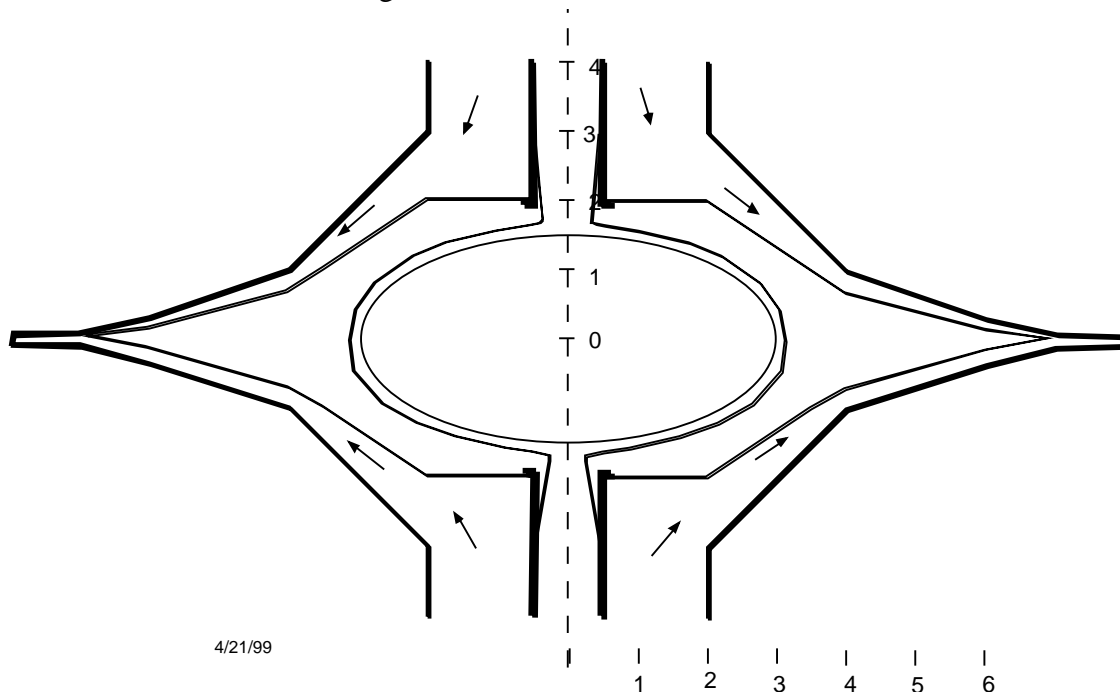


Figure 5.5-18 The alternative Spheromak configurational model with liquid feed from both ends, thus having shorter flow paths and possibly better exit nozzle design is shown.

The alternative design may have a problem due to the need for a coil on the mid-plane and need for a conducting wall there as well.

ST-The ST stands for Spherical Tokamak (Torus). The ST model we are adopting for purposes of analysis is shown in Fig. 5.5-19. Again we break the wall into zones with zone numbers shown in the figure. It is hoped this geometry will serve to illustrate a more general class of tokamak than just the ST.

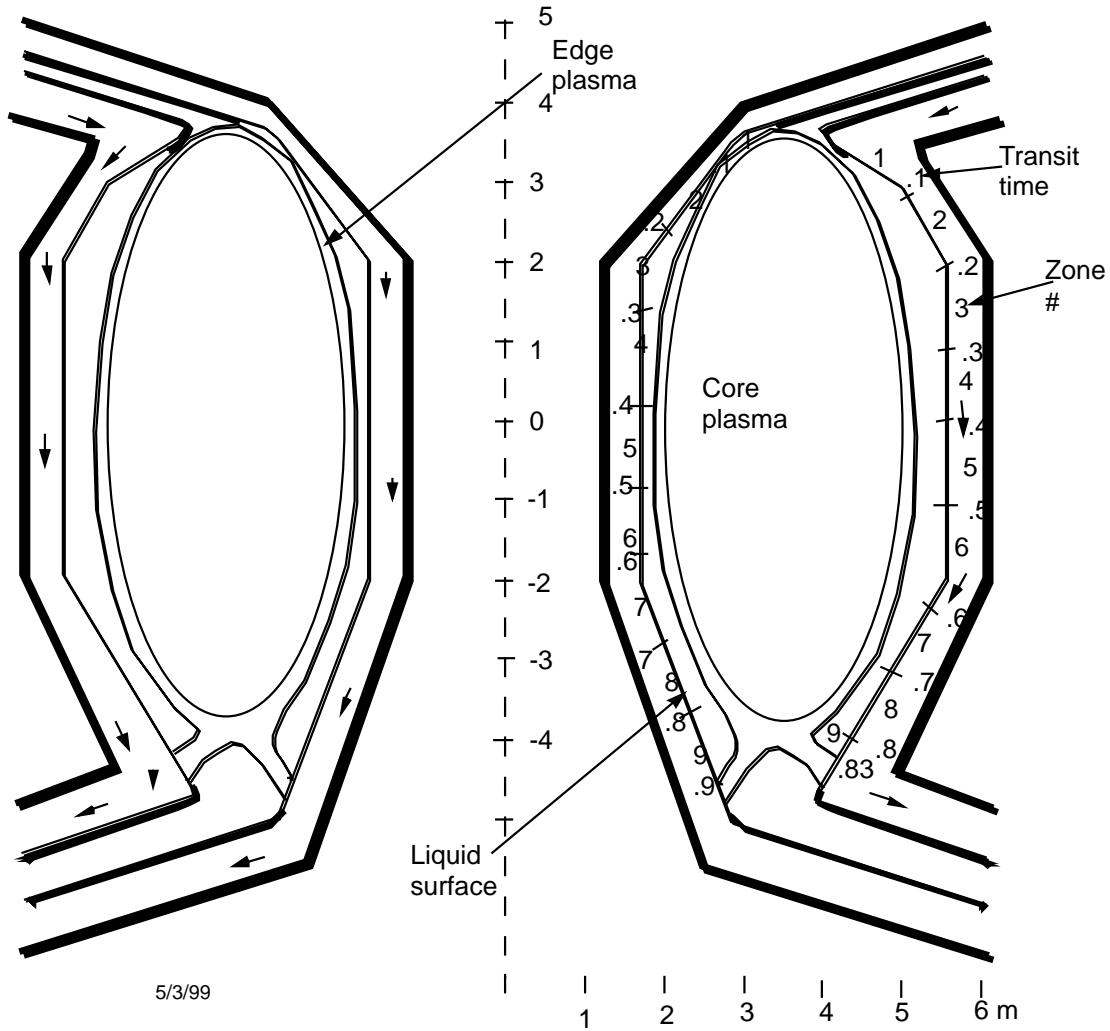


Figure 5.5-19 ST configuration for modeling. Note the very last thing the liquid “sees” before exiting is the edge plasma power. Then the liquid must enter and exit nozzle that guides it out of the configuration. This region might be modified with spray streams as discussed in the literature and later on here.

Outside or outboard zones:

Zone	1	2	3	4	5	
$A_{\text{outside wall}}$	$=2\pi \times 4.6 \times 1$	$+ 2\pi \times 5.2 \times 1$	$+ 2\pi \times 5.5 \times 1$	$+ 2\pi \times 5.5 \times 1$	$+ 2\pi \times 5.5 \times 1$	$+$
	28.90	32.67	34.56	34.56	34.56	
	6	7	8	9		
	$+ 2\pi \times 5.4 \times 1$	$+ 2\pi \times 5.2 \times 1$	$+ 2\pi \times 4.6 \times 1$	$+ 2\pi \times 4.2 \times 0.3$		
	33.93	32.67	28.90	7.92		
$A_{\text{outside wall}}$	$=234.1 \text{ m}^2$					

$A_{\text{outside divertor}} = 2\pi \times 4 \times 0.5 = 12.57 \text{ m}^2$

Inside or inboard zones:

Zone	1	2	3	4	5	
$A_{\text{inside wall}}$	$= 2\pi \times 2.9 \times 1$	$+ 2\pi \times 2.2 \times 1$	$+ 2\pi \times 1.6 \times 1$	$+ 2\pi \times 1.6 \times 1$	$+ 2\pi \times 1.6 \times 1$	+
	18.22	13.82	10.05	10.05	10.05	
	6	7	8	9		
	$+ 2\pi \times 1.6 \times 1$	$+ 2\pi \times 1.7 \times 1$	$+ 2\pi \times 2.2 \times 1$	$+ 2\pi \times 2.4 \times 1$		
	10.05	10.68	13.82	15.08		
$A_{\text{inside wall}}$	= 111.8 m ²					

$$A_{\text{inside divertor}} = 2\pi \times 2.7 \times 0.5 = 8.48 \text{ m}^2$$

$$A_{\text{wall total}} = A_{\text{outside wall}} + A_{\text{inside wall}} = 234.1 + 111.8 = 345.9 \text{ m}^2$$

$$A_{\text{divertor total}} = A_{\text{outside divertor}} + A_{\text{inside divertor}} = 12.57 + 8.48 = 21.05 \text{ m}^2$$

$$A_{\text{plasma}} = 2\pi R^2 \times [(a^2 + b^2)/2]^{0.5} = 2\pi \times 3.5^2 \times [(1.08^2 + 3.69^2)/2]^{0.5} = 375.6 \text{ m}^2$$

$$V_{\text{plasma}} = 2\pi R \times ab = 2\pi \times 3.5 \times 1.08 \times 3.69 = 275.3 \text{ m}^3$$

S = liquid flow path receiving power = 8.3 m

L = edge plasma length = S = 8 m

The transit time of the liquid is $S/V_{\text{axial}} = 8.3/10 = 0.83 \text{ s}$

Liquid flow cross sectional area = $2\pi \times 5.75 \times 0.5 = 18.06 \text{ m}^2$	outside
$= 2\pi \times 1.5 \times 0.5 = 4.71 \text{ m}^2$	inside

For a nominal 10 m/s axial (poloidal) flow of liquid

$\dot{V} = 18.06 \times 10 = 180.6 \text{ m}^3/\text{s}$	outside
$= 4.71 \times 10 = 47.1 \text{ m}^3/\text{s}$	inside

$\dot{m} = 2000 \times 180.6 = 3.61 \times 10^5 \text{ kg/s}$	outside
$= 2000 \times 47.1 = 0.942 \times 10^5 \text{ kg/s}$	inside

$= 2000 \times 47.1 = 0.942 \times 10^5 \text{ kg/s}$	inside
---	--------

If we take a nominal 10 m/s azimuthal flow on the outboard then the power in the flowing liquid which is a reasonable measure of the pumping power is as follows:

$\text{Power} = 0.5 \dot{m} v^2 = 0.5 \times 3.61 \times 10^5 \times (10^2 + 10^2) = 36.12 \text{ MW}$	outside
$= 0.5 \times 0.942 \times 10^5 \times (10^2) = 4.71 \text{ MW}$	inside

5.5.3.2 Heat transfer model

The temperature of the surface can be calculated knowing the heat load and the heat transfer characteristics of the liquid. The idea is to follow a fluid element on the surface from the time it leaves a nozzle till it enters an exit nozzle. The complications are many. The radiation can be absorbed over a distance larger (deeper) than the thermal diffusivity distance, x, which is the distance in a time, t, heat diffuses ($x^2 = tk/\rho c$). As an example x = 0.47 mm for Flibe and 4.2 mm for SnLi in 1 s. In this case the surface temperature is less than if all the incident energy flux were absorbed on the surface. The other complication

is the heat transfer can be greater for turbulent flow than for laminar flow. Heat conduction is a diffusive process. Reynolds analogy is the observation that mass transfer and heat transfer are analogous processes. Mass diffusion will carry heat when there is a temperature gradient just like heat is conducted (diffused). Mass transfer can be small due to molecular collisions or be enhanced by the action of turbulent eddies. Steady heat conduction is governed by the equation:

$$P/A = kdT/dx \quad (5.5-23)$$

Guided by Reynolds analogy one can augment this equation to account for heat transfer by eddy motion [15]

$$P/A = (k+k') dT/dx \quad (5.5-24)$$

$$K_{\text{eff}} = k + k' = k(1+F) \quad (5.5-25)$$

The parameter F represents the enhancement of heat conduction due to turbulence. When $F = 0$ the flow is laminar. When $F=1$ the conductivity is doubled. Magnetic fields will tend to laminarize the flow reducing F. Flow baffles can be added to create eddies or jets embedded in the liquid can enhance eddy motion both of which tend to increase F. Large values of F are possible with Flibe where the electrical conductivity is so low that turbulence may play a large role. In the analysis to follow, F is treated as a parameter. Analysis and experiments should elucidate the applicable range of F.

The temperature of the surface of the fluid element is then given by the equation

$$T = T_{\text{inlet}} + (P/A) \sqrt{2} (t/\pi\rho ck_{\text{eff}})^{0.5} \quad (5.5-26)$$

The time is t, c is the heat capacity, ρ is the mass density, k_{eff} is the enhanced thermal conductivity.

A key parameter is the incident power flux, P_{wall}/A on the liquid surface.

5.5.3.3 Model for incident power striking the liquid wall

The incident power is related to the fusion power, P_{fusion} . The power generated in the plasma that flows outward not counting neutron power since it is so deeply penetrating that the surface heats up only a little by it, is the alpha power with the small amount of current drive power that might be used.

$$P = P_{\text{alpha}} + P_{\text{current drive}} \quad (5.5-27)$$

The power that strikes the wall is radiation power composed of Bremsstrahlung in the range of energy up to T_e , and cyclotron radiation in the microwave range and optical line radiation mostly from impurities especially from the edge plasma. Except in the divertor

region, charged particle and charge exchanged neutral particle bombardment are probably overshadowed by radiation power.

A significant fraction of the power flowing out of the plasma into the edge plasma and from there to the divertor will be converted to optical radiation. This fraction called, F_{rad} , will be taken as a parameter but will likely be around 1/4. The formulation and example numbers are based on recommendations by C. Wong [16].

The power on the wall then is $P_{Brem} + P_{cyclotron} + F_{rad} (P_{alpha} + P_{current\ drive} - P_{Brem} - P_{optical\ core})$. P_{Brem} can be neglected because it is diluted by deep penetration for Flibe but not for SnLi and similarly $P_{cyclotron}$ can be neglected because it penetrates deeply for Flibe and is well reflected for SnLi. $P_{optical\ core}$ is small and can be neglected. The nonpenetrating wall power is,

$$P_{wall} / P_{fusion} = F_{rad} (P_{alpha} / P_{fusion} + P_{current\ drive} / P_{fusion} - P_{Brem} / P_{fusion} - P_{optical\ core} / P_{fusion})$$

$$P_{alpha} / P_{fusion} = 0.2$$

$$P_{current\ drive} / P_{fusion} = 0.01$$

$$P_{Brem} / P_{fusion} = 0.01$$

$$P_{optical\ core} / P_{fusion} = 0.001 \text{ (?) (This estimate should be improved.)}$$

$$P_{cyclotron} / P_{fusion} = 0.004 \text{ (?) (This estimate should be improved.)}$$

$$P_{wall} / P_{fusion} = F_{rad} (0.2 + 0.01 - 0.01) = 0.2 \times F_{rad}$$

$$P_{divertor} / P_{fusion} = (1 - F_{rad}) (P_{alpha} / P_{fusion} + P_{current\ drive} / P_{fusion} - P_{Brem} / P_{fusion} - P_{optical\ core} / P_{fusion})$$

A typical value for F_{rad} might be ~1/4. Then the nonpenetrating power on the liquid wall would be $P_{wall} / P_{fusion} = 0.05$; this is the value we will use in the examples to follow except for FRC where we use 0.03 to account for a more decoupled edge plasma. For a fusion power of 2400 MW, we have:

$$P_{wall} = 0.05 \times 2400 = 120 \text{ MW wall power}$$

$$P_{divertor} / P_{fusion} = (1 - 0.25) (0.2 + 0.01 - 0.01) = 0.15$$

$$P_{divertor} = 0.15 \times 2400 = 360 \text{ MW (divertor power)}$$

Assuming a fraction of ~0.67 of fusion power goes to the outboard and ~0.33 goes to the inboard, we have:

	FRC	Spheromak	ST outside	inside
$P_{wall} \text{ (MW)} / A \text{ (m}^2)$	$= 72 / 75.4$	$20 / 130.4$	$120 \times 0.67 / 234$	$120 \times 0.33 / 112$
	$= 0.95 \text{ MW/m}^2$	0.92 MW/m^2	0.34 MW/m^2	0.35 MW/m^2

	ST outside	inside
$P_{\text{divertor}}/A = 0.15 \times 2400 = 360 \text{ MW}$	$\times 0.67/12.57 \text{ m}^2$	$360 \text{ MW} \times 0.33/8.48 \text{ m}^2$
	$= 19.2 \text{ MW/m}^2$	14.0 MW/m^2

We can use these values for some exploratory examples using the parameter, for enhanced heat transfer and F_{rad} for the variable amount of nonpenetrating surface heating of the liquid as it passes through the chamber.

5.5.3.4 Temperature and evaporation rate versus time along fluid path

We treat two liquids as characteristic of the possibilities: Flibe, which is a low conductivity liquid that can cross magnetic fields with little effects from pressure drop, although galvanic corrosion needs to be watched and $\text{Sn}_{80}\text{Li}_{20}$ which is the lowest vapor pressure liquid metal. The significance for fusion applications of $\text{Sn}_{80}\text{Li}_{20}$ (or other mixtures near this one) was pointed out by D. K. Sze [17].

Then we calculate the temperature of a fluid element versus time using Eq. 5.5-26 for Flibe ($\rho=2000 \text{ kg/m}^3$, $c=2380 \text{ J/kgK}$, $k= 1.06 \text{ W/m}$) and $\text{Sn}_{80}\text{Li}_{20}$ ($\rho=6000 \text{ kg/m}^3$, $c=318.1 \text{ J/kgK}$, $k= 33.5 \text{ W/m}$). In Fig. 5.5-20 we show the results for 0.35 MW/m^2 for Flibe for the turbulence enhancement factor $F=0, 1, 10, 100$ and for $\text{Sn}_{80}\text{Li}_{20}$ for the laminar case or $F=0$. The inlet temperature is taken as $500 \text{ }^\circ\text{C}$. Using the temperature profile from Figure 5.5-20 we calculate the evaporation rate and plot the results in Figure 5.5-21.

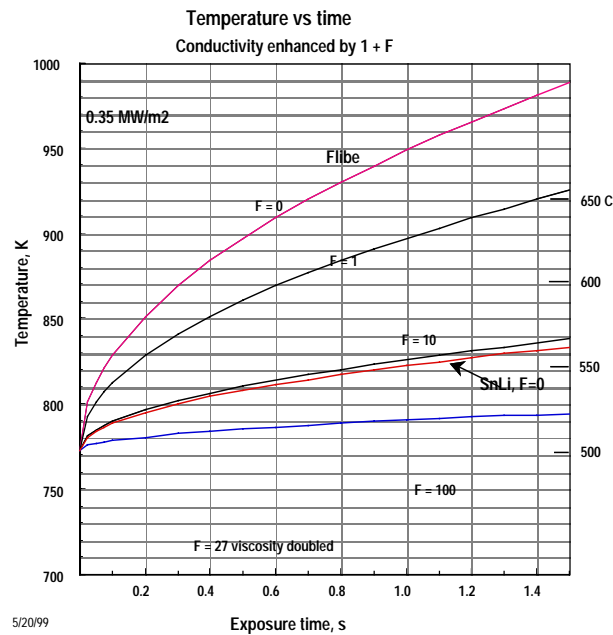
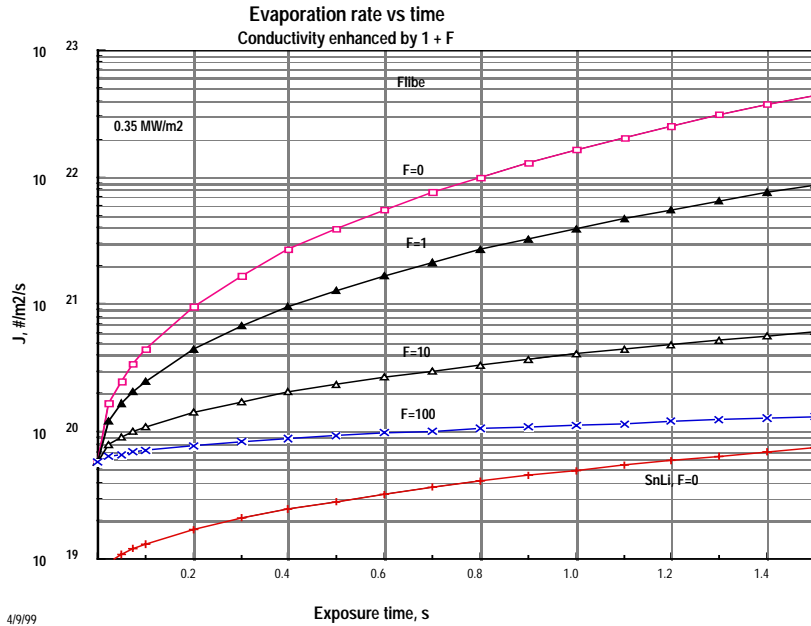


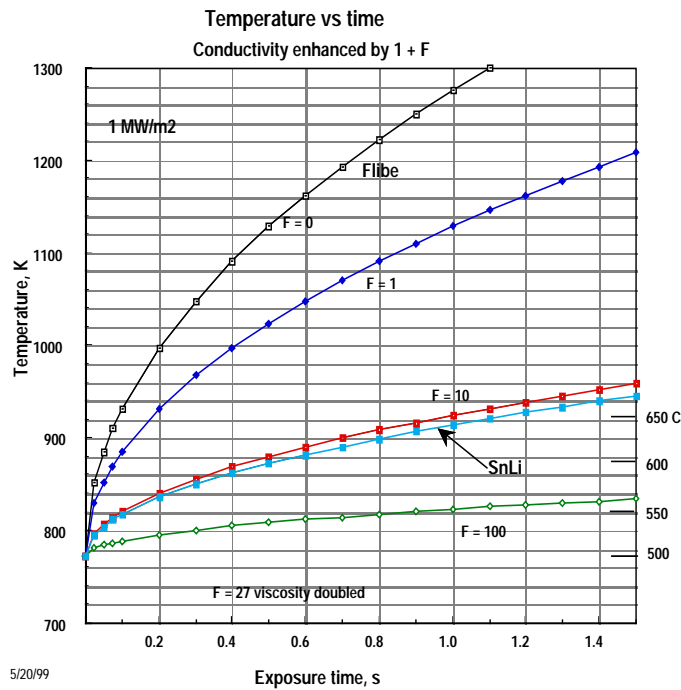
Figure 5.5-20 Temperature of the fluid element versus time at surface heat load of 0.35 MW/m^2 .



4/9/99

Figure 5.5-21 Evaporation rate versus time at surface heat load of 0.35 MW/m². In the case of Flibe the primary evaporation species is BeF₂ molecules and in the case of Sn₈₀Li₂₀ it is Li atoms.

The same procedure is used for 1 MW/m² and the results are plotted in Figures 5.5-22 and 5.5-23.



5/20/99

Figure 5.5-22 Temperature of the fluid element versus time at surface heat load of 1.0 MW/m².

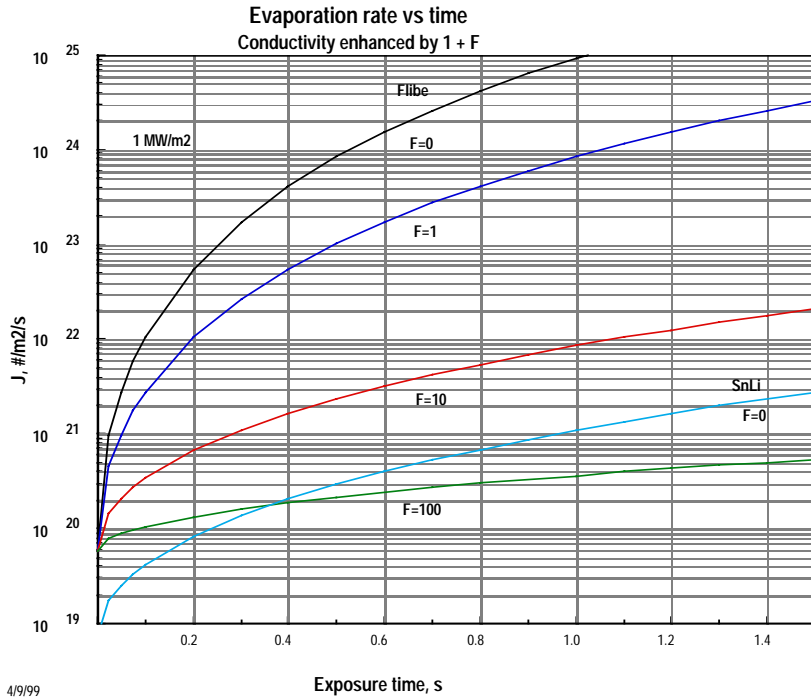


Figure 5.5-23 Evaporation rate versus time at surface heat load of 1.0 MW/m².

Next we compute the evaporation rates for each zone for the three configurations. The results are plotted in Figures 5.5-24, 25, 26, and 27.

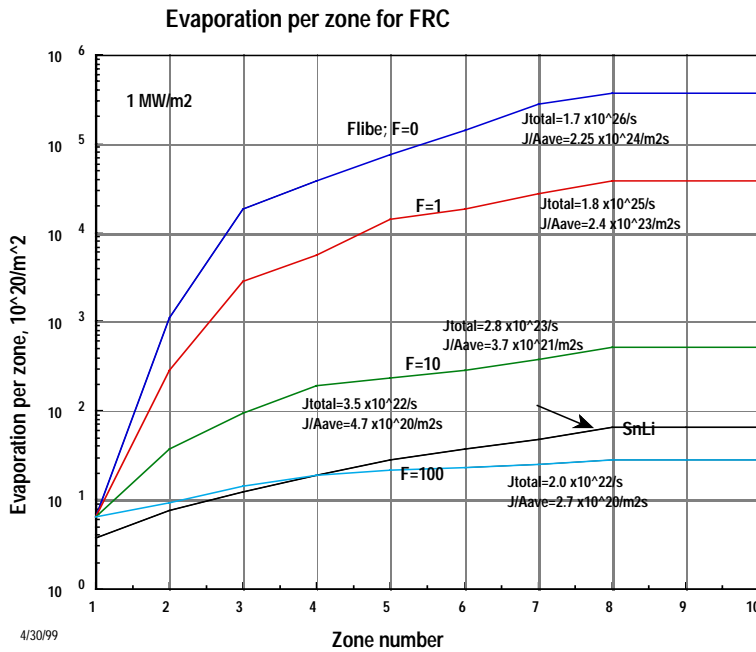


Figure 5.5-24 Evaporation per zone and total evaporation for FRC for 1 MW/m².

The alternative configuration has shorter flow paths to the exit nozzle. The evaporation has been estimated for the F=10 case as $0.90 \times 10^{23}/s$ which is a reduction by

a factor of 3.1. If the speed is increased from 10 to 15 m/s this is reduced further to $0.5 \times 10^{23}/s$ which is another factor of 1.8 reduction in evaporation rate or a total of a factor 5.6 reduction. The shorter path case would reduce the $F=100$ case to $1.2 \times 10^{22}/s$.

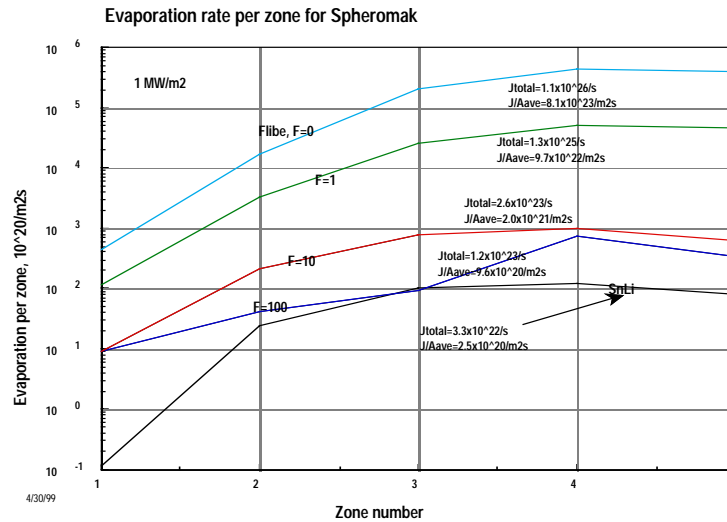


Figure 5.5-25 Evaporation per zone and total evaporation for Spheromak for 1 MW/m^2 .

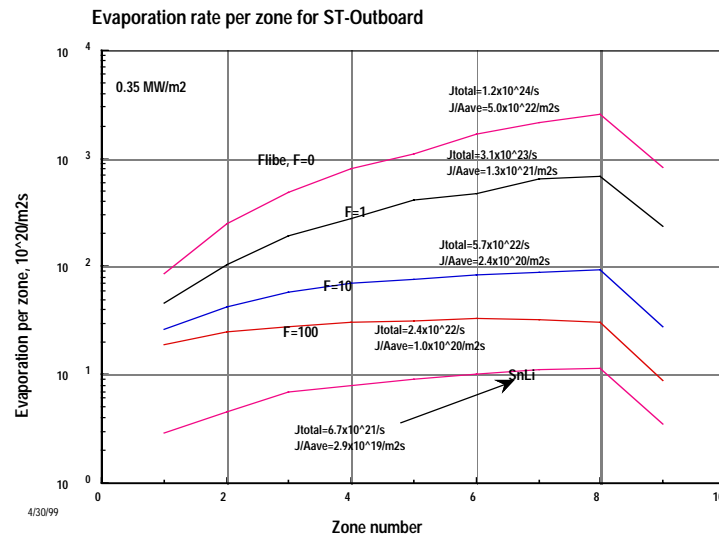


Figure 5.5-26 Evaporation per zone and total evaporation for ST-outboard for 0.35 MW/m^2 .

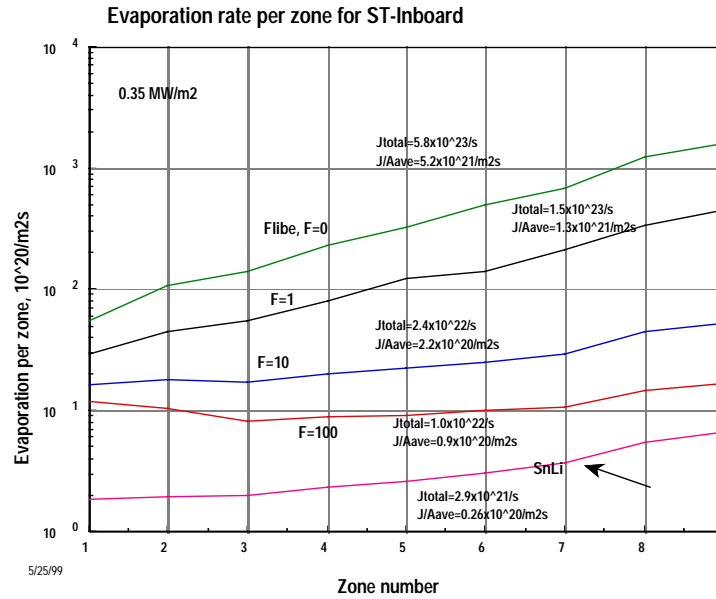


Figure 5.5-27 Evaporation per zone and total evaporation for ST-inboard for 0.35 MW/m².

5.5.3.5 Divertor Heat Load and Evaporation Discussion

This discussion covers the vigorous evaporation due to the extra high heat load in the divertor in the case where it is a liquid and discusses the ideas for enhanced heat transfer such as high speed liquid jets and droplet sprays across the divertor edge plasma. In particular see work by Wells [18], Yu et al. [19], and Moir [20], for high speed liquid Flibe droplet divertor calculations at up to 90 MW/m². The evaporation from the divertor in the ST is ~4.3 × 10⁵ times more BeF₂ molecules evaporating than He particles striking the divertor and 0.86 × 10⁵ times more Li atoms. The evaporation is so vigorous that collisions return much of the evaporated molecules to the surface making this evaporation rate an over estimate but still a very large number. This is clearly a topic for more study.

5.5.3.6 Estimate of Core Plasma Impurities Caused by Evaporation

In Chapter 12, the edge plasma calculations are discussed. The results there are shown in Figure 12-3. The core impurity density of either F ions or Li ions is given by the equation $n_F = 2.5 \times 10^{-3} \times \text{average wall evaporation in atoms/m}^2\text{s}$ and $n_{Li} = 1.5 \times 10^{-4} \times \text{average wall evaporation in atoms/m}^2\text{s}$. This relationship is questionable above the values shown as dashes in the figure. Using these results we come up with the impurity density in the core and give the ratio of this impurity to the DT fusion fuel in Table 1. Note that in our evaporation estimates we quote molecules whereas Figure 12-3 gives the evaporation as atoms so one must multiply by a factor of two. The allowed impurity density is given in Figure 12-1, $n_F/n_{DT} < 0.01$; $n_{Li}/n_{DT} < 0.03$.

Parameters for FRC, Spheromak and ST

A number of typical parameters are summarized from the forgoing discussion and listed in Table 5.5-5 with evaporation results from Flibe. The corresponding parameters for the Sn₈₀Li₂₀ are shown in Table 5.5-6.

Table 5.5-5 Parameters for FRC, Spheromak and ST

	FRC	Spheromak	ST
R, m	1	1.5	3.5
a, m	1	1.5	1.08
b, m	4	1.5	3.69
V_{plasma}, m³	16.8	75	275
S, m	8	8.3	8.3
L, m	8	?	?
A_{wall}, m²	75	130	346
A_{wall} / V_{plasma}, m⁻¹	4.5	1.7	1.3
T_i, keV	30 (15)	15	15
n_o, 10²⁰/m³	8.0(12.7)	6.2	4.3
n_{ave}, 10²⁰/m³	5.66 (8.96)	4.4	3.05
(P/V)_{ave}, MW/m³	143	32	8.7
(P/A)_{neut ave.}, MW/m²	26	15	5.5
P_{fusion}, MW	2400	2400	2400
P_e, MW	1000	1000	1000
V_{liquid}, m³/s	55	120	228
P_{liquid}, MW	11	24	40.8
τ_{liquid}, s	0.8	0.83	0.83
He source, 10²¹/s	0.7	0.7	0.7
P_{Brem}/P_{fusion}	0.01	0.01	0.01
P_{Optical}/P_{fusion}	0.03	0.05	0.05
P_{Cyclotron}/P_{fusion}			
P_{Divertor}/P_{fusion}	0.15	0.15	0.15
P_{Brem}/A, MW/m²	0.32	0.18	0.069
P_{Optical}/A, MW/m²	1.0	0.92	0.35
P_{Divertor}/A, MW/m²	0	0	17.1
T_{in}/T_{out} *, K	773/890	773/882	773/815
T_{ave}, °C	559	555	521
J_{evap}, BeF₂, 10²¹/s *out/in	280	260	56/24
J/A, 10²¹/m² s, *out/in	3.7	2.0	0.24/0.22
J_{Diver}/A, 10²⁵/m² s *out/in	0	0	2.5/0.34
J_{Diver}, 10²⁶/s *out/in	0	0	3/0.28
n_F, #/m³, 10²⁰/m³	0.28	0.15	0.015 **
n_F/n_{DT}, ~0.01 allowed	0.049	0.04	0.006 **

*The thermal conductivity is enhanced by a factor of 10 to account for turbulence

**Neglecting contamination from divertor evaporation

Table 5.5-6 Parameters for FRC, Spheromak and ST for SnLi

	FRC	Spheromak	ST
$n_{ave}, 10^{20}/m^3$	5.66 (8.96)	4.4	3.05
$T_{in}/T_{out} *$	773/900	773/900	773/840
$T_{ave}, ^\circ C$	564	564	534
$J_{evap}, Li, 10^{22}/s *out/in$	3.5	3.3	0.67/0.29
$J/A, 10^{20}/m^2 s, *out/in$	4.7	2.5	0.29/0.26
$J_{Diver}/A, 10^{24}/m^2 s *out/in$	0	0	5/0.6
$J_{Diver}, 10^{25}/s *out/in$	0	0	6/0.5
$n_{Li}, \#/m^3, 10^{16}/m^3$	7	3.8	0.44 **
$n_{Li}/n_{DT}, \sim 0.03 \text{ allowed}$	0.00013	0.000085	0.000014 **

Discussion

The forgoing discussion treated some specific cases with many questionable assumptions. We have a big job now to study the problem much more carefully. It would appear the evaporation from the liquid divertor has not been treated adequately. The results from SnLi look like the evaporation does not contaminate the core plasma too much. The problem then is to study ways to make liquid metal flow in spite of the magnetic field. For Flibe we need to somehow reduce the contamination by a factor of about 5 except for the ST where the calculated impurity concentration is adequately low. This can be accomplished by employing the alternative shorter flow path configuration and increasing the axial flow speed from 10 m/s to 15 m/s. We assumed an inlet temperature of Flibe of 500 °C. This can not be lowered much but possibly some. The melting point is about 460 °C which sets a limit of freezing in the heat exchangers, however, by reformulating the salt mixture the melting point can be lowered some at a cost of raising the evaporation rate as shown in Figure 8.5-4. It is not clear if there is a win here. Next let us consider the heat transfer model. Turbulence on the free surface brings cooler liquid to the surface to mix and cool the heated liquid. More study and experimentation can clarify the models used to calculate the surface temperature. If the turbulence is on the high end, the temperature will be considerably lower than we assumed with the parameter $F = 10$ and may be as high as 1500 or more according to the κ - ϵ model (Section 5.5.2). Next is the model of energy flowing from the core and edge plasma to the liquid surface. Our model has many parameters, which with further study can be narrowed down. Up till now we recommend study over a range for these parameters. We need to specifically treat the penetrating power in the form of x-rays and neutrons and add the optical radiation that also has a finite penetration. Also we need to treat the differences between the reference cases of FRC, Spheromak and ST. The present model treats them too much alike rather than model their important differences in appropriate detail.

5.5.4 Temperature Distribution in Blanket Core and Support Structural Elements

The overall temperature rises of various 45 cm thick liquid wall concepts range from 4 to 15 °C for Flibe and 10 to 32 °C for Sn-Li as listed in Table 5.5-7. Since these temperature rises are considerably small, one can expect a fairly uniform temperature across the blanket core. The average temperature of the blanket liquid can be estimated as the coolant inlet temperature plus the half of the overall temperature rise. Furthermore, temperature increase due to nuclear heating in the back structural wall is negligible (less than 10 °C).

Temperature calculations have been performed for the GMD with pocket liquid blanket. The temperature profiles of blanket compartment fluid at different time intervals are shown in Figure 5.5-28. The analysis assumes that there is no heat deposition inside the compartment before it is filled. Once the compartment is full of the Flibe, a non-uniform volumetric heat source profile based on a neutronics calculation (see section 5.3) applied to simulate the heat generation due to Flibe-neutron interaction. As shown, the coolant is gradually heated up once the heat is turned on while the hottest spot moves toward the core of the vortex, which reflects the flow circulation. More temperature analysis will be performed once the hydrodynamics configuration of a thick liquid concept is better defined.

Table 5.5-7 Characteristics of Non-Structure Thick Liquid Wall Concepts for Different Confinement Schemes

	ARIES-RS	ARIES-RS*¹	FRC	ST
Fusion Power (MW)	2170	5480/16439	2072	5470
Average Neutron Wall Load (MW/m²)	3.96	10/30	30	8.085
First Wall Area (m²)	438.38	438.38	55.26	541
Flow Area for 45 cm thick LW	30 m ²	30 m ²	3.744 m ²	14 m ²
Coolant Velocity (m/s)	10	10	10	10
Mass Flow Rate (Kg/s) Flibe	5.89x10 ⁵	5.89x10 ⁵	7.35x10 ⁴	2.748x10 ⁵
Mass Flow Rate (Kg/s) Sn-Li	1.877x10 ⁶	1.877x10 ⁶	2.343x10 ⁵	8.762x10 ⁵
Pumping Power (MW) Flibe	58.89	58.89	7.35	27.48
Pumping Power (MW) Sn-Li	187.74	187.74	23.43	87.62
Temperature Rise (K) Flibe	1.87	4.53/13.6	13.74	9.70
Temperature Rise (K) Sn-Li	4.21	10.64/27.5	32.24	22.76

*1 Assuming that beta is increased proportionally.

*2 Estimated for the whole primary loop system. The pumping power for the in-vessel pressure drop of 0.2 MPa & associated mass flow rate is 7.2 MW.

*3 Pumping power requirement for recovering the coolant from losing its kinetic energy.

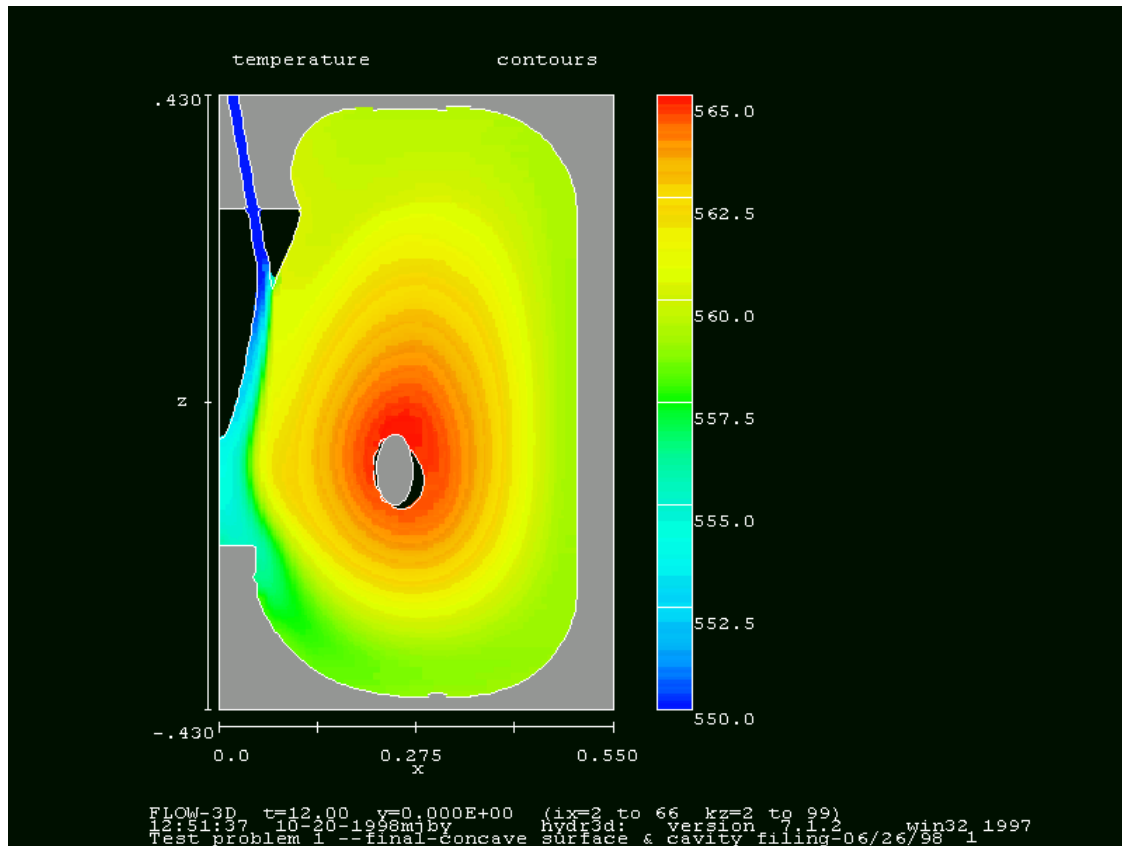


Figure 5.5-28 Flibe Temperature Distribution Inside the Blanket Pocket. Elliptical outlet located below the mid-plane of the blanket pocket. The hottest spot is located near the outlet. (A Volumetric Heat Deposition in the Compartment is used starting at 12 sec after the Compartment is filled)

5.5.5 Power Conversion and Pumping Power Requirements

The challenges of the liquid wall designs go beyond achieving a low enough surface temperature in order to be compatible with the plasma operations, but also to maintain a mean bulk temperature of greater than 600 °C to achieve a high thermal efficiency of greater than 45% (Figure 5.5-29). This temperature can be higher than the maximum allowable free surface temperature.

A primary motivation for considering a thick liquid first wall/blanket is to protect the structure behind it from radiation damage and from becoming highly activated. Previous neutronics calculation has shown that this can be obtained with about 45 cm thick of Flibe (see Section 5.3). By using this thickness, a simple energy balance calculation indicates that the temperature rise for the APEX specified power density is only about 4.5 °C in the ARIES-RS configuration for Flibe flowing at 10 m/s as shown in Table 5.5-7. Furthermore, the high heat capacity of the liquid adds into this effect as shown an unnoticeable temperature rise of less than 13 C even severely heated by a neutron wall load of 30 MW/m². Although a fairly uniform liquid temperature could be a

favorable condition for the thermal cycle, the blanket liquid needs to operate at high temperatures to achieve a high thermal conversion efficiency. (The velocity of about 10 m/s is needed to prevent the gravitational thinning and provide adequate centrifugal forces and momentum required for flow adhering to the structural wall behind.) Such an insignificant temperature rise makes the fluid temperature control practically impossible if the allowable temperature window for the plasma operation at the free surface is marginal. This can be illustrated as to reach the coolant exit temperature of 610 °C for achieving a high thermal conversion efficiency of an initial inlet temperature of 510 °C, the fluid has to be circulated 20 times inside the reactor before proceeding to the BOP. Yet, the surface temperature exceeds the allowable maximum limit for plasma operation (of < 600 °C) within 1 cycle if the surface temperature increase is more than 100 °C. Subsequently, the surface temperature becomes too high because of the increase of the inlet temperature. This situation can be somewhat alleviated if the power density of a fusion reactor can be made higher. In this case, the bulk temperature rise can be higher for the same amount of the liquid inventory. This can be seen in FRC as shown in the same Table, the overall temperature rise increases by about a factor of 3 due to its compactness and a much higher neutron wall load (e.g., 30 MW/m² compared to APEX 10 MW/m²). Yet, for this amount of temperature rise, the difficulty of temperature management remains unless the surface temperature can be reduced by turbulence or other heat transfer enhancement mechanisms. One possible solution for resolving temperature control is to de-couple the first wall cooling from the blanket liquids as done in the GMD with pocket design. In the design, the first wall liquid will have high velocity to remove the high surface heat flux while keeping the temperature of the liquid surface facing the plasma low. The liquid blanket flows at a lower velocity in order to achieve high temperature and to reduce pumping power requirements. A possible design option for power conversion would then include two cycles: one for the conversion of the thermal power in the first wall and divertor coolants, and the other for conversion of the thermal power in the blanket coolant, which has a much higher thermal conversion potential.

As pointed out previously, hydrodynamics (with or without the effect of magnetic field) calculations indicate that a fairly uniform thick liquid wall can be formed in various fusion relevant configurations as long as the injected fluid carries an adequate inertial momentum (e.g., corresponding to a velocity of 10 m/s). This leads to a large pumping power consumption for a typical thick liquid wall concept because of the high velocity. To reduce the pumping power consumption, the liquid wall design shall incorporate a head recovery system at the exit to recover the fluid kinetic energy. Such a head recovery system for any thick liquid wall concept is yet to be designed, but can involve a concept similar to the design adopted for HYLIFE-II [21]. The estimated efficiency for this head recovery system is about 50%. Based on this assumption, the fractional pumping power requirements for different liquid wall concepts are plotted in Figure 5.5-30.

As shown, it consumes about 2.4% of total fusion power to run a 45 cm thick Flibe wall flowing at 10 m/s. This power consumption goes up to about 6% if Sn-Li fluid is used. However, the pumping power requirement becomes less of a concern for higher and higher power density confinement concepts as shown in the same Figure for FRC cases.

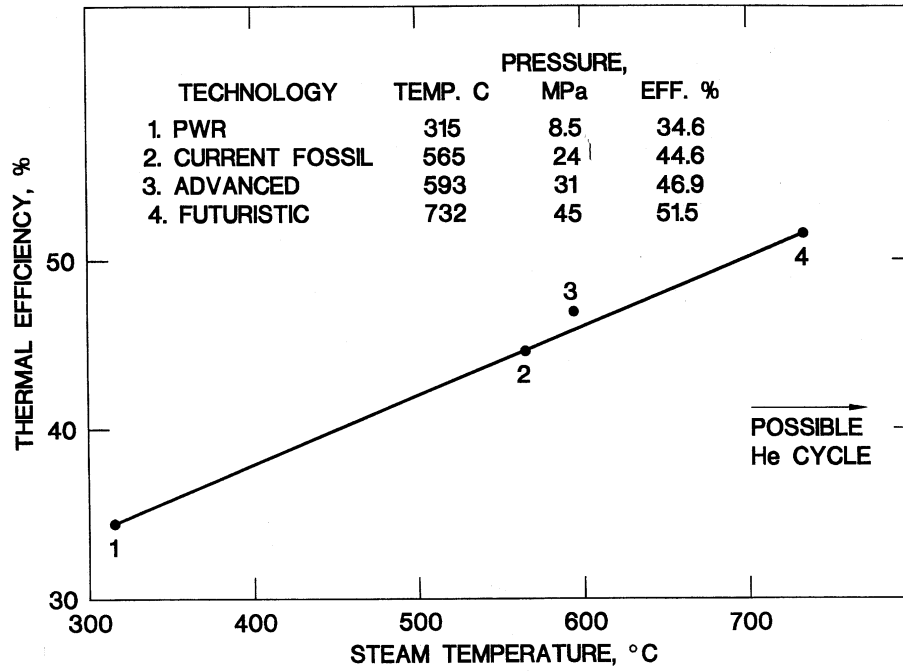


Figure 5.5-29 Thermal Efficiency as a Function of Steam Temperature.

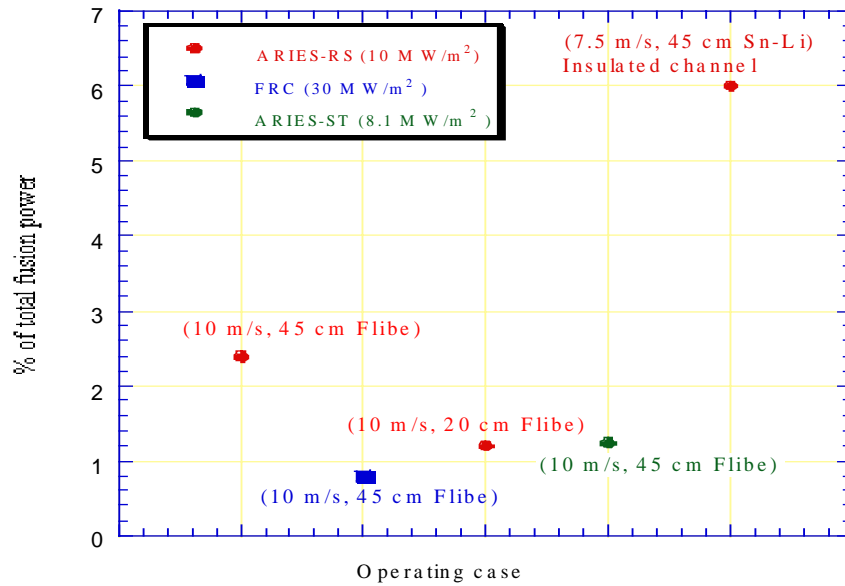


Figure 5.5-30 Pumping power requirement is less of a concern for a high power density FRC device

5.5 References

- 1 Rashidi, M., Hetsron, G., and Banerjee, S., 1991. Mechanisms of heat and mass transport at gas-liquid interfaces, *Int. J. heat Mass Transfer*, Vol. 34, No. 7, pp. 1799-1810.
- 2 Komori, S. Murakami, Y. and Ueda H., 1989. The Relationship between Surface-Renewal and Bursting Motions in an Open-Channel Flow. *J. Fluid Mech.* Vol. 203, pp. 103-123.
- 3 Levich, V. G., 1962. *Physiochemical Hydrodynamics*. Prentice-Hall, Englewood Cliffs, New Jersey.
- 4 Davies, J. T., 1972. *Turbulence Phenomena*. Academic press, New York, pp. 186-215.
- 5 Dittus, F. W. and L. M. K. Boelter, *Univ. Cali. Pub. Eng.* 2, 443 (1930)
- 6 Jones W.P., Launder B.E., The Prediction of Laminarization with a Two-Equation Model of Turbulence, *Int. J. Heat and Mas Transfer*, 15, 301 (1972).
- 7 Kitamura K., Hirata M. Turbulent Heat and Momentum Transfer for electrically conducting Fluid Flowing in Two-Dimensional Channel under Transverse Magnetic Field, 6th Int. Heat Transfer Conf., 3, 159 (1978).
- 8 Naot D., Rodi W. Calculation od Secondary currents in Channel Flow, *Proc. ASCE*, 108, No.HY8, 948 (1982).
- 9 Wilcox D.C. *Turbulence Modeling for CFD*, pp.460 (1994).
- 10 Takahashi M., Inoue A., Aritomi M., Matsuzaki M. Numerical Analysis for Laminar and Turbulent Liquid-Metal Flow in a Transverse Magnetic Field, *Fusion Engineering and Design*, 8, 249 (1989).
- 11 Inoue A., Kozawa Y., Takahashi M., Yoshizawa A. Characteristics of Flow and Heat Transfer in Air-Mercury Two-Phase Stratified Flow under a Vertical Magnetic Field, *Experimental Thermal and Fluid Science*, 8, 46 (1994)
- 12 Roberts G.O. Computational Meshes for Boundary Layer Problems, *Proc. Second Int. Conf. Num. Methods Fluid. Dyn., Lecture Notes in Physics*, 8, 171 (1971)
- 13 Naot D., Yacoub N., Moalem D. Dissipation Length Scale Dynamics, *Liquid Metal Flows and Magnetohydrodynamics: Progress in Astronautics and Aeronautics*, 221 (1991)
- 14 Youssef M.Z. et al. X-rays Surface and Volumetric Heat Deposition and Tritium Breeding Issues in Liquid-Protected FW in High Power Density Devices. Paper presented at thr 13th Topical Meeting on the Technology of Fussion Power, June 7-11, 1998, Nashville, Tennessee
- 15 W. H. Geidt, *Principles of Engineering Heat Transfer*, D. Van Nostrand Co, Inc., New Jersey (1957) p174-178.
- 16 C. Wong, private communications April, 1999
- 17 D. K. Sze, private communications, 1998
- 18 W. M. Wells, *Nucl. Technol./Fusion* **1** (1981) 120.
- 19 W-S. Yu, J. R. Powell, J. A. Fillo, and J. L Usher, "TRAIL—a tokamak railgun limiter," *Fusion Technology* **6** (1984) 181.
- 20 R. W. Moir, "Rotating liquid blanket with no first wall for fusion reactors," *Fusion Technology* **15** (1989) 674-679.
- 21 Palmer House, *HYLIFE-II Reactor Chamber Design Refinements*, *Fusion Technology*, Vol. 26, Nov. 1994, 1178.

5.6 Structural Materials Issues for Thick Liquid Blanket Concepts

As discussed in Chapter 13, several different materials are under consideration for thick liquid blanket concepts. The successful development of a viable thick liquid blanket design would likely reduce the importance of radiation damage effects in determining the structure lifetime, and may reduce the importance of tritium solubility (inventory) issues if the structural materials volume is minimized. In addition, relaxation of the requirement for Class C waste disposal would allow several new high performance structural materials to be considered.

The key structural materials issue for thick liquid blanket concepts is compatibility with the liquid that serves as the coolant and tritium breeder. Secondary issues include “low temperature radiation embrittlement” (typically important in all BCC alloys for temperatures below $\sim 0.3 T_M$ and doses above ~ 1 dpa), “high temperature helium embrittlement” (typically important in all materials for temperatures above $0.5 T_M$ and >100 appm He concentrations), joining and fabrication issues (unirradiated components and repair welds of irradiated materials), creep strength and fracture toughness, and tritium solubility and permeability.

The structural materials under consideration (Table 5.6-1) for the APEX thick liquid blanket concepts include oxide dispersion-strengthened ferritic steel, vanadium alloys, SiC/SiC composites, tungsten alloys, tantalum alloys, and austenitic stainless steel.

Table 5.6-1 Maximum allowable temperatures of structural alloys (bare walls) in contact with high-purity liquid coolants, based on a 5- μ m/yr corrosion limit. The Sn-Li corrosion limits are based on experimental studies conducted with liquid Sn.

	Li	Pb-17 Li	Sn-Li (Sn)	Flibe
F/M steel	550-600°C	450°C	400-500°C	700°C ? 304/316 SS
V alloy	$\sim 700^\circ\text{C}$	$\sim 650^\circ\text{C}$?	?
Nb alloy	$>1300^\circ\text{C}$	$>600^\circ\text{C}$ ($>1000^\circ\text{C}$ in Pb)	600-800°C	$>800^\circ\text{C}$
Ta alloy	$>1370^\circ\text{C}$	$>600^\circ\text{C}$ ($>1000^\circ\text{C}$ in Pb)	600-800°C?	?
Mo	$>1370^\circ\text{C}$	$>600^\circ\text{C}$	$<800^\circ\text{C}?$	$>1100^\circ\text{C}?$
W	$>1370^\circ\text{C}$	$>600^\circ\text{C}$	$\sim 800^\circ\text{C}$	$>900^\circ\text{C}?$
SiC	$\sim 550^\circ\text{C} ?$	$>800^\circ\text{C} ?$	$>760^\circ\text{C}?$?

Additional structural materials which may be worthy of consideration include ordered intermetallics (e.g., iron aluminides) and V-Ti-Al concentrated alloys. Consideration of corrosion effects may limit the upper operating temperature limit for several different

structural material/liquid blanket combinations. In particular, the refractory alloys do not appear to have good compatibility with Sn-Li at high temperatures (although the corrosion data are very limited). Very little is known about the chemical compatibility of most of the candidate structural materials with Flibe.

5.7 Mechanical Design Features and Configuration Layout

The mechanical design of the GMD concept is very challenging, since it must satisfy the basic APEX design goals listed in Table 5.7-1. These goals include minimum values for wall loading, shielding, tritium breeding, and availability as well as provisions for heating and diagnostic penetrations, vacuum pumping, and plasma exhaust (divertor).

Table 5.7-1 General Design Requirements

Function	Requirement	Value/Goal
Power Extraction	Neutron Wall Load	7 MW/m ² avg* 10 MW/m ² peak*
	Surface Heat Flux	2 MW/m ² *
Tritium Breeding	Self Sufficient	TBR > 1
Shielding	Radiation exposure of coils (insulation)	< 1x10 ⁹ Rad
	Nuclear heating of coils (sc cable)	< 1kW/m ³
	Re-weldable confinement boundary	< 1 appm He
Vacuum	Compatible with plasma	
	- Base partial pressure, non-fuel - Base pressure, fuel (H,D,T)	< 1x10 ⁻⁹ Torr < 1x10 ⁻⁷ Torr
Plasma Exhaust	Divertor required	to remove helium
Penetrations	Plasma Heating Power Density	~4 MW/m ² ~6 MW/m ²
	- NBI - ICH -	
	Diagnostics	viewing through labyrinth/mirrors
Operating Parameters	Pulse Length	Steady State
	Number of pulses	< 3,000
	Disruptions	TBD
Availability	Maximize total availability	A _{plant} > .75
		A _{blanket/FW} > .98
Safety	Confinement Boundaries	At least 2

* Values are minimum goals for steady state operation

The GMD thick liquid blanket concept is not limited to a particular fusion reactor configuration, and may be adapted to both magnetic and inertial confinement designs. For the purpose of the mechanical design and maintenance study, however, the ARIES-RS reactor design was chosen as the basic configuration. This choice provides a

relatively difficult design challenge and allows direct comparison between the “conventional” first wall/blanket design used for the ARIES-RS study and the GMD high power density, liquid blanket. Other configurations under consideration for a liquid blanket include a generic FRC design and the ARIES ST design.

In order to meet the intent of the APEX study and adapt the GMD concept, several changes were required to the baseline ARIES-RS design. First the power density was approximately doubled to obtain the correct surface heat flux and neutron wall load specified by the APEX design goals. A list of the ARIES-RS parameters and APEX modifications are listed in Table 5.7-2.

Table 5.7-2 ARIES RS Parameters & APEX modifications.

	<u>ARIES*</u>	<u>APEX</u>
Major Radius	5.52	same
Minor Radius	1.38	same
Plasma Aspect Ratio	4	same
Number of Sectors	16	same
Fusion power (MW)	2171	~ 4000
Neutron Power (MW)	1736	~ 3400
Alpha power (MW)	433	~ 600
Fusion power density (MW/m ³)	6.38	~ 12
Average neutron load (MW/m ²)	4.03	7
Peak neutron load (MW/m ²)	5.67	10
Average FW surface heat flux (radiative), MW/m ²	0.4	1.5
Peak FW surface heat flux, MW/m ²	0.47	2

* Ref <http://aries.ucsd.edu/PUBLIC/ariesrs.html>

Second, in order to accommodate the liquid wall, the ARIES-RS configuration was changed from double null to single null with the divertor and associated pumping at the bottom of the reactor. The shape of the first wall was also modified to reduce the horizontal component of flow at the upper part of the machine. Finally, the access port was enlarged to allow complete sector removal and replacement to reduce maintenance time. Figure 5.7-1 shows a comparison of the ARIES-RS and the modified configuration for the GMD concept geometry.

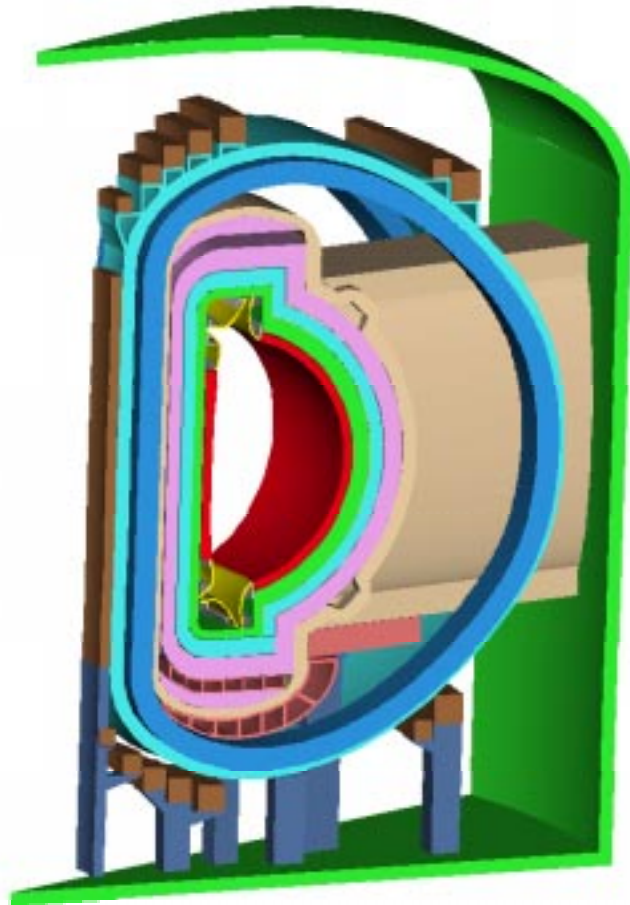
The GMD concept replaces the conventional first wall and blanket of a fusion reactor with a flowing layer of a low vapor pressure liquid. The liquids under consideration include lithium, Flibe or Sn-Li. Two fluid streams are envisioned for the GMD concept. The first is a thin, fast flowing layer at the plasma-facing surface to intercept the surface heat flux. The second is a thicker, slower moving stream to absorb the bulk of the neutron energy and provide the blanket functions of shielding and tritium breeding. The mechanical design must incorporate features for creating both of these streams and for accommodating other reactor requirements. Design features include a fast-flow forming system, a thick flow forming system, a flow collecting system, a concept for starting the

flow streams, a concept for providing heating and diagnostic penetrations, a vacuum pumping concept, and a divertor concept. A thick flow slowing system may also be required for the ARIES configuration. Figure 5.7-2 illustrates an elevation view of the baseline GMD configuration. Figure 5.7-3 shows the GMD liquid FW/Blanket with and without the liquid layer.

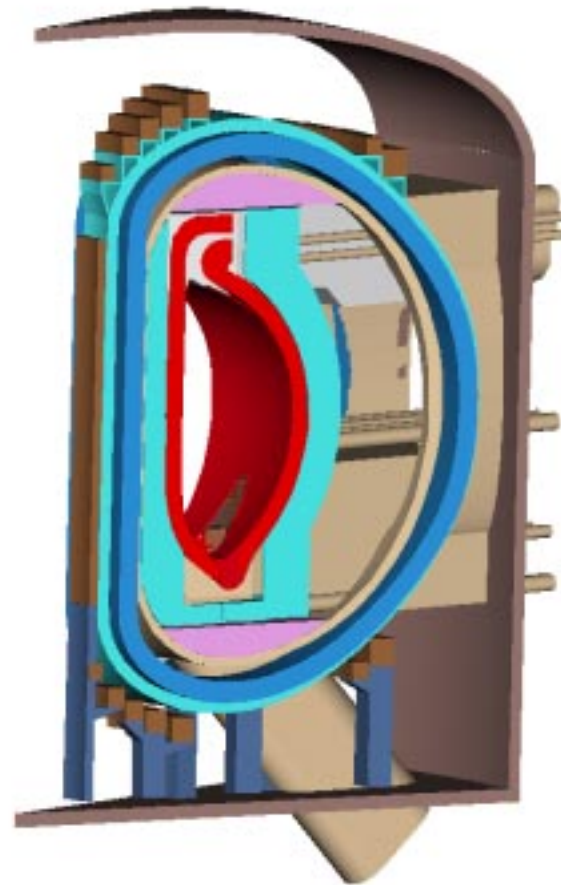
Fast flow forming system: The thin, fast flowing stream is created at the top of the blanket and flows on the surface of the thicker stream. The thin stream intercepts the surface heat flux and has enough velocity to prevent excessive temperature rise as it traverses the ~6 m height of the plasma. A velocity of about 20 m/s is required for this purpose. The stream is formed via nozzles that are arranged such that flow from one nozzle covers the plasma-facing surface of adjacent nozzles. For ease of maintenance the nozzles are integrated into a removable cassette. This system is described in more detail in Section 7.6.

Thick flow forming system: The thick bulk stream is also created at the top of the blanket and flows against the surface of the fixed shield. The velocity of the liquid must remain high for two reasons. First, it must keep the stream adhered to the walls via centrifugal force and second it must be fast enough to prevent flow thinning as the stream is accelerated by gravity. The combination of these two requirements result in a minimum flow velocity of about 8 m/s. The flow parameters are listed in Table 5.7-3 for Flibe as the working liquid.

The thick flow is introduced on the inboard side in the purely poloidal direction, with no toroidal component that would tend to separate the flow from the inboard shield surface. The outboard flow can be both poloidal and toroidal, with both components of velocity tending to force the liquid against the outboard blanket surface. The flow forming structure is located in a large, removable cassette at the top of the device. The forces on this structure are large, as the entire outboard flow must turn ~155 degrees. For the velocities and fluids under consideration, this force is in the range of 10 to 30 tons.



ARIES-RS Reactor Concept



Modifications for GMD Blanket

Figure 5.7-1 Comparison of ARIES-RS configuration and GMD modifications, including larger maintenance port, single null divertor, large exit duct, and modified wall shape.

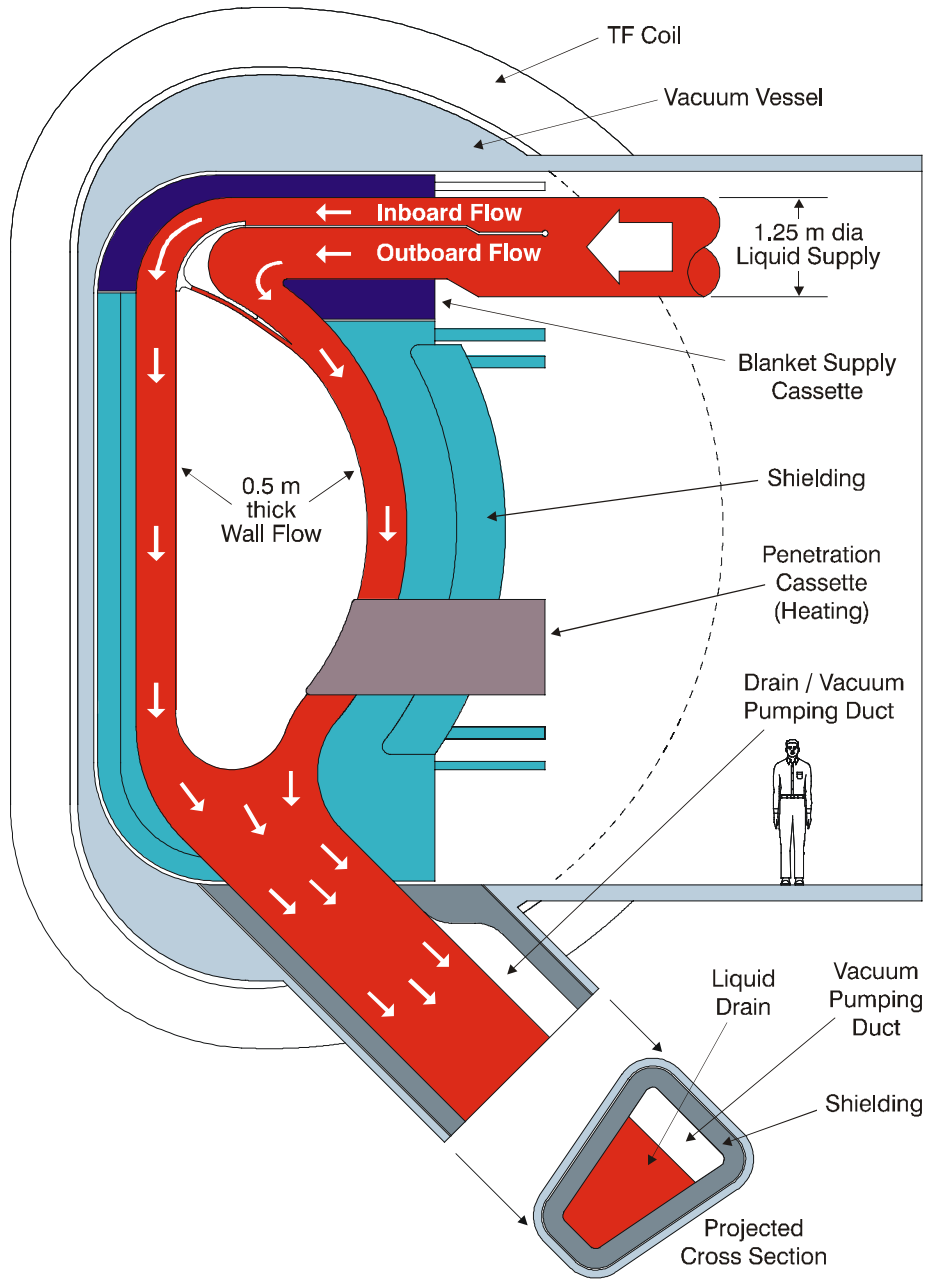
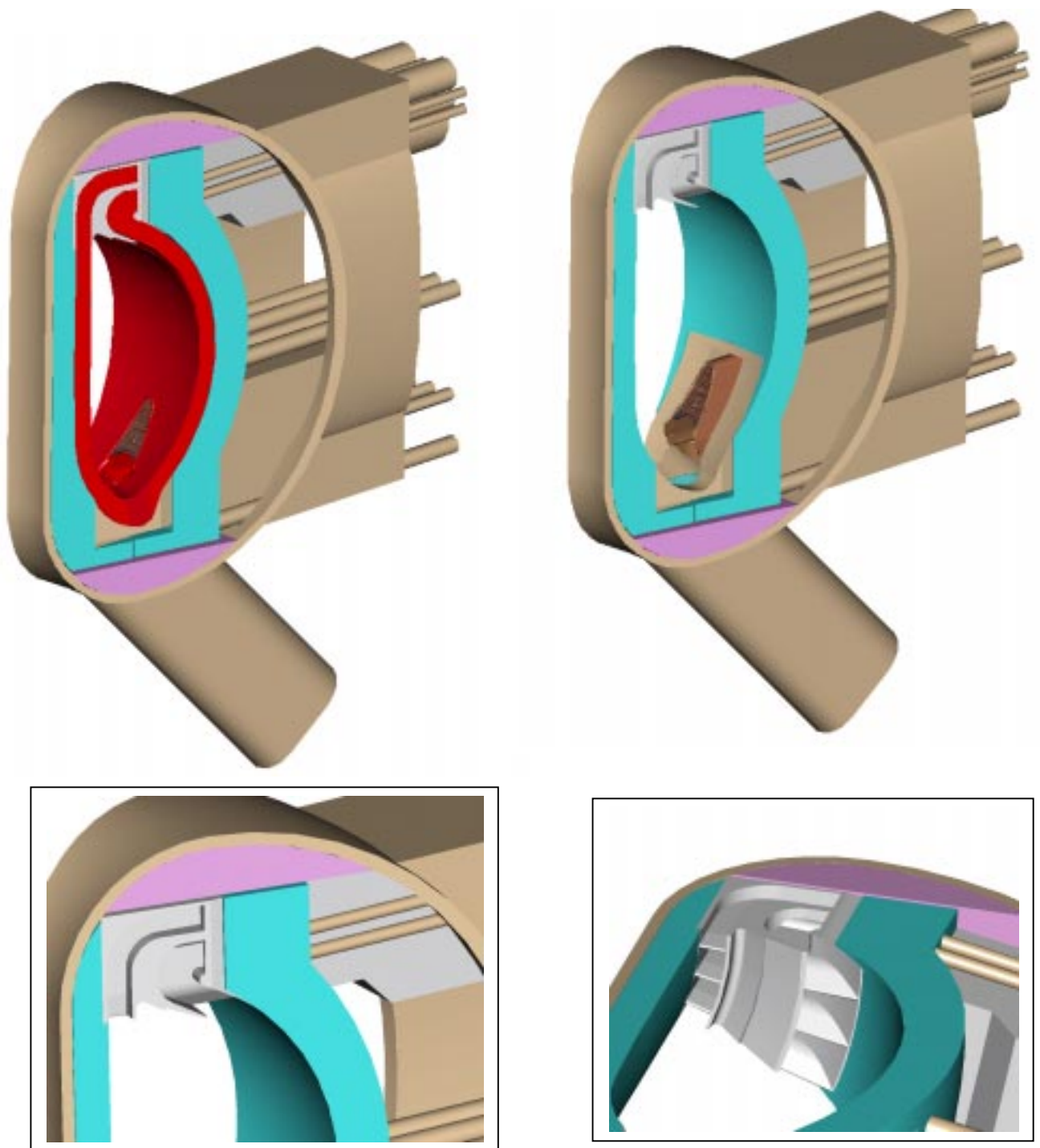


Figure 5.7-2 Elevation view of baseline GMD concept.



Figures 5.7-3 Features of GMD concept, shown with and without liquid.

Table 5.7-3 Flow parameters for Baseline GMD concept using Flibe.

	Inboard	Outboard	Total
Thin stream			
Thickness at midplane (mm)	10	10	
Velocity at midplane (m/s)	20	20	
Volume flow rate (l/s)	5.6	7.4	13.0
Mass flow rate (kg/s)	11,100.	14,500.	25,600.
Inlet Temperature (C)	565	565	
Outlet Temperature (C)	586	596	
Pumping power (MW)	14	12	26
Thick stream			
Thickness at midplane (mm)	450	450	
Velocity at midplane (m/s)	8	8	
Volume flow rate (m³/s)	6.4	8.3	235.2
Mass flow rate (kg/s)	12,000.	16,000.	461,000.
Inlet Temperature (C)	~600	~600	
Outlet Temperature (C)	~605	~606	
Pumping power (MW)	94	72	166

As shown in Table 5.7-3, the total flowrate is extremely large, similar to the flow through a medium sized hydroelectric power turbine. The cassettes and flow nozzles are also not well shielded from the neutron fluence, and the nozzles and internal piping are subject to erosion and degradation from the high velocity flow. It must be assumed that replacement of these cassettes will occur frequently. The design goal would be to replace the cassettes no more often than once every two years.

Flow collecting system, divertor and vacuum pumping system: The fluid must be collected at the bottom of the shield system in the region of the divertor and removed from the machine. At the same time there must be some method for providing vacuum pumping in the divertor region. In the GMD concept, these functions are combined in a removable trough connected to large exit pipes between each toroidal field coil. The trough is contained in a cassette that can be removed for maintenance, and the connecting pipes are lined with a removeable sleeve that provides thermal and nuclear shielding. The pipes must be large enough to provide adequate flow area (consistent with the free flow velocity) and an open channel for pumping. The current opening size is limited by the space between TF coils to less than 2 m², which would require an exit flow velocity of > 6 m/s. This velocity would seem very difficult to achieve.

The divertor consists of a flow diffuser system that locally breaks up the surface flow into droplets in the lower region of the machine. This exposes more surface to the plasma and should prevent excessive temperature and/or pressure rise.

The vacuum pumping is accomplished at the bottom of the duct, above the liquid recovery pool. It is assumed that most of the pumping is accomplished via particle entrainment in the liquid stream, but there is also some pumping down the open channel above the fluid stream. The pumps would be located in a well shielded area and should not represent a configuration or maintenance problem.

Flow slowing system: One of the most difficult challenges for the GMD concept is handling the thick stream with its very high flow rate and pumping power. An alternative is to provide a flow-slowing system. The flow slowing system, which reduces the flow-rate of the thick stream, is critical to increase the bulk temperature rise and reduce the pumping power. Both the bulk temperature rise and the pumping power are directly related to power overall energy conversion efficiency.

Two options for the flow slowing system were studied, including the “pocket concept”, and the “bag concept”.

GMD Pocket concept: In the pocket concept, the thick stream is formed in a series of horizontal channels that are open on the plasma side. Fluid is injected vertically downward at the top of each opening, creating a swirling flow with a toroidal axis. The fluid flows toroidally as it spins, exiting the pocket at the center of the vortex where the fluid temperature is the highest. Figure 5.7-3 illustrates the GMD pockets concept, showing the various systems.

The pocket structure is envisioned to be made from a high temperature material such as tungsten. The high thermal and electrical conductivity of the tungsten will help provide margin against transient heat loads as well as provide a passive stabilizing conductor for the plasma. The front edge of the pocket also provides a partial backing structure for the fast flowing surface stream.

For the pocket concept it should be possible to limit the flow rate of the thick stream to be the same as the thin stream, and the two streams could operate in series. Figure 5.7-5 illustrates a possible flow schematic. The fast flow would enter the system at the top, be collected at the bottom, be pumped back into the pocket fill manifold, and exit the bottom pockets. Since the flow rate is reduced substantially for the pocket concept, the pumping power is also substantially reduced.

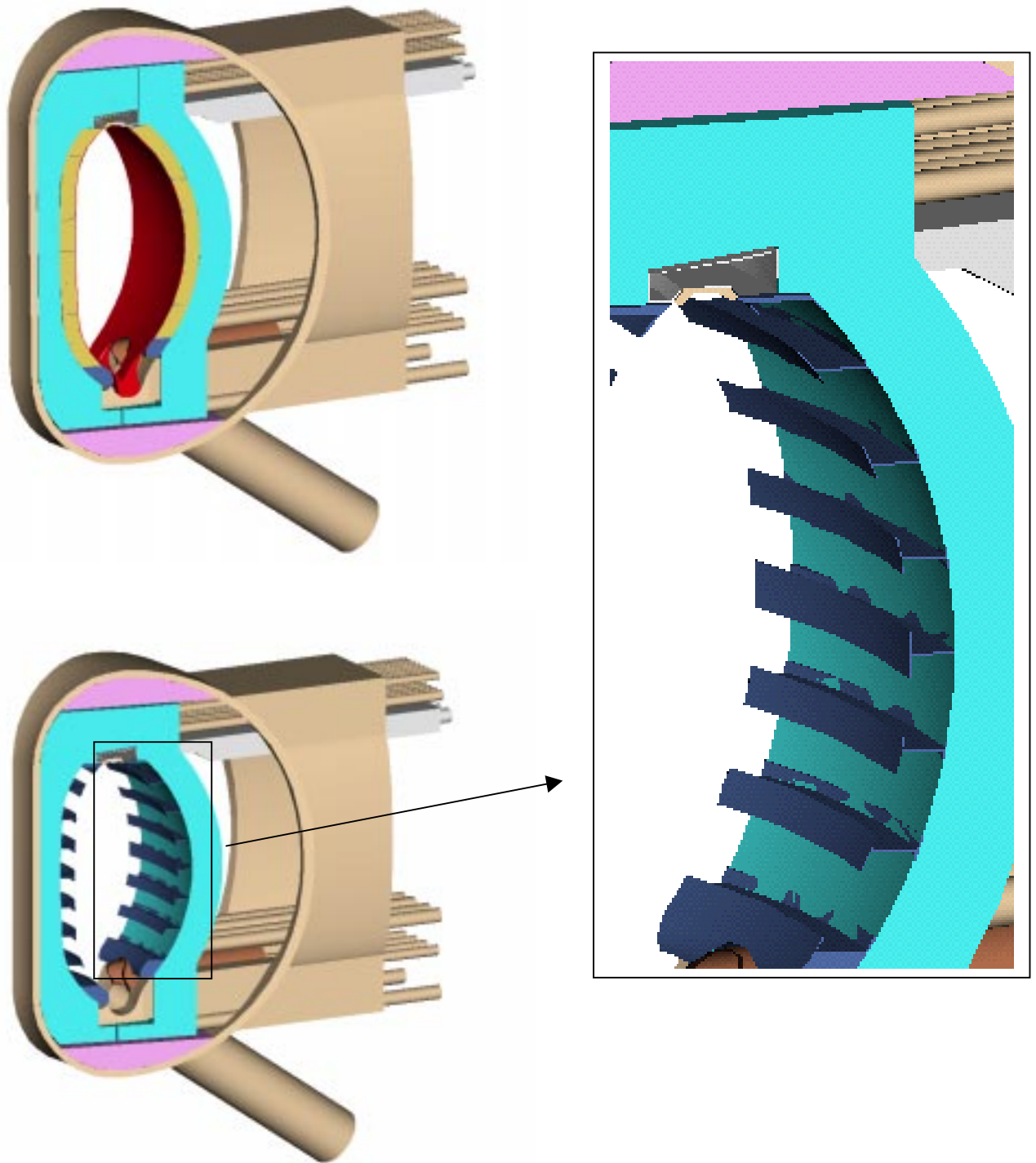


Figure 5.7-4 GMD "Pockets" concept showing overall configuration and detail of pocket structure

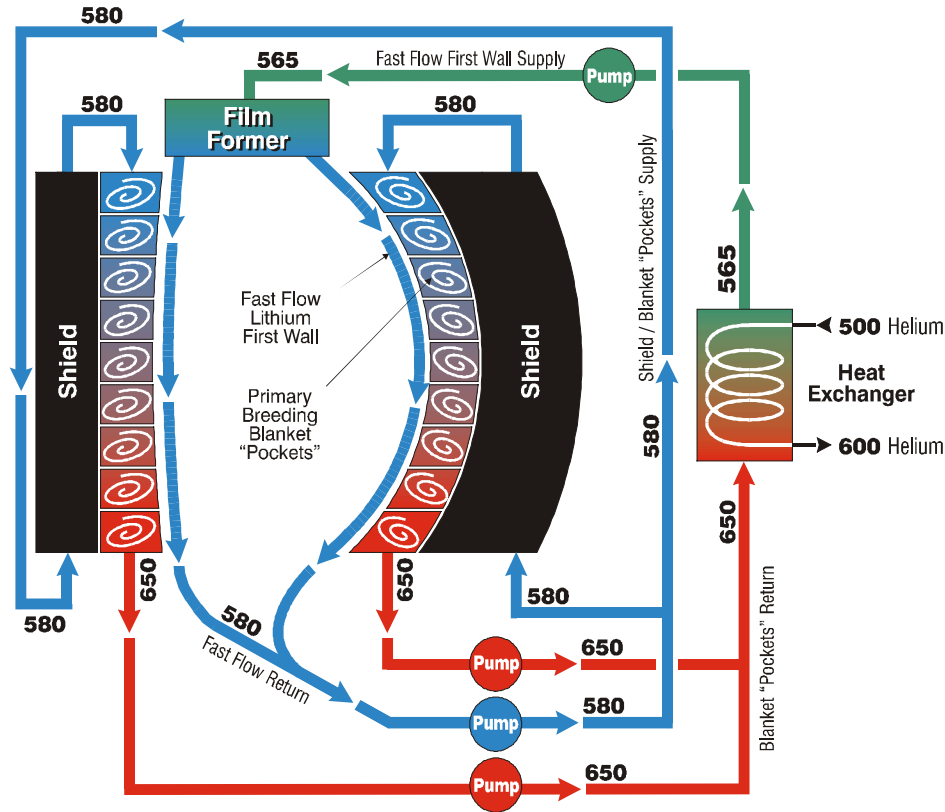


Figure 5.7-5 GMD "Pockets" – Flow / Temperature Schematic-Lithium option

Although the pocket concept may be able to reduce the flowrate, there are potential problems. First, the flow paths are tortuous and this concept may be limited to a non-conducting liquid such as Flibe to avoid MHD effects that would inhibit the swirling action of the flow. Second, there is a considerable amount of structure near the first wall that may require frequent replacement due to the high damage rate of up to 100 dpa/full power year. Third, the flow characteristics of the pockets limit the radial thickness to around 40mm, which may be insufficient to protect the backwall for the life of the reactor. Finally, the pocket structure and manifolding are somewhat complex and could be difficult to "tune" for proper operation.

GMD "Bag" concept : To address the concerns of the pocket concept, a second flow-slowsing concept is envisioned that contains the liquid in flexible, semi-permeable "bags". The bags would be the full height of the machine, and would be relatively narrow in the toroidal direction and deep in the toroidal direction. The bags could easily be deep enough to provide sufficient protection to the back structure to make it a lifetime component. Figures 5.7-6 and 5.7-7 illustrate the bag concept. The fast flowing stream would flow on the plasma side of the bags, while the bulk flow would be inside the bags.

The bags would have integral supply and return piping connections, and the flow would be controlled to provide the maximum temperature consistent with the vapor pressure of the liquid. The primary structural load on the bags would be limited to the head pressure of the liquid that is chosen and some small piping losses, but would be on the order of 3 Mpa.

The bags would be constructed of a very fine weave of wire or fiber. The material could be anything that is compatible with the fluid (SiC, W, Ta, F82H, V, etc.). A high temperature material is preferred, however, to provide protection against transient, localized loss of flow on the surface and better resistance to creep. Embrittlement of the bag fibers may not be a concern, since very small diameter fibers can remain in the elastic range and still provide a very flexible structure. Fiberglass cloth is a good example of a brittle material that is used as a flexible structure, and in this case the bags could be made of SiC fibers. Since the normal concerns about embrittlement may be eliminated, the allowable damage levels for the bags may greatly exceed the nominal 200 dpa maximum damage limit that is normally used for structural materials.

Another interesting benefit of the bag concept is that the thick liquid wall temperature and the backplate temperature can be decoupled. This is possible if we assume that the backplate is separately cooled and we are allowed to "freeze" some liquid as a thermal insulating barrier at the interface to the backplate. In this way the backplate can be made from ferritic steel (or austenitic, like 304L) and operate within its temperature limits while the main flow of liquid can operate at a much higher temperature. Freezing some material at the boundary of a molten pool is often used as a means of protecting crucibles.

For a two-stream concept such as the GMD system, two different fluids would be used. For example, the high and low melting temperature formulations of Flibe or a combination of lithium and Sn-Li may be considered. The cooler front stream fluid could be used to cool the backplate, which would mitigate concerns about leakage from separate backplate cooling circuits. Of course it must be proven that the "frozen" layer will not adversely affect the thick flow stream. In the case of the "bag" concept, the bags would contain the high melting temperature thick stream and provide a surface for the front stream to flow over. The front stream would be routed through the backplate to which the bags are attached. A frozen layer, or crust, would form both at the back of the bag to protect the structure and at the front of the bag where the fast, cool stream flows.

Concept for providing heating and diagnostic penetrations

Openings must be provided in the liquid wall for plasma heating and current drive systems and for diagnostics. The openings must be shaped to allow a smooth diversion of flow without splashing, or ejecting liquid into the plasma. An elongated shape, as shown in Figure 5.7-8, may be similar to what will work. Regardless of the shape, there must be a structure to deflect the liquid, and this structure will almost certainly be directly exposed to the plasma. For this reason, and because the heating and diagnostic systems themselves may need frequent maintenance, it is necessary to provide another cassette for each penetration. This is also shown schematically in Figure 5.7-2.

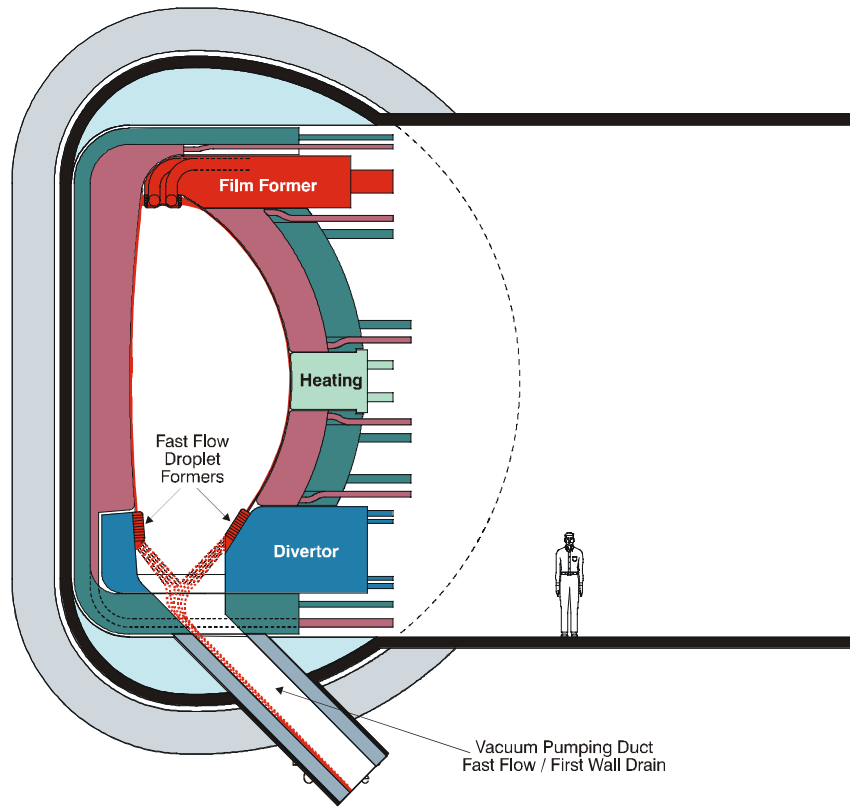


Figure 5.7-6 GMD "Bag" concept elevation view,(fast liquid flow on first wall and slow liquid contained in mesh bags)

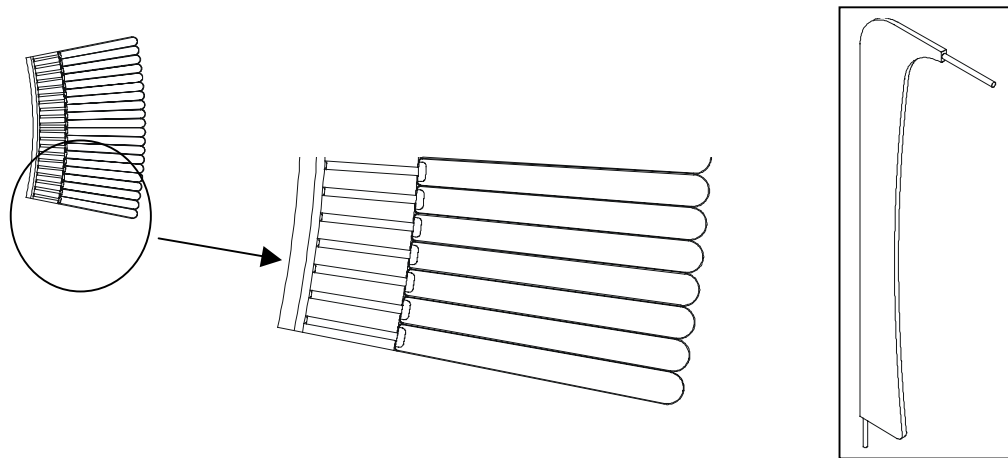


Figure 5.7-7 GMD "Bag" concept showing plan view at inboard midplane and single bag with integral inlet and outlet pipes

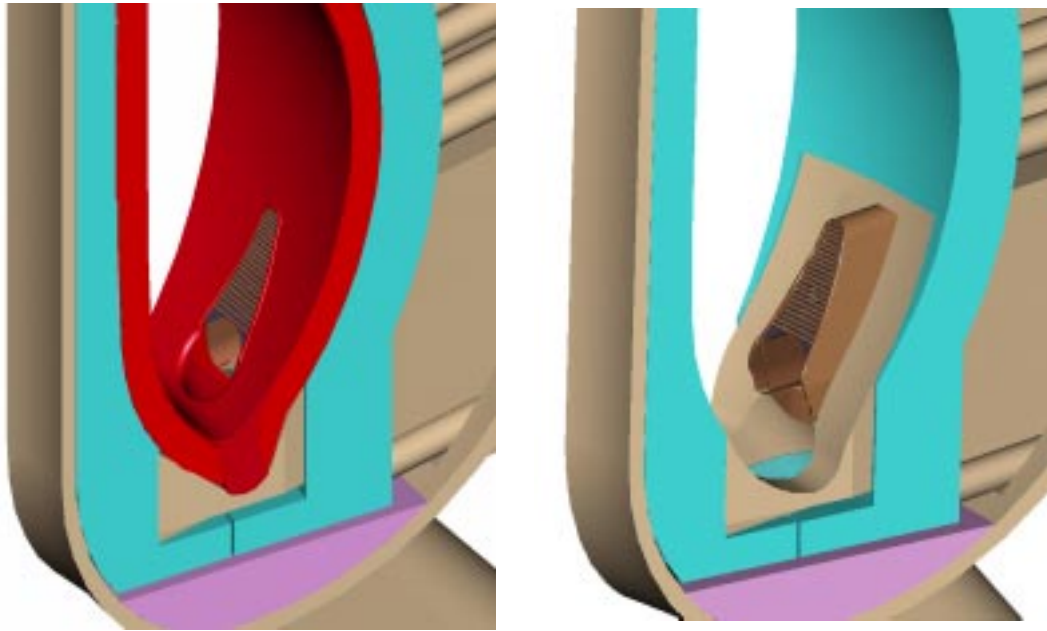


Figure 5.7-8 Possible arrangement for integral ICH grill and vacuum pumping opening

Piping arrangement

The piping arrangement for the GMD concept consists of several separate sets of pipes. The first set is for the fast flowing liquid on the plasma surface, with separate pipes for the inboard and outboard systems. The second set includes the large bulk flow pipes, also with a separate inboard and outboard circuit. All the supply pipes are integrated with the fluid supply cassettes for ease of maintenance. The exit piping is integral with the pump duct, as described above, and which carries the total flow into a reservoir from which it is pumped through a heat exchanger and back into the supply system. There are separate piping systems for each collection trough cassette and for each heating/diagnostic penetration cassette.

The pressures and temperatures for the piping systems depends on the particular liquid employed for the first wall and blanket system. A typical system is shown schematically for the GMD “pocket” concept in Figure 5.7-5.

5.7.2 Maintenance

The configuration of the first wall and blanket concept is largely governed by maintenance considerations. Each component can be assigned to one of three categories, high maintenance, low maintenance and lifetime components.

1. High Maintenance Components:

To increase the availability of the machine, it is imperative that high maintenance components can be rapidly replaced without having to disassemble the entire device. The components considered most likely to fail or require maintenance during operation include the liquid supply systems, nozzles, heating elements, diagnostics devices, and divertor elements. These components are integrated into removable cassettes. The piping, structural and instrumentation connections to these cassettes are all made from outside the torus.

This approach also provides easy incorporation of new design elements and modifications for these components by simply removing the old cassettes and replacing them with the ready-to-install new cassettes. Figure 5.7-9 illustrates the maintenance approach for the GMD "bag" concept.

2. Low Maintenance Components:

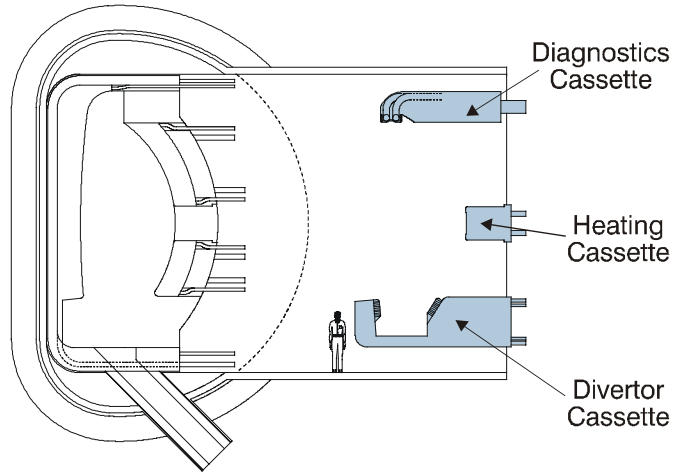
Repairing damage to the first wall / blanket / shield components or incorporating new modifications to these components will require "total sector removal". The sector consists of everything internal to the vacuum vessel boundary. The sector components are structurally integrated and are designed to be removed and replaced as a unit.

3. Lifetime Components:

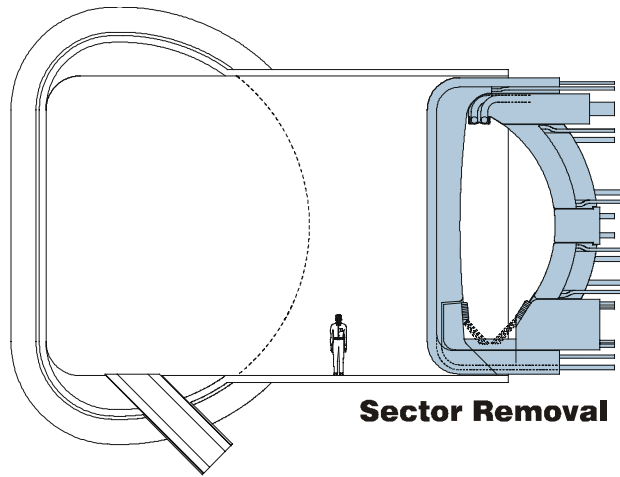
The vacuum vessel and coil sets are considered to be lifetime components and therefore need to be protected with adequate shielding. The shielding limits the neutron damage to the vacuum vessel material and makes it possible to cut, remove, replace, and re-weld sections of the vessel. If repairs to the vessel are required, the associated sector near the damaged region is removed to provide access to the vessel. If a toroidal field coil must be replaced, the three adjacent sectors must be removed, then the TF coil and associated vacuum vessel section can be removed. This is obviously an extreme event, and would not be expected to occur.

The primary reason for "total sector removal" is that there is simply no access through the back of the blanket, nor from the top of the liquid supply system to be able to insert a remote device, and certainly not enough clearance to extract the large, bulky components. In order to get to the inboard first wall / blanket region, the outboard region must be removed first. On balance, it would be easier, faster, and less risky to remove a sector module intact. This would provide the needed access to all of the components in a hot cell in order to make necessary repairs and scheduled maintenance.

Even if there was adequate access to allow for remote maintenance and remote handling of damaged components, the probability is high that components will "stick" to each other and make removal a difficult task if any of the liquid leaks and then "freezes". This situation is minimized with "total sector removal" because a component can literally



**Divertor / Heating / Diagnostics
Maintenance**



Sector Removal

**First Wall / Blanket / Shield
Replacement Maintenance**

Figure 5.7-9 Maintenance Approach for typical GMD concept

be destroyed in order to extract it. In so doing, it is likely that the adjacent or attachment components could be damaged trying to free a single component.

It is therefore deemed prudent to do all major repairs of non-cassette components outside of the machine in a hot cell room, while at the same time, a replacement sector can be in the process of being installed concurrently.

Design Issues for GMD concept

There are numerous mechanical design issues associated with the GMD concept, including:

- How to move mass quantities of liquid metal or salt in and out of the machine reliably
- How to provide sufficient access for supply piping and return ducts
- How to design the piping and nozzles for reliable operation at high fluid velocity
- How to start and stop the system safely
- How to keep the stream attached to the inboard wall (must prevent toroidal rotation of inboard stream)
- How to provide sufficient penetrations for heating and diagnostics
- How to account for image current effects from moving plasma

How to protect liquid from exposed surfaces (ie excessive vapor pressure if liquid hits hot spots)

5.8 Evaluation on Liquid Options

5.8.1 Impact of Magnetic Field on the Candidate Liquids

There are two problems with liquids crossing magnetic fields: 1-the induced currents can lead to pressure drops that tend to alter the liquid flow and, 2-a voltage appears that can lead to galvanic corrosion. The first is important for liquid metals and the latter for molten salts.

Pressure drop

The geometry is shown in Figure 5.8-1. The governing relationships are:

$$\nabla \vec{P} = \vec{J} \times \vec{B}$$

$$\vec{J} = \sigma \vec{E}$$

$$\vec{E} = \vec{v} \times \vec{B}$$

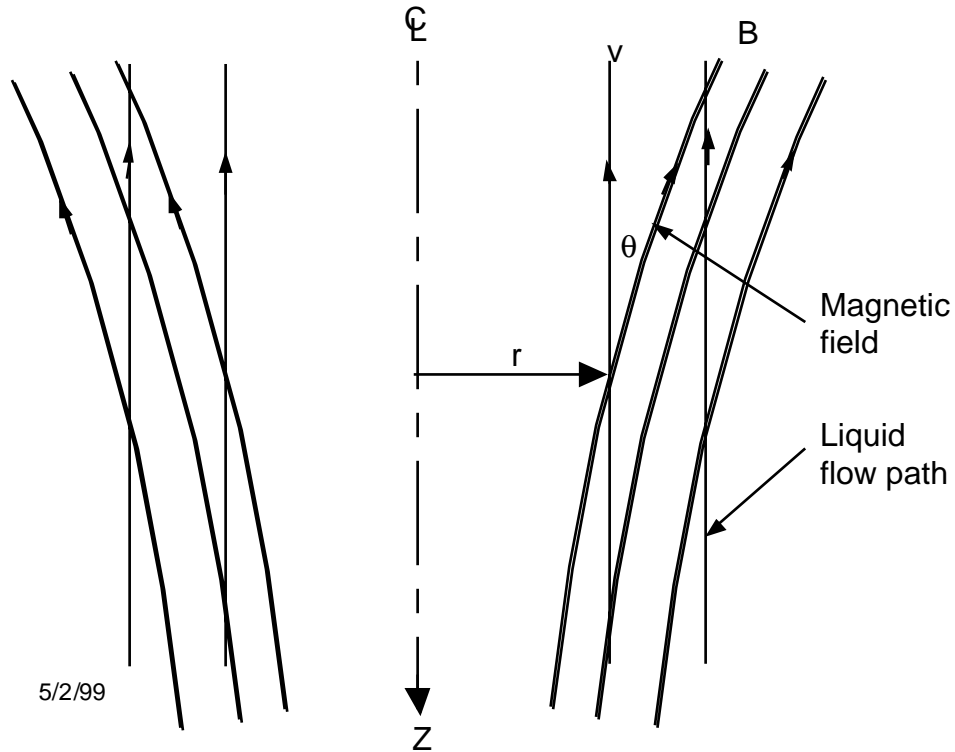


Figure 5.8.1 The geometry of the field interaction is shown above.

If the liquid is flowing only in the r-Z plane and the magnetic field has components only in the r-Z plane then the above vector equations simplify to the following:

$$E_{\phi} = vB \sin \theta$$

$$\frac{dP}{dz} = J_{\phi} B$$

$$J_{\phi} = \sigma E_{\phi}$$

The current paths are closed circular loops.

$$\frac{dP}{dz} = \sigma v B^2 \sin \theta$$

If the components of velocity in the azimuthal direction or more complex magnetic fields, there are more components to the current paths and the analysis becomes much more complex. We can compare the pressure drop per meter to that of the effect of gravity on the flow.

$$P = \rho gh = \frac{1}{2} \rho v^2 = head$$

As an example we take $v=10$ m/s, $B=3$ T, $\theta=10^\circ$

Table 5.8.1 Magnetic interactions.

	Flibe	Sn ₈₀ Li ₂₀
$\sigma, \Omega^{-1} m^{-1}$ @ 550° C	180	1.67×10^6
$\rho, kg/m^3$	2000	6000
$dP/dz, Pa/m^4$ or J/m^4	2813	2.61×10^7
$g, J/m^4$	19,600	58,800
$0.5 \rho v^2$	10^5	3×10^5
$(dP/dz)/\rho g$	0.14	461
$1 m \times (dP/dz) / 0.5 \rho v^2$	0.028	90.3

The last two rows in the Table 5.8.1 show that for Flibe the magnetic interaction is somewhat small compared to the forces of gravity or to changes in the velocity or inertial forces of the liquid whereas for Sn₈₀Li₂₀ the magnetic forces are huge compared to the gravity or inertial forces. It will be easy to push molten salts across magnetic fields but not so for liquid metals. If the flow rather than being 10° relative to the magnetic field is 0.01° then the kinetic energy change in one meter is only 10%. When other components of field and velocity are considered the problem becomes more complicated with some components canceling each other somewhat. If insulators are postulated to solve the problem then they need to be considered part of the system relative to survivability and development needs.

Galvanic corrosion

Galvanic corrosion has to do with voltage developed at a liquid electrode interface. When this voltage drop exceeds the chemical potential, the chemicals can be oxidized or reduced at the electrode. Be⁺ becoming Be metal, or F⁻ becoming F atoms or Li⁺ becoming Li atoms. This should be avoided when the voltage is less than of order unity.

$$\Phi = dvB \sin \theta$$

where d is the distance along the current flow path before the voltage increase is reduced by an electrode. Using the example above we get

$$\Phi = dvB \sin \theta = d \times 10 \times 3 \sin 10^\circ = 5.2d$$

For only one volt drop we would have to have an electrode every 0.2 m or 0.4 m if the entire voltage drop is taken equally at each electrode. The corrosion rate is current

limited and so depends on the entire closed current path. This subject is complex and is going to need careful attention by electrochemistry and is an important problem for molten salt usage.

5.9 Information Required for Scientific Evaluation

The information required for thick liquid wall concepts to facilitate performing the scientific evaluation is listed in Table 5.9-1.

Table 5.9.1 Scientific Evaluation Information

Parameters		
Sketches of the geometry of the in-vessel components	Figure 5.2-3	Figure 5.2-3
Outline of FW/blanket/shield radial build including approximate dimensions	Figure 5.3.1-12	Figure 5.3.1-12
Candidate materials - PFC - Structure - Breeder/coolant	W /ODFS W/ODFS Flibe	Vanadium Vanadium Lithium
Estimated values of the following parameters, based on a peak neutron wall loading of 10 MW/m ² , a peak surface heat flux of 2 MW/m ² , and a peaking factor of 1.4 for both a) Coolant parameters (temperature, pressure) at inlet/outlet of: • plasma facing surface (liquid FW) • FW cooling channel (solid FW) • breeding zone b) Maximum/minimum temperatures of • breeder material • structural material c) Maximum primary and total (primary+secondary) stress in the structural material d) Tritium breeding ratio (Overall TBR estimated from local 1-D calculations with heterogeneity) e) Maximum power density in structure, breeder and coolant material f) Energy multiplication in in-vessel components g) Maximum structure damage Structure activity, decay heat, and radwaste	550/600 °C 1 MPa NA 550; ΔT = 4.7 °C 600/550 °C 650/550 °C 1.24 90% Li-64 W/cc at 7 MW/m ² 1.13 200 dpa Class C	400/500 °C 1 MPa NA 500; ΔT= 10.9 °C 500/550 °C 600/550 °C 1.74 90% Li 54 W/cc at 7 MW/m ² 1.18 200 dpa Class C

classification		
For a full sector estimates for the following parameters have to be provided, assuming the heat loads given under D):	(see Figure 5.9-1 for FRC, ST)	
a) total surface heat load	54.8 MW	54.8 MW
b) total heat load (surface heat load + volumetric heat generation)	438 MW	438 MW
c) coolant mass flow rate (either total or for the different zones, depending on the concept)	3.9×10^4 kg/s	9.65×10^3 kg/s
d) coolant velocities in FW and breeding zone	10 m/s	10 m/s
e) coolant inlet and outlet manifold sizes	outboard: 2.75 x 0.5 m ² Inboard: 0.66 x 0.5 m ²	outboard: 2.75 x 0.5 m ² Inboard: 0.66 x 0.5 m ²
f) coolant inlet and outlet piping location and sizes	2 pipes at 1 m diameter located at top and bottom of the reactor	2 pipes at 1 m diameter located at top and bottom of the reactor
g) coolant pumping power	6.87 MW	1.75 MW
h) a brief indication of structural support needed	Figure 5.2	Insulator required
i) identification of external primary or secondary coolant pumping system		

A 2400 MW fusion power with blanket multiplication of 1.18. The blanket power is $2400 \times 0.8 \times 1.18 = 2745.6$ MW

$\Delta T = P / \dot{m} C = 2.7456 \times 10^9 \text{ J/s} / (4.552 \times 10^5 \text{ kg/s} \times 2380 \text{ J/kgK}) = 2.534 \text{ }^\circ\text{C}$ temperature rise on average passing through the blanket and shield

$\dot{m}' = 2.7456 \times 10^9 \text{ J/s} / (50^\circ\text{C} \times 2380 \text{ J/kgK}) = 2.307 \times 10^4 \text{ kg/s}$ mass flow rate to the heat exchanger

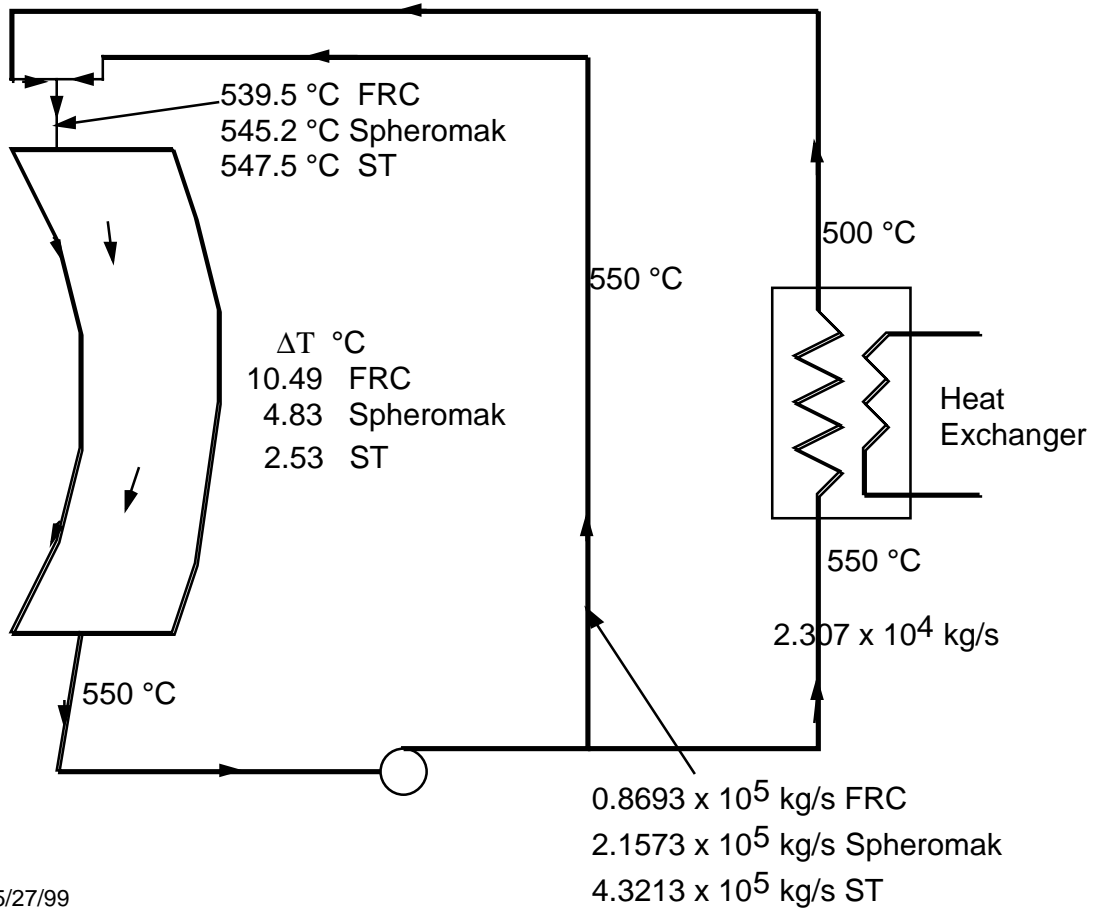


Figure 5.9-1 Temperature Flow Diagram of FRC, Spheromak, and ST.

5.10 Key Issues and R&D

Among the challenges of liquid walls being addressed in APEX are: 1) determining limits on the amount of material allowed to evaporate or sputter from liquid surfaces based on sophisticated plasma edge modelling, 2) evaluating temperature profiles on fast flowing free-surface liquids in the fusion environment, 3) establishing hydrodynamic models and exploring various thick-liquid formation schemes in different MFE confinement configurations, 4) developing a 3-D free surface hydrodynamic and heat transfer simulation code that incorporates MHD effects, 5) assessing multidimensional effects (e.g. penetrations) and the impact of time-varying magnetic fields on the flow characteristics, and 6) identifying high-temperature structural materials that are compatible with flibe and SnLi for use in nozzles, vacuum vessel, and other regions behind the liquids.

R&D

1. Identification of the most promising hydrodynamics configurations with respect to different MFE confinement schemes.
2. Experimental data on the achievable minimum liquid surface temperatures w/o MHD effects for turbulent Flibe and MHD laminarized lithium/tin-lithium flow under high power density conditions.
3. Identification of practical heat transfer enhancement schemes necessary for minimizing liquid surface temperatures.
4. Experimental characteristics of small-scale hydrodynamics configurations applicable to MFE confinement schemes w/o MHD effects.
5. Computer simulation results of MFE relevant 3-D free surface liquid wall thermal and hydrodynamics performance with MHD effects. In particular, hydrodynamics characteristics near the penetrations and supply and return lines.
6. Modelling and test results of the maximum allowable evaporation rate from the liquid surface with respect to different MFE confinement schemes.
7. Hydraulic component development for liquid walls. Implementation of the liquid wall idea relies on the successful development of inlet and exit nozzles that are drip and splash free and are efficient in head recovery at outlet.